An integrated approach to assessing mobile crane mat requirements based on a novel approach to ground bearing pressure calculations and a redefining of crane mat selection and optimization

by

Ghulam Muhammad Ali

A thesis submitted in partial fulfillment of the requirements for the degree of

Doctor of Philosophy

in

Construction Engineering and Management

Department of Civil and Environmental Engineering
University of Alberta

ABSTRACT

Modular construction is adopted to increase construction efficiency and curtail waste. The fortitude of modular construction is high-capacity mobile cranes, of which hydraulic and crawler cranes are the most widely used. With the surge in weight of modules, the mobile crane's ground bearing pressure also escalated. The traditional primary status quo technique to avoid ground failure is to estimate the ground bearing pressure employing the fundamentals of statics, considering uniform ground bearing pressure under hydraulic crane mats and crawler crane tracks along the width of the track, which contradicts the finite element analysis results.

Additionally, these cranes count on the stability of the ground for safe rigging and heavy lifting. The conventional approach uses timber crane mats under the crane tracks/outriggers. The crane rental industry's primary cost driver is crane mat crowding (2–3 layers of timber crane mats), directly linked with crane mat selection, on-site optimization, and crane mat design. Moreover, timber crane mats are not durable as they last for 2–3 years only and entail wood waste (crashed timber) as a by-product. The proposed research aims to reassess the crane mat requirement on-site by proposing a novel mobile crane ground bearing pressure calculation methodology to overcome the limitations of the traditional method. In contrast to the traditional approach, the present study proposes a new methodology to not only calculate the ground bearing pressure under mobile crane tracks/crane mats employing a combined loading approach but also to calculate the ground bearing pressure anywhere on the crawler crane track or hydraulic crane mat area, which can establish the ground bearing pressure profile in detail. In the form of a computer application, the proposed ground bearing pressure methodology for hydraulic cranes is linked with five crane mat selection criteria for the practitioners to select the suitable crane mat for the job.

This thesis proposes an agent-based greedy algorithm and Reinforcement Learning approach for automated crane mat layout optimization as an innovative approach to developing sustainable crane mat layouts. This approach takes into account the site constraints and can be applied to mitigate crane mat crowding on construction sites. The crane mat optimization, using both methods, is applied to achieve the maximum area covered with the minimum number of crane mats used. The results demonstrate that the practitioner time spent preparing a crane mat layout plan/drawing can be reduced considerably, in some cases by minutes, with more uniform and cost-effective crane mat optimization outcomes.

The allowable soil bearing capacity is another substantial factor affecting the selection and optimization of crane mats, exceeding the ground bearing pressure under the crane mat for safe operation. Existing allowable soil bearing capacity equations, which are based on shallow foundations, need to incorporate crawler and hydraulic crane ground footing area with variable loading. Typically, crane rental companies rely on the client to provide the allowable soil bearing capacity value based on which to estimate the requirements for remedial efforts to stabilize the ground. In this regard, crane mats and soil compaction can be applied to overcome poor soil bearing capacity and ensure a safe lift. The pragmatic approach adopted in this thesis is to develop an algorithm, formalized in a computer application, that can estimate the allowable soil bearing capacity (particularly in the context of crane work) based on a construction site's geotechnical reports and crane ground footing.

PREFACE

This thesis is the original work of Ghulam Muhammad Ali. Four journal papers and six conference papers related to this thesis have been submitted or published as listed below.

1. **Ali, G. M.**, Bouferguene, A., and Al-Hussein, M. (Submitted July 2022). "Crane mat Layout Optimization Based on Agent-Based Greedy and Reinforcement Learning Approach." Journal of Construction Engineering and Management.
2. **Ali, G.M**., Mansoor, A., Liu, S., Bouferguene, A., and Al-Hussein, M. "A decision support system for estimate mating allowable soil bearing capacity for mobile crane work." Proceedings of the 2nd International Conference on Civil Engineering Fundamentals and Applications (ICCEFA'21), Nov. 21–23.
3. **Ali, G.M**., Imam, H.Z., Rana, S., Ahmad, R., Bouferguene, A., and Al-Hussein, M. "Use of frozen silt crane mat, an alternative to crane timber crane mat to minimize energy as ninth waste and to reduce CO_2 emissions." Proceedings of the 2nd International Conference on Civil Engineering Fundamentals and Applications (ICCEFA'21), Nov. 21–23.
4. **Ali, G. M.**, Mansoor, A., Liu, S., Olearczyk, J., Bouferguene, A., and Al-Hussein, M. (2021). "Decision support for hydraulic crane stabilization using combined loading and crane mat strength analysis." Automation in Construction, 131, 103884.
5. **Ali, G. M.**, Tamayo, E.C., Mansoor, A., Olearczyk, J., Bouferguene, A., and Al-Hussein, M. "An automated approach to generating optimized crane mat layout plans." Accepted (Apr., 2021) for publication in Proceedings of the CSCE Construction Specialty Conference, Niagara Falls, ON, Canada, May 26–29.

6. **Ali, G. M.**, Kosa, J., Bouferguene, A., and Al-Hussein, M. (2021). "Competitive assessment of ice and frozen silt crane mat for crane ground support using finite element analysis." Journal of Construction Engineering and Management, 147(6), 04021038.

7. **Ali, G. M.**, Olearczyk J., Bouferguene A., and Al-Hussein, M. (2021). "Implementation of combined loading to calculate ground bearing pressure under crawler crane tracks." Journal of Construction Engineering and Management, 147(7), 04021051.

8. **Ali, G. M.**, Mansoor, A., Liu, S., Olearczyk, J., Bouferguene, A., and Al-Hussein, M. (2021). "Simulation of ground bearing pressure profile under hydraulic crane outrigger crane mats for the verification of 16-point combined loading." Procedia Computer Science (Proceedings of the 2nd International Conference on Industry 4.0 and Smart Manufacturing, Linz, Austria, Nov. 23–25, 2020), Vol. 180, pp. 482–491.

9. **Ali, G. M.**, Mansoor, A., Olearczyk, J., Bouferguene, A., and Al-Hussein, M. (2020). "Attaining global optimized solution by applying Q-learning." Proceedings of the European Modeling and Simulation Symposium, Sep. 16–18, pp. 112–119.

10. **Ali, G. M.**, Al-Hussein, M., Bouferguene, A., and Kosa, J. (2019) "Competitive finite element analysis (ANSYS) for the use of ice & frozen silt as a supporting structural crane material, an alternative to the traditional crawler crane mat material (s355, g40.21 & Coastal Douglas-Fir)." Proceedings of the 7th CSCE International Construction Specialty Conference (jointly with Construction Research Congress), Laval, QC, Canada, Jun. 12–15, 10 pages.

Dedication

This thesis is dedicated to my wife, Gulfishan, my two little velociraptors, Omer and Mohid, and my little princess, Khadija, for their continuous support since the early stages of my research. Without their support, this thesis could have been completed a term earlier.

ACKNOWLEDGEMENTS

First, I want to thank God for providing me with the strength, thoughts, health, and supportive people needed to finish my research work.

I would like to express my deepest gratitude and sincere appreciation to my supervisors, Dr. Ahmad Bouferguene and Dr. Mohamed Al-Hussein, for their guidance, motivation, immense knowledge, and continuous support throughout my research and writing of this thesis.

I greatly appreciate the commendable assistance and encouragement provided by Jonathan, Claire, Kristin, Hamida, Dr. Jacek Olearczyk, and other faculty members, staff, and graduate students of the Construction Engineering and Management research group.

TABLE OF CONTENTS

LIST OF TABLES

LIST OF FIGURES

LIST OF ABBREVIATIONS

ASBC	Allowable soil bearing capacity calculator
ATBA	Actual Track Bearing Area
ATMBA	Actual Total Crane mat Bearing Area
COG	Center of Gravity
CoLMA	Combined loading Crane mat Analysis
ETBA	Effective Track Bearing Area
ETMBA	Effective Total Crane mat Bearing Area
FEA	Finite Element Analysis
GBP	Ground Bearing Pressure
GHG	greenhouse gases
GRG	Generalized Reduced Gradient
PL	Pad Load(s)
RL	Reinforcement Learning
SARSA	State-Action-Reward-State-Action
VB	Visual Basics

CHAPTER 1: INTRODUCTION:

The adoption of modularization in the heavy construction industry has primarily modified the design and project delivery paradigm. Though many factors are involved, the main cost driver is shifting major construction work to an indoor environment. In this approach, modules are manufactured in a controlled indoor environment, converting the construction process to more effective and productive manufacturing. As a result, many practitioners, over time, tried to front-load these modules with maximum functionalities to minimize the related on-site construction activities. This increase in functionalities also affected the module's weight to be transported and installed at the final position, which has risen to tens, if not hundreds, of metric ton (Gamayunova et al. 2019). This rise in weights tends to use heavy mobile cranes with high lifting capacity for module installation, with increased structural complexity and heavier weights. As a result, the resultant pressure of the crane and payload on the ground can be so high that gaining a better understanding of ground bearing pressure (GBP) has resurfaced as an essential safety issue in the heavy construction industry, modular construction in particular. About the ground stability under mobile cranes, it is important to mention that soil stability (11%) is categorically linked to most crane accidents from 1997 to 2003 in the US (Beavers et al. 2006). Not only that, in Malaysia, from 2011 to 2015, overturning of mobile cranes due to tipping covers about 45% of all crane accidents, which are directly or indirectly related to human error in (incorrectly) estimating GBP and/or allowable soil bearing capacity (Milazzo et al. 2016). Many other studies also revealed ground failure as the primary cause of crane accidents (Milazzo et al. 2016, Cho et al. 2017, Raviv and Shapira 2018, Abdul Hamid et al. 2019, Aikhuele 2019, Dhalmahapatra et al. 2019). Cranes lift heavy and oversized objects and move them to their required location.

Usually, there are two types of mobile cranes, crawler cranes and hydraulic cranes. Both types, in general, are composed of two major parts, a moving part (superstructure) and a stationary part (carrier) (see Section 2.1). For crawler cranes, the crane is supported by tracks, and in the case of hydraulic cranes, the outriggers are used to support the crane. One of the advantages of using a hydraulic crane over a crawler crane is the flexibility of speedy mobilization to the job site (Shapiro and Shapiro 2010). Due to the self-extendable boom (hydraulic boom), the crane setup time is shorter than the lattice boom crawler cranes. Not only that, but the hydraulic cranes are also used for setting up heavy crawler cranes on construction sites. In multiscale construction projects, crawler cranes are often preferred since crawlers can lift hefty human-made structures and, if necessary, travel with the payload (Becker 2001, Shapiro and Shapiro 2010). In practice, the ground support design for mobile crane stability presupposes the evaluation of the pressure under the tracks of the crawler crane (or under the outriggers in the case of a hydraulic truck crane). Traditionally, according to a status quo GBP calculation procedure, the weights of the crane-payload system components are assumed to be static forces that generate pressure on the ground through the support layer, usually in the form of crane mats. Practitioners use these crane mats (wood or steel) to uphold an overall pressure less than the ground bearing capacity. The GBP calculations' basis is that the GBP along the width of the crane track (crawler crane) and under the hydraulic crane mat is uniform.

Ali (2018), meanwhile, in conducting finite element analysis (FEA) on the behaviour of crane mats under crawler crane tracks, concluded that the GBP also varies along the width of the crane track, contrary to the findings generated by traditional GBP calculations using various software programs or GBP charts (American-Hoist 1979, Manitowoc 2019). The research conducted by Ali (2018) found that the four edges (left-front and left-rear, right-front and right-rear) of one crawler track exert different pressure values instead of only considering the front and rear for each of the two tracks (see Figure 1.1). Ali (2018) also found that GBP under hydraulic crane outrigger crane mat is non-uniform, which illustrates that the GBP under all four corners of a crane mat is not the same. The GBP values show 4-point GBP under each outrigger crane mat, making 16-points (see Figure 1.2). The traditional GBP calculation methods can be misleading ignoring the non-uniform nature of GBP under hydraulic crane and crawler crane.

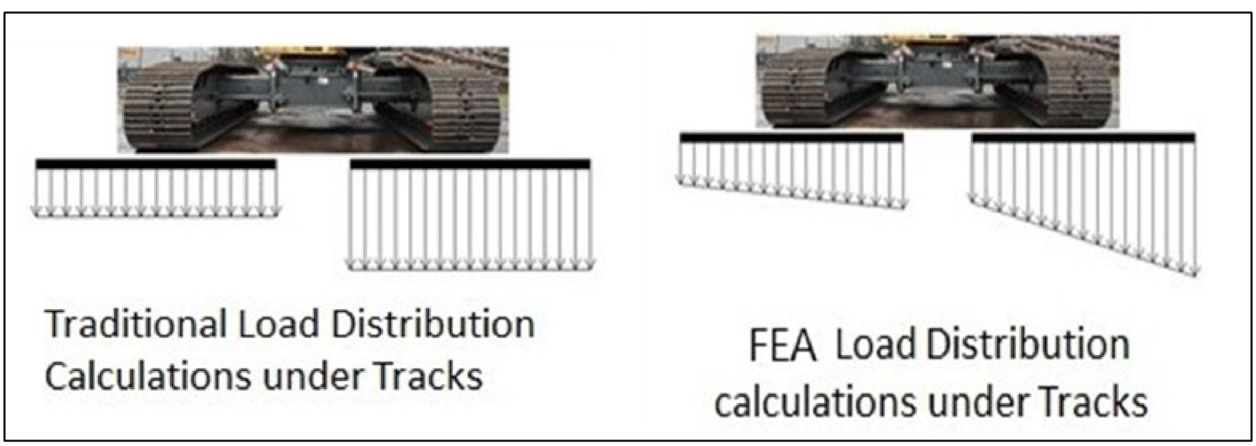

Figure 1.1: Traditional and FEA GBP under crawler crane tracks

As recently as a few years ago, these GBP variations could have been ignored, but now, when every lift is categorized as a critical lift for the project and workers, ignoring these minor variations can lead to severe consequences resulting from ground failure. Ali (2018) applied FEA and found that the resulting GBP values along the track width were higher as compared to those generated by traditional GBP values under the same boundary conditions. Moreover, it was observed that a crane mat designed using traditional GBP values will not be sufficient to ensure safe lifting operations, as the GBP values associated along crawler track width are higher than those associated with a traditional GBP approach. This also creates serious concerns regarding the safety of the workers operating in the vicinity of the crane, as failure of a crane mat can lead to crane tipping. As stated above in this regard, many crane accidents are the direct result of ground failure under mobile crane loading. As such, proper calculation of the GBP under the crane is essential for ensuring the stability of mobile cranes.

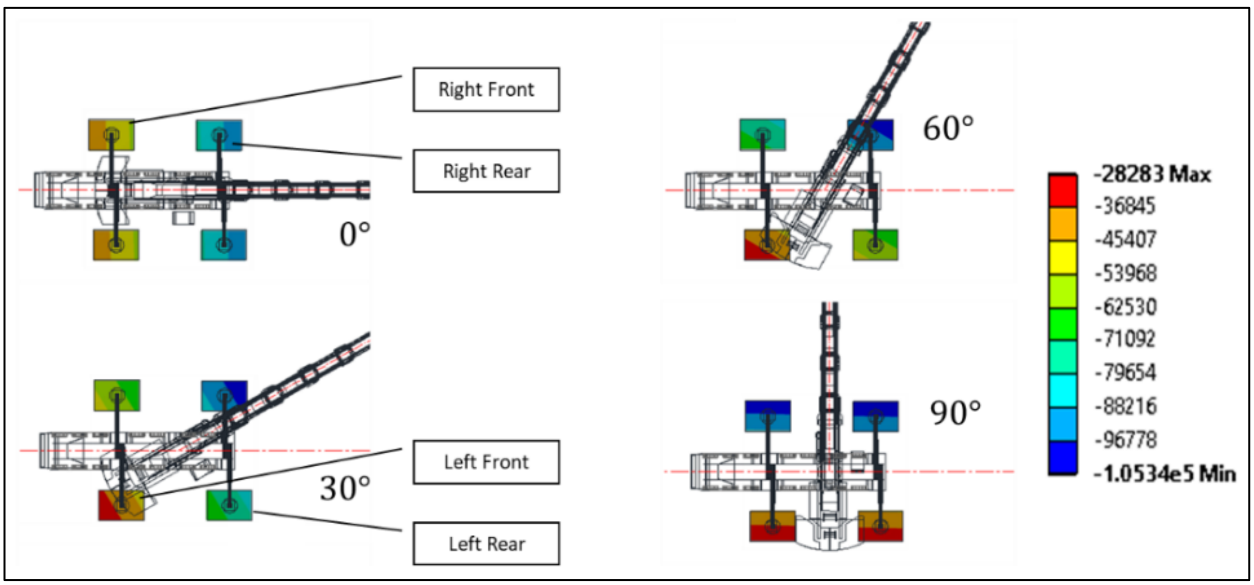

Figure 1.2: FEA GBP (Pa) variation under hydraulic crane mat along with crane superstructure slew

Moreover, due to these shortcomings in the traditional approach to GBP calculations, practitioners tend to over-design (safety factor of 3~5) crane mats or apply crane mat crowding (2–3 layers of crane mats) to overcome these variations (i.e., the risk of "unknown unknowns"). This over-design or crowding of crane mats, in turn, leads to wastage of timber resources. Targeting this research gap with respect to GBP estimation, the research described in this thesis develops a novel algorithm based on the basic concept of combined loading to compute GBP under crawler crane tracks (further distributed using crane mats) and hydraulic crane mats (Hibbeler 2011). FEA is applied for verification purposes. Furthermore, a computer application, '*CoLMA*,' is developed in Visual Basic (VB) that calculates the GBP profiles and displays them in graphical form for ease of use. In addition to performing the GBP calculations and generating a graphical display, the developed application incorporates crane mat strength analysis, based on five crane mat strength parameters, as the basis for checking the suitability of a given crane mat for a particular job. In this regard, the work published in Duerr (2010) and Duerr and Duerr (2019) involved the development of a practical procedure for the selection of timber crane mats based on the allowable deflection of the crane mat, of crane mat length based on allowable soil bearing capacity, of crane mat length based on the bending and shear stress developed in the crane mat during loading, and of the compressive strength limit.

The first task with respect to crane stability, it should be noted, is to ensure that the ground's soil bearing capacity can accommodate the pressure due to the crane's compounded weights and its payload to ensure cranes can operate safely on the construction site. The crane industry uses the soil bearing capacity calculations derived from shallow foundation design. Crane rental companies rely on clients' data regarding allowable soil bearing capacity value to plan the crane mats and soil compaction. However, despite the importance of GBP for the safety of crane operations, several relevant aspects need additional research that would bridge the gap between analyses and practitioners' rules of thumb. The outcome of this endeavour is an algorithm in the form of a computer application that can calculate allowable soil bearing capacity for crane work

On the construction site, there are two ways to overcome this soil bearing capacity issue, (i) using compacted aggregate to increase the soil bearing capacity; and (ii) using layer(s) of crane mats to distribute the ground bearing pressure to make it less as compared to the allowable soil bearing capacity. Higher capacity crane operation increased crane mats utilization on the construction site for every crane work, regardless of the ground condition. The surge also initiated crane mat layout plans/drawings preparation for every crane work on the construction site. Figure 1.3 explains the process of crane mat laying in detail. Usually, the crane mat layout plan/drawings' preparation takes 20~30 minutes for a practitioner (field observation[1]) to complete, based on the site

[1] NCSG (Northern Crane Services Group, Edmonton, Alberta, Canada)

constraints. An algorithm can save the time consumed by the crane mat layout plan/drawing preparation, implementing the same constraints for the automated crane mat layout plan/drawing preparation. By integrating an algorithm, the crane mat layout can be optimized to minimize the number of crane mats required. The algorithm proposed herein is based on an agent-based greedy optimization and reinforcement learning (RL) approach in which a practitioner's preparation of the crane mat layout plan/drawing is simulated. The proposed application will also assist practitioners at the planning stage to estimate the total crane mat requirement for a project in a more accurate and timely manner, thereby boosting efficiency and performance from the early project planning stages to execution.

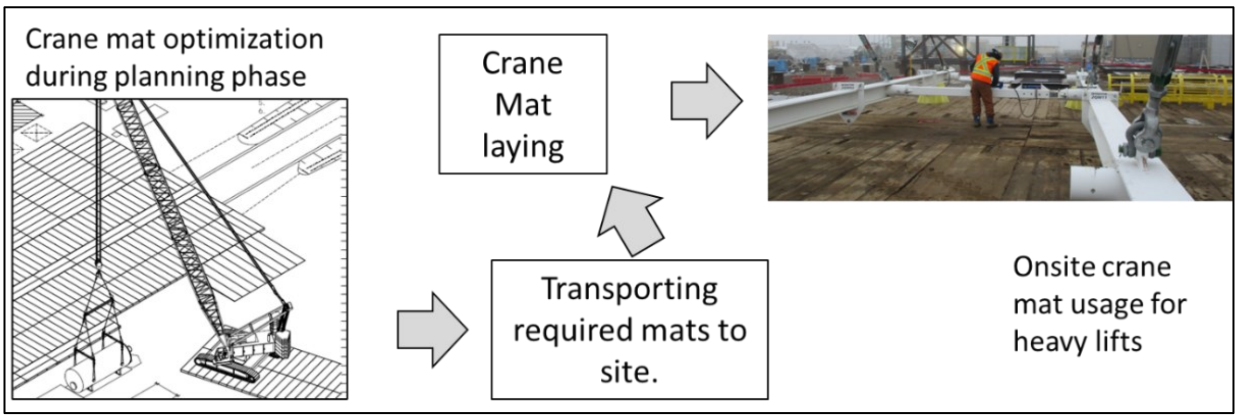

Figure 1.3: Lifecycle of crane mat planning to utilization

The crane industry in Canada uses 2–3 layers of crane matting for crane work, as discussed earlier. Moreover, timber crane mats are not durable as they only last for 2–3 years and entail wood waste as a by-product (see Figure 1.4). With the espousal of the modular construction archetype, the demand for crane mats has augmented. Market research conducted by Golden Environmental Crane mat Services (2015) documented this surge. As per their report, Canada's total annual crane mat demand was 450,000–750,000, although annual crane mat production in North America in 2014 was approximately 300,000–600,000, and the number of crane mats manufactured in Canada alone in 2014 was approximately 20,000–25,000. The crane mat industry amplified 200% from 2009 to 2014 (Golden Environmental Mat Services 2015). This research aims to overcome this gap in industry practice with respect to crane mat crowding by generating a GBP profile based on actual crane mat requirements and optimizing the crane mat layout accordingly.

Environmental pollution, it should be noted in this regard, is a global issue of growing concern that poses a significant threat to industries unless meaningful change can be brought to bear (Jituri et al. 2018a, 2018b). Adverse environmental effects can be thought of as 'green wastes'. As in lean production, eight wastes are categorized under green waste: greenhouse gases (GHG), eutrophication, excessive resource usage, excessive water usage, excessive power usage, pollution, rubbish, and poor health and safety (Garza-Reyes 2015). In 2015, Canada's total GHG emissions was 722 mega tonnes (Mt) of CO_2eq, as shown in Figure 1 (The Canadian Press 2014, Government of Canada 2018). Residential, commercial, and industrial buildings in particular are responsible for 17% of Canada's GHG emissions (Koskela et al. 2013). The International Energy Agency (IEA) has highlighted the need for energy efficiency measures to reduce by two-thirds the energy intensity of the global economy by 2050 (Apostolos et al. 2013). Canada in particular contributes 2% of global emissions and has the highest emissions per capita (Union of Concerned Scientists 2020). Apart from government initiatives to curb emissions, the construction industry is increasingly seeking solutions to boost productivity and reduce its carbon footprint. Nevertheless, the construction industry accounts for approximately 50% of natural resource use (including 70% of wood resources), and this is an important contributing factor in this sector's high levels of CO_2 emissions (Bergman et al. 2014).

Figure 1.4: Examples of inefficiencies in current crane mat practice

The modular method uses lean principles to convert internal processes to external ones and reducing project completion time and CO_2 emissions. Al-Hussein et al. (2009) conducted a comparative study of the construction of a residential building in which both construction approaches (traditional and modular) were applied and analyzed. They found that on-site construction produces 431 metric ton of CO_2 emissions, whereas modular construction (off-site construction) produces only 247.23 metric ton of CO_2 emissions, representing a 42.6% reduction. Another indicator of carbon footprint is waste of energy resources. In this context, the timber crane mat lifecycle (from embodied emissions to disposal) represents a significant source of CO_2 emissions. A mind map of the CO_2 emissions associated with crane mat use is shown in Figure 1.5.

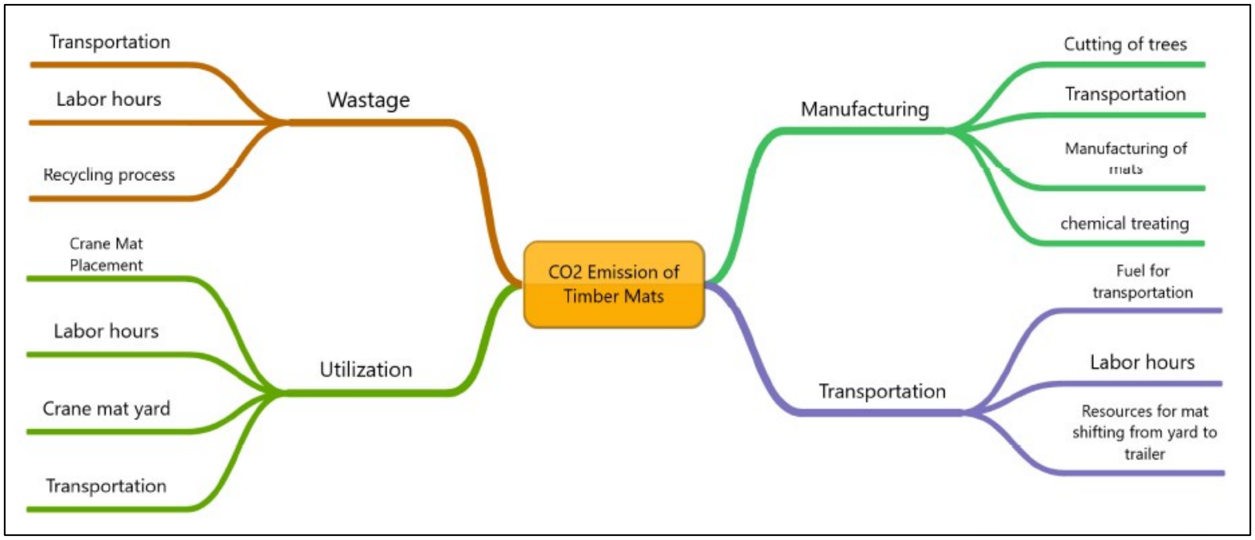

Figure 1.5: CO_2 emissions linked with crane mats

To address the environmental and safety issues noted above, the present research develops a novel approach to carrying out GBP calculations. The approach, in the form of a VB application, is then integrated with industrial crane mat design criteria to ensure the suitability and adequacy of the crane mat requirements on a construction site. This research also targets the as-yet unexplored area of crane mat optimization by building a VB application that can generate crane mat layout plans/drawings based on a novel agent-based greedy/RL approach. The developed approach can be applied to minimize crane mat usage on a given construction site, resulting in a reduction in the capital and operational costs, and CO_2 emissions associated with the crane mat lifecycle. The developed application achieves this by generating allowable soil bearing capacity estimates, particularly for crane work, based on the geotechnical data and crane ground footing. The developed application for the soil bearing capacity can further reduce the usage of crane mats for heavy cranes, further reducing the capital and operational costs and the CO_2 emissions linked with crane mat lifecycle.

1.1. Motivation

The primary motivation of this research is to improve the environmental and safety performance of crane operations on construction sites by streamlining crane mat planning/layouts. As a construction worker while working around heavy mobile cranes, the first fear is the failure of lift plan. A lift plan is composed of many sections, and one of them is the crane ground support, as shown in Figure 1.6. The section of crane ground support in a lift plan consists of GBP calculations, crane mat structural analysis, crane mat layout and allowable soil bearing capacity calculations. In specific, the aim is to approach the crane track/outrigger by developing a novel approach to GBP calculations integrated with intelligent crane mat selection criteria, crane mat optimization, and a robust algorithm for calculating the allowable soil bearing capacity for safe high-capacity crane operation. The two most significant contributions of this research are the development of the aforementioned novel GBP calculation method (which promotes the safety of workers during crane operations) and the use of an agent-based greedy/RL approach for the optimization of crane mats on a construction site (reduction of the lifecycle CO_2 emissions associated with crane mat use).

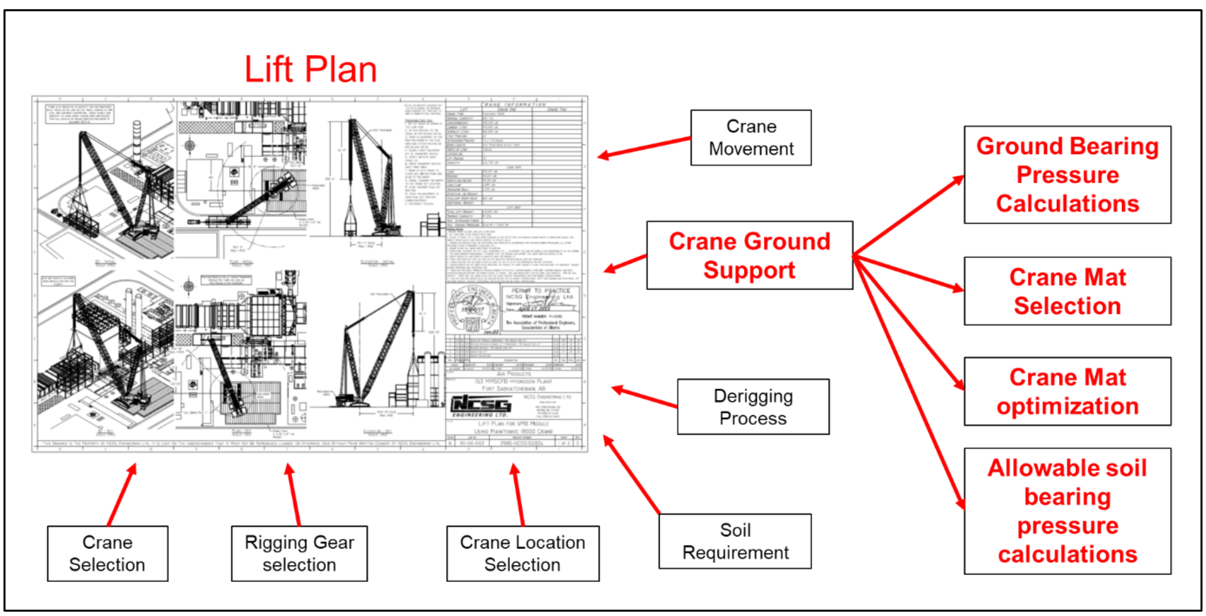

Figure 1.6: Sections of a lift plan

1.2. Hypothesis

This research is built on the following hypothesis:

> *In the context of modularization, the use of combined loading calculations can overcome the limitations associated with traditional GBP calculations, while an approach combining RL and greedy algorithm can be used to optimize crane mats on a given construction site.*

1.3. Objectives

Based on the motivation (mentioned above) and to test the above hypothesis, the research described herein is structured around the following three primary objectives.

Objective 1: *To overcome the limitation of traditional GBP methodology by applying combined loading and developing a novel methodology to calculate the GBP under mobile cranes, including crawler cranes and hydraulic cranes.*

Objective 2: *The objective is to develop an optimization methodology for the unexplored area of crane mat layout planning on a construction site. Moreover, to compare greedy and RL algorithms to optimize the crane mats layout on a construction site.*

Objective 3: *To develop an algorithm to estimate allowable soil bearing capacity for high-capacity mobile crane work based on crane ground footing and soil geotechnical reports.*

Based on the above three objectives, the following four milestones are pursued in sequence.

Milestone 1: Develop a novel methodology using combined loading to calculate the GBP under crawler crane tracks and hydraulic crane mats to overcome the limitations of traditional GBP procedures used in the crane industry. These traditional norms assumed GBP as uniform under crawler track widthwise; similarly, the GBP under the hydraulic crane mat is considered uniform.

Milestone 2: Develop a computer application (design support system for crane support design) that integrates GBP calculation under hydraulic crane mats with crane mat. The developed application can check the suitability of the crane mat based on five design parameters, allowable soil bearing capacity, bending stress limit, shear stress limit, deflection limit, and compression stress limit.

Milestone 3: Develop an algorithm to optimize crane mat layouts using greedy and RL. The idea here is to develop a VB application that provides an efficient and accurate automated crane mat optimization approach for preparing layout plans/drawings. One of the leading hypotheses is to use RL for the optimization process, mimicking crane practitioners' behaviour to optimize crane mats on a construction site, and comparing it with a greedy algorithm.

Milestone 4: Develop an algorithm for determining allowable soil bearing capacity for high-capacity crane work based on the data available in geotechnical reports for a given construction site. In specific, the aim here is to develop a computer application in VB by which to calculate allowable soil bearing capacity for crane work, using the concept of crane ground footing in place of the traditional shallow foundation approach.

Based on the research motives, and industrial and academic gap, the research road map is outlined in Figure 1.7.

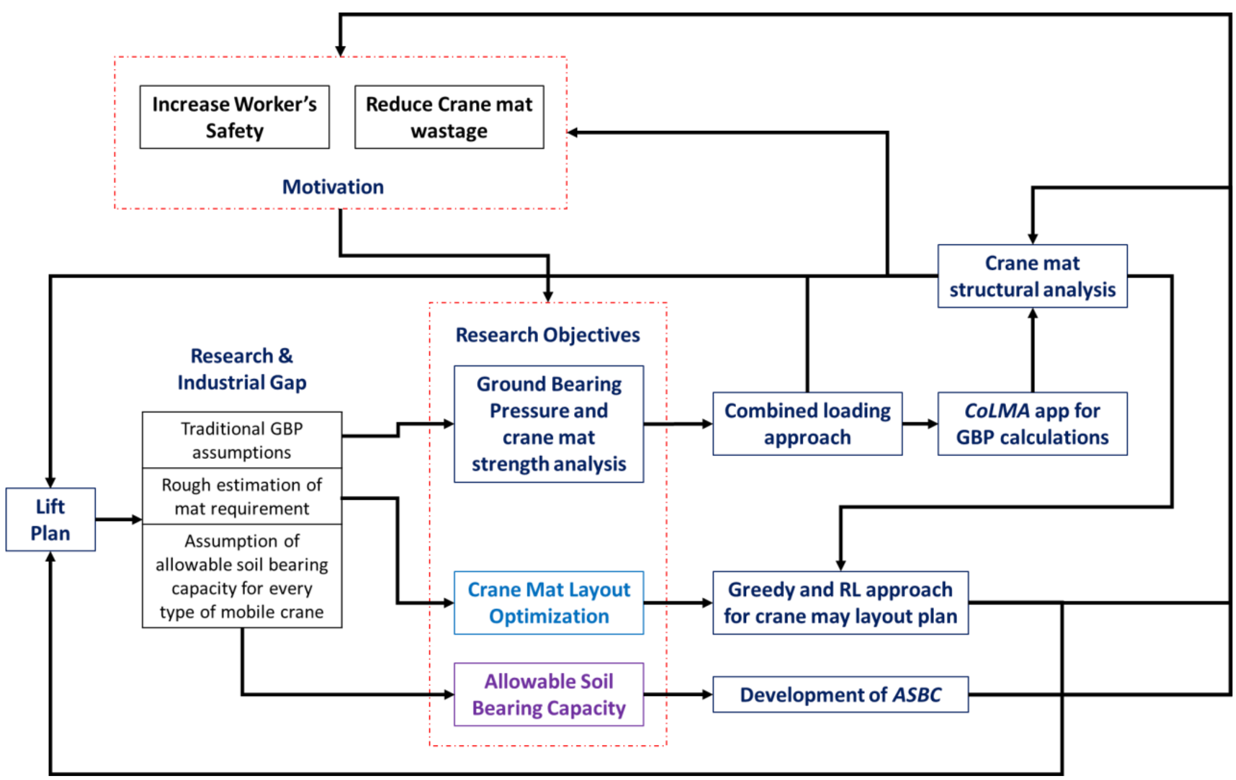

Figure 1.7: Motivation, industrial & academic gap, and objectives flow chart

1.4. Thesis Organization

The first chapter (Introduction) outlined the gaps in the literature and current practice, culminating in the problem statement motivating the present research. This included briefly describing the challenges associated with the conventional approach to crane mat use as a solution for soil support. The objectives underlying the present research were also discussed in detail in this chapter.

Chapter 2 (Literature Review) outlines the traditional method for calculating the ground bearing pressure under crawler tracks and pad loads (PLs) under hydraulic crane outriggers, as well as the general crane mat design criteria. This chapter also describes the optimization techniques currently in use in the construction industry for crane work. A review of the literature on greedy algorithms and RL is already provided in order to evaluate their practicability for crane mat optimization. This chapter also discusses various soil bearing capacity theorems relevant to estimating the allowable soil bearing capacity values for high-capacity crane work.

Chapter 3 (Ground Bearing Pressure Calculations under Mobile Cranes) presents a novel approach to calculating GBP under mobile cranes. This chapter encompasses the application of combined loading to calculate GBP under crawler crane tracks and hydraulic crane mats, as well as the use of FEA to validate and verify the GBP values generated based on various case examples of crawler cranes and hydraulic cranes. This chapter also introduces the developed VB application, *CoLMA*, for hydraulic crane operations.

Chapter 4 (Structural Requirement of Crane Mats) discusses crane mat selection for mobile crane operations based on GBP and allowable soil bearing capacity. The selection criteria are based on five main parameters: bending strength, shear, GBP, deflection, and compression. This chapter also discusses the use of the developed *CoLMA* application for the selection of a suitable crane mat for hydraulic crane operations.

Chapter 5 (Optimized Layout Planning of Crane Mats) discusses the optimization of crane mat layouts on construction sites using an agent-based approach with greedy and RL agents. An algorithm is developed in which the greedy and RL agents generate crane mat layout plans/drawings based on the constraints of the given construction site.

Chapter 6 (Allowable Soil Bearing Capacity for Mobile Cranes) describes the method for calculating the allowable soil bearing capacity for high-capacity mobile cranes, with the development of a VB application, *ASBC*, based on GBP and crane track/crane mat ground footing.

Chapter 7 (Summary and Conclusion) outlines the contributions of this research to academia, industry practice, and society, as well as the research limitations, and recommendations for future research.

CHAPTER 2: LITERATURE REVIEW

The primary aim of this chapter is to compile the previous research work conducted on mobile crane ground support. The traditional approach to calculating ground bearing pressure (GBP) assumes static forces and is considered uniform. This chapter outlines the traditional method of calculating the GBP under crawler tracks and pad load (PL) under hydraulic crane outriggers. These calculations, it should be noted, are different for crawler cranes than for hydraulic cranes. For crawler cranes, the pressure under the crawler track is obtained through a combination of statics and mathematical modelling calculations. On the other hand, the corresponding calculation for a hydraulic crane is based on the PLs. These PLs are used to calculate the pressure under the outrigger crane mat based on the surface area and material used to manufacture the crane mat.

In this context, there are primarily two ways to overcome poor ground stability: (i) using compacted aggregate to increase the soil bearing capacity; or/and (ii) using one or more layers of crane mats to redistribute the crane GBP to satisfy the allowable soil bearing capacity. The selection of a suitable crane mat is crucial in this regard. Considering the case of timber mats made of Coastal Douglas-Fir, the five main parameters used in crane mat selection (GBP, bending limit, shear limit, deflection limit, and compression limit) are discussed in this chapter .

This chapter also summarizes previous research on crane planning optimization as it pertains to this discussion. Optimization of crane operations and crane mat layout are crucial tasks, as crane operations and crane mat use are significant drivers of the cost performance of any construction project involving crane work. (According to field studies, a project involving cranes typically utilizes 800~1100 crane mats.[1]) With regard to optimization techniques, the greedy approach is widely used in the industry, whereas reinforcement learning (RL) is relatively new but gaining acceptance within industry as an optimization solution for complex problems. With respect to RL in particular, two algorithms, Q-Learning and State–Action–Reward–State–Action (SARSA), are discussed in this chapter. Both have been widely used by both researchers and practitioners, given their relative ease of implementation. Moreover, both are agent-based and similar in nature to the greedy approach (Wang et al. 2013).

[1] NCSG (Northern Crane Services Group, Edmonton, Alberta, Canada)

The last section of this chapter reviews the literature on the development of theorems for calculating the allowable soil bearing capacity, which can be broadly categorized as either direct[1] or indirect[2] (Eslami and Gholami 2005). As discussed below, in current practice the allowable soil bearing capacity is typically obtained from a geotechnical reports of the site. The various equations that have been developed for this purpose over the years are briefly outlined in this chapter.

2.1. Traditional method for calculating GBP under mobile cranes

Mobile cranes lift heavy and oversized objects and move them to their required location. The history of cranes can be dated back to Greek architecture. The process of hoisting and lifting was based on the compound pulley system (Coulton 1974). William Smith Otis invented the modern era of mobile cranes. He invented a steam-powered device for excavation during railroad construction in 1837 (Stueland 1994). Steam-powered excavator performed in the same pattern as a man with the shovel. This invention gave birth to the concept of mobile cranes (Stueland 1994).

Usually, there are two types of mobile cranes, crawler cranes and hydraulic cranes. Both types, in general, are composed of two major parts, a moving part (superstructure) and a stationary part (carrier). Crawlers (tracks) for crawler cranes support the crane, and in the case of hydraulic cranes, the outriggers support the crane (see Figure 2.1 and Figure 2.2).

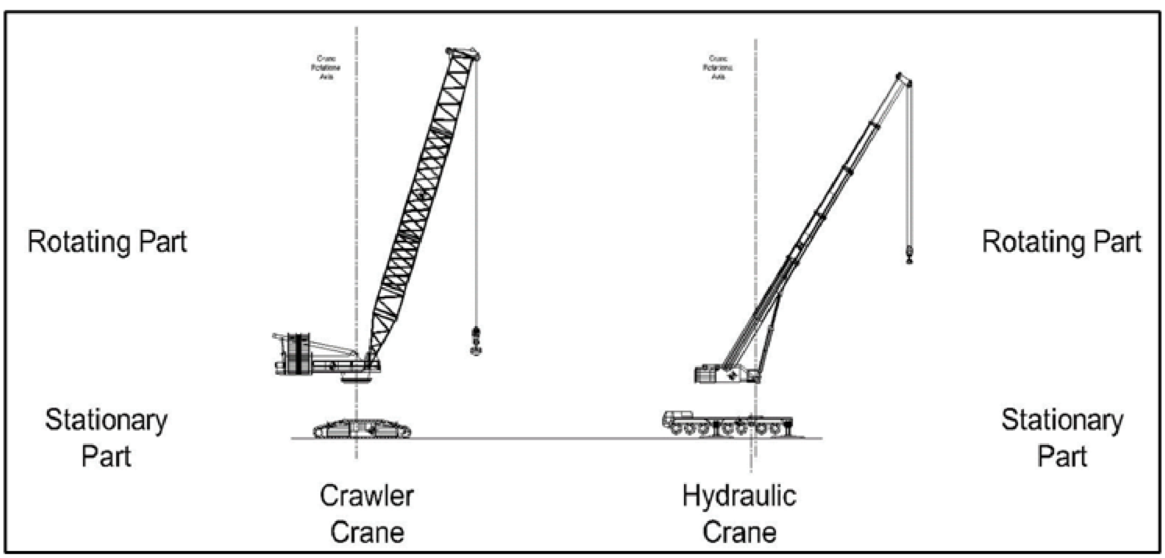

Figure 2.1: Rotating and stationary parts of crawler crane and hydraulic crane

[1] Cone penetration test.
[2] Friction angle and undrained shear strength calculations.

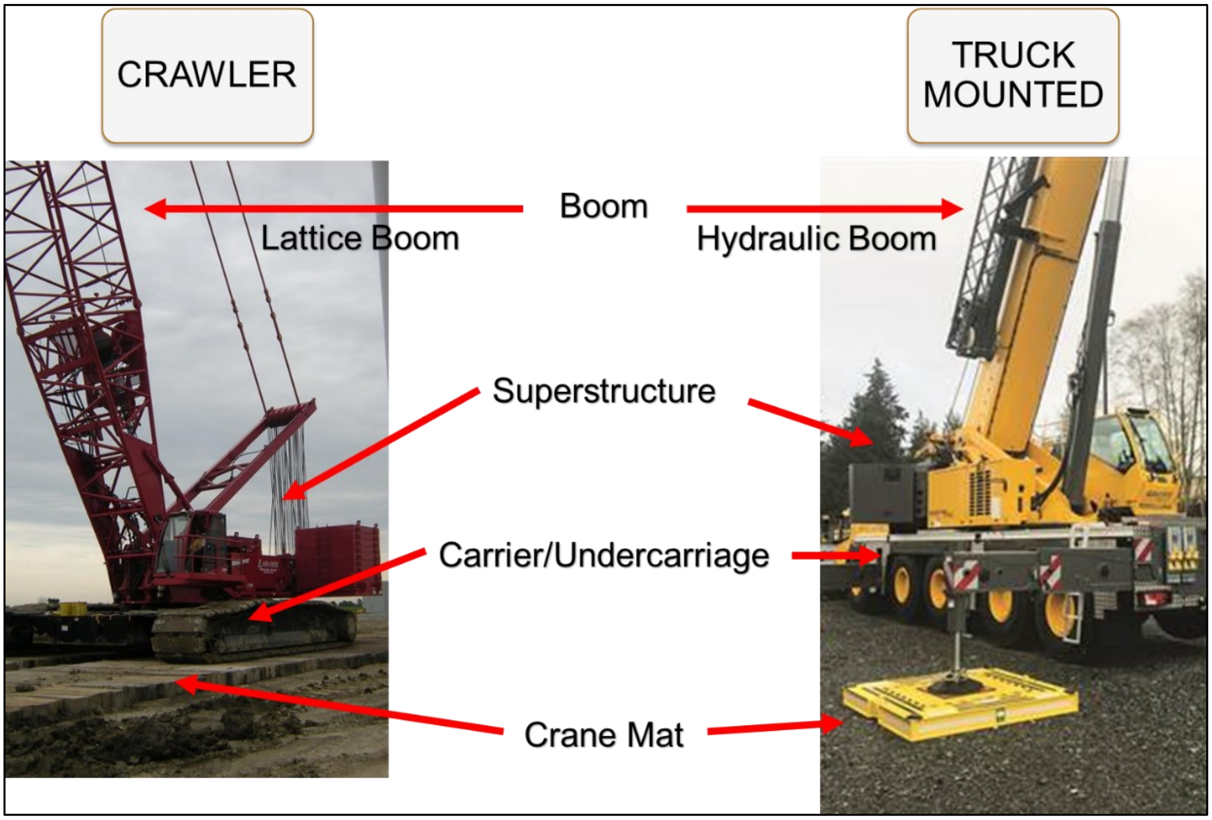

Figure 2.2: Mobile crane parts

In major construction projects, crawler cranes are often preferential over hydraulic cranes since crawler cranes can lift hefty manufactured structures and, if necessary, travel with the payload. Furthermore, in contrast to crawler cranes, hydraulic cranes are built for flexibility and speedy mobilization to a job site. Due to the self-extendable boom (hydraulic boom), the crane setup time is shorter than the lattice boom crawler cranes.

In practice, the ground support design for mobile crane operations presupposes the evaluation of the pressure under the tracks of the crawler crane. Traditionally, the ground support calculation is performed by practitioners according to a procedure in which the respective weights of the crane components and payload are assumed to be static forces that generate pressure on the ground that is mediated through a ground support system (usually crane mats) to ensure that the overall pressure exerted is less than the soil bearing capacity. The crane itself has a fixed center of gravity (COG), but the COG of the superstructure changes based on the lifting radius, boom angle, and boom rotation. Shapiro and Shapiro (2010) presented in-depth and detailed calculations covering all crane weights and their COGs and developed equations to calculate GBP under crawler crane tracks and PL under hydraulic crane outriggers. Becker (2001) also formulated equations for GBP calculations, which were slightly different from Shapiro and Shapiro (2010). Shapiro and Shapiro (2010) considered moments to calculate the GBP and PL values, whereas Becker (2001) took the distribution of forces to calculate the GBP and PL. First, the outrigger loads in reaction forces (i.e., PL) under the outriggers are calculated in hydraulic cranes. Later, these outrigger reaction forces use the outrigger crane mat's surface area to calculate the GBP exerted by that outrigger (see Figure 2.3) (Becker 2001, Shapiro and Shapiro 2010). Many researchers later utilized these approaches to build the selection criteria for mobile cranes based on crane and ground stability (Hasan et al. 2010, Di et al. 2011). The basis for these calculations is that the GBP along the width of the crane track/crane mat is uniform in nature.

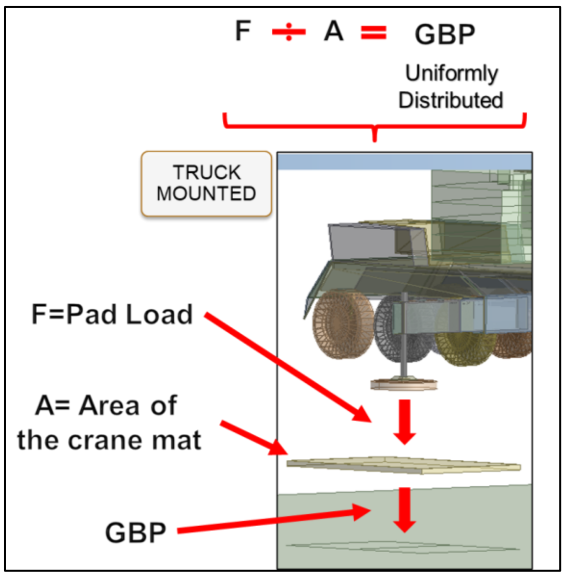

Figure 2.3: Hydraulic crane load distribution

Contrary to this, Ali (2018), while researching the behaviour of crane mats under crane tracks, concluded that the GBP also varies along the width of the crane tracks/crane mats. This finding contradicted that of the traditional method of calculating the GBP using various software programs or GBP charts (American-Hoist 1973, 1979, Grove 2019, Manitowoc 2019). The research conducted by Ali (2018) found that the four edges (left-front and left-rear, right-front and right-rear) of one crawler track exert different pressure values instead of only considering the front and rear for each of the two tracks. The work done by Shapiro and Shapiro (2010) and Becker (2001) considered the GBP along the width of the crawler crane track to be uniform. The crane industry continues to use 4-point calculations without considering the limitations of this method (Becker 2001, Shapiro and Shapiro 2010). The work done by Hibbeler (2011) stated that the axial forces and the moments acting on a surface do not exert uniform pressure along any side until the axial forces directly act on the centroid of the surface. This evidence leads to the hypothesis that there are 8-points in the GBP profile based on the eight edges of two crawler tracks, instead of a 4-point GBP distribution. Moreover, the equations presented by Shapiro and Shapiro (2010) and Becker (2001) can only provide GBP values at the edges of the track, with the presumption of uniform stress along crane track width. This means the GBP midway on the track cannot be calculated. The output is often limited to pressure values that are calculated at specific points (edges of the crane track) (Becker 2001, Shapiro and Shapiro 2010).

To calculate the GBP under crawler tracks and the PL under hydraulic crane outriggers, the first step involves calculating the sum weight (kN) of the crane, including the payload and the location of the center of gravity (COG) using Equations (1), (2) and (3), as shown below:

$$W = \sum_{i=1}^{n} W_{si} + \sum_{j=1}^{m} W_{cj} + W_l \tag{1}$$

$$R = \sqrt{{R_y}^2 + {R_x}^2} \tag{2}$$

$$\theta = tan^{-1} \frac{R_y}{R_x} \tag{3}$$

where

W_{si} = weight (kN) of n parts in crane superstructure, $i = n$,

R_{si} = distance (m) between respective part COG and the superstructure rotational axis,

θ_{si} = angle (°) of respective part COG with the x-axis when $\theta_l = 0°$,

W_{cj} = weight (kN) of m parts in crane carrier, $j = m$,

$R_{cj=}$ distance (m) between respective part COG and the superstructure rotational axis,

θ_{cj} = angle (°) of respective part COG with the x-axis,

W_l = weight (kN) of the payload,

R_l = crane radius (m), and

θ_l = crane superstructure slew angle (°).

Figure 2.4 shows all these variables in detail.

The variables in Equation (2) and (3), R_y and R_x are calculated using Equations (4) and (5).

$$R_y = \frac{1}{W}\left(\sum_{i=1}^{n} W_{si}R_{si}\,sin(\theta_{si}+\theta_l) + \sum_{j=1}^{m} W_{cj}R_{cj}\,sin\,\theta_{cj} + W_l R_l\,sin\,\theta_l\right) \tag{4}$$

$$R_x = \frac{1}{W}\left(\sum_{i=1}^{n} W_{si}R_{si}\,cos(\theta_{si}+\theta_l) + \sum_{j=1}^{m} W_{cj}R_{cj}\,cos\,\theta_{cj} + W_l R_l\,cos\,\theta_l\right) \tag{5}$$

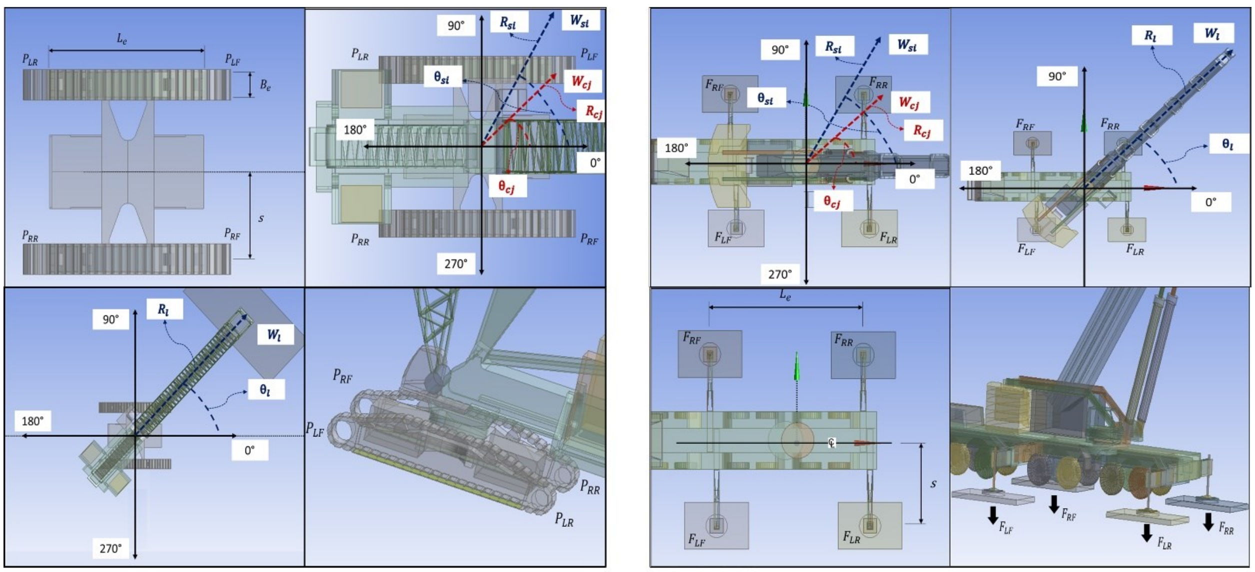

Figure 2.4: Parameters used for (a) crawler crane GBP (Pa), and (b) hydraulic crane PL (kN) calculations

Based on the above equations, the GBP under the crawler crane tracks and the PL under hydraulic crane outriggers can be calculated using the Equations (6) and (7), respectively, in a unified crane matrix:

$$\begin{bmatrix} P_{LF} & P_{RF} \\ P_{LR} & P_{RR} \end{bmatrix} = \frac{4G_c}{aL_eB_e}\begin{bmatrix} \nu\lambda & (1-\nu)\lambda & (1-\lambda)\nu \\ (1-\nu)\lambda & \nu\lambda & (1-\nu)(1-\lambda) \end{bmatrix}\begin{bmatrix} (ab)(2-a) & (ac)(2-a) \\ (ab)(a-1) & (ac)(a-1) \\ b & c \end{bmatrix} \tag{6}$$

$$\begin{bmatrix} F_{RR} & F_{LR} \\ F_{RF} & P_{LF} \end{bmatrix} = G_c\begin{bmatrix} \nu & 1-\nu \\ 1-\nu & \nu \end{bmatrix}\begin{bmatrix} b(1+2d) & c(1+2d) \\ b(1-2d) & c(1-2d) \end{bmatrix} \tag{7}$$

where P_{LF}/P_{LR} is the GBP under the left-front/-rear track of the crawler crane, P_{RF}/P_{RR} is the GBP under the right-front/-rear track of the crawler crane, F_{RR}/F_{RF} is the PL on the right-rear/-front outrigger of the hydraulic crane and F_{LR}/F_{LF} is the PL on the hydraulic crane's left-rear/-front outrigger. The factors in Equations (6) and (7) are defined by Equations (8)–(16):

$$\mu = \frac{1}{2}\left(\frac{|cos\,(270+\theta)|}{cos\,(270+\theta)}+1\right) \tag{8}$$

$$\nu = \frac{1}{2}\left(\frac{|cos\,\theta|}{cos\,\theta}+1\right) \tag{9}$$

$$r = R|sin\,\theta| \tag{10}$$

$$G_c = \frac{W}{4s} \tag{11}$$

$$\lambda = \frac{1}{2}\left(\frac{\big|L_e - 6R|cos\,\theta|\big|}{L_e - 6R|cos\,\theta|}+1\right) \tag{12}$$

$$a = \frac{3}{2L_e}(L_e - 2R|cos\,\theta|) \tag{13}$$

$$b = s - r + 2\mu r \tag{14}$$

$$c = s + r - 2\mu r \tag{15}$$

$$d = \frac{R|cos\,\theta|}{L_e} \tag{16}$$

where

$s =$ the distance from the crane center to the center of crawler width/outrigger,

$B_e =$ the width of the track, and

$L_e =$ the effective track length/distance between two outriggers (lengthwise).

For hydraulic cranes, practitioners consider the PLs as the main criterion in crane mat selection, whereas, for crawler cranes, the GBP under the track is considered the main criterion in crane mat selection. Moreover, in the context of crawler cranes, the effective/bearing length and width of the crane track (contact area) is smaller than the actual physical length and width of the crawler tracks, as shown in Figure 2.5 (Al-Hussein et al. 2005, Hasan et al. 2010, Shapiro and Shapiro 2010). Another method for calculating the GBP under mobile cranes is the use of FEA (Ali 2018, Ali et al. 2019). It is important to mention in this regard that the use of FEA is time consuming and requires specialized computer applications for modelling the crane and payload.

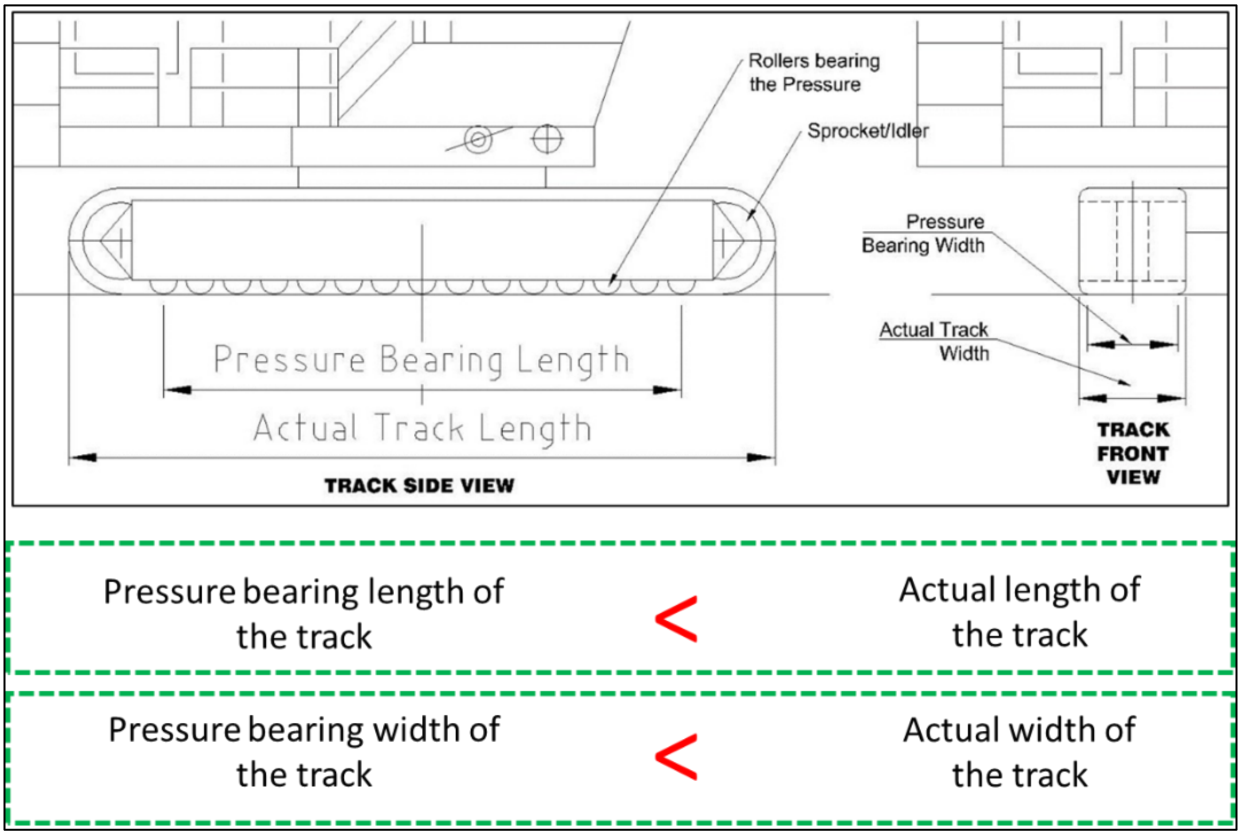

Figure 2.5: Pressure bearing length and width of crawler crane track

2.2. Crane mat selection criteria

Regarding crane mat strength analysis and crane mat suitability for a job, although practitioners in the crane mats industry use different approaches to design and calculate the strength of a crane mat (timber/steel), these approaches share a common starting point: the calculated maximum GBP values. In this respect, Shapiro and Shapiro (2010) provided a guideline for selecting the crane mats. If the maximum GBP exerted by the hydraulic crane outrigger is larger than the allowable soil bearing capacity, the crane outrigger will sink into the ground, likely resulting in crane tipping. As a result, crane rental companies use crane mats made of wood or steel under the outriggers to distribute the crane's load and its components (including the lifted object) on the ground, thus keeping it below the allowable soil bearing capacity. Duerr (2010), Duerr and Duerr (2019) presented the industry practice for selecting timber crane mats based on the allowable soil bearing capacity, crane mat deflection, crane mat bending moment compressive strength limit, and shear limit. Many researchers used these parameters to develop crane mat selection criteria (Hasan et al. 2010, Mahamid and Torra-Bilal 2019). The first crane mat selection method based on ground bearing pressure and allowable soil bearing capacity is straightforward. The crane mat in question is selected for further calculations if the maximum GBP under the crane mat is equal to or lower than the allowable soil bearing capacity (Duerr 2010, Hasan et al. 2010, Ali 2018, Duerr and Duerr 2019).

This crane mat length of the crane mat selected is later used to calculate bending and shear stresses in the crane mat. The crane mat is accepted if the bending and shear stresses are within the crane material's prescribed limits. The design parameters for the crane mat selection also include allowable deflection and allowable compression stress. The deflection of ±1% is considered safe for crane stability (ISO 2014). However, this research has taken a conservative approach of 0.75% deflection of the total crane mat length (Ali 2018). The above exercise considers all the crane mat strength parameters in a graphical presentation and plots them against the crane mat's length (Liftinglogistics.com 2016).

It should be mentioned that there are many other crane mat design parameters available to practitioners, such as extreme fibre stress bending limit, repetitive member design value, transverse fracture properties, etc. (American Wood Council 2018, Truss Plate Institute of Canada 2019). The research described herein integrates into the developed application only the five design parameters used most widely within the crane industry in the design and planning of crane mat layouts for crane operations (Duerr 2010, Shapiro and Shapiro 2010, Al-Hussein et al. 2011, Mahamid et al. 2017).

2.3. Crane mat design factors

There are also external design factors associated with wood manufacturing that affect a crane mat's strength. The factors most widely referenced in the crane industry are listed below:

1. Load duration factor K_D, which depends on the duration of use of the crane mat (American Wood Council 2018, Truss Plate Institute of Canada 2019). Crane mats can withstand their design loads for short durations (load duration factor of 1.15 for

short duration and 0.65 for permanent). However, the ability to withstand these loads decreases with time (American Wood Council 2018).

2. Temperature factor C_t governs the strength of the crane mat due to ambient temperature (American Wood Council 2018).
3. Treatment factor K_T, incorporates the effects on the strength of the crane mat due to the fire-retardant chemical treatment of wood used for crane mat manufacturing. For Coastal Douglas-Fir treated timber, the treatment factor is about 1.0 (American Wood Council 2018, Truss Plate Institute of Canada 2019).
4. System factor K_H accounts for the increase in the bending and shear strength of the crane mat when three or more parallel wood members in the crane mat spaced no more than 610 mm support the load mutually (Truss Plate Institute of Canada 2019).
5. Size factor K_Z, the compression resistance perpendicular to the wood grain can be multiplied by the size factor to compensate for bearing (American Wood Council 2018, Truss Plate Institute of Canada 2019).
6. Service condition factor for bending K_{Sb} and compression K_{Sc}, which depends upon dry or wet service conditions (Truss Plate Institute of Canada 2019).
7. Resistance for bending $\emptyset_{bv}$ and compression $\emptyset_c$, are factors applied to account for the variability of dimensions and material properties, quality of work, type of failure, and uncertainty in predicting resistance (CSA Group 2019).

2.4. Crane mat layout optimization

The increasing use of cranes in construction has also increased the use of crane mats. This, in turn, has led to the use of crane mat layout plans/drawings as a default practice for every crane operation on the construction site. Figure 1.3 shows the detailed sequence of crane mat laying. The crane mat layout plan/drawing is typically prepared to accommodate a worst-case scenario in terms of soil bearing capacity. Trailers transport the crane mats from the crane mat yard to the construction site, and workers lay these crane mats on the construction site in accordance with the crane mat layout plan/drawing. After the lift, these crane mats are transported back to the crane mat yard for storage and future use. This cycle iterates every time a high-capacity crane lift is performed on the construction site.

Practitioners typically prepare the layout plans/diagrams using the commercial software, AutoCAD. These plans/drawings are designed in consideration of various construction site constraints. The primary constraint is to minimize the crane mats required to achieve coverage of a given area. Another notable constraint is the laying sequence, starting from an edge of a required crane mat coverage area, and continuing until the entire area is covered with crane mats. Typically, it takes a practitioner about 20~30 minutes (field study) in current practice to prepare a crane mat layout plan/drawing for an area comprising 15~20 crane mats.

Many researchers have developed various approaches to facilitate practitioners optimizing site layout based on construction site restraints (Tam et al. 2001, Sivakumar et al. 2003, Lim et al. 2005). Some constraints such as safety, time, and costs are accounted for in these approaches to determine the best possible locations. Reddy and Varghese (2002) developed a tool using configuration space (C-space) to identify the crane lift paths and optimize paths within a constrained search space. Deen et al. (2005) also proposed a genetic algorithm approach for automated path planning of mobile cranes. Crane optimization has developed a lot in recent years with the help of computer integration (Tam et al. 2001, Al-Hussein et al. 2005, 2011, Han et al. 2012, Lei et al. 2013, Lin et al. 2017, Taghaddos et al. 2018, Liu et al. 2019). However, any germane work on crane mat optimization is not prominent in academic literature. Most of the time, crane lift optimization is reviewed by researchers as the main cost driver, but when it comes to cost optimization, crane mats can significantly reduce the capital cost (Ali 2018). Practitioners usually determine the crane mat requirement based on mobile crane ground bearing pressure and soil bearing capacity on the construction site but avoid the crane mat utilization and optimization in bulk (Duerr 2010, Hasan et al. 2010). The research conducted by Taghaddos et al. (2018) also provided crane optimization, including crane positioning, rigging gear optimization, lift optimization, crane path optimization, and crane mat requirement, but lacks the crane mat optimization requirement on site.

The research work presented in this thesis uses two approaches to address this requirement. The first is based on an agent-based greedy approach to optimize the crane mat layout. The second uses RL (specifically the SARSA algorithm) for the crane mat optimization. There are several methods that have been employed by researchers for linear and non-linear optimization—greedy, brute-force, and dynamic programming being a few of the notable ones and have potential to be used for crane mat optimization. The prospective use of RL for crane mat optimization is explored in this research in the context of the broader canvas of modular construction. RL, it should be noted, is already being used in healthcare (Yu et al. 2021), in Natural Language processing (NLP) (Paulus et al. 2017), and in the automobile industry as part of the development of self-driving cars (Kiran et al. 2021).

As the construction industry lags in productivity in comparison to other industries (Graham 2019), construction enterprises are seeking innovative approaches to optimize construction work and increase productivity. Time and cost, of course, are major considerations in this endeavor (Zelentsov et al. 2021). In this respect, given its successful application in other industries, RL constitutes a promising solution for optimizing the resources associated with construction work and thereby minimizing cost and time.

2.4.1. Agent-based greedy algorithm

The greedy algorithm is a widely used meta-heuristic optimization methodology to achieve an optimal solution for complex problems that are time-consuming when tackled with manual methods (Bang-Jensen et al. 2004, Cormen et al. 2009). The greedy algorithm uses an agent-based greedy approach by electing the best/worst-case scenario at each state to move forward to the next state. An agent-based greedy approach is not novel for resource optimization. This approach was satisfactorily employed to optimize dynamic ridesharing, resulting in higher user cost-saving and minimum vehicle kilometres travelled, integrating multi-passenger rides (Nourinejad and Roorda 2016). The agent-based greedy approach is also employed successfully to model evacuation traffic plans (Madireddy et al. 2011).

However, one of the drawbacks of the greedy algorithm is that the agent can get confined to the local optimum (Bang-Jensen, Gutin and Yeo, 2004; Gutin, Yeo and Zverovich, 2002). To overcome this situation, the agent needs to explore the states beyond the local optimum by increasing the number of layers or steps for further exploration (future steps). The greedy agent must probe the layers down the heuristic tree for the minimum or maximum point to proceed further, similar to A* algorithm, without storing any data (Doran and Michie, 1966).

2.4.2. Reinforcement Learning (RL)

RL is a branch of machine learning. The concept of RL is based on the core methodology of learning without any previous experience or available data. The interaction with the environment generates a wealth of information depicting cause and effect, which leads to the improvement of actions and achievement of goals. Such interactions with the environment are a significant source of awareness to decide what action to take next (Hilgard et al. 1961). Inspiring the same perspective and approach, RL can be considered for the optimization of complex problems, to initiate an action, or develop a strategy to achieve the goal, with the supplement of reward or punishment as the criterion for action preference. The structure of RL is composed of four parts: policy, a reward signal, a value function, and a model. A policy is how an RL agent acts at a given state. The value function defines the amount of reward/punishment the RL agent receives from the environment, and the model (optional) mimics the integration of the environment (Sutton and Barto 2018). Figure 2.6 shows the basic concept of RL.

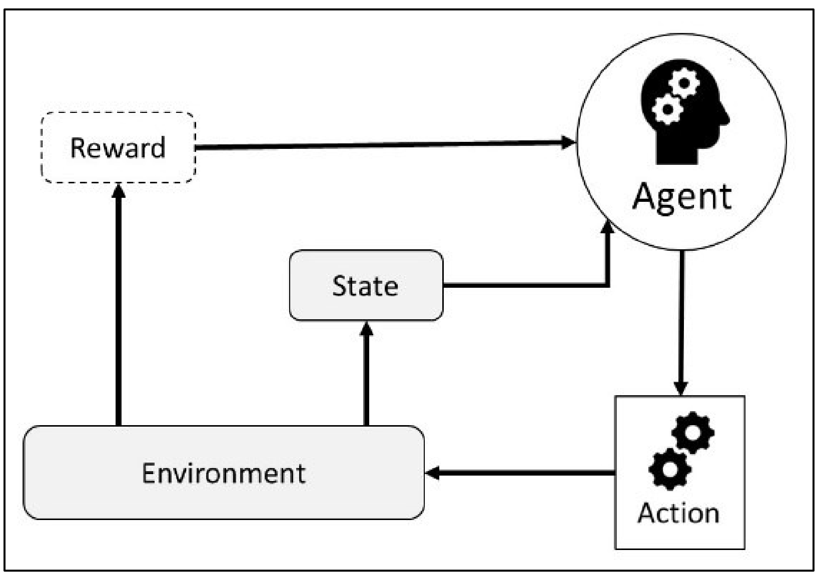

Figure 2.6: Basics of Reinforcement Learning

RL is a significant paradigm with the artificial intelligence field that has seen broad application (Polydoros and Nalpantidis 2017). The use of RL for robotics, for instance, is gaining popularity, where the ongoing refinement of RL is contributing to the rapid development of intelligent robots (Deisenroth et al. 2013). Moreover, Kormushev et al. (2013) have noted that the exploratory aspect of RL can be beneficial for the learning process on the part of robots. As another example, Lakshmanan et al. (2020) used RL to optimize path planning for floor-cleaning robots to minimize energy utilization. Their findings demonstrated that the proposed method resulted in a lower-cost path that took less time to generate compared to a traditional approach. It can generate path in any pretrained arbitrary environment. As mentioned above, RL is now being used in healthcare as well, for applications ranging from automated disease diagnosis, to dynamic treatment of chronic diseases, as well as various control and scheduling problems in healthcare administration (Yu et al. 2021). As mentioned, RL is also being used for Natural Language Processing (NLP) within the field of data mining, with the increasing importance of big data analytics. The use of RL is to gather important and relevant information (Paulus et al. 2017). Car industry is working on developing a self-driving cars based on RL (Kiran et al. 2021).

Nevertheless, the application of RL in construction is still in its infancy. Sartoretti et al. (2019) used RL to solve a multi-robot construction problem, where agents were used to arrange simple block elements into a specific structure. The agents collaborated to build the structure under a single centralized policy and critic learning. The results showed that RL can be successfully applied to assemble a structure using robots, where the robots learn and refine the procedure accordingly (Sartoretti et al. 2019). Similarly, Apolinarska et al. (2021) used RL to control robotic movement in the assembly of lap joints for custom timber mats. Their results demonstrated that the policy of RL can be generalized according to real-world situations that may not be seen in training data for robotic machine learning (Apolinarska et al. 2021). Soman and Molina-Solana (2022) used RL for the automating look-ahead schedule generation for construction. They employed RL to link the data-driven constraints in order to generate a schedule of construction activities. They found RL to be capable of generating a conflict-free look-ahead schedule, and to do so in less time compared to conventional methods. In general, their study showed that RL can be useful and applicable as a decision support system for construction activities, demonstrating that, with the help of RL as the main machine learning algorithm, fully autonomous earth-moving heavy equipment are able to operate without any human intervention. Kurinov et al. (2020) used RL to train an excavator to perform earth-moving activities. The excavator trained using RL successfully loaded the hopper within the required time, avoiding obstructions, and was able to perform the required behaviours after only a short training time.

The numerical formation underlying RL, it should be noted, is based on the Markov Decision Process proposed by Bellman (1957) and further developed by van Otterlo and Wiering (2012). According to this theory, future decisions depend upon the current state, not the previous outcome. The state transition probability defines the selection of the next state. For RL, this transition is based on the reward the RL agent receives at the current state (Bellman 1957). Q-learning is among the best known RL algorithms, Q-learning being a model-free approach that can optimize the stochastic states and rewards (Lillicrap et al. 2015, Sutton and Barto 2018). Q-learning, though it derives its basics from Bellman's finite Markov decision process, was introduced decades later by Watkins (1989). In Q-learning, the learning process follows a pattern similar to that of temporal difference learning (Sutton 1988). The RL agent learns from the current state's reward or punishment, decides based on the expected future state, and updates the current state accordingly. The equation of Q-learning is as shown in Equation (17):

$$Q(s_t, a_t) = Q(s, a_t)(1 - \alpha) + \alpha\{R_t + \gamma\ maxQ_a(s_{t+1}, a)\} \tag{17}$$

where $Q(s_t, a_t)$ is the value of Q at the state s_t after employing the action a_t, α is the learning rate, γ the discount factor, R_t the reward received by the agent at the state s_t after taking the action a_t based on the value function for reward, a the successive action to reach s_{t+1} and $maxQ_a$ is the value of Q of the following state (from a set of possible immediate future states) with a maximum Q value. This way, the value of Q for each state is refined and updated with each episode. The policy of the RL agent is to maximize the reward and minimize the steps (number of actions) in between. Due to its off-policy approach, the action taken by the agent depends on the future maximum Q value, not the reward it will get at that state (Watkins 1989, Watkins and Dayan 1992, Sutton and Barto 2018).

State-Action-Reward-State-Action (SARSA) was proposed by Sutton (1996), as an on-policy temporal-difference control algorithm and an evolution of Q-learning (Wang et al. 2013). An on-policy agent, it should be noted, learns only about the policy that it is executing. Any action on the part of the agent is taken in consideration not only of all the current states but also the next state in its pursuit of the maximum reward. The significant advantage of the on-policy algorithm is its quick convergence (Wiering and Van Hasselt 2008). The value of $Q(s_t, a_t)$ is estimated by applying a_t in state s_t, as shown in Equation (18):

$$(s_t, a_t) = Q(s, a_t)(1-\alpha) + \alpha\{R_t + \gamma\, Q_a(s_{t+1}, a_{t+1})\} \tag{18}$$

Looking at the Q-learning and SARSA algorithm in Equation (17) and Equation (18), there are two factors involved: learning rate α and the discount factor γ. Researchers and practitioners value both these factors between 0 and 1. The learning rate controls how much the newly acquired information supersedes the previously gathered information. The RL agent will learn nothing when the learning rate value is 0. While the learning rate of 1 forces the agent to credit only the most recent information. The discount factor determines the significance of future rewards. The discounted factor of 0 makes the future reward value null and void, and the RL agent becomes "*shortsighted*" (Sutton and Barto 2018). On the other hand, a discount factor value of 1 will drive the agent to take future rewards more strongly, making it "*farsighted*" (Sutton and Barto 2018). Most researchers have used a learning factor of 0.1 and a discount factor of 0.9 (Sutton and Barto 2018). $Q_a(s_{t+1}, \mathrm{a}_{t+1})$ can be calculated using Equation (19):

$$Q_a(s_{t+1}, a_{t+1}) = \varepsilon\, meanQ_a(s_{t+1}, a) + (1-\varepsilon) maxQ_a(s_{t+1}, a) \tag{19}$$

Another factor introduced in Equation (19) is ε, which defines the greedy policy. It creates an equilibrium between the maximum Q-value and the weighted sum Q-value for the following expected action. The change initiated in SARSA directs the agent towards convergence, integrating future rewards.

2.5. Allowable soil bearing capacity for crane work

It is worth noting that most crane-related accidents on construction sites are linked to soil stability (11%), and mobile crane fatalities account for (approximately) 84% of all the fatalities involving cranes/derricks (Beavers et al. 2006). The number of accidents linked with soil stability shows that proper estimation of allowable soil bearing capacity is essential for a safe lift. In poor soil support, the crane track/outrigger/crane mat can sink in the ground, resulting in crane tipping leading to an irreversible chain reaction of crane overturning. Figure 2.7 shows an example of crane tipping in general. Due to the poor ground support, the crane track presses the ground at the front of the track, resulting in the rear track rollers leaving the track and ground (see Figure 2.7).

It is critical to prepare the ground for safe crane lifting activities. The status quo approach is to prepare the ground by backfilling with aggregate and compacting it to make it suitable for crane work (as shown in Figure 2.8). In most cases, an extra layer of crane mats is used underneath the mobile cranes to increase the safety of the crane operation. The whole exercise of area preparation can become expensive if the practitioners do not adequately calculate soil bearing capacity to judge the soil stability.

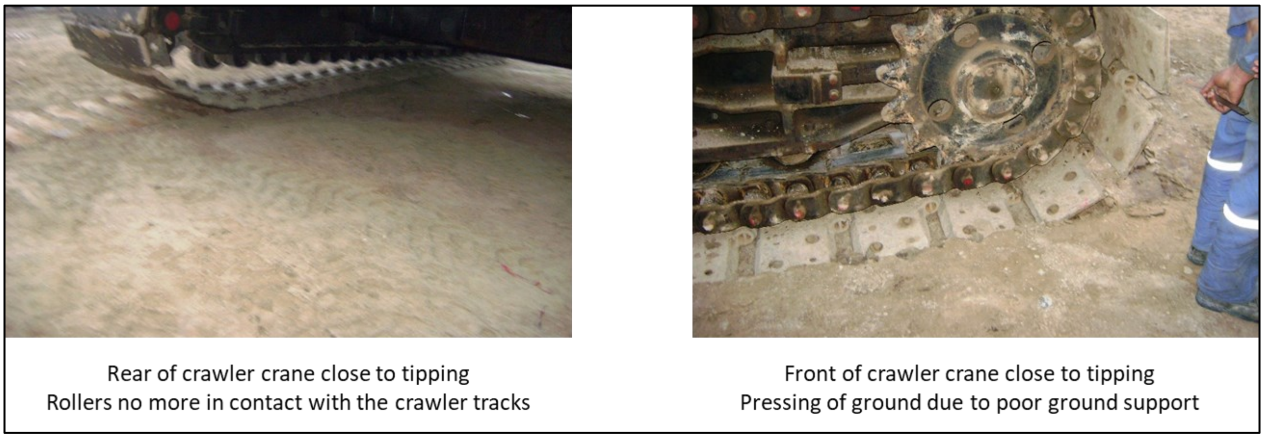

Figure 2.7: Crane tipping due to poor ground support

Considering the allowable soil bearing capacity calculations, in 1857, Rankine proposed the first-ever approach (Du et al. 2017). Later, Terzaghi (1943) presented a formula to calculate the ultimate soil bearing capacity under a foundation. The crane track/outrigger/crane mat is a foundation for estimating soil bearing capacity calculations for crane work. Meyerhof (1963) further refined the equation to add some factors. Later, Hansen (1970) and Vesic (1975) refined these factors to develop and refine the soil bearing capacity equation.

The traditional approach employed by crane rental companies for determining the allowable soil bearing capacity is to simply use the information provided by the client. However, this approach fails to take into account the impact of crane tracks/outriggers/crane mats on the allowable soil bearing capacity (Onyelowe 2017, Du et al. 2017, Gaonkar et al. 2021, Patwardhan and Metya 2021, Tahmid et al. 2021). The research conducted in this thesis utilizes the equations developed by Terzaghi (1943), Meyerhof (1963), Hansen (1970), and Vesic (1975) to calculate the soil bearing capacity based on the crane ground footing. For the foundation design and construction stability, these soil bearing capacity calculation approaches are used widely by practitioners in the construction industry (Tahmid et al. 2021).

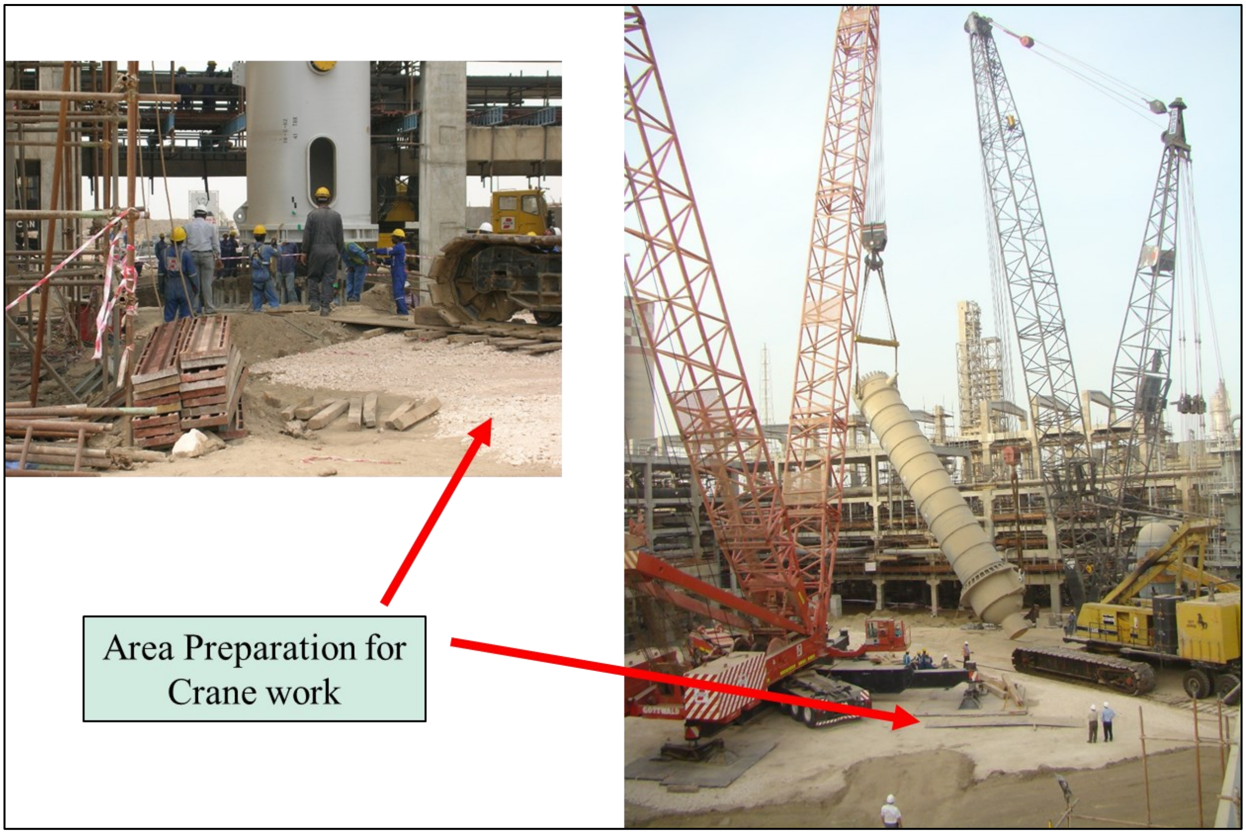

Figure 2.8: Area preparation for crane work to avoid ground settling and crane tipping

CHAPTER 3: GROUND BEARING PRESSURE UNDER MOBILE CRANES

This chapter summarizes the notable advancements in the calculation of GBP. As stated in Chapters 1 and 2, the traditional method of calculating ground bearing pressure (GBP) under a crawler crane is slightly different than the method for hydraulic cranes. Accordingly, this chapter is divided into two main sections, one for each of these crane types.

The crawler crane section of this chapter discusses the research carried out on GBP calculations and the development of a novel method. To verify the method, two crane examples are also presented in this section. The values are counter-checked against traditional values and then against finite element analysis (FEA) results.

The hydraulic section covers the work executed on the GBP calculations under hydraulic crane mats. The developed algorithm is discussed, and the values are later obtained for verification purposes. One hydraulic crane example is conducted to verify the methodology. The results obtained are later compared against the manual values and the FEA results.

The development of a visual basic (VB) application, '*CoLMA*', is then discussed. The application '*CoLMA*' is based on the algorithm developed for hydraulic crane GBP calculations. As discussed below, the practical advantage of using '*CoLMA*' is that it can display GBP in a graphical form for the practitioner's ease.

3.1. GBP under crawler cranes

Given the research gap with respect to GBP calculations, for the purpose of the present study we begin the GBP calculation from scratch and develop a novel set of algorithms by which to compute GBP under crawler crane tracks. The method developed herein is based on the basic concept of combined loading (Hibbeler 2011). Moreover, for the verification of this new methodology, FEA is used. In the research presented herein, the calculation of the GBP under the crawler tracks is simulated using ANSYS simulation software (version 19.2). A crane model is built in the FEA platform to develop a realistic setup for the analysis. Based on the weight of each of the crane's components, a map representing the distribution of the pressure exerted on the ground is developed as the superstructure rotates, mimicking a real-life lift. The research presented herein compares GBP values selected at specific locations from the FEA pressure map with those calculated using the new methodology developed. Later, these values are compared with the GBP software/chart values to check the difference. This study will provide practitioners with an in-depth look at how the GBP changes throughout the track bearing area. Likewise, with high-capacity cranes on construction sites to move heavy modules, which are getting heavier and heavier due to modularization, it is not advisable to overlook the GBP at the corners of the crane track. The traditional calculation method can be misleading by ignoring the values at the edges of the crawler track and assuming an average for a uniform distribution of GBP. A decade ago, these variations in GBP could have been ignored, but now, due to the modularization, every lift is categorized as critical and ignoring these minor variations can lead to severe consequences resulting from the ground failure.

As stated before, advances in modular construction have increased the usage of heavy cranes, and heavy crawler cranes in particular. It would be naïve to underestimate the GBP under the crawler crane tracks by assuming it is uniform along the width of the crawler crane track. Modularization is becoming more widely adopted for industrial projects and in infrastructure and residential projects. For this reason, the overall number of cranes and critical lifts has increased, increasing the number of crane accidents (Abdul Hamid et al. 2019). The research conducted examines the limitations of 4-point GBP calculations and, in particular, makes it evident that it is critically important to consider these limitations given the increased use of heavy crawler cranes for modular construction.

3.1.1. Methodology for GBP under crawler cranes

The GBP under the crawler crane tracks is a typical example of combined loading (Hibbeler 2011). Before computing the GBP values under the crawler track, it is imperative to know the resultant forces due to the weight of the crane parts, including payload and their locations. For ease of calculations and reference, the crane load bearing track area ($A1$ & $A2$), the width of the track B_t, length of the track L_e, the distance of track from crane track bearing area centroid s, the resultant W (sum of all the weights acting on crawler tracks), location R, and θ from x-axis can be drafted on a Cartesian coordinate system as shown in Figure 3.1. The resultant W is the sum of all crane part weights, but the location of W, in the form of R (location of the resultant weight W from the crawler crane track bearing area centroid) and θ (angle from x-axis) depends on the crane parts' COG, their location, and crane slew angle α from x-axis (Becker 2001). These calculated values are mandatory to determine the combined loading on the track's load-bearing area.

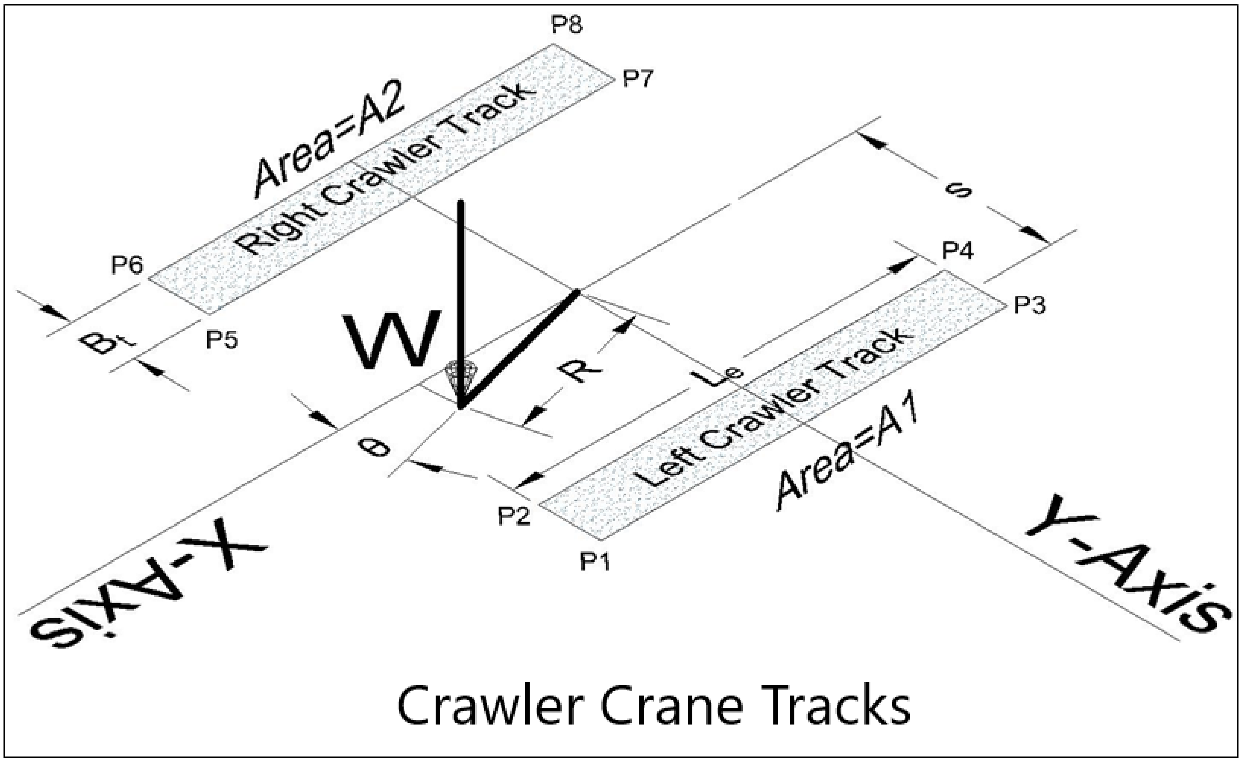

Figure 3.1: Crawler crane track bearing area on Cartesian coordinate system

Combined loading combines normal forces, shear forces, the overturning moment, and the torsional moment acting on an area of a body under investigation. Hibbeler (2011) commented on combined loading in detail. In the case of the crawler crane track area, it is assumed that no deformation occurs for GBP calculations, so shear force and torsional moment are deemed negligible. The normal force results from uniform normal-stress distribution based on the weight W and area $(A1 + A2)$. The whole weight of the crane is anticipated to be offset from the centroid (X, Y) of the actual track bearing area (ATBA), as shown in Figure 3.1. This offset creates a overturning moment along the *x*-axis and *y*-axis. The edges/corners of the crawler track $P_i(x_i, y_i)$, where $i = 1,2, \cdots, 8$, are used to calculate the 8-point GBP values, to determine the GBP profile. The value of normal stress remains the same across the profile, but the value of overturning moment at a particular location depends on how far away that location of W positioned from the *x*-axis and *y*-axis. The stress σ_i due to the overturning moments, plus the normal forces at a particular location can be derived as shown in Equation (20).

$$\sigma_i = \frac{W}{A1 + A2} + \frac{WR(cos\theta)y_i}{I_{xx}} + \frac{WR(sin\theta)x_i}{I_{yy}} \tag{20}$$

I_{xx} and I_{yy} in Equation (20) are the moments of inertia of ATBA along the x-axis and y-axis, respectively. It is vitally important to mention that the compression stress is assumed to be positive for calculations for this analysis, and tensile stress is assumed to be negative. The first part of Equation (20) consists of the normal stress due to the weight of the crane acting on the ATBA $(A1 + A2)$, and the second and the third parts of Equation (20) are the overturning moments operating along x-axis and y-axis, respectively, as shown in Figure 3.2.

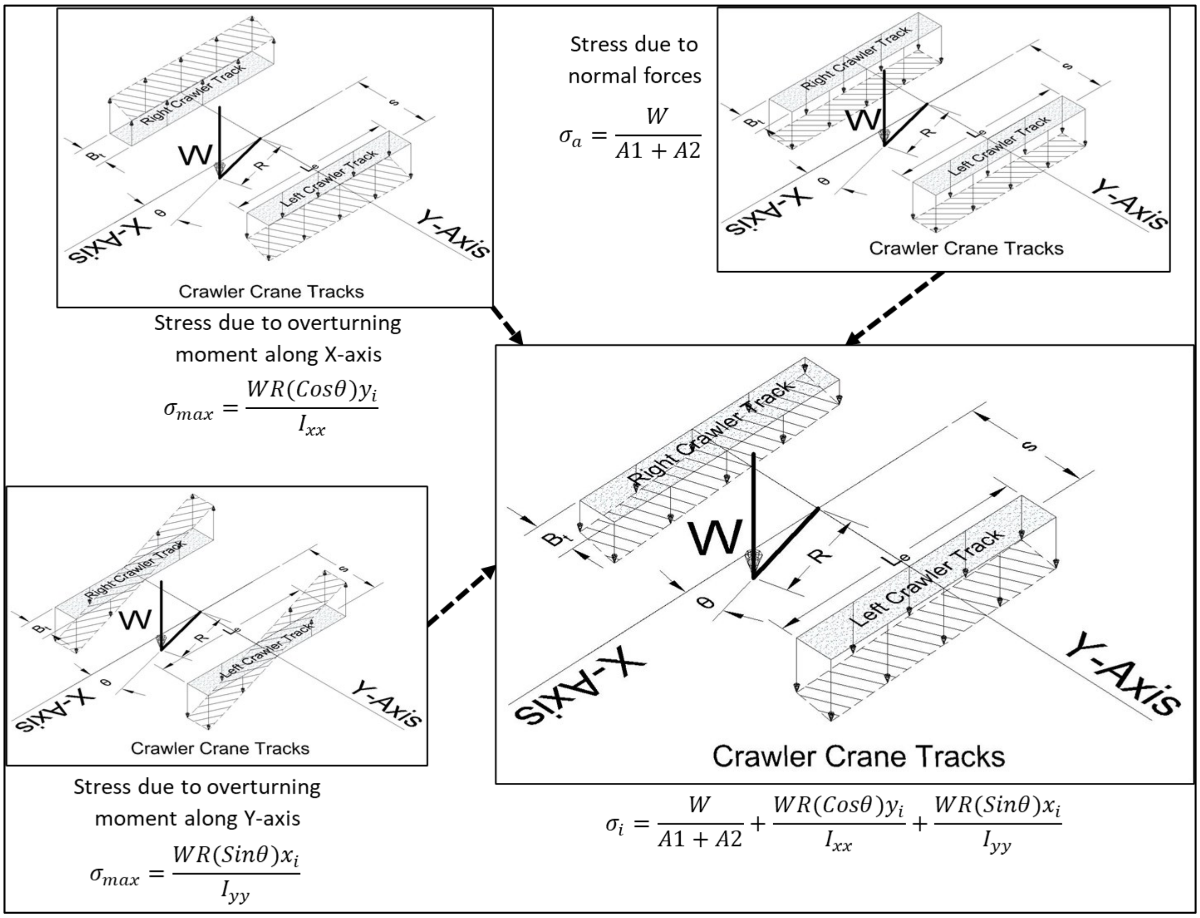

Figure 3.2: Combined loading on the actual track bearing area (ATBA)

The central part of Equation (20) is the ATBA, which can be readily calculated using Surveyor's area formula, as shown in Equation (21) (Braden 1986). Moreover, the ATBA can also be obtained from the crane manufacturer's specifications sheet.

$$Area = \frac{1}{2}\left|\sum_{i=1}^{n} x_i(y_{i+1} - y_{i-1})\right| \tag{21}$$

For the estimate of overturning moment, the moment of inertia of ATBA (I_{xx} and I_{yy}) needs to be evaluated, using Equations (22) and (24) (Hally 1986). Hally (1986) also specified that the vertices of a polygon n should be numbered in a counterclockwise direction.

$$I_{xx} = \frac{1}{12}\sum_{i=1}^{n}(x_i y_{i+1} - x_{i+1} y_i)(x_{i+1}^2 + x_i^2 + x_i x_{i+1}) \tag{22}$$

$$I_{yy} = \frac{1}{12}\sum_{i=1}^{n}(x_i y_{i+1} - x_{i+1} y_i)(y_{i+1}^2 + y_i^2 + y_i y_{i+1}) \tag{23}$$

$$I_{xy} = \frac{1}{24}\sum_{i=1}^{n}(x_i y_{i+1} - x_{i+1} y_i)[x_{i+1} y_i + x_i y_{i+1} + 2(x_i y_i + x_{i+1} y_{i+1})] \tag{24}$$

Using Equation (20), along with Equations (21), (22), and (23), the GBP under the crawler track at any spot can be calculated. In the context of the present study, the most significant locations are the corners of the track, which formulate the profile of GBP pressure, as shown in Figure 3.2.

Observing the overturning moments, the neutral axis is located where the stress is 0. When the stresses due to normal force and overturning moment are added together, as per Equation (20), the neutral axis, most of the time, lies outside the boundary of the ATBA, which leads all 8-point GBP values to be compressive. The distance from this neutral axis to the centroid (X, Y) of the ATBA and from the neutral axis to the edge of the ATBA depends on the value of R.

If the neutral axis enters the ATBA, the stresses are projected to be compressive on one side of the neutral axis and tensile on the other (Hibbeler 2011). Because the crawler crane track is not in bonded contact with the ground, the track will show 0 GBP in the tensile stress area. This tensile stress area changes the whole scenario by shifting the centroid and reducing the ATBA $(A1 + A2)$ to the effective track bearing area (ETBA) $\left(A1' + A2'\right)$. The value of R determines whether the ETBA is equal to ATBA or is less than ATBA. Equation (25) provides the effective track bearing area cut-off E_f. When the value of E_f is plotted against the angle θ, a polygon of 4 sides is projected as shown in Figure 3.3, which denotes a boundary for ETBA and ATBA. If $R \leq E_f$, the ETBA is equal to ATBA. In the event where $R > E_f$, the ATBA is reduced to the ETBA. If the location of W in the form of R remains within the projected boundary of E_f, the ATBA is used for the 8-point

GBP values. When the location of W is outside the projected boundary of E_f, the ETBA is used for the 8-point GBP calculations.

$$Effective\ Track\ Bearing\ Area\ Cut-off = E_f = \frac{L_e(B_t^2 + 12s^2)}{6[(B_t^2 + 12s^2)\cos\theta + L_e(2s + B_t)sin\theta]} \qquad (25)$$

Where,

$s =$ the distance from the crane center to the center of crawler width/outrigger,

$B_t =$ the width of the track, and

$L_e =$ the effective track length/distance between two outriggers (lengthwise).

θ = Angle of resultant W from x-axis

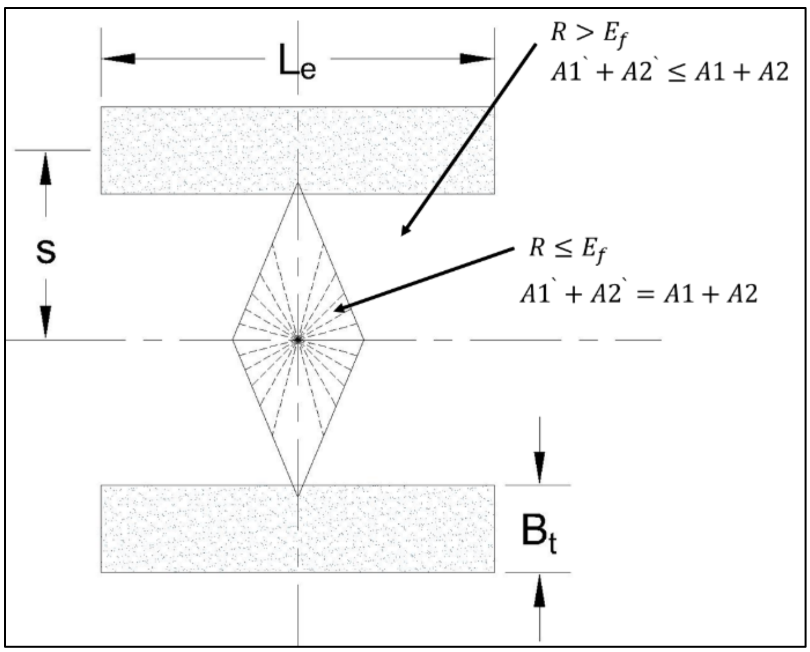

Figure 3.3: Effective track bearing area (ETBA) cut-off for a generic crawler crane track

In order to obtain the GBP values while the payload is at the front and $R > E_f$, the GBP points at the rear shift closer to the centroid, with a new assumed set of points $P_i^{'}(x_i^{'}, y_i^{'})$. The updated points $P_i^{'}(x_i^{'}, y_i^{'})$ creates an updated edge of the track aligned with the neutral axis, thus making the rear edge the neutral axis (see Figure 3.4). The neutral axis passes through these points at the rear of the crane to exert 0 GBP. Due to the transition of these points, the ATBA $(A1 + A2)$ shrinks to ETBA $(A1^{'} + A2^{'})$, which in turn moves the location of the centroid (X, Y) to (X', Y'), as shown in Figure 3.4. Moreover, the axes also move from the previous centroid to the new location as x'-axis and y'-axis. Due to the transposition of the axis, the GBP points further realign themselves to $P''_i(x''_i, y''_i)$, using Equation (26).

$$P_i''(x_i'', y_i'') = \left(x_i' + X', y_i' + Y'\right) \tag{26}$$

The updated values of $I_{x'x'}$, $I_{y'y'}$ and $I_{x'y'}$ are determined using Equations (22), (23) and (24). However, the principal axis must be defined to create the neutral axis aligned with the GBP points at the rear. An angle β inclines the x'-axis and y'-axis to overlap the principal axis, calculated using Equation (27) (Hibbeler 2011).

$$tan2\beta = \frac{2I_{x'y'}}{(I_{x'x'} - I_{y'y'})} \tag{27}$$

With this angle β, the x'-axis and y'-axis are rotated with respect to the principal axes as shown in Figure 3.4 as x''-axis and y''-axis. The rotation of these axes further alters $P_i''(x_i'', y_i'')$ to $P_i'''(x_i''', y_i''')$, which can be calculated using Equation (28).

$$P_i'''(x_i''', y_i''') = \left(x_i'' \cos\beta + y_i'' sin\beta, -x_i'' \sin\beta + y_i'' cos\beta\right) \tag{28}$$

At this juncture, the assumption is that the payload is at the front of the crane, which means that $P_1 = P_1'$, $P_2 = P_2'$, $P_5 = P_5'$ and $P_6 = P_6'$. At the rear, points are different; however, as the points are on the edges of the crawler track, $y_3 = y_3'$, $y_4 = y_4'$, $y_7 = y_7'$ and $y_8 = y_8'$. This change reduces the number of variables to x_3', x_4', x_7' and x_8'. The constraint for these points is that they cannot leave the boundary of the ATBA, as shown in Equation (29).

$$x_3', x_4', x_7', x_8' \geq \begin{cases} -\dfrac{L_2}{2} \\ x_3, x_4, x_7, x_8 \end{cases} \tag{29}$$

To calculate the GBP, the values of $I_{x'x'}$ and $I_{y'y'}$ need to be updated to $I_{x''x''}$ and $I_{y''y''}$ with respect to the x''-axis and y''-axis and also due to the upgraded track edges P_i'''. Due to the shift and rotation of the axes, the values of R and θ also transform to R'' and θ''. Equation (20) is updated with these new values to obtain the GBP for ETBA in the form of Equation (30).

$$\sigma_i' = \frac{W}{A1' + A2'} + \frac{WR''(cos\theta'')y_i'''}{I_{x''x''}} + \frac{WR''(sin\theta'')x_i'''}{I_{y''y''}} \tag{30}$$

The line joining the points at the rear is parallel with the neutral axis situated at the updated centroid without the normal stress, as shown in Equation (31), which also works as constraints (Hibbeler 2011). Additionally, the points on the rear join together to form a line, which means the gradient of the line joining two points should be equal to the gradient of the line joining the other points, as shown in Equation (32). Moreover, the values of $\sigma_3^{'}, \sigma_4^{'}, \sigma_7^{'}, \sigma_8^{'}$ are constrained to be positive (compressive in nature), as shown in Equation (33).

$$tan^{-1}\left(\frac{y_8^{'''} - y_7^{'''}}{x_8^{'''} - x_7^{'''}}\right) + 180^{\circ} = tan^{-1}\left(\frac{I_{y''y''}tan(\theta^{''})}{I_{x''x''}}\right) \tag{31}$$

$$\frac{y_8^{'''} - y_7^{'''}}{x_8^{'''} - x_7^{'''}} = \frac{y_8^{'''} - y_4^{'''}}{x_8^{'''} - x_4^{'''}} = \frac{y_8^{'''} - y_3^{'''}}{x_8^{'''} - x_3^{'''}} = \frac{y_4^{'''} - y_3^{'''}}{x_4^{'''} - x_3^{'''}} = \frac{y_7^{'''} - y_4^{'''}}{x_7^{'''} - x_4^{'''}} = \frac{y_7^{'''} - y_3^{'''}}{x_7^{'''} - x_3^{'''}} \tag{32}$$

$$\sigma_3^{'}, \sigma_4^{'}, \sigma_7^{'}, \sigma_8^{'} \geq 0 \tag{33}$$

The value of $\sigma_i^{'}$ is required, at the same time, the objective function is to minimize the GBP values at the rear, with the variables $x_3^{'}$, $x_4^{'}$, $x_7^{'}$ and $x_8^{'}$, as shown in Equation (34).

$$Min\ z = \sigma_3^{'} + \sigma_4^{'} + \sigma_7^{'} + \sigma_8^{'} \tag{34}$$

To solve such complex GBP problem, which is nonlinear, it is appropriate to use a generalized reduced gradient (GRG). The GRG approach is one of the algorithms used to solve nonlinear optimization problems (Drud 1985). GRG was first introduced for solving linear optimization problems (Smeers 1977). Later, this approach was introduced to solve nonlinear programs with the addition of polyhedral constraints (Wolfe 1963). A GRG module of MS Excel solver was introduced in 1990 after the successful launch for Lotus 1-2-3 (Fylstra 2019). In the present study, an Excel solver is utilized for solving the GBP quadratic equations to obtain the eight points on the ETBA that satisfy all the constraints. If the payload is at the rear, the whole process is performed in reverse order.

To verify the proposed methodology, finite element analysis (FEA) is used to simulate the crane slew. The GBP values under the ATBA are collected from FEA and crane matched with the values obtained from Equation (20). For the ETBA, the area under the crane model in FEA is regulated to obtain the values, and later, are compared with the values obtained from Equation (30).

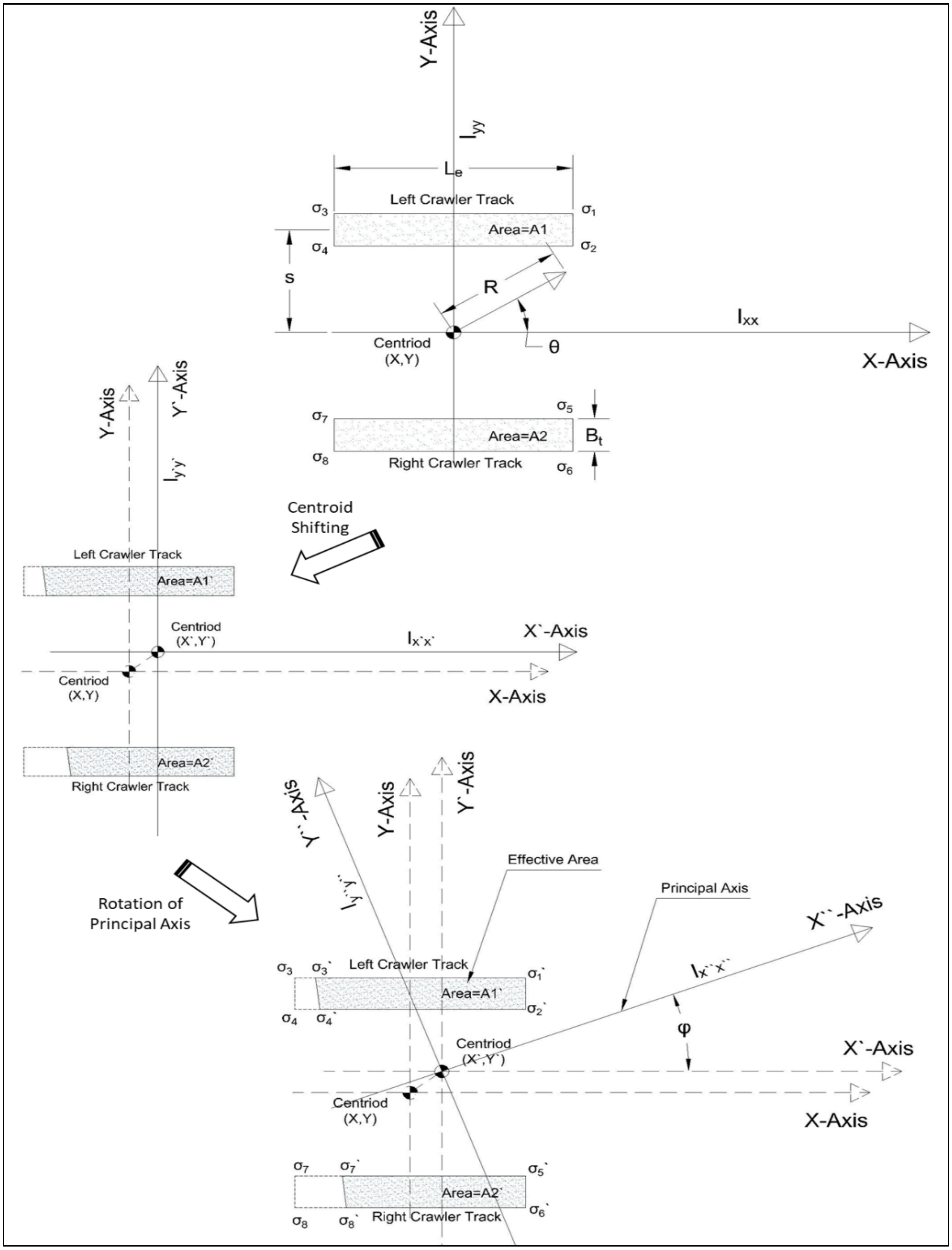

Figure 3.4: Transformation of ATBA to ETBA

To develop the FEA model, the weights of various parts of the crane and their centroids are required, which are provided by the manufacturer of the selected crawler crane. The next step is to develop a crawler crane model. For this, all the major dimensions of the crawler crane under investigation are obtained from the 3D AutoCAD drawing of the model. ANSYS Workbench (version 17.1) is used to carry out the FEA in the present research. All parts (carrier, superstructure, boom, mast, and load) are assumed to be rigid. In general, the load-bearing length of the track is smaller as compared to the actual length of the track and in the case of a solid surface, the effective width is also shorter as compared to the actual width of the track. To obtain these readings, a thin plate (≈25 mm thick) of dimensions equal to the bearing length and the bearing width is placed under each track. This thin plate functions as a sensor to obtain the values for the pressure exerted by the tracks. The developed crane geometry is uploaded to a static structural mechanical workbench APDL solver. The stiffness behaviour of all crane parts is assumed to be rigid to consider forces only, with the exception of the thin plates under the tracks, which are assigned flexibility in order to measure the track pressure. The lowermost surface of the plates is loaded with fixed support. The weights and COGs of the various crane parts are adjusted by adding material blocks until the overall weight and COG of each part corresponds with the available data. The model is then loaded with gravity. After the model is solved, the results are assumed to be normal stress and minimum principal stress. (When only the three normal stresses remain, and all the shear stresses are zero, these normal stresses are known as principal stresses.) ANSYS provides negative values of principal stresses due to compression.

3.1.2. Case studies for the verification of new methodology

It is important to mention that this novel method is applicable to any type of crawler crane. The case study has been selected to reflect what is likely to be encountered in modular construction. In general, when heavy modules are required to be lifted, a crawler crane is the crane of choice (when spatial constraints allow for it) since, in some instances, the crane walks with the payload before installation. For the case studies, two crawler cranes are selected. One is American Hoist AH-11320 (450 metric ton capacity), and the second is Manitowoc 18000 (750 metric ton capacity). For each crane, two case examples are developed for the verification of new methodology, one where $R \leq E_f$ and other where $R > E_f$. These case examples sum up to 4 case studies, two for each crane.

American Hoist AH-11320 is a crawler crane designed in compliance with ANSI B30.5 (published in 1968) (ASME 2018). It is an 1100 series crane with a lifting capacity of 450 metric ton with a standard configuration. The lift rating of AH-11320 indicates that the "Sky Horse" configuration increases the load moment (American-Hoist 1979). Note that the crane's lifting capacity, as per the lift rating of AH-11320, can be increased to 544 metric ton by using the "Guy Derrick" configuration (American-Hoist 1979). Moreover, The lift rating of AH-11320 also states that the crane's lifting capacity can be further increased to 907 metric ton by using the "Super Sky Horse" configuration (American-Hoist 1979). These high capacities imply that the manufacturer designed the crane structure for heavy loads.

For this reason, the manufacturer of the AH-11320 called this crane a 6-in-1 machine, with Standard, Jib, Tower, Sky Horse, Guy Derrick, and Super Sky Horse configurations (American-Hoist 1979). The configuration of the crane AH-11320 used in this research is listed in Table 3.1. Regardless of the crane configuration, the arrangement of ATBA remains the same, and only the capacity and the weight of the crane increase.

Table 3.1: Crane configuration for case examples

	Description	Crane	
1	Crane	American Hoist 11320	Manitowoc 18000
2	Capacity of Crane	450 metric ton	750 metric ton
3	Configuration	Standard	Standard
4	Boom	45.7 m (150 ft)	85.3 m (280 ft) #55 OR #55A
5	Carbody Counterweight	0 kg	145,150 kg (320,000 lb)
6	Superstructure Counterweight	104,330 kg (230,000 lb)	239,500 kg (528,000 lb)

The crane model of AH-11320 with a dummy load as the payload was developed for FEA for GBP simulation. A picture of the crane AH-11320 and the FEA crane model is shown in Figure 3.5a. It is essential to obtain the same GBP values by crane matching the FEA crane model (AH-11320) part weights and their respective COGs with the manual calculations. Part weights and COGs are enumerated in Table 3.2, along with the crane parameters L_e, s and B_t. This data was acquired from the crane manufacturer in drawings or software, as depicted in Figure 3.6.

Manitowoc 18000 is a crawler crane designed in compliance with ASME B30.5 (ASME 2018). It has four configurations: standard, Luffing Jib, Fixed Jib, and MAX-ER for maximum lifting capacity (750 metric ton) (Manitowoc 2019). The configuration of Manitowoc 18000 is listed in

Table 3.2, along with the configuration of AH-11320. A crane model for Manitowoc 18000 was developed for FEA with a dummy load as the payload for the GBP simulation. A picture of Manitowoc 18000 and the FEA crane model is shown in Figure 3.5b. The crane part weights, COGs, and crane parameters, L_e, s and B_t are listed in Table 3.3 and are taken from Manitowoc GBP software (see Figure 3.6).

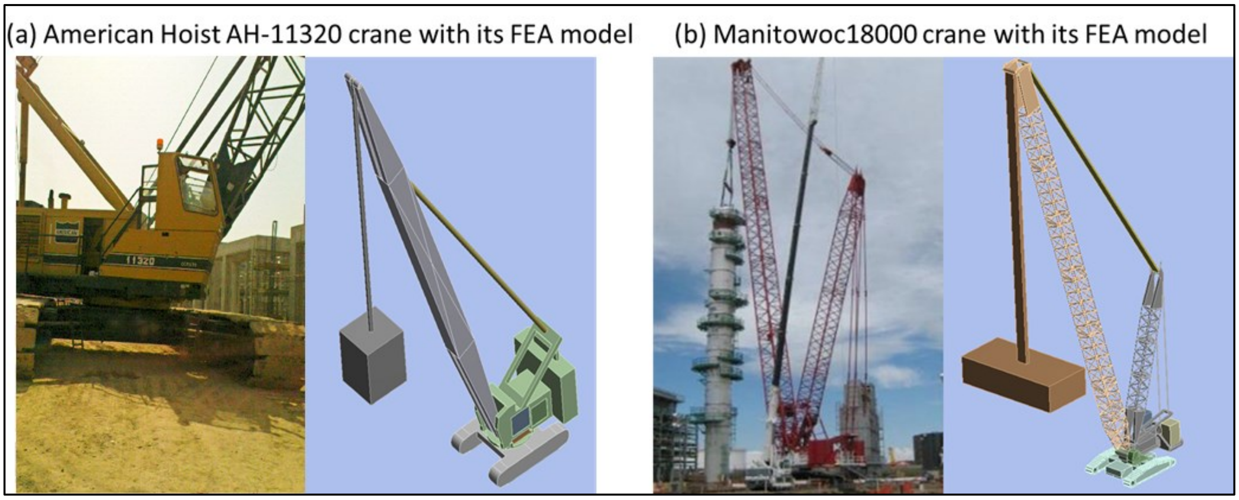

Figure 3.5: (a) American Hoist AH-11320 with its FEA model, (b) Manitowoc18000 with its FEA model

Table 3.2: American Hoist 11320 crane part weights and respective COG locations

	Description	Manual Calculations	FEA Values
1	Superstructure weight (metric ton)	172.55	172.55
2	Superstructure COG from crane center (m)	−3.91	−3.91
3	Undercarriage weight (metric ton)	101.56	101.56
4	Undercarriage COG from crane center (m)	0	0
5	Length L_e of load-bearing crawler track (m)	6.89	6.89
6	Distance s between crawler tracks and axis (m)	3.32	3.32
7	Effective width B_t of crawler tracks (m)	1.52	1.52
	Case 1		
8	Boom weight (metric ton)	22.23	22.23
9	Boom COG from crane center (m)	6.37	6.37
10	Payload (metric ton)	54.00	54.00
11	Crane radius (m)	10.97	10.97
	Case 2		
12	Boom weight (metric ton)	22.23	22.23
13	Boom COG from crane center (m)	9.59	9.59
14	Payload (metric ton)	54.00	54.00
15	Crane radius (m)	17.41	17.41

Table 3.3: Manitowoc 18000 crane part weights and respective COG locations

	Description	Manual Calculations	FEA Values
1	Superstructure weight (metric ton)	346.35	346.35
2	Superstructure COG from crane center (m)	−5.99	−5.99
3	Undercarriage weight (metric ton)	249.72	249.72
4	Undercarriage COG from crane center (m)	−0.18	−0.18
5	Length L_e of load-bearing crawler track (m)	8.84	8.84
6	Distance s between crawler track and axis (m)	4.27	4.27
7	Effective width B_t of crawler tracks (m)	1.27	1.27
	Case 1		
8	Boom weight (metric ton)	118.360	118.36
9	Boom COG from crane center (m)	11.26	11.27
10	Payload (metric ton)	50.00	50.00
11	Crane radius (m)	25.92	25.92
	Case 2		
12	Boom weight (ton)	118.36	118.36
13	Boom COG from crane center (m)	11.26	11.27
14	Payload (ton)	80.00	80.01
15	Crane radius (m)	25.92	25.92

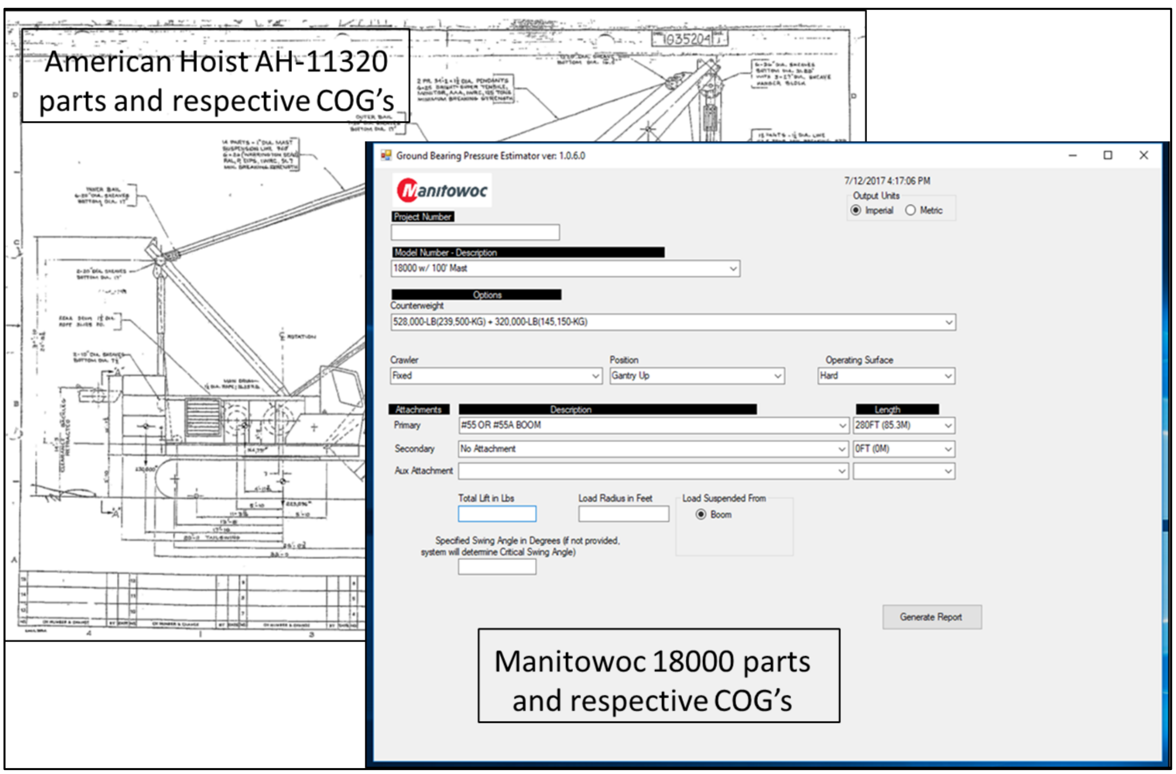

Figure 3.6: Crane parts and respective COGs (American-Hoist 1979, Manitowoc 2019)

3.1.2.1. Case studies for American Hoist AH-11320 (450 metric ton)

As previously mentioned in the methodology section, there are two case scenarios for AH-11320: one where $R \leq E_f$, and the second case scenario where $R > E_f$, which leads to the reduction of the ATBA to the ETBA along the boom slew angle. Both case scenarios for AH-11320 are described in Table 3.2. An identical payload is used for both cases, but at a different lifting radius so that R can be altered to achieve the effective area cut-off (E_f) for both cases. Before proceeding to the FEA simulation, it is necessary to obtain the GBP values using the traditional 4-point loading system, which can be collected from the available GBP chart for American Hoist AH-11320 (American-Hoist 1979).

Surprisingly the centroid (X, Y) of the ATBA for AH-11320 is the same as the rotational axis of the superstructure, resulting in symmetry for the GBP profile along the x-axis and y-axis. Typically, the manufacturers design the cranes so that the ATBA centroid and the rotational axis lie on the same point. This design means it is possible to use the same load chart (chart showing rated capacities of the crane at various lifting radii) for the front and rear without any modification. If the ATBA centroid and the rotational axis differ, the load chart at the crane front differs from the crane rear. The American Hoist AH-9310 crane is a typical example of this scenario, where the manufacturer designs the centroid of the track bearing area to offset from the rotational axis of the superstructure. The crane's capacity at the front is different from at the rear at the same lifting radius (American-Hoist 1973).

3.1.2.1.1. Case 1: $\boldsymbol{R \leq E_f}$

In this case scenario, the ETBA is the same as the ATBA $(A1' + A2' = A1 + A2)$. The normal stresses are compressive across the ATBA. The calculations are straightforward, as described in the methodology. The 4-point GBP values are used to compare the 8-point and FEA GBP values. For this case study example, the crane superstructure is rotated from 0° to 180° in increments of 15°. The 4-point GBP values are displayed in Figure 3.7a. The manual calculations using Equation (6) along the respective superstructure slew angle are plotted against the 4-point values obtained from the GBP chart for the AH-11320 crane (Figure 3.8). Moreover, the FEA model is also rotated in increments of 15°, and the values obtained are plotted against the 8-point manual calculations and 4-point values from the GBP chart (see Figure 3.8). The main concern is the variation of these 8-point GBP values from the 4-point values.

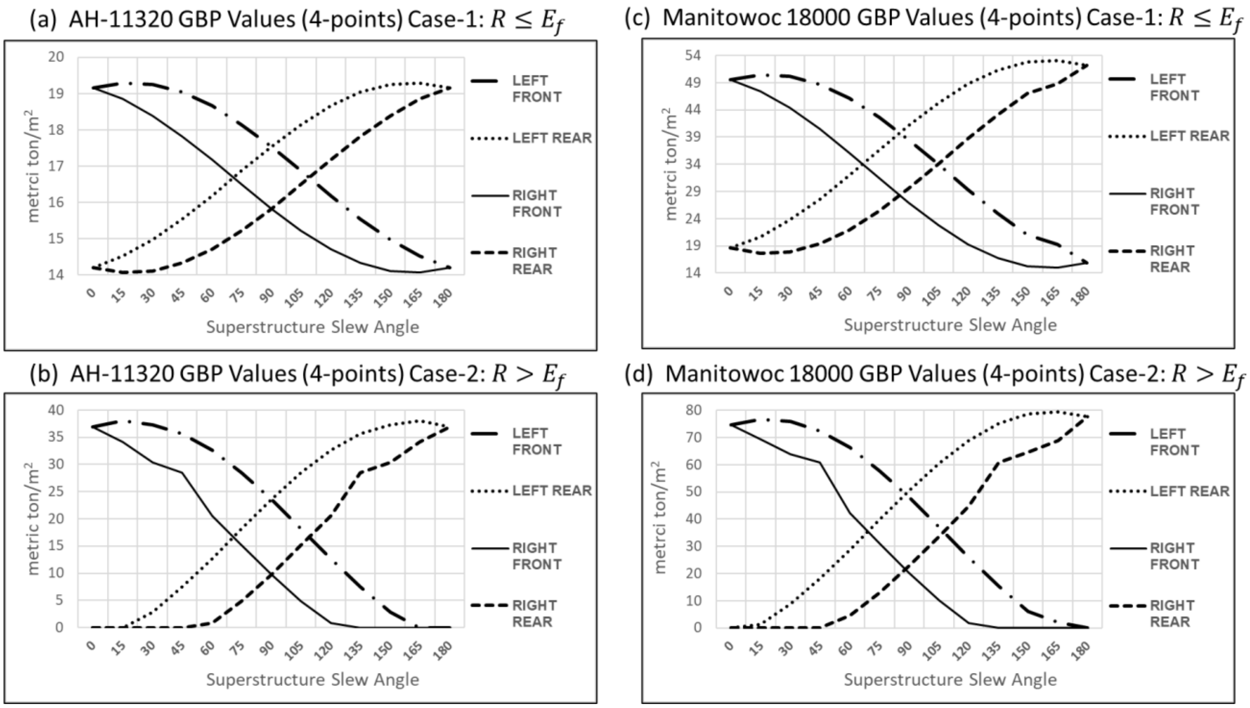

Figure 3.7: (a & b) 4-point GBP for AH-11320 and (c & d) Manitowoc 18000 (Case 1 and Case 2)

It is satisfactory that the FEA results are close to the 8-point GBP manual calculations with an average error of 0.05 metric ton/m^2 and a standard deviation of 0.03 metric ton/m^2 (sample size of 180/15) which provides validation of the developed methodology with a percentage mean error of 0.16% (standard deviation of 0.08%) with respect to the average FEA value of 34.05 metric ton/m^2.

3.1.2.1.2. Case 2: $R > E_f$

In this scenario, the ETBA $(A1' + A2')$ is smaller than the ATBA $(A1 + A2)$. The 4-point GBP values are shown in Figure 3.7b. The GBP values for the left and right-rear are 0 ton/m^2 at the start (0° boom slew angle), then increase from 0 ton/m^2 after 15° crane slew angle, but the pressure under the right-rear remains the same until a boom slew angle of 45°. As the centroid of ATBA is concurrent with the axis of rotation, the GBP profile for left and right-rear are identical in mirror image across crane slew angle of 90°, which shows that the x-axis and y-axis work as axes of symmetry for the GBP profile.

For the manual calculations, the ATBA decreases to the ETBA as the crane rear GBP points shift further towards the centroid, with the load at the crane front. For the FEA simulation, the ETBA is used for the GBP values. If the load is at the rear of the crane (90° to 270°), the front load bearing points move closer to the centroid. The manual 8-point calculations using GRG for nonlinear optimization and the FEA values are plotted against the 4-point values in Figure 3.9. The right-front and the right-rear GBP profile are symmetrical but opposite in direction (see Figure 3.9).

Figure 3.8: Deviation of manual and FEA 8-point GBP values from 4-point GBP values (AH-11320 Case 1)

3.1.2.2. Case Studies for Manitowoc 18000 (750 metric ton)

Following the same approach, there are two case scenarios for Manitowoc 18000, one where $R \leq E_f$, and the second case scenario is where $R > E_f$ (see Table 3.3). To simulate these two scenarios, different payloads are used for each of the case studies but using the same lifting radius so that R can be altered to achieve the effective area cutoff E_f for both cases. Before proceeding to the simulation, the GBP values must be determined employing the traditional 4-point loading system, which can be obtained from Manitowoc online GBP freeware as shown in Figure 3.7c and Figure 3.7d (Manitowoc 2019).

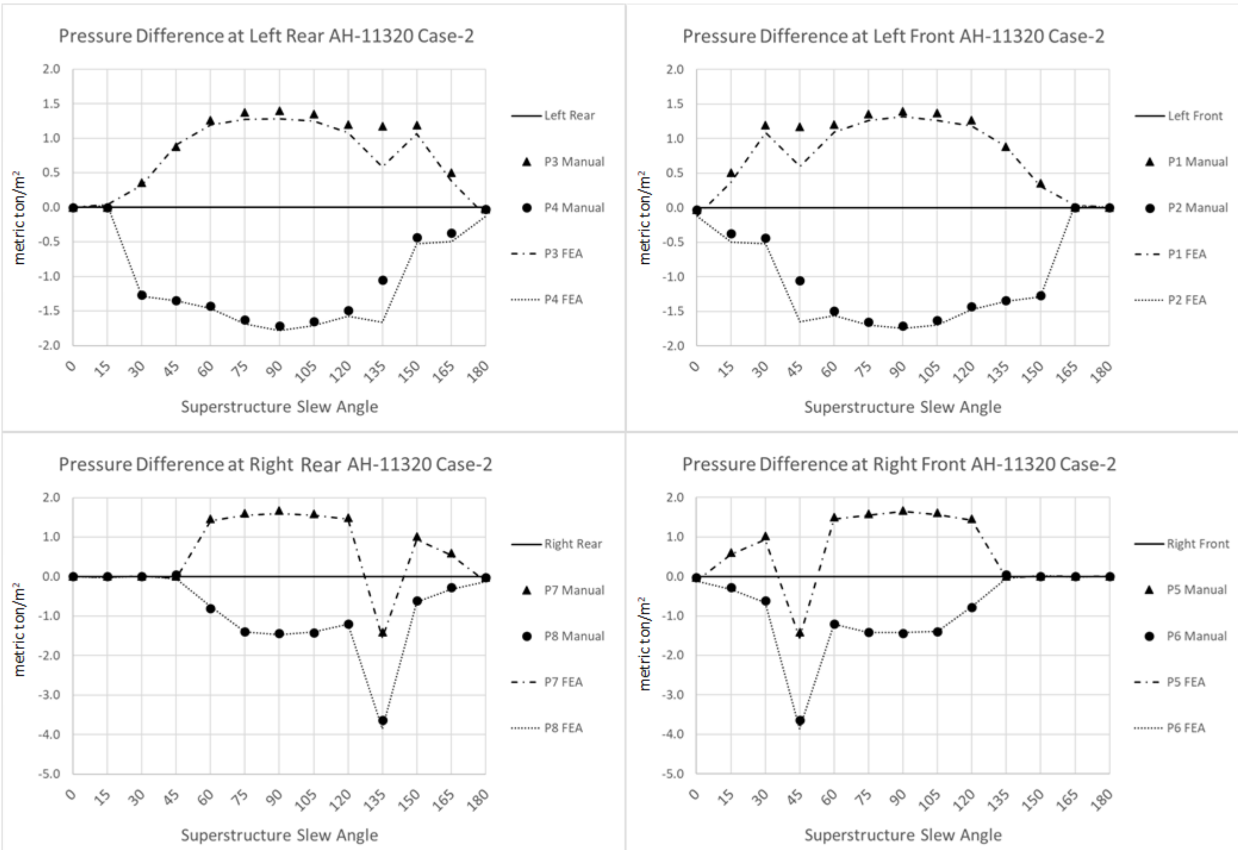

Figure 3.9: Deviation of manual and FEA 8-point GBP values from 4-point GBP values (AH-11320 Case 2)

In the case studies of the AH-11320 crane, different loads at the same radius create the same value of R, but for the Manitowoc 18000 crane, different values of R are generated. The reason is that the COG of the crane undercarriage is offset from the crane's rotational axis of the superstructure. However, the centroid (X, Y) of ATBA for the Manitowoc 18000 is the same as the rotational axis of the superstructure. Due to the centroid constraint and undercarriage COG offset, the load chart is the same for the front and rear, but the GBP profile is different because R and θ vary with respect to the crane superstructure slew angle α.

3.1.2.2.1. Case 1: $R \leq E_f$

In this scenario, the ETBA remains the same as the ATBA ($A1' + A2' = A1 + A2$). For this case example, the crane superstructure is rotated from 0° to 180° in increments of 30°. The 4-point GBP values are shown in Figure 3.7c. The maximum GBP value is when the payload is at the rear of the crane, as the COG is offset from the rotational axis and closer to the rear of the crane. The manual calculations using Equation (6) along the respective superstructure slew angle are plotted against the 4-point values obtained from Manitowoc software (Manitowoc 2019). Similarly, the FEA model is also rotated, and the results are plotted against the 8-point GBP manual calculations and the traditional 4-point GBP values (see Figure 3.10).

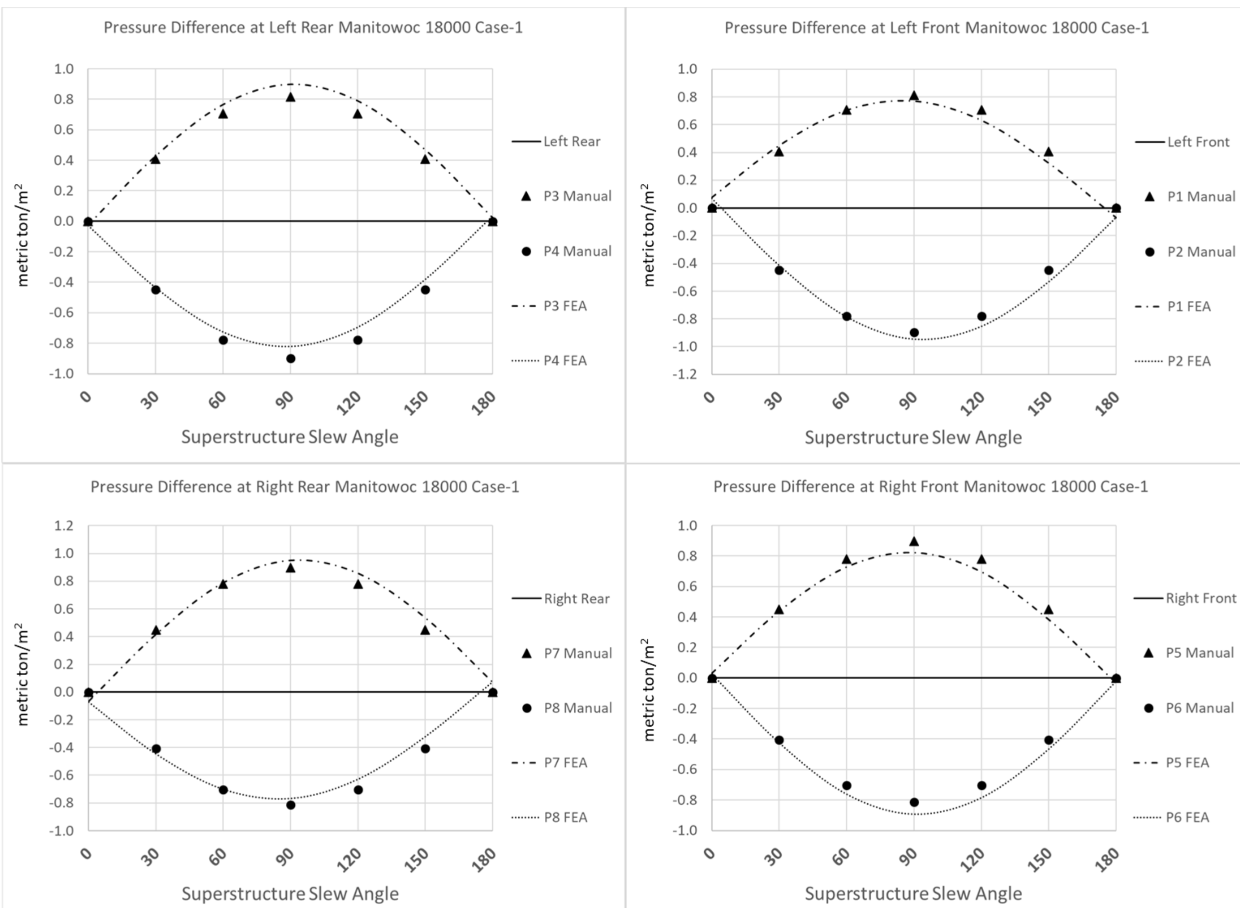

Figure 3.10: Deviation of manual and FEA 8-point GBP values from the 4-point GBP values (Manitowoc 18000 Case 1)

3.1.2.2.2. Case 2: $\boldsymbol{R > E_f}$

In this scenario, the ATBA $(A1 + A2)$ depreciates to the ETBA $(A1^{\prime} + A2^{\prime})$. The 4-point GBP values are shown in Figure 3.7d. The GBP values for the left-rear and right-rear are 0 metric ton/m^2 at the start (0° boom slew angle). The GBP values under the left-rear increase from 0 metric ton/m^2 midway to 30°, but the right-rear values remain constant until the boom slew angle is 30° and later increases from 0 metric ton/m^2 midway between 30° and 60°. The centroid of ATBA is aligned with the axis of rotation; however, the COG of the crawler (undercarriage) is offset from the rotational axis. For the manual calculations, the same GRG nonlinear optimization technique is used as before. For the FEA simulation, the ETBA is used for the GBP values. The manual 8-point calculations and the FEA values are plotted against the traditional 4-point values in Figure 3.11.

3.1.3. Outcome and verification

Considering Case 1 for both of the crawler cranes, it can be seen in Figure 3.8 and Figure 3.10 that the maximum difference of 8-point and 4-point as well as FEA values to 4-point occurs when the angle θ is 90° (a difference of ±0.9 metric ton/m^2 between 8-point versus traditional 4-point and a difference of ±0.9 metric ton/m^2 between FEA values versus traditional 4-point). This variation is also shown in Appendix A. It is important to note that if the COG of crawler undercarriage is the same as the centroid (X, Y) of the ATBA, then $= \alpha$. When the COG of the crawler undercarriage is offset from the centroid (X, Y) of ATBA, θ can deviate from the crane slew angle α. The deviation of 8-point GBP values from the traditional 4-point GBP values implies that the 4-point GBP values can be limited in real-world scenarios. Furthermore, the variation/difference of 8-point and 4-point GBP values converges to 0 when the θ is 0° or 180° (see Appendix A).

Concerning the GBP values, the maximum GBP difference (8-point and traditional 4-point) for AH-11320 for the given Case 1 scenario is +0.27 metric ton/m^2 for the right-rear when θ is 90°. For the left-front, the maximum variation (8-point and traditional 4-point) is 0.19 metric ton/m^2, while, for the left-rear, the maximum variation (8-point and traditional 4-point) is +0.23 metric ton/m^2.

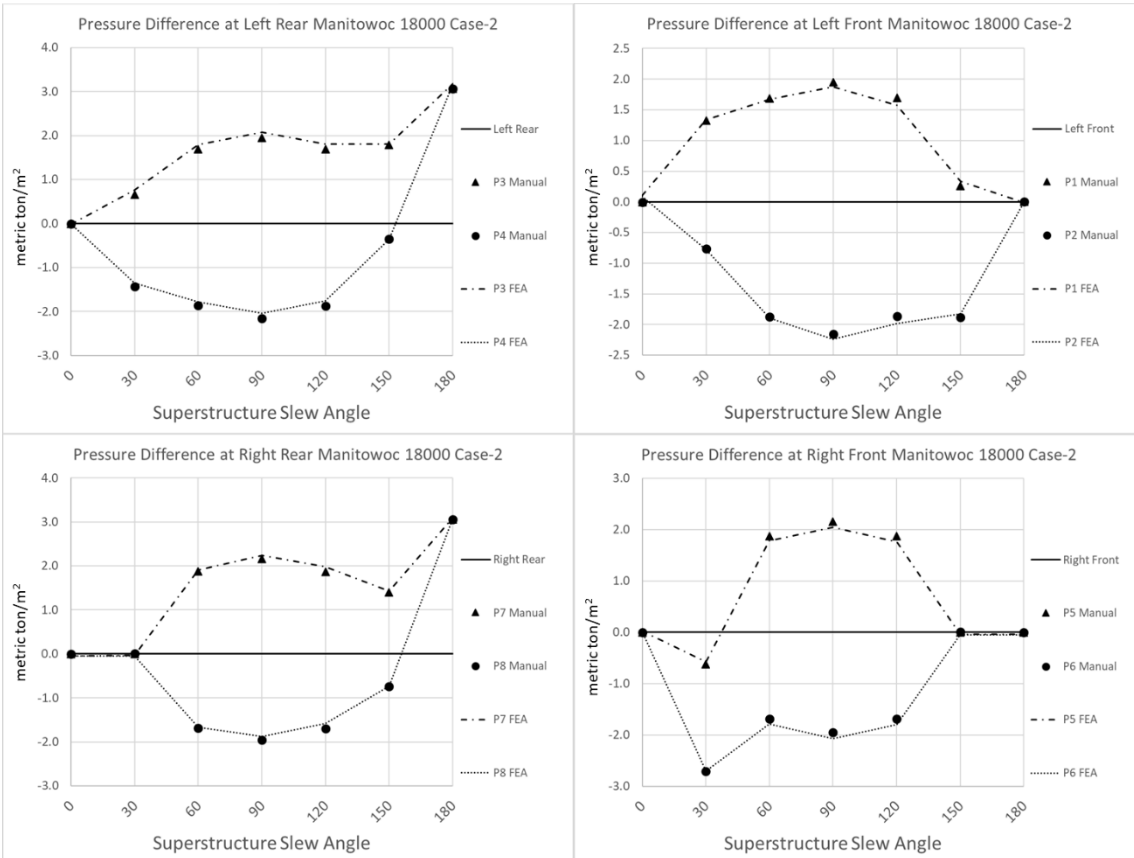

Figure 3.11: Deviation of manual and FEA 8-point GBP values from the 4-point GBP values (Manitowoc 18000 Case 2)

For the Manitowoc 18000 crane, Case 1 is similar to AH-11320 Case 1 ($R \leq E_f$), except the value of θ. The crane slew angle α is different from θ, which means $\theta = 90°$ when $\alpha = 94.54°$. Observing the values, the maximum variation (8-point and traditional 4-point) is +0.9 metric ton/m^2 for left-rear, right-front, and right-rear when the crane slew angle $\alpha = 90°$. The maximum difference (8-point and traditional 4-point) for the left-front is +0.8 metric ton/m^2 provided $\alpha = 90°$. A bird's eye view of both the cranes for Case 1 also gives a sense that as the crane capacity increases, the difference increases between 8-point GBP values and 4-point GBP values, even with the same payload. It appears that the weight of the crane excluding the payload is a significant factor in the context of GBP values.

In the case where $R \leq E_f$, the calculations are straightforward; however, when $R > E_f$The 8-point GBP calculations are intricate and extensive. When $R = E_f$, the edges of the crawler tracks opposite to the payload are subject to 0 load. As the value of R increases and crosses the threshold of E_f, the GBP points at the rear move towards the center of the crane, in parallel with the neutral axis (Hibbeler 2011). This movement reduces the ATBA to ETBA. Considering Case 2 for the AH-11320 crane, the variation (8-point and traditional 4-point) of the GBP values is greater than Case 1 for the AH-11320 crane (see Figure 3.9 and Appendix A). For left-front, the 8-point GBP offset is +1.4 metric ton/m^2 and −1.7 metric ton/m^2 from traditional 4-point GBP values. For the left-rear, 8-point GBP offset is +1.4 metric ton/m^2 and −1.8 metric ton/m^2 from 4-point GBP values. This significant variation (8-point and traditional 4-point) shows that when the crane is close to the crane tipping, the actual GBP value is different and worse from the 4-point GBP values. Moreover, for right-front, the GBP variation (8-point and traditional 4-point) is +1.7 metric ton/m^2 and −3.9 metric ton/m^2 and for right-rear, +1.7 metric ton/m^2 and −3.8 metric ton/m^2. Another aspect to discuss is the fluctuation of the moment of inertia of the ETBA regarding the crane slew angle. As the ATBA is reduced to the ETBA, the value of $I_{x''x''}$ also decreases from I_{xx}. The same is observed in the case of $I_{y''y''}$ which varies from I_{yy}. This variation in the moment of inertia for AH-11320 Case 2 is shown in Figure 3.12b and Figure 3.12d. The ETBA for AH-11320 Case 2 is minimum (19 m^2) at 0° and 180° (see Figure 3.12a). At the same point, $I_{x''x''} = 212.45$ m^4 and $I_{y''y''} = 61.56$ m^4, which is lower as compared to I_{xx} =234.83 m^4 and $I_{yy} = 3.13$ m^4 (ATBA values). The inclination angle is maximum (5.65°) halfway between the minimum ETBA and ATBA (see Figure 3.12b). After 60°, the inclination angle becomes 0° (see Figure 3.12).

Examining the behaviour of the Manitowoc 18000 crane in the case where $R > E_f$, the 8-point GBP values are not symmetrical as observed for the AH-11320 crane. An explanation is that the crane undercarriage COG is offset from the superstructure rotational axis. With respect to the variation of GBP (8-point and traditional 4-point) at the left-front, it is observed to be +2.0 metric ton/m^2 and −2.2 metric ton/m^2, which is significantly higher than Case 2 for the AH-11320 crane (+1.7 metric ton/m^2 and −1.7 metric ton/m^2). The left-rear 8-point GBP varies from +3.2 metric ton/m^2 to −2.2 metric ton/m^2 compared to the 4-point GBP values. This creates a serious concern regarding the accuracy of 4-point GBP values obtained from online software because 3.2 metric ton/m^2 is equal to 31,381 Pa, which is about 7% of the maximum 4-point GBP value (47.97 metric ton/m^2 at $\alpha = 90°$) for Case 2 (see Figure 3.11 and Appendix A).

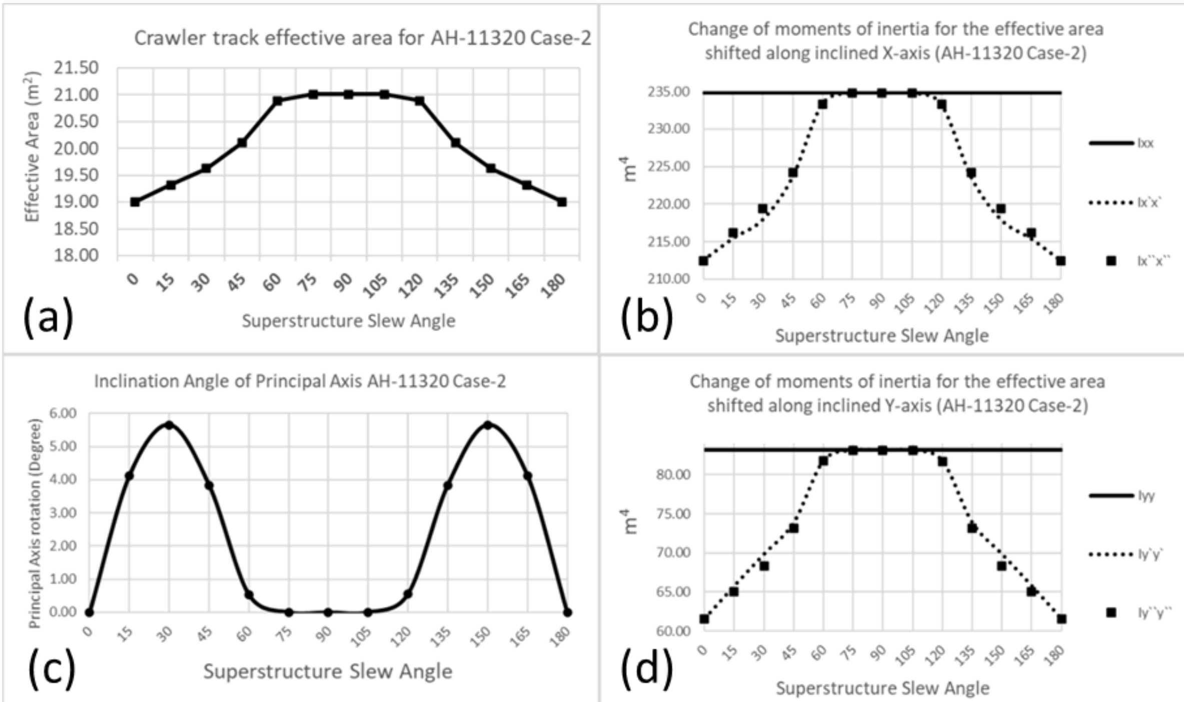

Figure 3.12: Factors influencing ETBA along crane slew angle (AH-11320 Case 2)

Moreover, in Case 2 for Manitowoc 18000, the minimum ETBA is 20.47 m^2 at 180°. The ETBA profile for Manitowoc 18000 Case 2 is not symmetrical along the x-axis, as it is in Case 2 for the AH-11320 crane. Moreover, as shown in Figure 3.13b and Figure 3.13d, the minimum value of $I_{x''x''} = 375.52$ m^4 at 180°, as compared to $I_{xx} = 411.84$ m^4. A similar pattern for Manitowoc 18000 is observed for $I_{y''y''}$: the minimum value is 101.82 m^4, as compared to 146.18 m^4 Figure 3.13a. The pattern for inclination angle (Manitowoc 18000 Case 2) for the principal axis (Figure 3.13c) is not symmetrical along the x-axis. This shows that as ATBA changes to ETBA, the crane moves closer to tipping as the area in contact with the ground decreases.

Next, the research presented herein seeks to quantify the difference between FEA values and the 8-point GBP values. The average error and percentage error with respect to the average FEA value in each case are shown in Appendix A. The percentage errors for all four cases are less than 1%. Typically, for the stability of a crane, ±1% is the standard, meaning that the values from FEA and from the 8-point manual calculations are relatively close to each other, which verifies the accuracy and precision of the method developed for manual 8-point GBP calculations (International Organization for Standarization 2014).

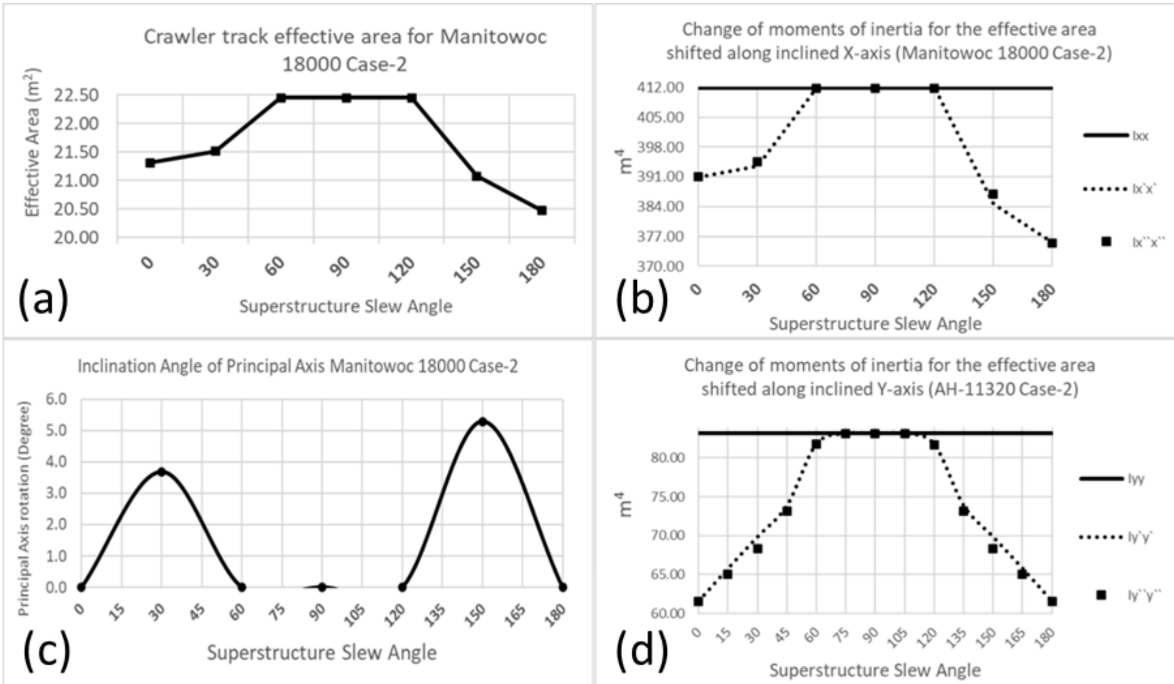

Figure 3.13: Factors influencing ETBA along crane slew angle (Manitowoc 18000 Case 2)

3.2. GBP under hydraulic crane mats

The GBP calculations for hydraulic cranes are slightly different from those used for crawler cranes. Traditionally, the GBP is calculated directly under the crawler tracks (Becker 2001, Shapiro and Shapiro 2010). In hydraulic cranes, first, the outrigger loads (in the form of reaction forces under the outriggers) are calculated. These outrigger reaction forces are then used in conjunction with the outrigger crane mat's surface area to calculate the GBP exerted by a given outrigger (Becker 2001, Shapiro and Shapiro 2010). These approaches provide the GBP under each crane mat, assuming uniform GBP over the crane mat area. However, Ali (2018) found in this regard that the GBP under a hydraulic crane outrigger crane mat is not uniform, meaning that the GBP under the four corners of the mat is not equal. Instead, it should be characterized as 4-point GBP under each outrigger, or 16-points total for four outriggers. Hibbeler (2011) argued in this regard that the axial forces and moments acting on a surface area do not exert uniform pressure along any side unless they are applied directly at the centroid of the surface area (i.e., in this case, the hydraulic crane mat). This outcome concluded that 16-points generate the GBP profile based on the 16 edges of 4 outrigger crane mats, instead of a 4-point GBP distribution under four outrigger crane mats, considering GBP as uniform under each crane mat. In this regard, calculating the GBP based on the assumption of uniform pressure (and thus a 4-point approach for the 4 outriggers) can lead to crane tipping without knowing the root cause of excessive GBP employed due to the non-uniform nature of GBP distribution.

Targeting the research gap with respect to the calculation of GBP under hydraulic crane mats, the research presented in this thesis develops a novel algorithm to compute GBP under hydraulic crane mats, drawing upon the basic concept of combined loading (Hibbeler 2011). The research conducted herein uses FEA for GBP verification purposes. The GBP values calculated using the proposed method are verified using ANSYS simulation software (version 19.2). Based on the weight of each of the crane's components, a map representing the distribution of the GBP exerted on the ground by each hydraulic crane mat is built as the superstructure rotates, mimicking a real-life lift. The weights and the COGs of all the major parts of the hydraulic crane are required. These are obtained from the hydraulic crane model manufacturer. The model of the hydraulic crane is developed in ANSYS mechanical workbench. All crane parts (carrier, superstructure, hydraulic boom, and load) are assumed to be rigid. Given that only the reaction forces are required, rather than those of the thin plate, crane mats are used for crane ground support and load reading.

The hydraulic crane geometry is uploaded to a static structural mechanical workbench APDL solver. The stiffness behaviour of all parts is assumed to be rigid in order to consider forces only, with the exception of the outrigger mats. The lowermost surface of the outrigger mats is loaded with fixed ground support, along with a thin plate, similar to crawler crane FEA model, to obtain stress values. All parts of the cranes are assigned with their respective weights and COGs. The weights and COGs are then adjusted by adding material blocks to the particular parts with various density and location until the overall weight and COG of the part corresponds with the given data. Once the model is solved, the solution is applied in the form of stresses on all four outriggers mats.

3.2.1. Development of methodology for GBP computation for hydraulic crane mats

Before computing the GBP values, it is important to have a detailed understanding of the complex forces acting on the hydraulic crane mat (i.e., a configuration of crane components and payload each of a particular weight and having its own COG). The resultant W (the sum of all the weights acting on the outrigger crane mats), location R (the distance of the sum of all weights W from the superstructure's rotational axis), and θ (angle of the resultant R) with respect to the x-axis can be drafted on a Cartesian coordinate system as shown in Figure 3.14. The values of W, R, and θ are calculated using the data from the crane parts (including payload) and their respective COGs, as shown in Figure 3.15. These calculated values are essential for deriving the combined loading on the hydraulic crane mats.

The combined loading, it should be noted, combines the normal forces and the overturning moments acting on the crane mat's surface area, as shown in Figure 3.16. The edges/corners of the crane mat are the distinct points that will project the GBP profile under a crane mat. The GBP is non-uniformly distributed (trapezoidal distribution) under the crane mat area, but the GBP at the crane mat corners creates upper and lower bounds for the trapezoidal GBP distribution along any direction under the crane mat. The crane mat corners of each outrigger crane mat can be named $P_1, P_2, \ldots, P_n$ for a total of $n=16$ points (four points on each of the four outriggers). These points for each outrigger are as $P_i(x_i, y_i)$, where $i = 1,2,\cdots,16$. Equation (35) calculates the GBP under the hydraulic crane mat

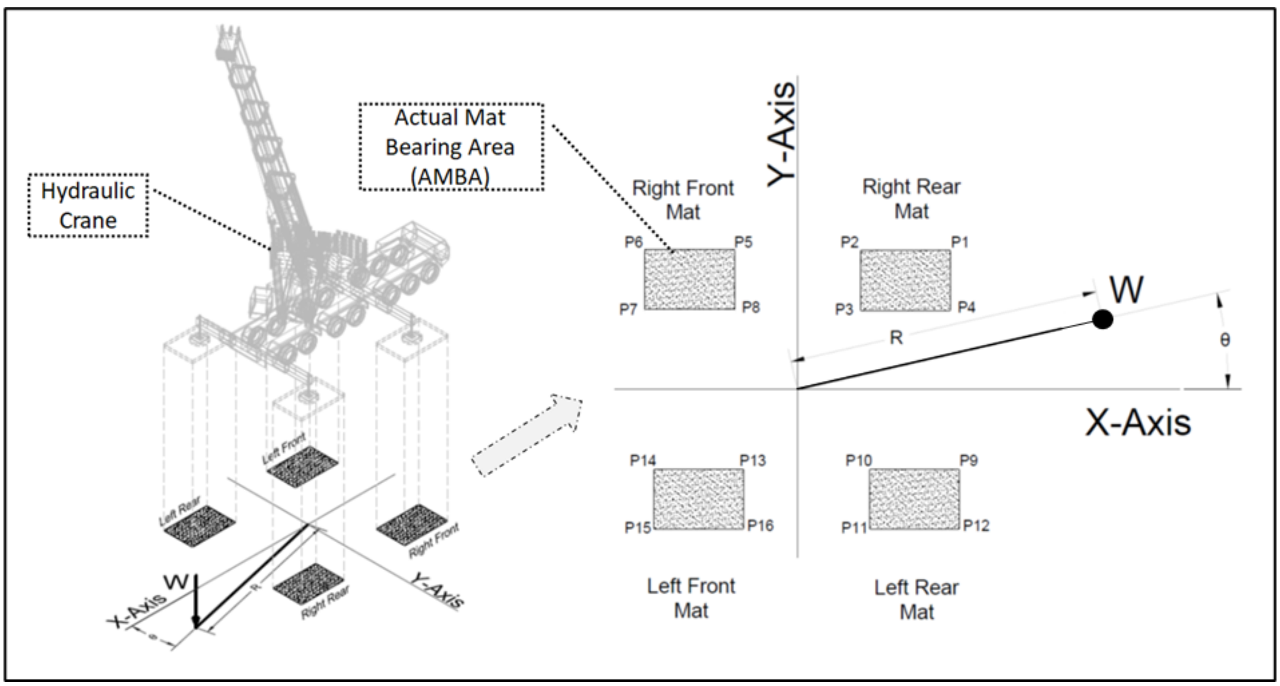

Figure 3.14: Resultant weight and the actual total crane mat bearing area (ATMBA) for a hydraulic crane

$$\sigma_i = W\left[\frac{1}{A_o} + \frac{R(cos\theta)y_i}{I_{xx}} + \frac{R(sin\theta)x_i}{I_{yy}}\right] \tag{35}$$

where A_o is the actual total crane mat bearing area (ATMBA), where I_{xx} and I_{yy} are the second moments of crane mat surface area along *x*-axis and *y*-axis on the Cartesian coordinates and can be calculated by Equations (22) and (23) (Hally 1986).

The first part of Equation (35) consists of the normal stress due to the weight of the crane acting on the ATMBA A_o. The second and third parts of Equation (35) are the overturning moments operating along the *x*-axis and *y*-axis, respectively, as shown in Figure 3.16. Note that the compression stress is assumed to be positive for GBP calculations, and tensile stress is negative. It is important to mention that Equation (35) can calculate the GBP value anywhere under the crane mat area, but the GBP values at four edges/corners will generate a GBP profile covering the total area of the crane mat. It is recommended for the maximum GBP to use four edges/corners to obtain the GBP values.

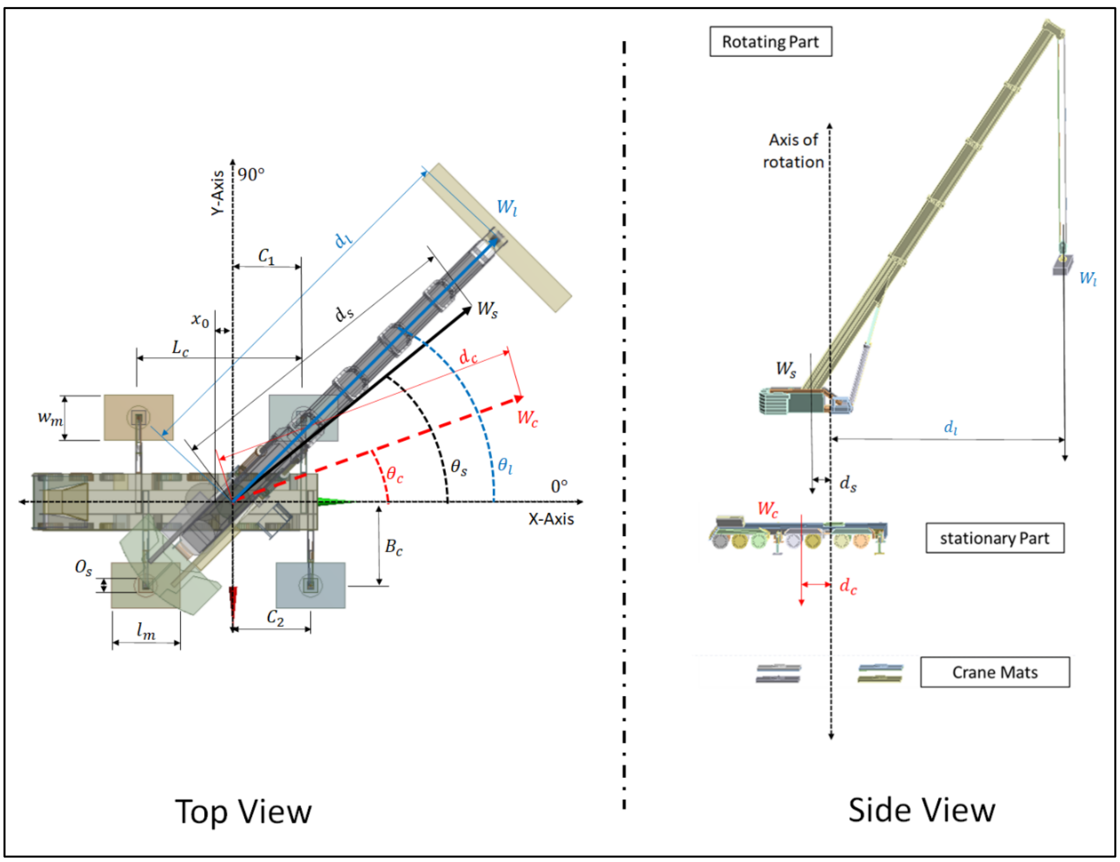

Figure 3.15: Hydraulic Crane Grove GMK7550 FEA model on the Cartesian coordinate system

For $x_0 = 0$ (distance between the centroid of outriggers and the crane rotational axis) and $C_1 = C_2$, the calculations are easy, as the centroid of A_o is the same as of rotational axis of the crane superstructure. In case, $x_0 \neq 0$ and $C_1 \neq C_2$, the values of I_{xx} and I_{yy} needs to be calculated as per the centroid of A_o. For that, the points $P_i(x_i, y_i)$ are moved from the crane superstructure rotational axis x-axis and y-axis to the new axis x'-axis and y'-axis with the origin at the centroid of A_o. Due to the movement of the axis, the GBP points further realign themselves to $P'_i(x'_i, y'_i)$. For the principal axis, the values of I_{xx} , I_{yy} and I_{xy} are updated to $I_{x'x'}$, $I_{y'y'}$ and $I_{x'y'}$ using Equations (22), (23) and (24). Using these updated values, Equation (27) calculates the inclination angle β for the neutral axis as the principal axis x''-axis and y''-axis are always parallel to the neutral axis. Figure 3.17 defines the whole process in detail.

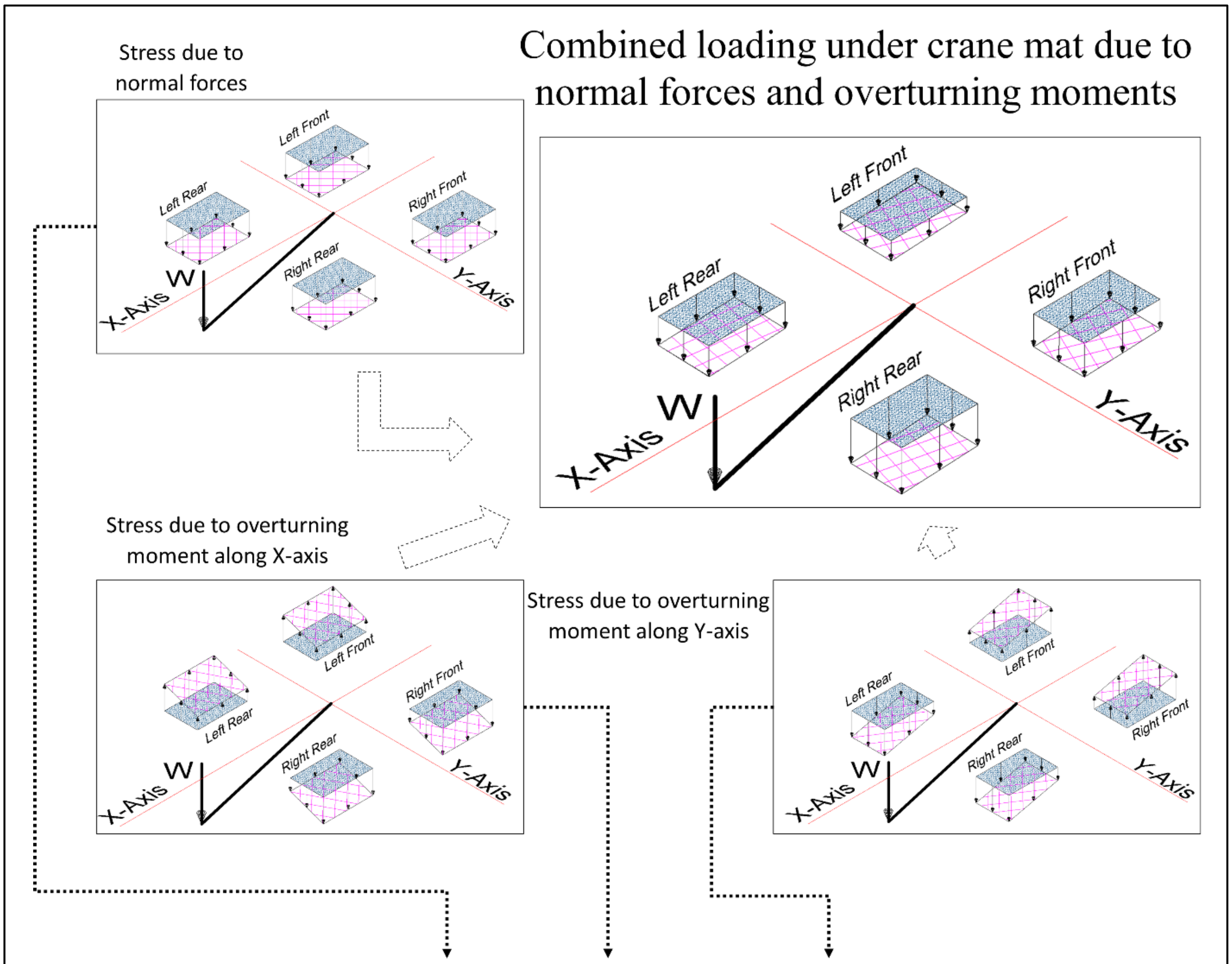

$$\sigma_i = W\left[\frac{1}{A_0} + \frac{R(cos\theta)y_i}{I_{xx}} + \frac{R(sin\theta)x_i}{I_{yy}}\right]$$

Figure 3.16: Combined loading on crane mats under the hydraulic crane

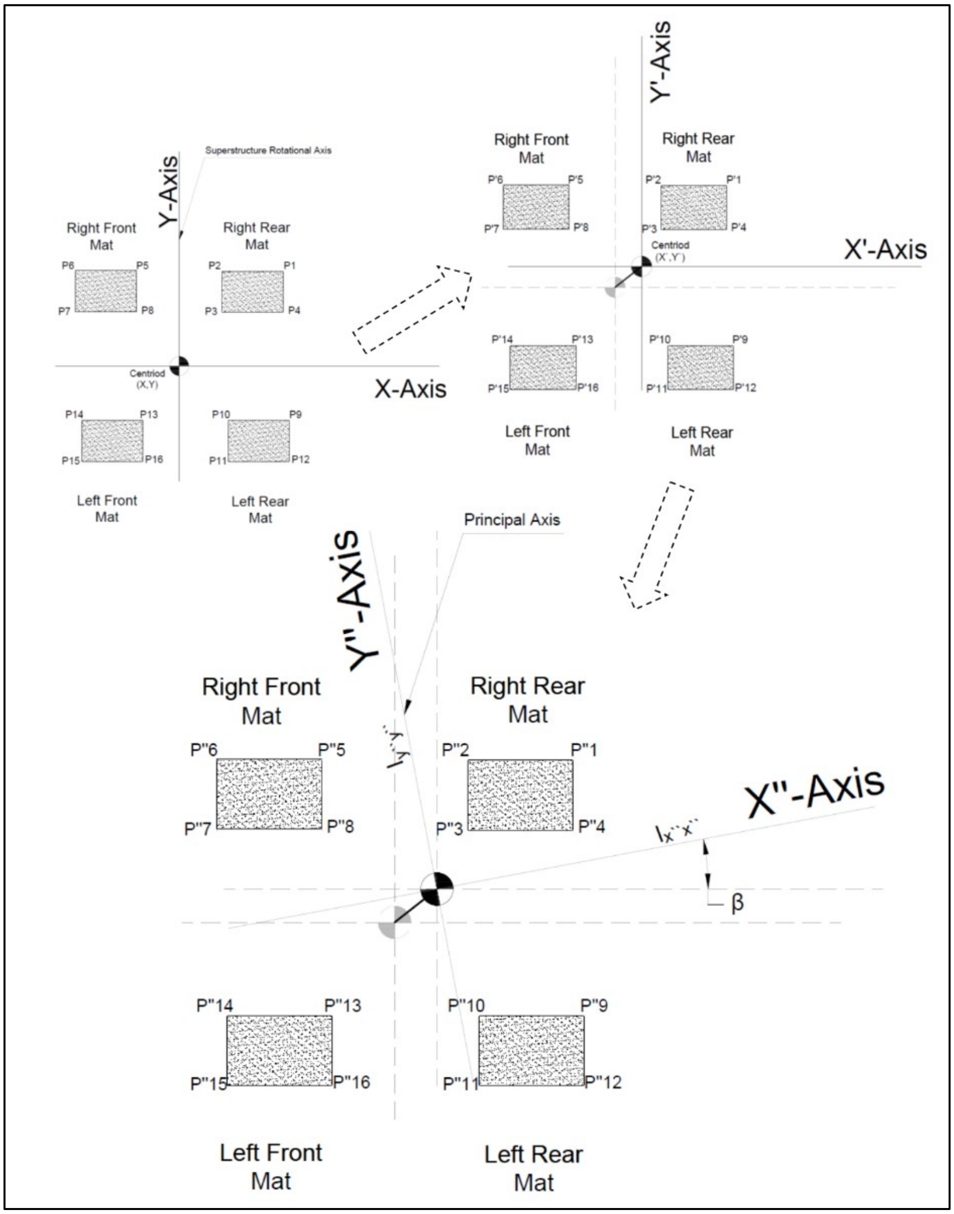

Figure 3.17: Centroid shift from crane superstructure rotational axis to ATMBA centroid

The stress at the neutral axis is 0 (see Figure 3.18). Most of the time, the neutral axis lies outside ATMBA when the normal stresses and stresses due to moments add together, as per Equation (35). Theoretically, when the neutral axis enters ATMBA, the surface area's stresses cut by the neutral axis are opposite across the neutral axis. This cutting results in there being 0 stress at the neutral axis, positive stress (compression) on the sliced crane mat area directly under the payload, and negative stress (tensile) on the remaining sliced area cut by the neutral axis, considering the crane mat the ground as bonded. However, pragmatically, the crane mat is not bonded to the ground, which creates a different scenario for the combined loading calculations. Due to the separation between the crane mat and the ground, the crane mat's sliced area experiences 0 pressure. The crane mat sliced area that experiences 0 stress does not play any part in the GBP calculations, thus reducing ATMBA by slicing ATMBA through the neutral axis. When the neutral axis slices ATMBA, this converts ATMBA to the effective total crane mat bearing area (ETMBA) A_0', which is always less than ATMBA, as shown in Figure 3.18.

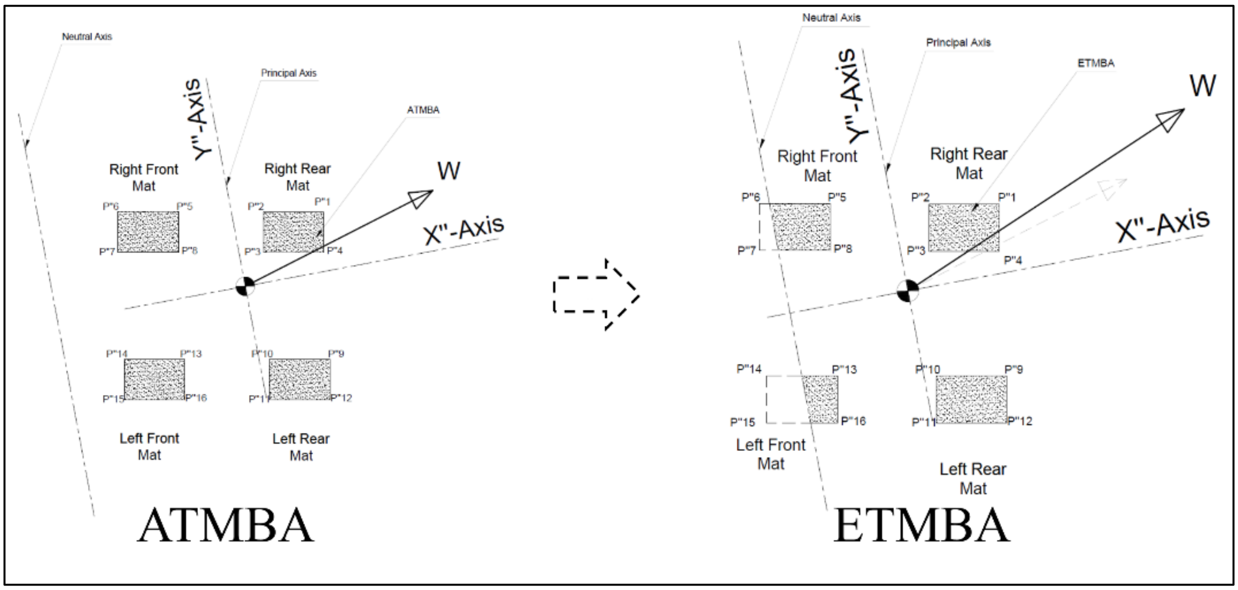

Figure 3.18: Slicing of ATMBA to ETMBA

The slicing of ATMBA is a typical example of a polygon clipping algorithm presented by Greiner-Hormann (Greiner and Hormann 1998, Fan et al. 2018, Foster et al. 2019, Zhao et al. 2020). The Greiner-Hormann polygon clipping algorithm consists of three parts: *intersection, labeling*, and *tracing phase* (Greiner and Hormann 1998, Foster et al. 2019). The clipping algorithm is adapted for ATMBA slicing to obtain ETMBA. The procedure is the same as Greiner-Hormann's (Greiner and Hormann 1998, Foster et al. 2019). First, the *intersection phase* observes the intersection between the neutral axis and ATMBA; later, in the *labelling phase,* the intersection points are established, and at the end, ETMBA is calculated based on the intersection of the neutral axis and ATMBA (*tracing phase*). Each crane mat is treated as a separate polygon to check the neutral axis intersection for the intersection phase. There could be six conditions for each crane mat for the neutral axis intersection. These 6 ATMBA slicing conditions are shown in Figure 3.19 for the crane mat under the right-rear outrigger. The crane mat vertices are $M_1(M_{1x}, M_{1y})$, $M_2(M_{2x}, M_{2y})$, $M_3(M_{3x}, M_{3y})$ and $M_4(M_{4x}, M_{4y})$. The neutral axis is a line segment joined by two neutral points $N_1(N_{1x}, N_{1y})$ and $N_2(N_{2x}, N_{2y})$. The first approach is to evaluate which ATMBA slicing conditions are applicable. This can be investigated using two factors, $factor_a$ and $factor_b$ for each condition. For example, for Condition 1 (see Figure 3.19), these factors can be calculated using Equation (36)and (37) (Greiner and Hormann 1998, Foster et al. 2019).

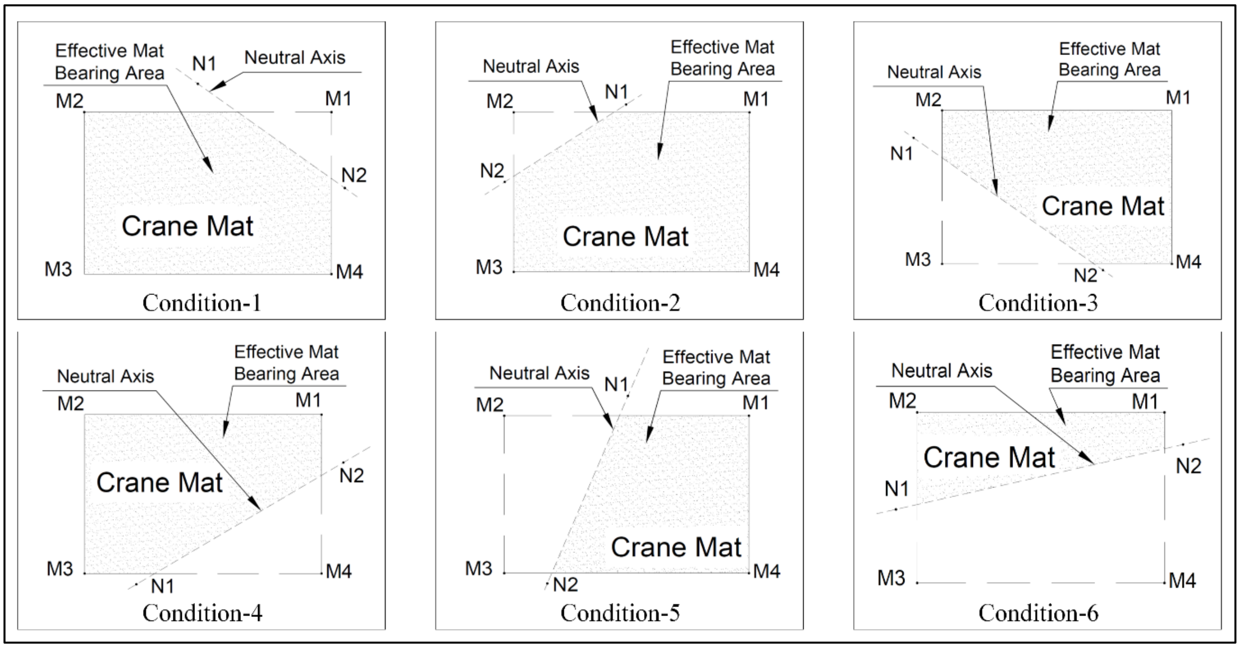

Figure 3.19: Neutral axis slicing conditions for a single crane mat

$$factor_a = \frac{\left\| \begin{bmatrix} N_{1y} & N_{1x} \\ N_{2y} & N_{2x} \end{bmatrix} - \begin{bmatrix} M_{2y} & M_{2x} \\ M_{2y} & M_{2x} \end{bmatrix} \right\|}{\left\| \begin{bmatrix} N_{1x} & N_{1y} \\ N_{2x} & N_{2y} \end{bmatrix} - \begin{bmatrix} M_{1x} & M_{1y} \\ M_{1x} & M_{1y} \end{bmatrix} \right\|} \tag{36}$$

$$factor_b = \frac{\left\| \begin{bmatrix} M_{1y} & M_{1x} \\ M_{2y} & M_{2x} \end{bmatrix} - \begin{bmatrix} N_{2y} & N_{2x} \\ N_{2y} & N_{2x} \end{bmatrix} \right\|}{\left\| \begin{bmatrix} M_{1x} & M_{1y} \\ M_{2x} & M_{2y} \end{bmatrix} - \begin{bmatrix} N_{1x} & N_{1y} \\ N_{1x} & N_{1y} \end{bmatrix} \right\|} \tag{37}$$

For the applicability of Condition 1, it is essential that $factor_a \geq 0$ and $factor_b \geq 0$. If the neutral axis is intersecting the crane mat edge M_1 and M_2, $factor_a$ and $factor_b$ satisfy $factor_a \geq 0$ and $factor_b \geq 0$. If $factor_a < 0$ or/and $factor_b < 0$, this implies that the neutral axis is not intersecting the crane mat edge M_1 and M_2 and the neutral axis is outside the range of crane mat edge M_1 and M_2. Similarly, the algorithm investigates the neutral axis intersection against each crane mat edge to identify one of the six conditions prescribed in Figure 3.19, using Equation (36)and (37) with respective updated Cartesian coordinates of crane mat edges and neutral axis. After obtaining the condition selection and the intersection points, the next step is to identify the area requiring clipping from the crane mat area. The *labelling phase* creates the intersecting points. In the end, during the *tracing phase*, the updated effective crane mat area is calculated, along with updated I_{xx} , I_{yy} and I_{xy}.

Similarly, the whole process for each crane mat and the results accumulates to obtain ETMBA, I_{xx} , I_{yy} and I_{xy}. One crucial factor which needs to be clarified is the calculations for the neutral axis. When the neutral axis slices ATMBA, the stresses on one side are positive (compression), and on the flip side of the neutral axis, it is negative (tensile). The GBP values take into account the area A_0 (ATMBA). The GBP at the neutral axis intersecting ATMBA is always 0. When the area reduces from A_0 (ATMBA) to A_0' (ETMBA), this reduction alters the stresses on the already identified neutral axis. This outcome implies that the placement of the neutral axis needs non-linear optimization in such a way that the area A_0 (ATMBA) reduces to A_0' (ETMBA) in conjunction with 0 stress at the neutral axis. The neutral axis needs to be aligned and overlaps the slicing of the area A_0 (ATMBA) with 0 stress. Another way to obtain this non-linear optimization, endorsed in this section, is through an iterative process. Initially, the area A_0 (ATMBA) is sliced using GBP values obtained using A_0 (ATMBA). The sliced A_0 (ATMBA) converts to A_0' (ETMBA). The GBP values based on A_0' (ETMBA) is calculated, which differs from the previously calculated GBP values. The GBP values based on A_0' (ETMBA) replaces the previously calculated values for the next iteration. The area A_0 (ATMBA) is sliced on each iteration based on the GBP values on the crane mat corners obtained from the previous iteration. This cycle repeats till the GBP at the neutral axis reaches close to 0 or minimizes to 0. This way, the area A_0 (ATMBA) is reduced to A_0' (ETMBA) on each iteration, bringing the neutral axis to perfectly align and overlap the slicing of A_0 (ATMBA) by neutral axis. Algorithm 1 (Appendix B) outlines the whole methodology. Figure 3.20 shows the flow chart for the algorithm (Appendix B) in simple terms.

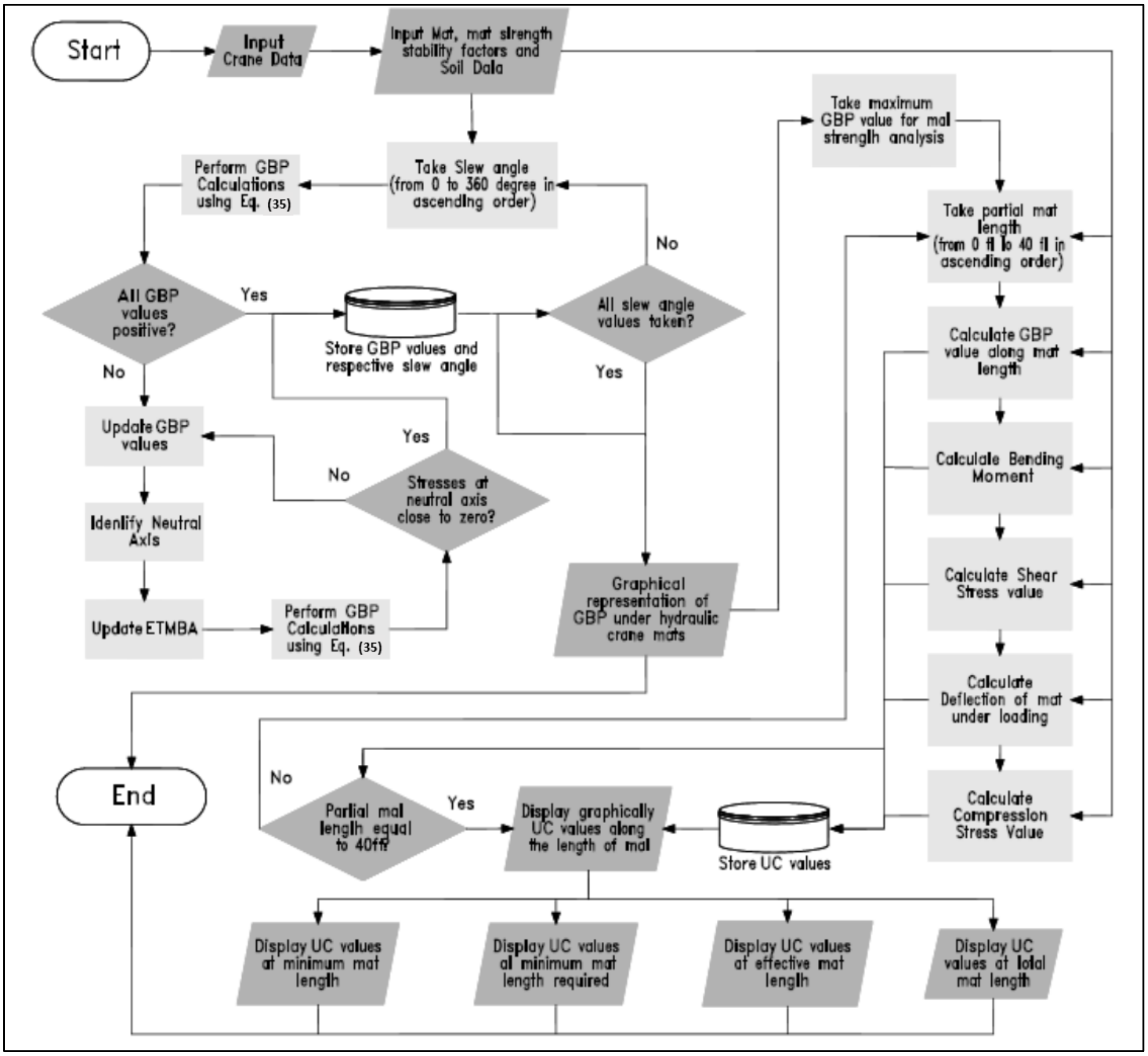

Figure 3.20: Flow chart for GBP under the hydraulic crane and crane mat analysis

3.2.2. Combined loading crane mat analysis '*CoLMA*' application

The developed computer application '*CoLMA*' performs all the calculation work mentioned above for the hydraulic crane. The application displays the results graphically. The application is divided into four main sections, two for input and two for output, as shown in Figure 3.21.

The user fills the first section with crane-related data. This data input also includes the input section for payload and the respective lifting radius. The superstructure and crane carrier section is placed separately and need data input separately. Outrigger configuration also needs to be filled along with the value of O_s (see Figure 3.21) for the crane mat analysis. For the current research, the outrigger area in contact with the crane mat is considered rectangular, with all four sides equal in dimension. Many hydraulic cranes have circular outrigger support in contact with the crane mat. As the variation is minor, the circular outrigger's diameter can be assumed as one side of the square area outrigger. The first output section generates the GBP profile under all four outriggers using Equation (35) and crane superstructure slew angle from 0° to 360°. Moreover, the output section also provides the maximum GBP value along the crane superstructure slew angle from 0° to 360°. The second output section provides crane mat strength analysis, discussed in Chapter 4.

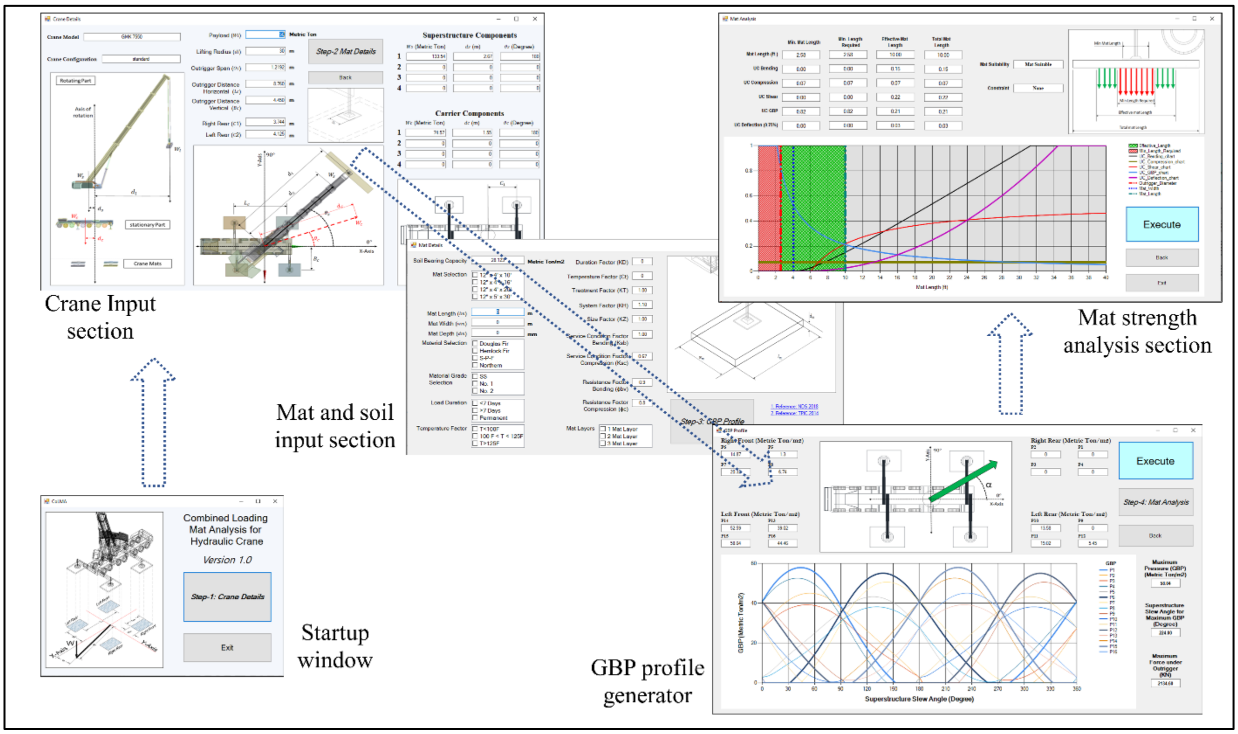

Figure 3.21: '*CoLMA*' application overview

3.2.3. Theoretical case examples and results

For the theoretical case study, a hydraulic crane Grove GMK7550 with a 550 metric ton maximum capacity is configured (Manitowoc 2020). Table 3.4 shows the details of the crane configuration used for the theoretical case study example. Figure 3.22 shows an FEA model of the hydraulic crane. For numerical work, three different payloads, 35,000 kg, 45,000 kg, and 55,000 kg, are used. The GBP output section of the application '*CoLMA*' displays the GBP profile for each crane mat under the outriggers. Figure 3.23 summarizes the profiles associated with each of the above-enumerated weights. For the first two weights (i.e., 35,000 kg and 45,000 kg), the application calculates GBP using ATMBA, but for the last case example, it shows that at some crane superstructure slew angle, the ATMBA changes to ETMBA. Since the non-bonding of the crane mat and the ground, the GBP values on the crane mat reach 0 at locations opposite the payload, showing no resistance from the ground. The application also displays the maximum GBP and the respective crane superstructure slew angle for the crane mat strength analysis.

Table 3.4: Hydraulic Crane Configuration (GMK7550) for GBP profile

Description	Detail
Boom length	38.13 m
Boom configuration	[0-100-100-0]
Superstructure counterweights	119,975 kg
Lifting radius	19.81 m
Lifting Load 1	35,000 kg
Lifting Load 2	45,000 kg
Lifting Load 3	55,000 kg
Outrigger span	8.90 m × 8.70 m
Surface operating condition	Solid
Crane mat Size	3,048.0 mm × 1,219.2 mm × 304.8 mm

Figure 3.22: Hydraulic Crane GMK7550 FEA model

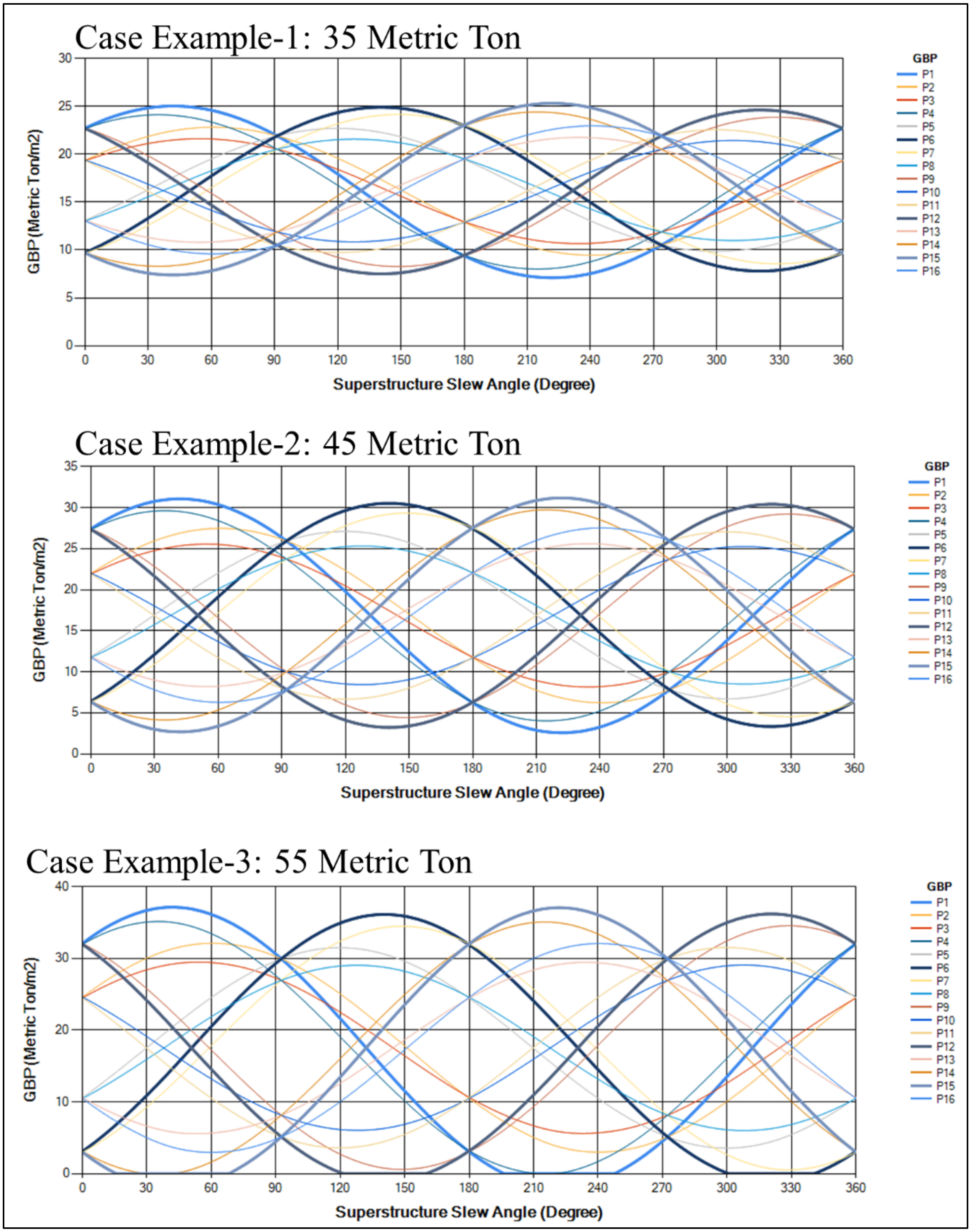

Figure 3.23: GBP profile under hydraulic crane GMK7550 for three case examples

Comparing the GBP values generated using traditional calculations based on Equation (7) with those obtained using Equation (35) is essential. Equation (7) provides a single value for each crane mat and assumes that the GBP under a crane mat is uniformly distributed based on the resultant force on the outrigger. For the comparison, the same crane model, with the same configuration and the payload of 35,000 kg and 45,000 kg, is used for the manual traditional GBP calculations. The results created a genuine concern since the widely used traditional approach in the crane mat industry showed some GBP calculation limitations and assumptions (see Section 2.1.). For example, considering the right-rear outrigger, for the payload of 35,000 kg (see Figure 3.24), the GBP values calculated using Equation (35) are different from the traditional GBP calculations using Equation (7). The solid line in Figure 3.24 shows the traditional GBP values with a payload of 35,000 kg. To further verify the correctness of the newly developed method for GBP calculations, the FEA model of the hydraulic crane (see Figure 3.22), with the same configuration and payload (35,000 kg and 45,000 kg), was simulated. The FEA GBP profile under the crane mat for the payload of 35,000 kg is colour-coded in Figure 1.2 to emphasize its non-uniformity. FEA provides negative values for compressive stress. The GBP under the crane mat changes with the change in crane slew angle. Under the outrigger crane mat, the GBP value is maximum (compression) when the payload is directly over that outrigger.

Figure 3.24 shows that establishing ground support requirements solely on the traditional GBP calculations can lead to ground failure. Nevertheless, the practitioners apply safety factors (3~5 times) to accommodate crane design and mat selection inaccuracies. Practitioners determine which outrigger crane mat has the maximum GBP for the crane mat selection criteria and consider it a critical location for potential ground collapse. Figure 3.24 shows that locations on the crane mat where the GBP values are determined using Equation (35) and FEA are more significant than the traditional GBP value. The traditional method calculates the average over the crane mat, but the GBP values calculated using Equation (35) and FEA provide the upper and the lower values. Crane mat selection based on the traditional GBP calculations is feasible if the GBP is uniform throughout the crane mat's surface area. However, when the GBP over the crane mat's surface is markedly different from uniform, this can lead to (some) values being more significant than the GBP values as calculated using the traditional method.

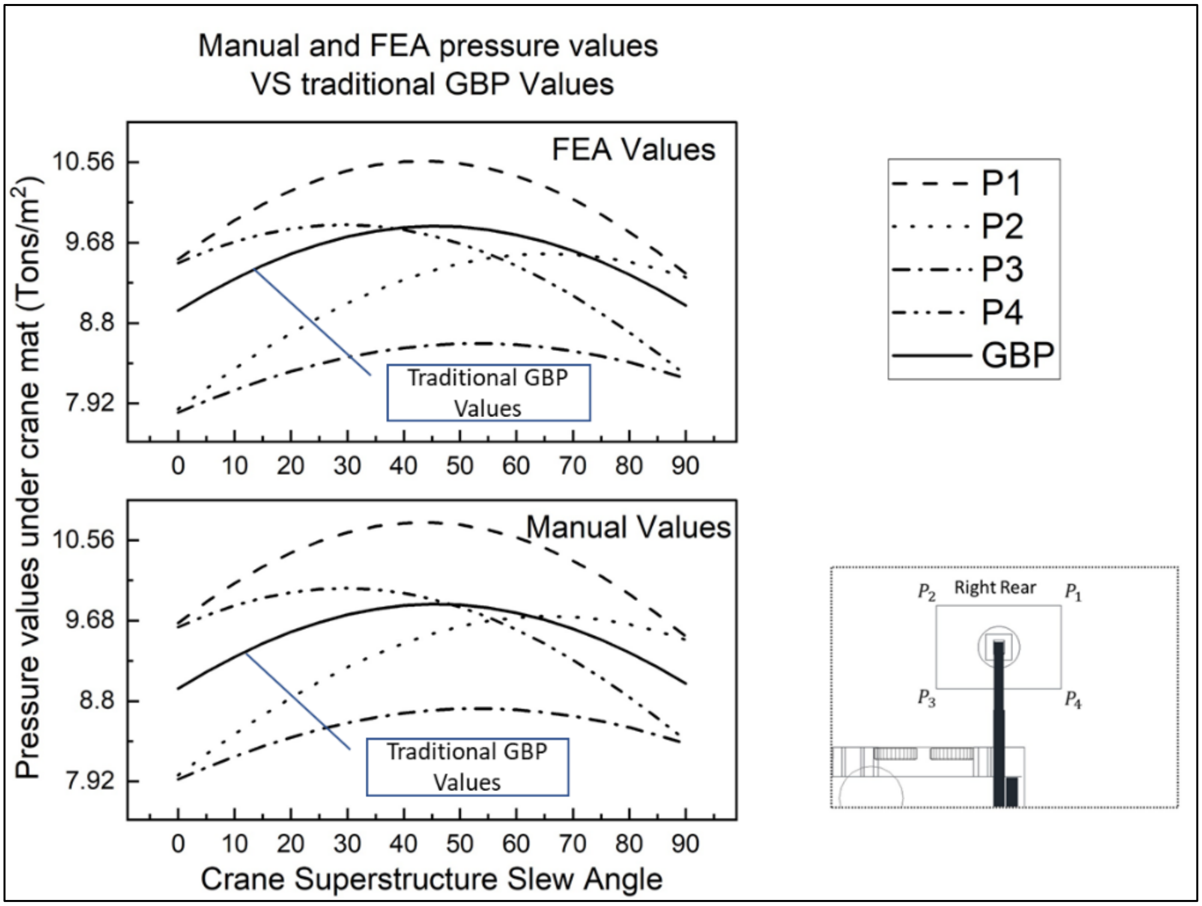

Figure 3.24: GBP variation under crane mat (right-rear outrigger) along with the crane superstructure slew (payload of 35,000 kg)

For P1 of the right-rear outrigger (35,000 kg payload), the GBP values from FEA and manual calculations are more significant than the traditional GBP, and it is maximum when the boom is directly over the outrigger (as shown in Figure 3.24). It clearly shows that the traditional calculation method is limited and underestimates the GBP under hydraulic crane mats. This limitation implies that the chances of ground failure under a crane outrigger increase, increasing the probability of crane tipping. The values of P3 for the right-rear show that the actual pressure (FEA and manual) is less than GBP values as calculated using the traditional method, creating a trapezoidal pressure diagram under each outrigger crane mat. The average percentage difference between FEA and the proposed method, i.e., the manual calculations using Equation (35), is between 0.5% to 1%, which is negligible compared to the GBP values calculated using the traditional method.

The FEA results verify the new GBP methodology's accuracy, but the GBP variation's sensitivity between the traditional method and the new GBP methodology raises a serious concern, as shown in Appendix C (for the payload of 35,000 kg). To observe the trendline of GBP variation along the increasing crane weight load (increasing payload) is plotted for three payloads of 35,000 kg, 40,000 kg, and 45,000 kg at the same lifting radius of 19.81 m in Figure 3.25. It is worth noting that the variation increases as the payload increases. The increase in payload increases the value of W, and the value of R also increases. This implies that as the weight of the crane increases, the difference also increases between the 16-point GBP (beneath crane mat) and the GBP as calculated using the traditional method. The input section for the crane mat details needs selection from a set of crane mats. Table 3.5, for the purpose of this research, lists four crane mat sizes for the crane mat analysis with their dimensions.

Table 3.5: Crane mats used in '*CoLMA*'

Description	Detail
Boom length	38.13 m
Boom configuration	[0-100-100-0]
Superstructure counterweights	119,975 kg
Lifting radius	19.81 m
Lifting Load 1	35,000 kg
Lifting Load 2	45,000 kg
Lifting Load 3	55,000 kg
Outrigger span	8.90 m × 8.70 m
Surface operating condition	Solid
Crane mat Size	3,048.0 mm × 1,219.2 mm × 304.8 mm

3.3. Chapter summary

This chapter summarizes the novel approach to GBP calculations under crawler and hydraulic cranes. This chapter aims to overcome the assumptions in the traditional GBP approaches by introducing a novel approach. The verification is done using the FEA model. Two case examples are used for crawler crane verification, and one case example is used for hydraulic crane verification. This will help remove traditional GBP assumptions to increase the worker's safety by providing the GBP profile under crawler tracks and hydraulic crane mats.

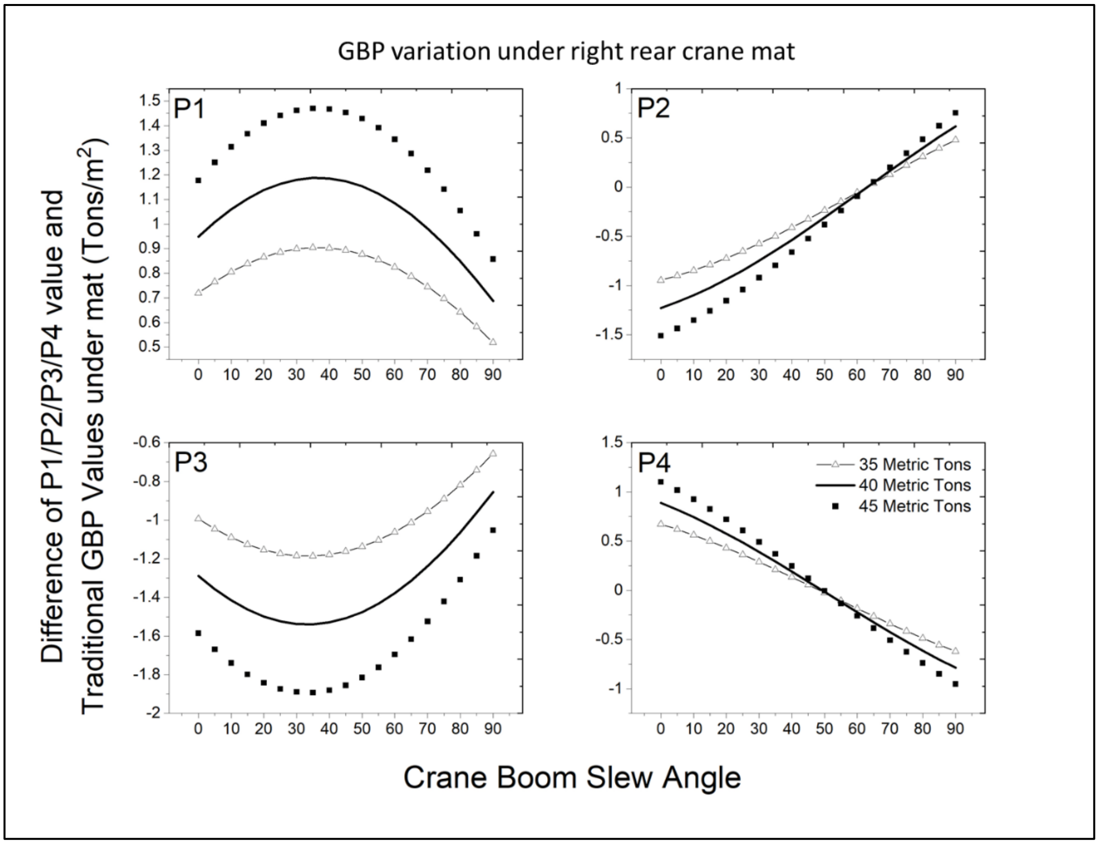

Figure 3.25: GBP variation for right-rear crane mat (16-point GBP and traditional GBP values)

CHAPTER 4: STRUCTURAL REQUIREMENT OF CRANE MATS

This chapter describes the criteria used for crane mat selection. In this regard, Chapter 2 briefly reviewed the literature on crane mat selection criteria. Chapter 3, meanwhile, discussed the GBP calculations that are a key input in crane mat selection. The five design parameters widely used for crane mat selection, as noted earlier in Chapter 2, are GBP, bending, shear, compression, and deflection. In this chapter, a method to capture these five parameters in graphical form to illustrate the design criteria as a decision support tool for crane mat selection is presented. To support crane mat selection, various crane mat sizes are incorporated with industry design factors. Subsequently, the development of a VB application, '*CoLMA*', is discussed. *CoLMA* is based on the algorithm developed for hydraulic crane GBP calculations. The same application also incorporates the crane mat selection criteria and displays the crane mat design parameters as mentioned above.

4.1. Methodology for crane mat suitability and strength analysis

As stated above, for the crane mat strength analysis, five crane mat design parameters are examined to check the appropriateness of a crane mat for crane work based on the crane (with payload) selected and allowable soil bearing capacity. The crane with the payload will provide the maximum GBP value for the crane mat strength analysis. The application in a sequence calculates the crane mat strength parameters. The GBP parameter (using maximum GBP value) initially identifies the minimum crane mat length required. Later, having the maximum GBP within the allowable soil bearing capacity, based on ATMBA or ETMBA, respectively, the bending and shear stress is calculated. In the end, the deflection and compression criteria check the appropriateness of the crane mat for the job. Appendix E and Figure 3.20 show the crane mat strength analysis process.

4.1.1. GBP parameter for a crane mat selection

The first crane mat selection parameter UC_{gbp} is based on the allowable soil bearing capacity and the maximum GBP value, and can be calculated using Equation (38), where σ_{max} is the maximum GBP value. If $UC_{gbp} \leq 1$ (maximum GBP value less than the allowable soil bearing capacity), the crane mat (regardless of number of crane mat layers) is suitable for the job; otherwise, the crane mat gets replaced by another crane mat, which goes through the same checking process.

$$UC_{gbp} = \frac{\sigma_{max}}{Allowable\ Soil\ Bearing\ Capacity} \tag{38}$$

The main concern for further crane mat strength analysis is the required minimum length of crane mat to satisfy the allowable soil bearing capacity. The required minimum length of the crane mat along l_m (the total length of the crane mat) is when UC_{gbp} (calculated along the length of the crane mat) reaches 1. This required minimum length of the crane mat governs the crane mat bending, shear, and deflection limit (see Figure 4.1).

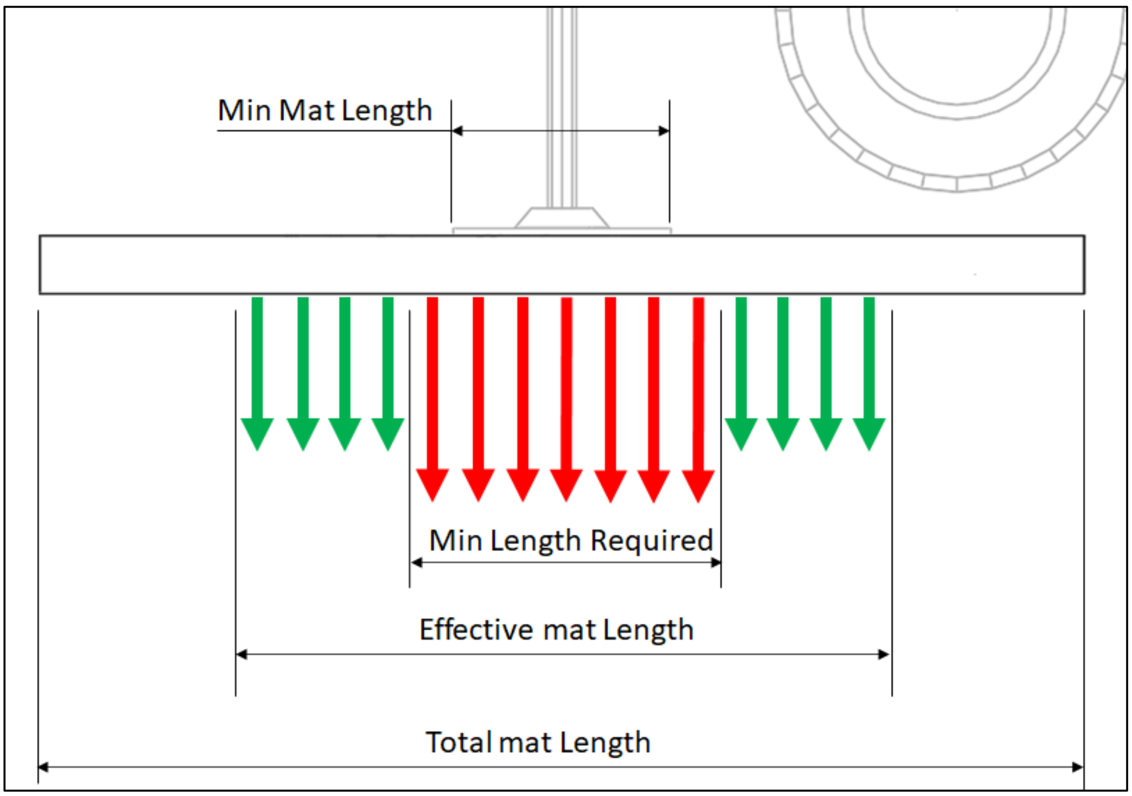

Figure 4.1: Minimum length and total length of a crane mat

4.1.2. Crane mat bending stress limit

When the crane mat satisfies the GBP parameter for the suitability, the crane mat proceeds for further strength analyses, one of which is the crane mat bending stress limit. The application compares the bending stress (due to the bending of the crane mat) with the allowable bending stress limit for the prescribed crane mat material (Duerr 2010, Duerr and Duerr 2019, Mahamid and Torra-Bilal 2019). UC_{bend} can be calculated using Equation (39) (Duerr 2010, Duerr and Duerr 2019, Mahamid and Torra-Bilal 2019).

$$UC_{bend} = \frac{\sigma_{max}\, w_m\, (l_m - O_s)^2}{8\, n\, K_D\, C_t\, K_T\, K_H\, K_{Sb}\, K_Z\, \emptyset_{bv}\, S\, f_b} \tag{39}$$

where n is the number of crane mats layered together (parallel), K_D is load duration factor (American Wood Council 2018, Truss Plate Institute of Canada 2019), C_t is temperature factor (American Wood Council 2018), K_T is treatment factor (American Wood Council 2018, Truss Plate Institute of Canada 2019), K_H is system factor (Truss Plate Institute of Canada 2019), K_Z is size factor (American Wood Council 2018, Truss Plate Institute of Canada 2019), K_{Sb} is service condition factor for bending (Truss Plate Institute of Canada 2019), $\emptyset_{bv}$ is resistance for bending (CSA Group 2019), S is sectional modulus of crane mat, O_s is the width/length of outrigger and f_b is allowable bending stress of the crane mat material (shown in Figure 3.15). For the suitability of the crane mat, it is crucial that, at the required minimum length of the crane mat, $UC_{bend} \leq 1$ provided that $UC_{gbp} < 1$. Along the length of the crane mat, the maximum effective length of the crane mat is when the UC_{bend} reaches 1, after that the crane mat will fail under bending. If the maximum effective length of the crane mat is less than l_m, this shows that the crane mat is oversized (overdesigned) for the job.

4.1.3. Crane mat shear stress limit

Besides the bending moment stress limit, the shear stress limit is also essential to check the crane mat's suitability. The outrigger exerts shear stress at the joining of the outrigger and the crane mat itself. The shear stress produced due to this force needs to be within the prescribed longitudinal shear stress limit. For the crane mat suitability, it is vital that at the required minimum length of the crane mat, $UC_{shear} \leq 1$ provided that $UC_{gbp} < 1$, using Equation (40), where f_v is the maximum allowable stress of the crane mat material. Along the length of the crane mat, the maximum effective length of the crane mat due to shear is when the $UC_{shear} = 1$. This means that, if the shear value is greater than 1, the crane mat will fail due to shear. If the maximum effective length of the crane mat is less than l_m, this indicates that the crane mat is oversized for the job. (Duerr 2010, American Wood Council 2018, Duerr and Duerr 2019, Truss Plate Institute of Canada 2019, Mahamid and Torra-Bilal 2019).

$$UC_{shear} = \frac{3\, \sigma_{max}\, (l_m - O_s - 2d_p)}{4\, n\; K_D\, C_t\, K_T\, K_H\, K_Z\, K_{Sb}\, \emptyset_{bv}\, d_p\, f_v} \tag{40}$$

4.1.4. Crane mat maximum deflection limit

Practitioners in the crane mat industry tolerate 0.75% of the crane mat length as the maximum limit for the crane mat deflection. Using Equation (41), at the required minimum length of the crane mat, $UC_{def} \leq 1$ provided that $UC_{gbp} < 1$ to satisfy the deflection parameter, where $L_{def} = 0.75\%$, E is the modulus of elasticity of the crane mat material and d_p is the thickness of the crane mat (Duerr 2010, Duerr and Duerr 2019, Mahamid and Torra-Bilal 2019).

$$UC_{def} = \frac{\sigma_{max}\, w_m\, (l_m - O_s)^4}{64\, L_{def}\, l_m\, E\, S\, d_p} \tag{41}$$

The same criterion of maximum effective length used in bending and stress limits applies here. Periodically, all three parameters (bending stress limit, shear stress limit, and deflection) may generate three different maximum effective lengths. The minimum value of all three maximum effective lengths works as the final maximum effective length. The crane mat length beyond the maximum effective length experiences no stresses, and it is a wastage of crane mat length.

4.1.5. Crane mat compression stress limit

The fifth crane mat suitability criteria are the compression strength of the crane mat, which is represented by UC_{comp} as shown in Equation (42). For the crane mat to be within the design criteria of compression, it is imperative that $UC_{comp} \leq 1$, where f_{cp} is the compression limit of the crane mat material (perpendicular to the grain).

$$UC_{comp} = \frac{\sigma_{max}}{K_D\, C_t\, K_{Sc}\, K_T\, K_Z\, \emptyset_c\, f_{cp}} \tag{42}$$

Where, K_{Sc} is service condition factor for compression (Truss Plate Institute of Canada 2019) and $\emptyset_c$ is the resistance factor for compression.

4.1.6. Combined loading crane mat analysis 'CoLMA' application

The developed computer application '*CoLMA*' performs all the calculation work mentioned above regarding crane mat selection and suitability. The application displays the results graphically. The application is divided into four main sections, two for input and two for output, as shown in Figure 3.21.

One input section is for the crane mat and soil data input. It requires the dimensions of the crane mat and the allowable soil bearing capacity value. Further, a crane mat material selection section selects the crane mat crane material. The database used in applying the crane mat material and their respective parameters are shown in Table 4.1 (CSA Group 2019). The user must then select design factors, as mentioned above in the literature review (Section 2.3.) (American Wood Council 2018, CSA Group 2019, Truss Plate Institute of Canada 2019).

Table 4.1: Specified strengths and moduli of elasticity for crane mat crane material.

	Description	Grade	Bending (f_b) MPa	Longitudinal Shear (f_v) MPa	Compression perpendicular to grain (f_{cp}) MPa	Modulus of elasticity (E) MPa
1	Douglas Fir-Larch	SS	19.5	1.5	7.0	12,000
		No. 1	15.8			12,000
		No. 2	9.0			9,500
2	Hem-Fir	SS	16.8	1.2	4.6	11,500
		No. 1	14.4			11,000
		No. 2	14.4			11,000
3	Spruce-Pine-Fir	SS	13.6	1.2	5.3	8,500
		No. 1	11.0			8,500
		No. 2	6.3			6,500
4	Northern Species	SS	12.8	1.0	3.5	8,000
		No. 1	10.8			8,000
		No. 2	5.9			6,000

Sources: Data adapted from CSA 086:19, Engineering design in wood, (2019) 344. https://cwc.ca/how-to-build-with-wood/codes-standards/wood-standards/csa-o86-engineering-design-in-wood/.

The first output section generates the GBP profile under all four outriggers using Equation (8) and crane superstructure slew angle from 0° to 360°. Moreover, the output section also provides the maximum GBP value along the crane superstructure slew angle from 0° to 360°. The crane mat strength analysis uses the maximum GBP value generated from this. The last section creates a graphical representation of crane mat strength analysis along the crane mat's length, as shown in Figure 3.21. The red section in the graphical description of crane mat strength analysis along the crane mat length provides the minimum crane mat length required to satisfy the suitability. The green section along the length of the crane mat describes the maximum effective length of the crane mat. The output section of crane mat strength analysis also provides UC_{gbp}, UC_{bend}, UC_{shear}, UC_{def} and UC_{comp} at the minimum length of the crane mat (O_s), minimum required length of the crane mat, the maximum effective length of the crane mat, and the total length of the crane mat (see Figure 4.1).

4.2. Theoretical case examples and discussion

The input section for the crane mat details needs selection from a set of crane mats. Table 4.2, for the purpose of this research, lists four crane mat sizes for the crane mat analysis with their dimensions. An option is included in the crane mat input sheet to stack the crane mats for extra load distribution. Another critical factor is the allowable soil bearing capacity of the ground underneath the crane mat. The input of allowable soil bearing capacity will determine UC_{gbp} for the required minimum crane mat length. The end-user can change all the design factors (mentioned in the literature review) in the developed application as per the site conditions.

Table 4.2: Crane mats used in '*CoLMA*'[1]

Description	Dimensions in SI units	Dimensions in Imperial units
Crane mat Type 1	3.048 m × 1.219 m × 304 mm	10 ft × 4 ft × 12 inches
Crane mat Type 2	4.877 m × 1.219 m × 304 mm	16 ft × 4 ft × 12 inches
Crane mat Type 3	6.096 m × 1.219 m × 304 mm	20 ft × 4 ft × 12 inches
Crane mat Type 4	9.144 m × 1.524 m × 304 mm	30 ft × 5 ft × 12 inches

The crane mat analysis's output section provides values for each crane mat design parameter at different lengths. It also calculates whether the crane mat is suitable for the job or not. If the crane mat is unsuitable, the output section also displays its reason. Another parameter that is very important for optimizing crane mats on site is the required minimum length of the crane mat and the maximum effective length of the crane mat. Taking into consideration the payload of 55,000 kg at the lifting radius of 19.81 m, the maximum GBP as per the GBP output section in the application is about 19.39 metric tons/m^2 with crane mat Type 3, this leads to 23.92 metric tons/m^2 with crane mat Type 2, and 37.16 metric tons/m^2 with crane mat Type 1 (regardless of the crane mat material and design factors). The crane mat strength analysis and suitability require the design factors, allowable soil bearing capacity, and the crane mat crane material. Figure 4.2 displays the graphical representation of all the crane mat selection parameters across the crane mat length for crane mat Type 3. As per the graphical representation of crane mat Type 3, the required minimum

[1] Data from NCSG (Northern Crane Services Group, Edmonton, Alberta, Canada).

length of the crane mat is about 3.474 m (11.40 ft), with the allowable soil bearing capacity of 35 metric tons/m^2 and material of Northern Species with grade No. 2. The graphical representation shows that the required minimum length of the crane mat is when the UC_{gbp} moves below 1. That is the point when the UC_{gbp} equals allowable soil bearing capacity.

The green shaded part in Figure 4.2 depicts the maximum effective length of the crane mat, which is 5.462 m (17.92 ft), as the UC_{bend} reaches its limit and reaches one before all other parameters. This value shows that the crane mat is oversized for the job, and about 0.634 m (2 ft) of crane mat length experiences no pressure. It implies that, for this particular job, using a smaller size crane mat is a cost-effective approach.

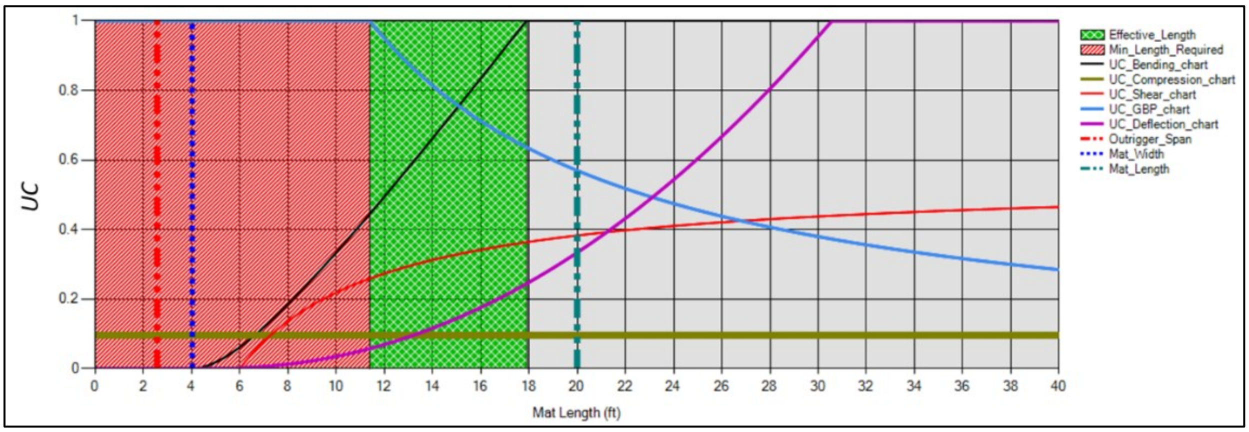

Figure 4.2: Crane mat strength analysis for the crane mat Type 3, with crane mat material Northern Species, Grade No. 2

Changing the crane mat size to the smaller one (crane mat Type 2) while keeping all other parameters the same generates a crane mat analysis diagram, as shown in Figure 4.3. The length of the crane mat is less than the UC_{bend} limit so the crane mat length works as the maximum effective length of the crane mat. This outcome implies that the crane mat is suitable for the job and is neither oversized nor undersized.

If a smaller crane mat (crane mat Type 1) is chosen for the job, with the same parameters as before, the crane mat analysis diagram (see Figure 4.4) shows that the crane mat is unsuitable for the job, and GBP is the crane mat constraint for the suitability. The crane mat analysis diagram shows that the length is less than the required minimum crane mat length, about 3.474 m (11.40 ft). It also shows that the allowable soil bearing capacity is less than the maximum GBP.

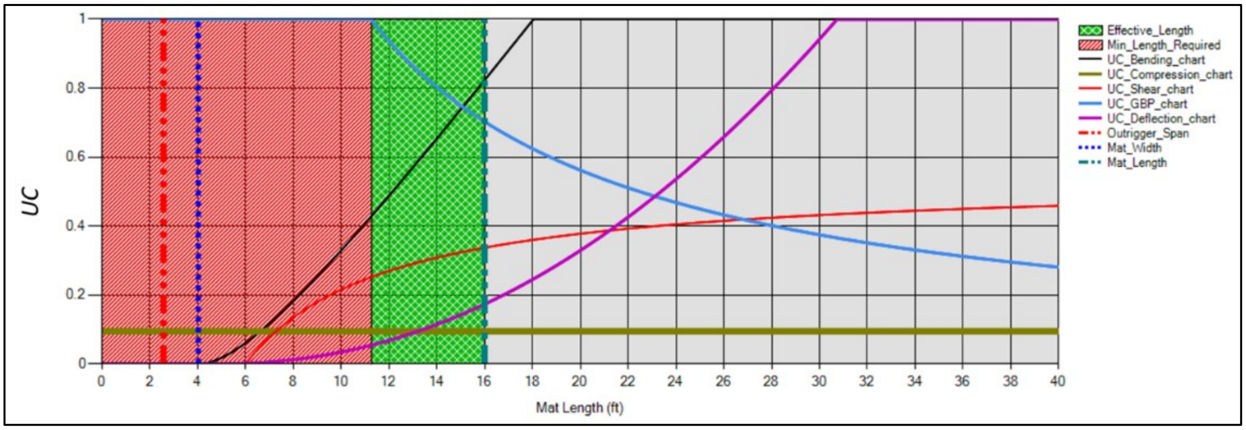

Figure 4.3: Crane mat strength analysis for the crane mat Type 2, with crane mat material Northern Species, Grade No. 2

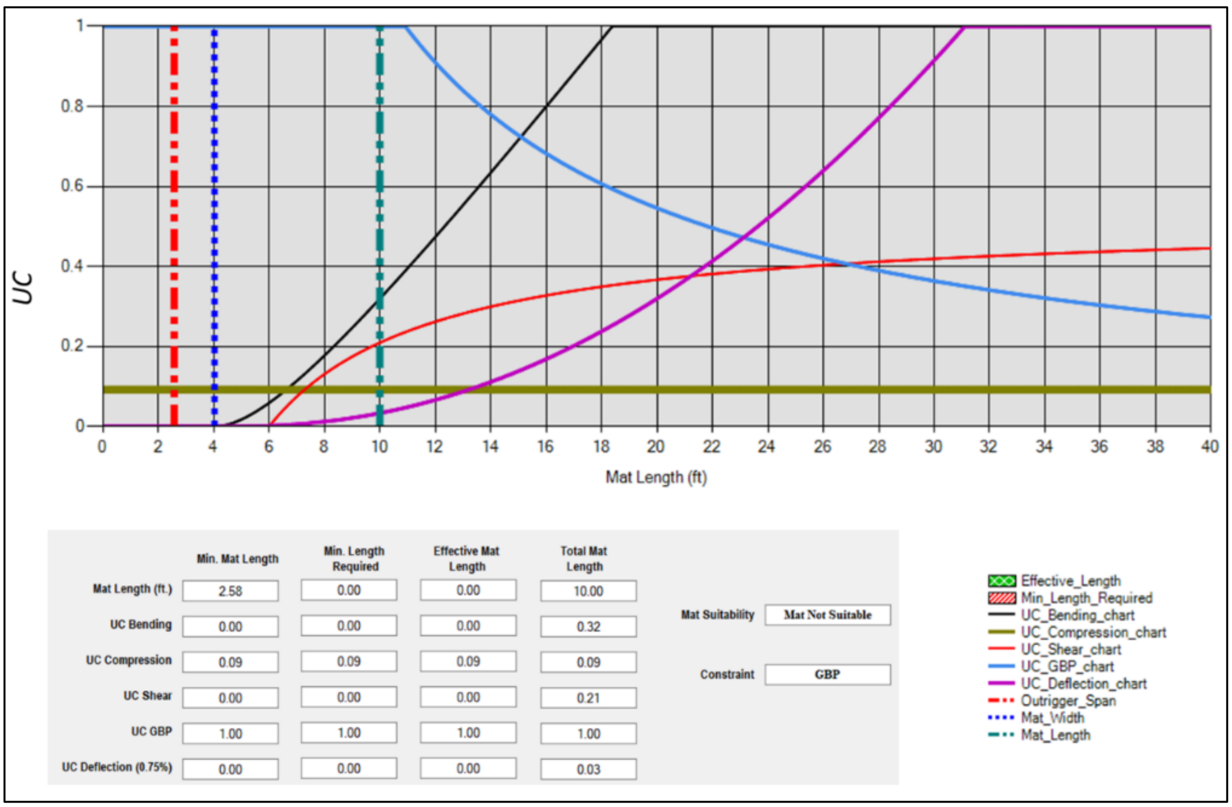

	Min. Mat Length	Min. Length Required	Effective Mat Length	Total Mat Length
Mat Length (ft.)	2.58	0.00	0.00	10.00
UC Bending	0.00	0.00	0.00	0.32
UC Compression	0.09	0.09	0.09	0.09
UC Shear	0.00	0.00	0.00	0.21
UC GBP	1.00	1.00	1.00	1.00
UC Deflection (0.75%)	0.00	0.00	0.00	0.03

Figure 4.4: Crane mat strength analysis for the crane mat Type 1, with crane mat material Northern Species, Grade No. 2

If the number of crane mats is increased and layered together under the outrigger, this decreases the value of UC_{bend} and UC_{shear} and so the maximum effective length of the crane mat increases. If the number of crane mats increases to 2 (layered) with the crane mat Type 4, the payload of

55,000 metric tons/m^2 at the lifting radius of 19.81 m, with all the remaining parameters same as used before, the value UC_{shear} decreases from 0.39 to 0.24, with the maximum effective length from 5.060 m to 8.083 m. If the crane mat numbers (the number of crane mat layers) increases to 3, the value of UC_{bend} changes from 1.00 to 0.59 and UC_{shear} changes to 0.12 from 0.24, increasing the maximum effective length reaching total crane mat length. This change implies that when the crane mats are stacked together under the crane outrigger, the load distribution under the crane mat increases, making it more stable to handle any dynamic loading. The crane mat analysis section of the application '$CoLMA$' identifies all the required design parameters to select a crane mat and its suitability. Changing the design factors and parameters also influences the results associated with the crane mat suitability.

4.3. Chapter summary

This chapter summarizes the structural requirement for a crane mat on a construction site. This chapter comprises five major design parameters for crane mat suitability. The limitation is the assumption of the ground as a rigid body, exerting allowable soil bearing capacity. The crane mat selection is based on the GBP and the allowable soil bearing capacity. After selecting the crane mat, the next step is to optimize the layout of the crane mats on the construction site. The traditional GBP values were used previously for the structural analysis of crane mat suitability. This chapter provides a structural analysis of the crane mat using combined loading GBP calculations.

CHAPTER 5: OPTIMIZED LAYOUT PLANNING OF CRANE MATS

The focus of this chapter is on optimizing the crane mat layout on the construction site. As stated in Chapters 2 and 3, heavier cranes require proper ground stability for safe crane operation. The first task in this regard is to ensure that the soil bearing capacity of the ground is sufficient to withstand the pressure generated by the compounded weight of the crane and its payload. In the construction industry, there are two ways to overcome poor soil bearing capacity, (i) using compacted aggregate to increase the soil bearing capacity; and/or (ii) using layer(s) of crane mats to redistribute the crane ground bearing pressure to satisfy the allowable soil bearing capacity. As noted earlier, the increasing use of cranes in construction has also increased the use of crane mats. This, in turn, has led to the use of crane mat layout plans/drawings as a default practice for every crane operation on the construction site.

In this context, this chapter covers the as-yet unexplored topic of crane mat optimization. In current practice, practitioners prepare layout plans/diagrams using AutoCAD. Typically, a practitioner takes about 20~30 minutes (field observations) to prepare a crane mat layout plan/drawing for a coverage area of 15~20 crane mats. Practitioners design these crane mat layout plans in such a way as to satisfy various construction site constraints, where the primary aim is to minimize the crane mat usage.

5.1. Crane mat layout optimization using greedy and RL approach

The algorithms developed in this research and presented in this chapter (i.e., greedy and SARSA) can be used to prepare the crane mat plan/drawing automatically in accordance with the site constraints and can thereby save practitioners a considerable amount of time. There are many techniques that can be used to obtain an optimal solution. The ones most widely used by researchers and practitioners are dynamic programming, brute-force, and greedy algorithm. Crane mat optimization is a combinatorial optimization problem, where all the mat placements needed to cover the area are interdependent, meaning that any given crane mat placement can affect the other placements needed to cover the area (Korte et al. 2011). One of the major considerations in the development of any combinatorial optimization algorithm is the running time for the algorithm (Korte et al. 2011). Accordingly, with respect to the problem at hand, the main concern other than saving crane mat resources is to reduce the time taken by practitioners to develop the crane mat drawings (see Chapter 1). These crane mat estimations are typically required at the project bidding stage, where quick calculations and cost estimates are needed to ensure timely submission of a competitive bid. Although dynamic and brute-force programming can be considered as options for crane mat optimization, the notable drawback with these optimization techniques is the computation time required to arrive at the optimal solution (Bird and de Moor 1993, Bang-Jensen et al. 2004, Korte et al. 2011, Simmons et al. 2019), which, as mentioned, is a significant consideration for construction enterprises estimating a project at the bidding stage. It is important to mention that the greedy algorithm is one of the simplest algorithms to use for combinatorial optimization problems (Bang-Jensen et al. 2004). One of the major benefits of the greedy algorithm, specifically with respect to the need for an expeditious method for the bidding stage, is its short processing time to develop the optimized solution. For this reason, the first approach considered in this research is a greedy approach. The results described in Section 5.1.2.1 demonstrate that the greedy approach saves a significant amount of practitioner time (20~30 min) compared to manual crane mat layout preparation.

RL is another promising solution to combinatorial optimization problems (Mazyavkina et al. 2021). Although, as noted above, combinatorial optimization problems can be solved using brute-force or dynamic programming, the results presented in 5.1.2.1 and the discussion in 7.3.2 demonstrate that the time required to perform dynamic or brute-force programming can be considerably more than that required to implement the greedy approach. For this reason, RL is pursued as a potential solution to the complex problem of crane mat optimization (and to optimization problems in construction more broadly). As noted above, the construction industry is already lagging in productivity compared to other industrial sectors (Graham 2019), with this lag often being attributed to resource allocation, management, and decision-making processes (Mitropoulos and Tatum 1999). In this regard, RL has been successfully applied in other industries (Mehr 2019, Waxenegger-Wilfing et al. 2020, Kiran et al. 2021, Yu et al. 2021), and it successful application for crane mat optimization may be an important step towards a robust RL-aided decision support paradigm for the construction industry. As noted above in Section 2.4.2, RL is relatively new to the construction industry and its application to construction problems need to be further explored. The successful application of RL for crane mat optimization can open the door to further autonomous construction methodologies.

It is important to mention that the scope here is limited to a comparison between the greedy and RL approaches for crane mat optimization. Another potential area of RL application, though, could be in design optimization (see Appendix G), such as crane mat design optimization. The design problem presented in Appendix G is similar to crane mat design in that there are many forces (weights), such as the crane superstructure, crane boom, payload, counterweights, and crane undercarriage, acting on a crane mat at different locations. With respect to crane mat design, the placement of supporting elements, such as an H-beam, I-Beam, or plates, requires optimization, given the variations in load and crane radius. The methodology described in Appendix G could be applied with slight modifications to optimize the design of a crane mat to be used under crawler crane tracks or outrigger mats with varying loads and crane radii. The main purpose of crane mats, it should be noted in this regard, is to distribute the load acting on them with a minimum amount of crane mat deflection. Therefore, the objective of crane mat design and the design problem in Appendix G is to determine the locations to place the supports (H-beams, I-beams, or plates) that will achieve minimum deflection. This design optimization can be extended by adding cost and fabrication constraints. The surface area of the plate is assumed to be 112 m × 112 m, instead of traditional mat dimensions (3.6 m × 2.4 m), to observe and differentiate the variations in greater detail. For crane mat design optimization, the steel plate size will be reduced to match the traditional crane mat dimensions. The results from Appendix G show that RL can be successfully applied to optimize machine design within the given constraints. The exploratory aspect of RL pushes the RL agent to initiate various decisions and update the Q-table in accordance with the reward it stands to receive.

Returning to the original problem of crane mat optimization, as discussed in greater detail below, the results show that the developed algorithms are capable of generating a simple crane mat layout in just seconds/minutes, whereas a manual approach takes roughly 20~30 minutes. The time saved in preparing these plans/drawings can be reallocated to other productive work, resulting in more efficient resource utilization. Not only that, but the developed algorithms can also optimize the use of crane mats on site by eliminating human error. It should be noted that, while the greedy approach provides more rapid results, RL (i.e., SARSA), although it requires more computation time, provides an optimized solution, and does so in considerably less time compared to a manual approach. Both of the developed algorithms follow an agent-based approach, simulating a practitioner's behaviour to prepare a crane mat layout plan/drawing. As an indication of their robustness, the algorithms are capable of providing salient details about the crane mats used, the area covered, and crane mat wastage in terms of extra area covered. Moreover, it is a common occurrence in the traditional manual approach for the practitioner to make a series of revisions to the crane mat layout plan/drawing in order to optimize the minimum crane mats with the maximum area covered. The use of these algorithms eliminates this rework by optimizing the crane mat layout on the first attempt. This algorithm can be helpful at the project bidding stage, as more accurate information pertaining to crane mat utilization/requirements can be obtained in considerably less time.

5.1.1. Methodology underlying crane mat optimization algorithm

5.1.1.1. Development of greedy algorithm

The optimization process is divided into small parts to reach the optimal solution for the greedy agent. The first crane mat is placed based on practical constraints (mentioned later). After choosing the location and orientations of the first crane mat, the next consecutive crane mat location and orientation is determined based on practical constraints (mentioned later) related to the crane mat laying on-site adjacent to the first laid crane mat. This process continues till the whole area is covered with the crane mats by the optimization agent (greedy agent-based agent). Figure 5.1 shows the general procedure to prepare the crane mat layout plan/drawing. As stated before, the process is divided into two main sections for ease of understanding.

5.1.1.1.1. Selecting the first crane mat location and orientation

The greedy optimization agent must calculate the area required for the crane mat placement. The selection of the area required provides a set of Cartesian points enclosing the area for crane usage and crane mat layout. Let $P_n(x_n, y_n)$, where $n \in [3, \mathbb{R}]$, be the polygon's vertices (area selected for the crane mat layout). These Cartesian coordinates allow determining the polygon's area A_o that needs to be covered by the crane mats. The next step is to indicate the edge from where the layout of the crane mat will start (crane mat laying starting point). That can be taken as $R_k(x_k, y_k)$, where $k = 1,2$ and $R_k(x_k, y_k) \subset P_n(x_n, y_n)$. These $R_k(x_k, y_k)$ are the adjacent vertices of the polygon $P_n(x_n, y_n)$. This edge works as the plan/drawing's starting location for the crane mat laying process.

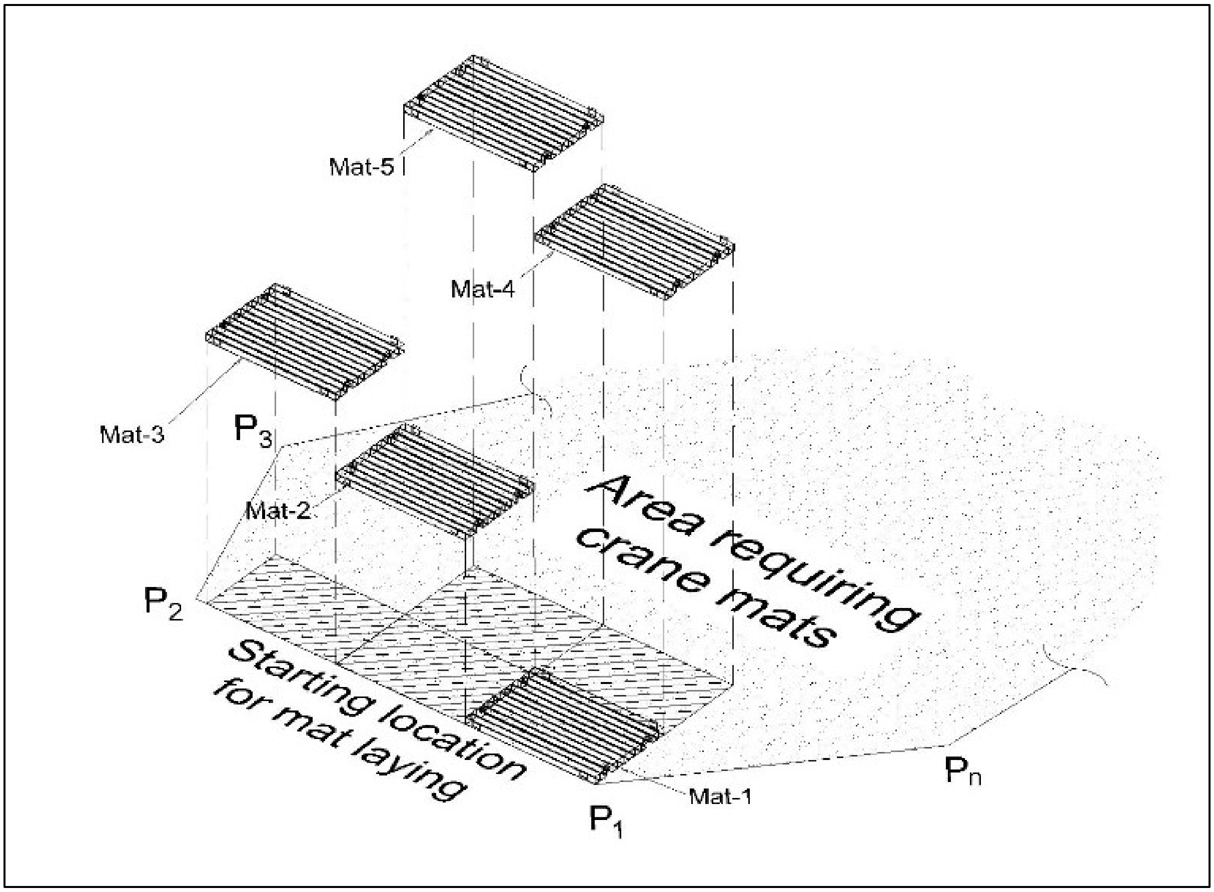

Figure 5.1: Crane mat layout sequence

The optimization agent places the first crane mat on R_1. Eight crane mats orientations are available at one location, as shown in Figure 5.2. The greedy agent must select one crane mat (one size only) orientation with the maximum area covered from these eight crane mat orientations. The first constraint is to check whether the crane mat is inside or outside the area required for the maximum area covered, as shown in Figure 5.3. Let $M_i(x_{ij}, y_{ij})$ be the crane mat coordinates (8 orientations), $x_i, y_i \in \mathbb{R}$, $i \in [1,8], j \in [1,8]$, be the coordinates for the crane mats covering the required area. Let A_i, where $i = 1,2, \cdots, 8$, the area of the first crane mat with eight orientations placed on R_1 along the line joining R_1 and R_2.The crane mat placement constraint (inside area) needs to follow that the intersection of these two sets A_i and A_o cannot be 0 if the crane mat is inside the required area, as shown in Equation (43).

$$Mat\ Placement = \begin{cases} Inside\ A_o \cap A_i \neq \emptyset \\ Outside\ A_o \cap A_i = \emptyset \end{cases} \tag{43}$$

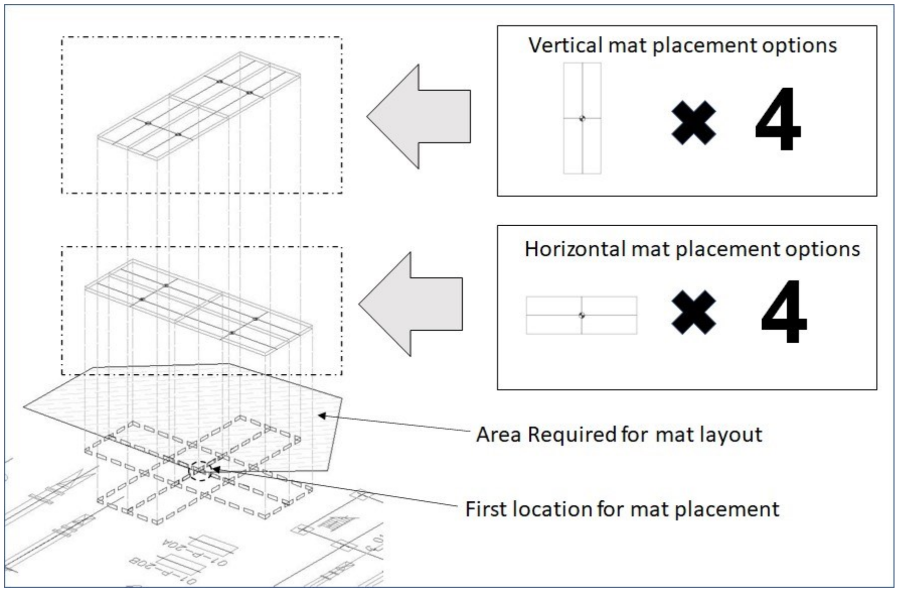

Figure 5.2: Available crane mat orientations on one crane mat location

As shown in Figure 5.3, only two crane mat orientations got selected from eight possible orientations. The RL agent selects these two crane mat orientations for further optimization based on crane mat centroid distance from the starting location edge $R_k(x_k, y_k)$. As shown in Figure 5.4, the centroid distance of the first selected crane mat (horizontal) is C_o, and the centroid distance of the selected crane mat (vertical) is C_m. The approach is to place the crane mat with minimum centroid distance from the line joined by R_k. The greedy optimization agent selects the crane mat orientation with minimum distance, which means if $C_o < C_m$, horizontal crane mat is selected by the greedy agent, and if $C_o > C_m$, vertical crane mat is selected by the greedy agent. After the selection of the first crane mat orientation and location, the area required for the crane mat laying decreases by $A_o \cap A_i$. This also implies that the required area changes to AR_owhich is shown in Equation (44).

$$AR_o = A_o \setminus (A_o \cap A_i) \tag{44}$$

As only one crane mat is placed by the agent in the required area, the coordinates of the crane mat work as the location for the succeeding adjacent crane mats. Let $O_m(x_m, y_m)$ be the list of locations for crane mat placement. As the number of crane mats increases, so does the number of locations on the list $O_m(x_m, y_m)$ also increases till the area required is fully covered by the crane mats.

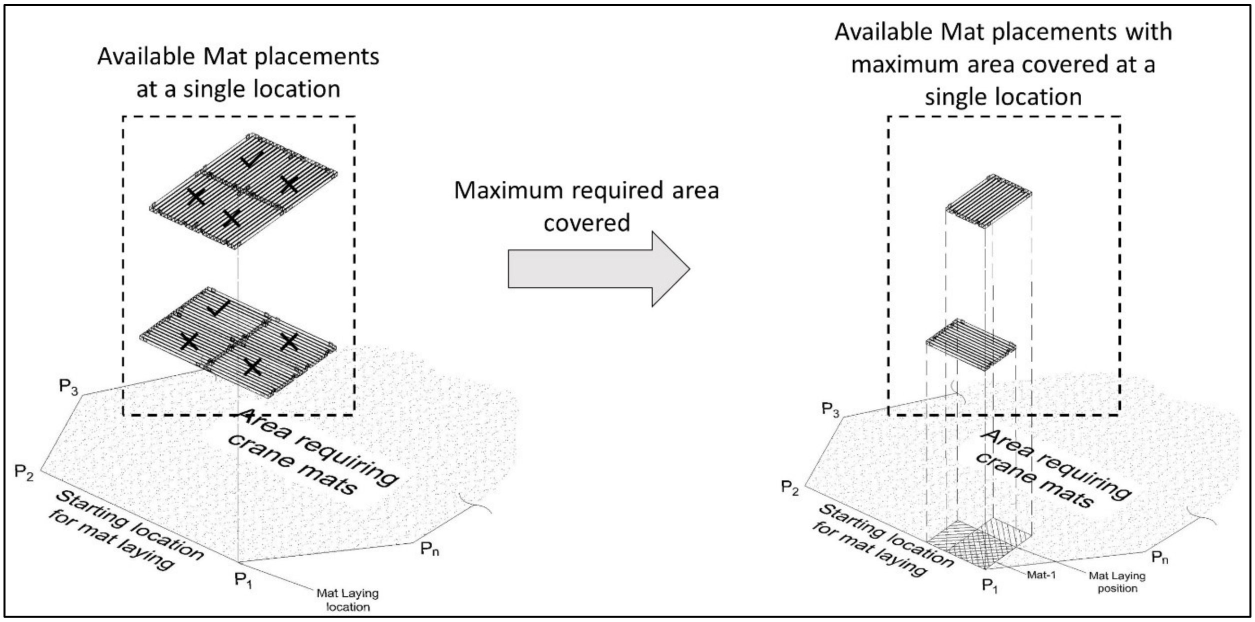

Figure 5.3: Crane mats residing inside the required area

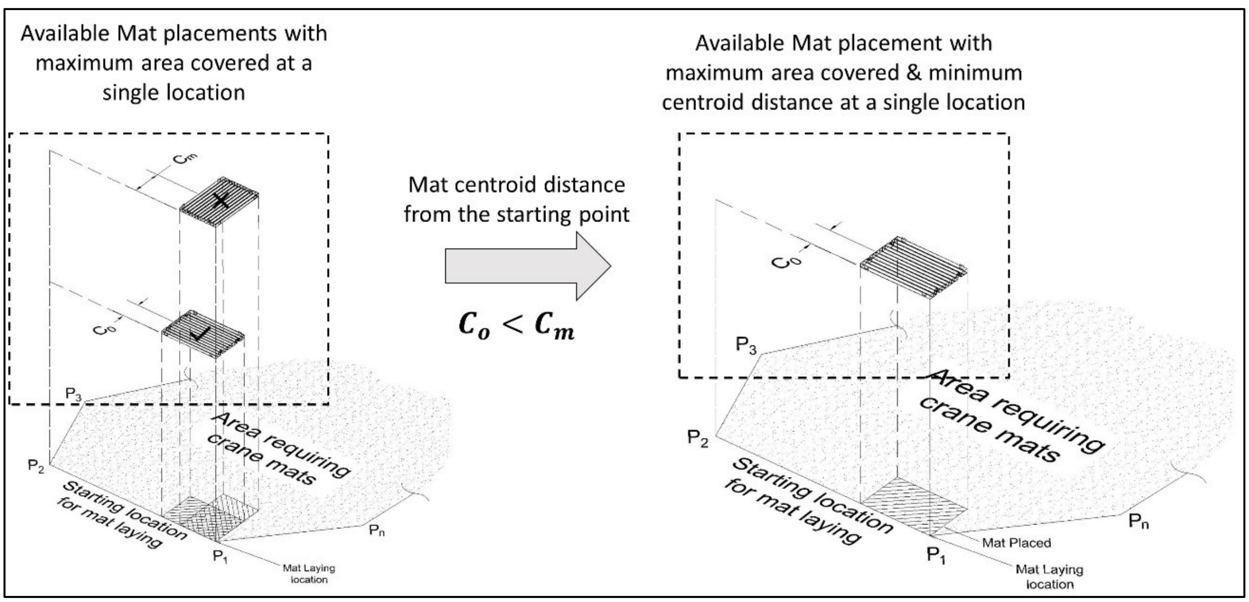

Figure 5.4: Crane mat layout condition for centroid distance from starting edge $R_k(x_k, y_k)$

5.1.1.1.2. Selecting succeeding crane mat locations

After selecting the location and orientation of the first crane mat, the next crane mat also follows some construction site constraints. For the first crane mat, there was only one location R_1, *m=1*, but for the succeeding crane mat, the available locations increase to $O_m(x_m, y_m)$, *m=m+8* for each succeeding crane mat. The greedy crane mat optimization agent uses each location to satisfy the crane mat selection criteria by projecting eight orientations at each crane mat placement location, as shown in Figure 5.5 for one location. One of the main constraints is that the next crane mat in line should not overlap the previously laid crane mat (as shown in Figure 5.6).

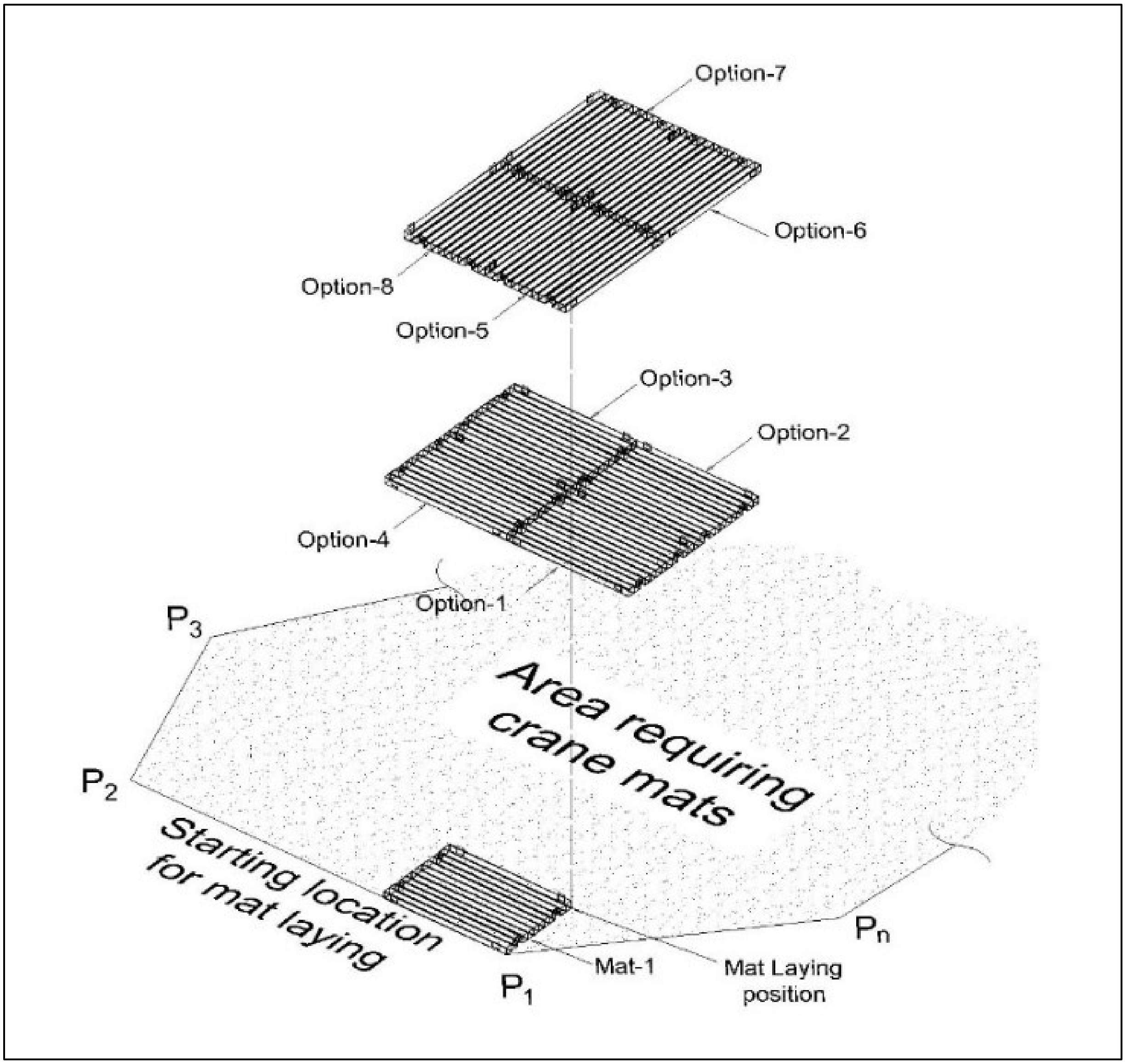

Figure 5.5: Available crane mat orientations (8 options) for the succeeding crane mats at one of the available locations from $O_m(x_m, y_m)$

Considering overlapping crane mat constraints, $AC_o \cap A_i$ should be equal to 0 if there is no overlap. If the selected location results $AC_o \cap A_i \neq \emptyset$, the optimization agent moves to the next location in $O_m(x_m, y_m)$. This crane mat overlapping constraint also works as a filtration system to decrease the quantity of available crane mat locations $O_m(x_m, y_m)$. The crane mat's orientation at a location overlaps the previously placed crane mat is marked "*Reject*." The remaining crane mat orientations are marked "*Accept*". The greedy agent avoids the "*Reject*" orientations for determining the succeeding crane mat location and orientation.

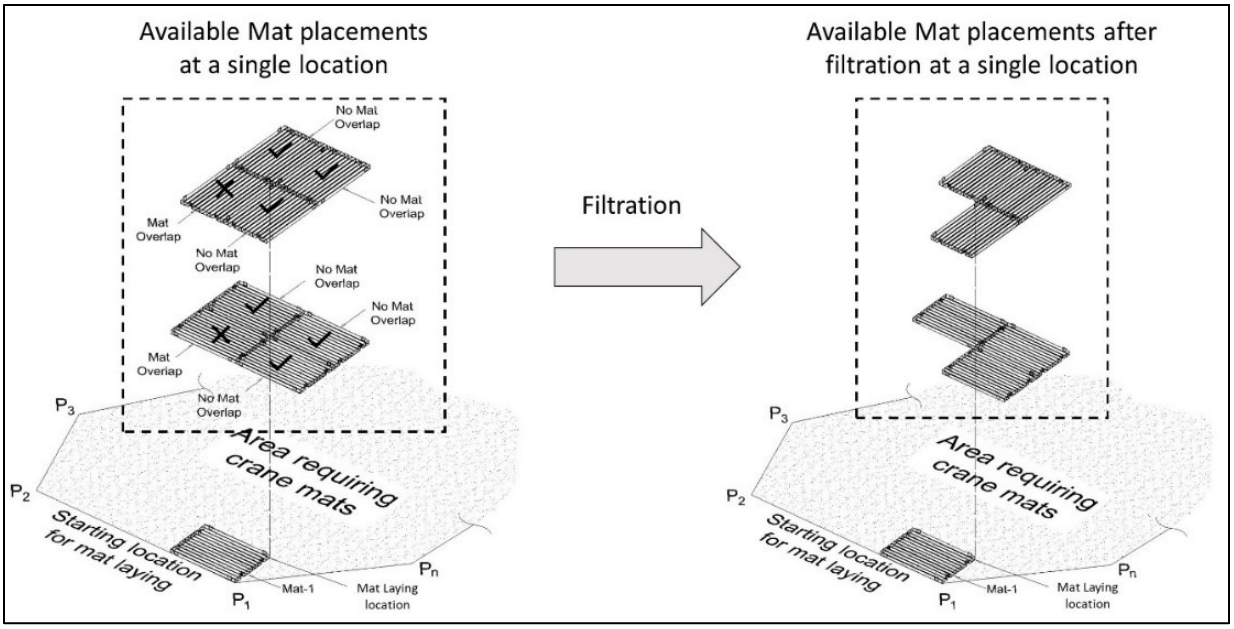

Figure 5.6: Filtration system for crane mat overlap constraint

The greedy agent also uses the similar crane mat location and orientation selection criteria used for the first crane mat to select the succeeding crane mat location and orientation. The greedy agent visits each location of $O_m(x_m, y_m)$ and selects the location and crane mat orientation based on maximum area covered, minimum centroid distance and no overlap. Figure 5.7 shows the flow chart. The greedy agent adds the coordinates of the succeeding crane mat to $O_m(x_m, y_m)$ to be used for the next crane mat location and an orientation selection. The whole process of selecting the crane mat location and orientation is shown in Appendix E Algorithm 3. The greedy agent follows Algorithm 3 to optimize and place the crane mats to cover the required area. The greedy optimization process stops when the required area is fully covered with the minimum number of mats for the job.

5.1.1.2. Development of SARSA algorithm

In terms of structure, RL comprises policy, a reward signal, a value function, and a model. Policy refers to the manner in which an RL agent behaves at a given time. The value function defines the amount of reward or punishment the RL agent receives, where the model (optional) mimics the behaviour of the agent within the environment (Sutton and Barto, 2018). As noted in Chapter 2, Q-learning is an example of off-policy RL, whereas SARSA is an example of on-policy RL. For the crane mat optimization problem at hand, SARSA as an on-policy RL algorithm is deemed to be better suited. Equations (17), (18), and (19) help to clarify the difference between on-policy and off-policy RL approaches. As can be seen, off-policy RL algorithms (e.g., Q-Learning) only consider the future Q-value, $maxQ_a(s_{t+1}, a)$, regardless of the overall Q-values of the states in question—in this case, regardless of the area covered with the minimum crane mats used. In the case of the on-policy algorithm, SARSA, in contrast, the RL agent considers the Q-values for all states $Q_a(s_{t+1}, a_{t+1})$ in accordance with the policy of minimum mats used to achieve maximum coverage within the given constraints for crane mat laying as mentioned in 5.1.1. This means that the off-policy algorithm only targets the states with the maximum Q-value in the case of exploitation. In on-policy RL, however, the target is not only the maximum Q-value, but also the mean value of all the states, as expressed in Equation (19). This taking into account the mean Q-value of all states raises the Q-value.

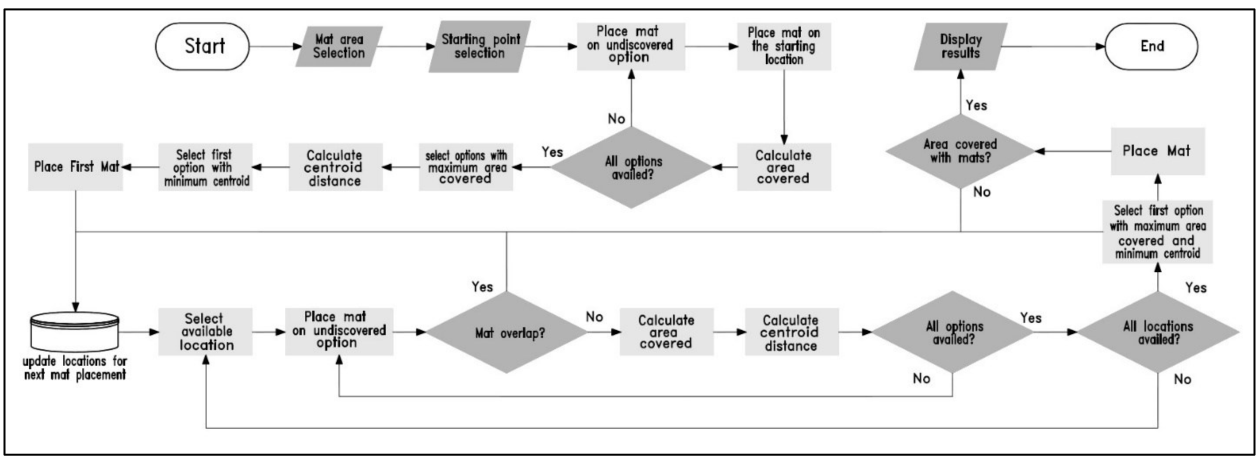

Figure 5.7: Flowchart for greedy crane mat optimization approach

Another notable consideration with respect to RL is the availability of models. For the problem at hand (i.e., crane mat optimization), for SARSA there is no model available on the basis of which for the RL agent to predict the future reward. It should be noted that a model can be an obtained based on the experience of previous implementations of the algorithm (Sutton and Barto, 2018). In the case of the crane mat optimization, for instance, the model could be obtained based on the interrelationships observed between the crane mats already placed. Models obtained in this manner can be implemented in future optimizations to further decrease the processing time, where the model can be updated with each new iteration of crane mat optimization. To develop a robust model applicable to the present case, though, further research and investigation is required. For the purpose of the research described herein, each iteration is executed without a model on the basis of which to predict rewards, making the crane mat optimization described herein a model-free RL problem.

For RL, the first task is to define the states. The RL agent moves from one state to the next, updating the Q-value at the corresponding state for future episodes. For crane mat optimization, there are eight orientations at the start of the optimization at R_1 with eight different centroids as the states for RL optimization. Further placing the crane mats at the periphery, these crane mats provide the set of states (centroid locations) for succeeding crane mat placement, as the succeeding crane mat is placed by the RL agent adjacent to the already placed crane mat (practical constraint). Let $O_m(x_m, y_m)$ be the locations for the crane mat placement, with two crane mat orientations at each location (horizontal and vertical), work as two states for the RL agent. The crane mat centroid positions of these crane mats within the required area work as the RL agent states. The generation of these locations is shown in Figure 5.8.

Considering Equations (17) and (18), one of the major concerns is the reward at each location. For this RL optimization, the value of reward depends upon the area covered, the crane mat centroid distance from the R_k (see Figure 5.8), and overlap constraint. The value of reward gradually decreases as the crane mat placement moves away from R_k till the required area is covered by the crane mats, based on the shaping reward function. The shaping reward function provides a fraction of the final reward on each state and increases/decreases the intensity of the reward as the agent moves closer to the final state (Gullapalli and Barto, 1992).

A filtration system is introduced for the RL agent to avoid using the same location twice. This filtration system assigns *"Reject"* to the locations covered by already laid crane mats. The RL agent only considers the remaining locations for the subsequent crane mat placement. With the addition of each crane mat, the number of available locations decreases, as shown in Figure 5.9.

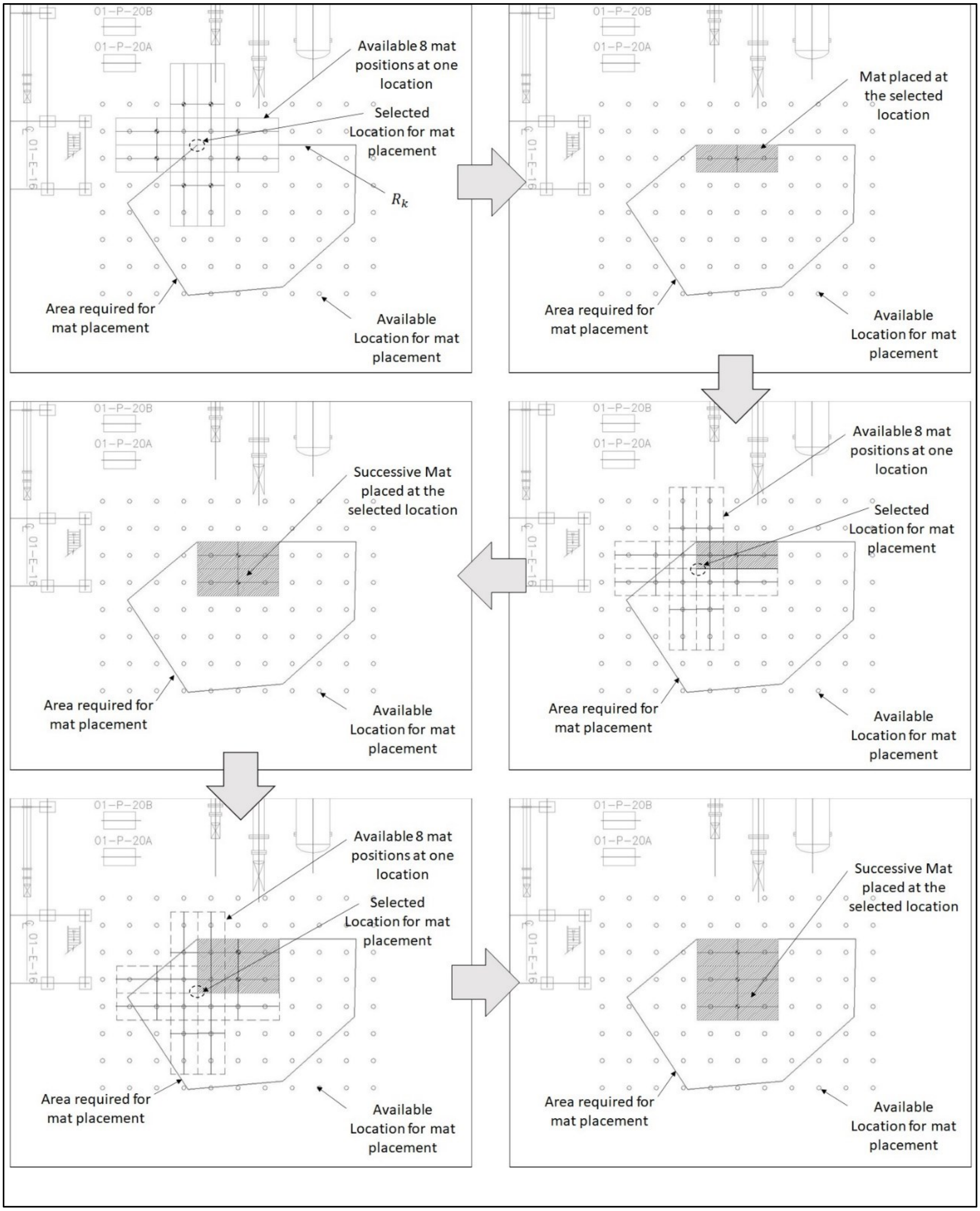

Figure 5.8: Crane mat centroids as the expected locations for crane mats for RL optimization

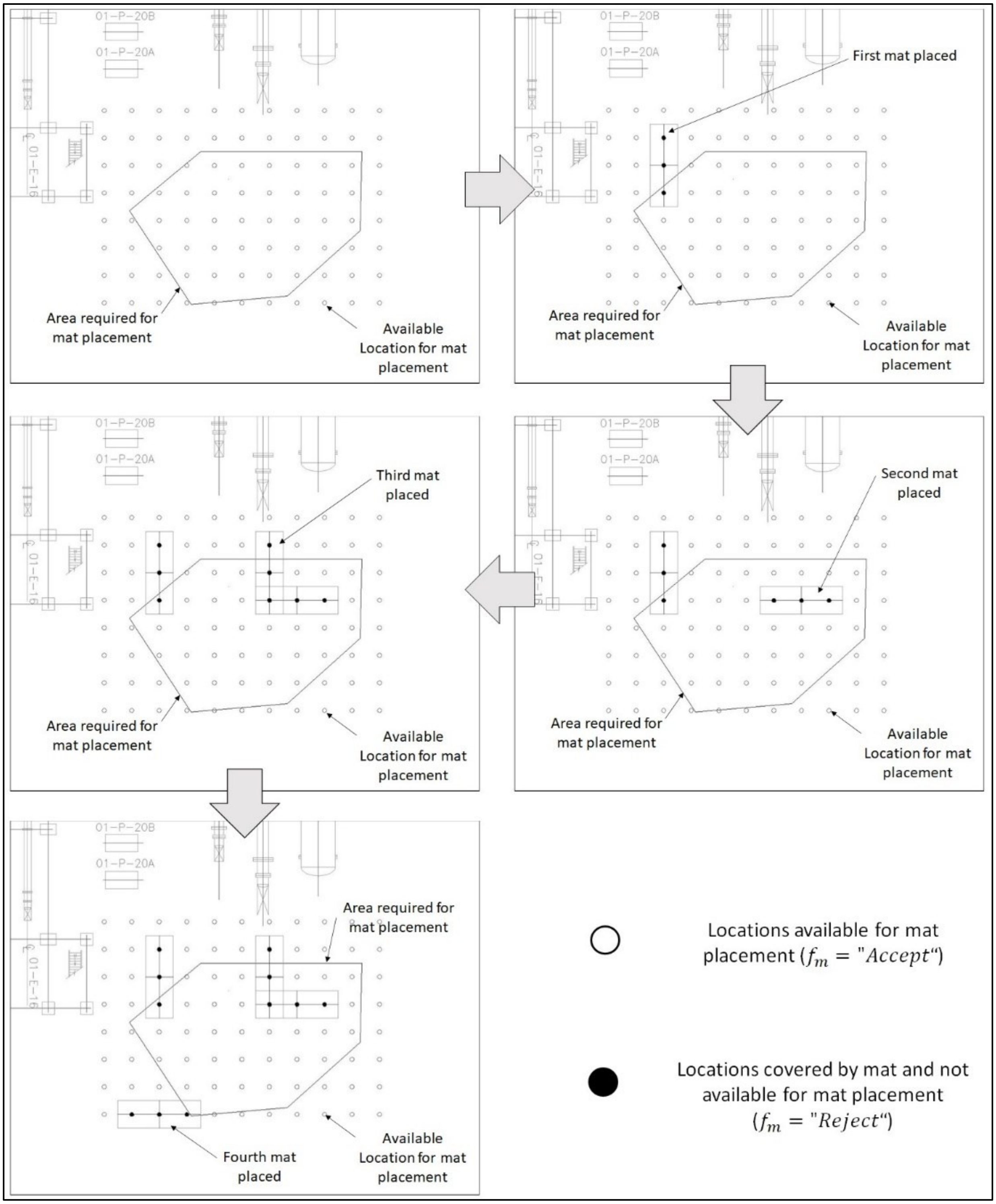

Figure 5.9: Filtration system for crane mat locations for RL optimization

At the start of the RL optimization, the agent picks a random location and a random orientation (horizontal or vertical) to place crane mats. The RL agent updates the Q-value of the state as per the reward based on maximum area covered, centroid distance, and mat overlap constraints. The RL agent updates the Q-value of all the states as the episodes proceed. Later, the RL agent picks states with maximum Q-value. The RL agent performs the optimization process on each episode till the area is covered by the targeted crane mats, without overlap. The numbers of crane mats obtained from the greedy approach from the previous section work as the targeted crane mat numbers for the RL agent. Figure 5.10 shows the flowchart of the process. Algorithm 4 (Appendix F) shows the framework of the RL algorithm. At the start of RL optimization, the policy is stochastic to explore maximum states. Later, the exploration becomes low as the system accumulates knowledge.

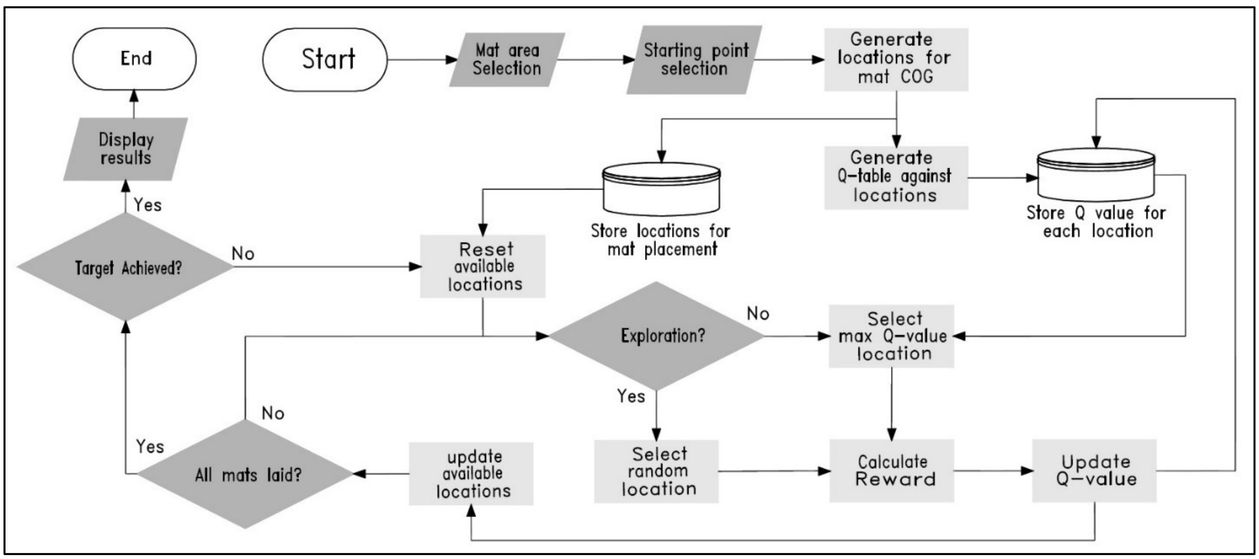

Figure 5.10: Flowchart for RL optimization approach

5.1.2. Theoretical case examples and Discussion

Both of the optimization approaches presented in this thesis are capable of accommodating different crane mat sizes depending on the construction site requirements. The examples provided are limited to one size of crane mat at a time only in the interest of simplicity in demonstrating the practicability of these optimization approaches. For the case examples, crane mats with dimensions of $6\ \mathrm{m} \times 2\ \mathrm{m}$ are taken as the subject crane mat for optimization, which is widely used in the construction industry. The area of the crane mat is $12\ \mathrm{m}^2$. It is assumed that four areas require crane mat placement and optimization, as shown in Figure 5.11. The greedy and RL agent optimizes each area for the optimization process. AutoCAD developed Visual Basic algorithms are executed individually for each required area, as shown in Figure 5.11. First, the greedy approach is applied, and later, the RL approach is applied. The results from both approaches are compared in this chapter. For both approaches, the area in which the crane mats need to be laid out is defined using a sequence of straight segments that form a polygon. Later the user selects the starting edge for the agent to calculate the centroid distance. The optimization agent starts laying the crane mats till the whole area is covered with the crane mats, as shown in Figure 5.12.

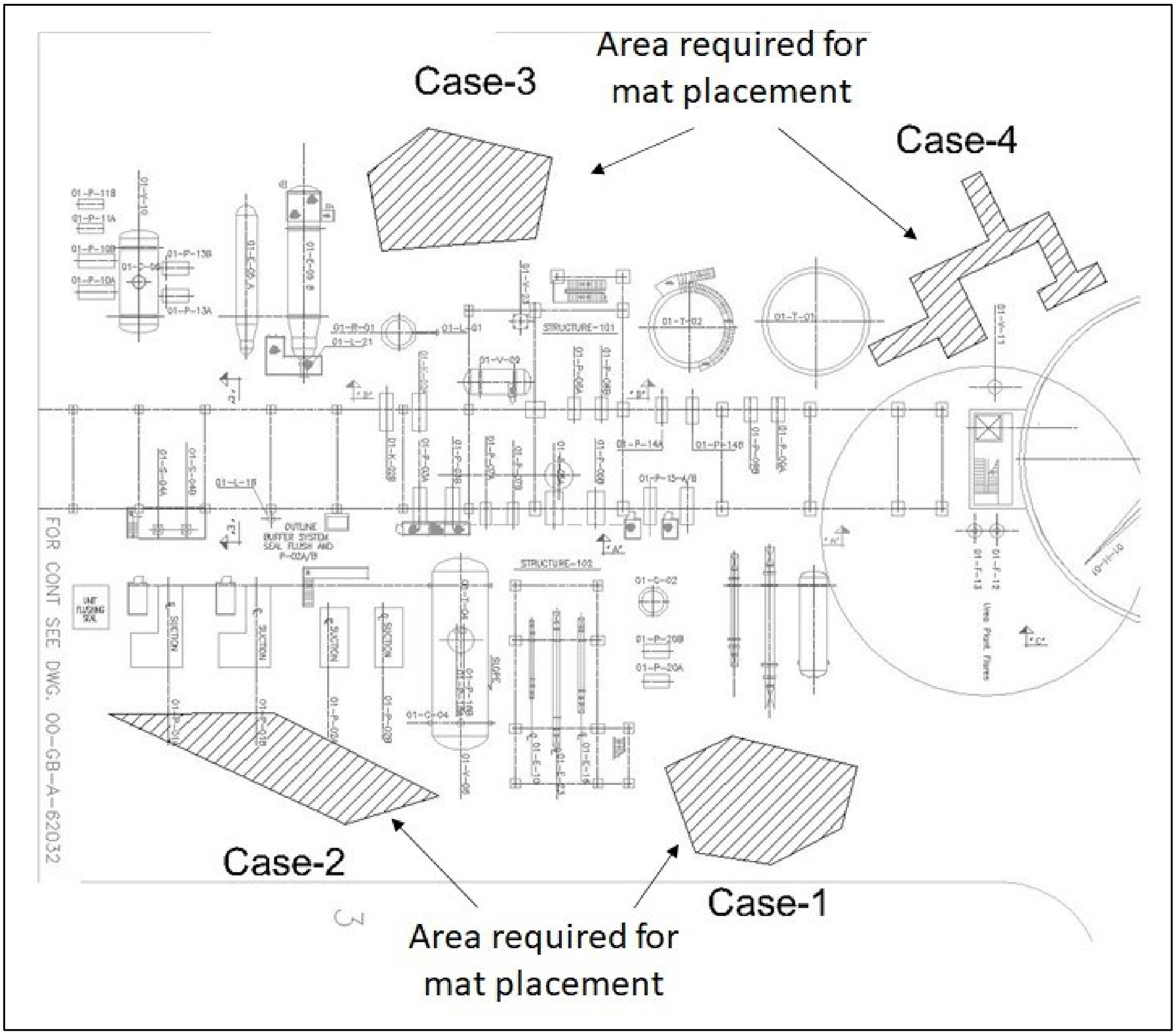

Figure 5.11: Case examples for crane mat optimization (greedy and RL approach)

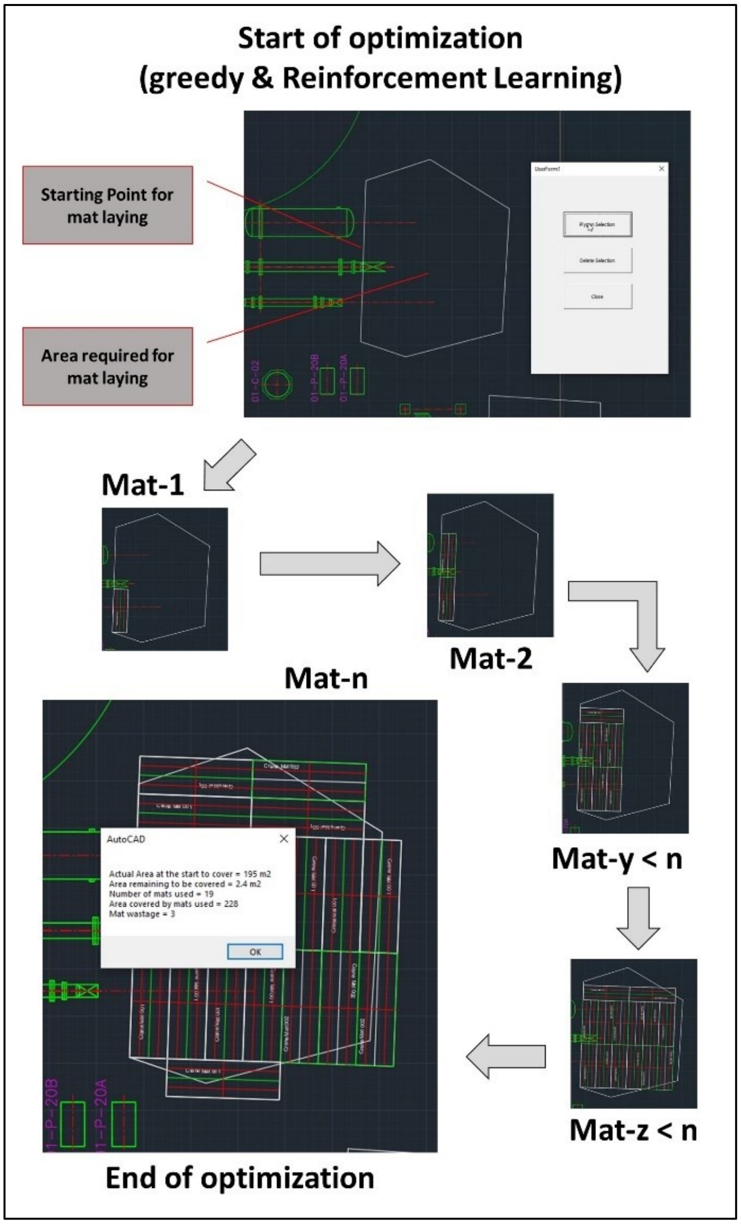

Figure 5.12: Crane mat laying sequence

5.1.2.1. Greedy optimization approach results

For the greedy approach, the agent follows the procedure illustrated in Figure 5.7 to place the first crane mat. It is important to mention that the starting edge $R_k(x_k, y_k)$ is based on the crane placement close to the payload pick/set location (construction site practical constraint). After placing the first crane mat, the greedy optimization agent proceeds to the next crane mat location and orientation selection, as shown in the flowchart in Figure 5.7. After selecting the second crane mat's location and orientation, the algorithm performs the same procedure to identify the remaining crane mats' location and orientation. At the end of the optimization, the outcome states the required area, the number of crane mats used, the area covered, the crane mat wastage, the remaining area, and the computation time taken to complete the optimization. The same procedure is performed on these four areas covered by the greedy agent with the crane mats. Figure 5.13 shows the crane mat layout using the greedy approach. Table 5.1 provides the details for greedy crane mat optimization for each case example. The results show that each layout plan/drawing takes seconds to complete (Intel(R) Core(TM) i7-6700 CPU @ 3.40 GHz using 16.0 GB RAM, running Windows 10) (Table 5.1). The optimization also provides the number of crane mats used, the area covered with the crane mats, and the crane mat wastage.

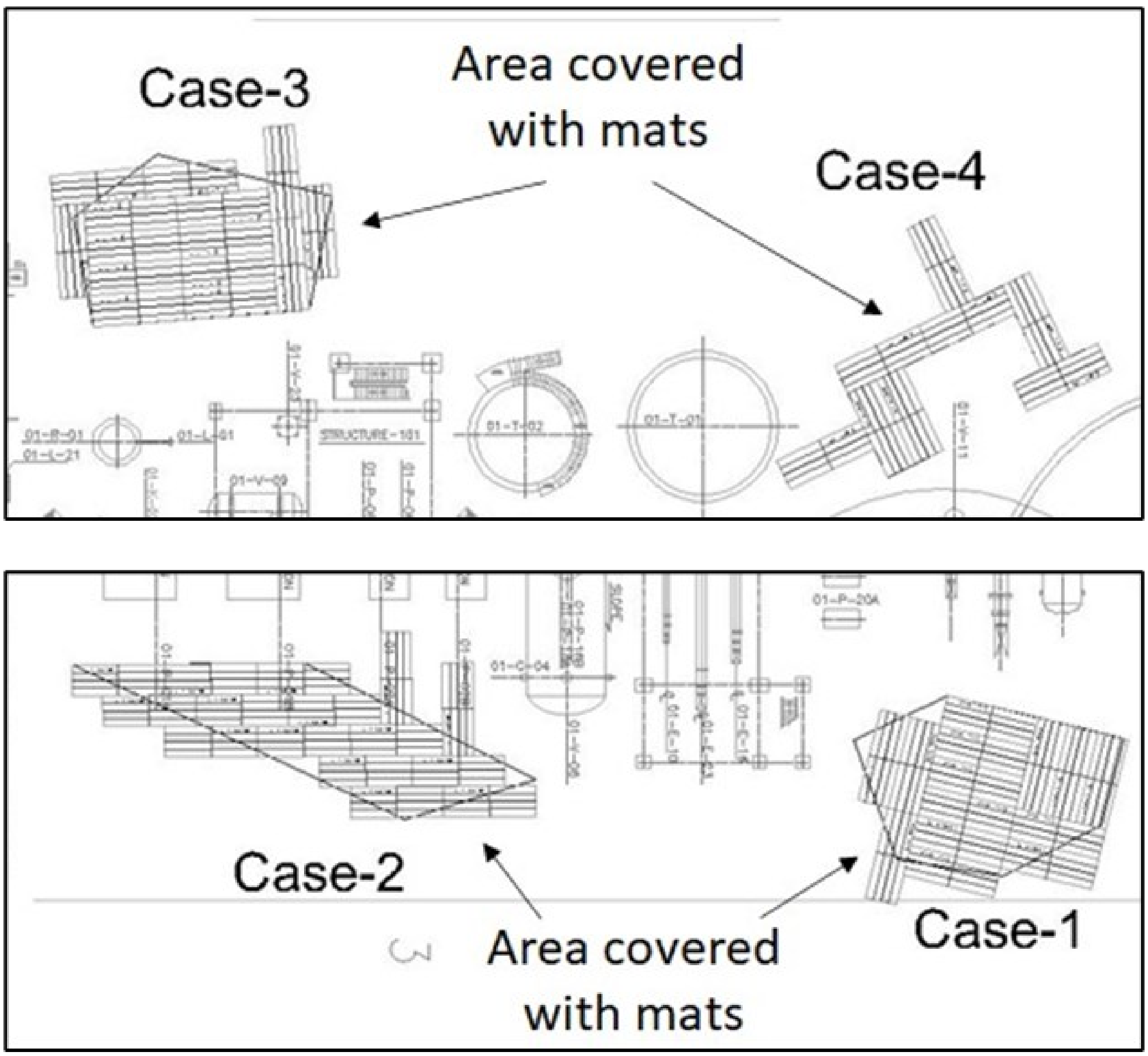

Figure 5.13: Crane mat layout using a greedy approach

Table 5.1: Details of four case examples for crane mat optimization (greedy and RL)

	Case 1		Case 2		Case 3		Case 4	
	Greedy	RL	Greedy	RL	Greedy	RL	Greedy	RL
Actual area to cover (m^2)	142.30	142.30	127.10	127.10	141.20	141.20	96.00	96.00
Area remaining (m^2)	4.82	4.48	4.87	4.11	3.90	4.88	0.07	0.07
Number of crane mats used (nos.)	14	13	15	14	14	13	8	8
area covered by crane mats (m^2)	168.00	156.00	180.00	168.00	168.00	156.00	96.00	96.00
crane mat wastage (nos.)	2.10	1.14	4.40	3.41	2.20	1.23	0.00	0.00
time taken (seconds)	10.95	296.79	12.08	1,678.01	10.57	295.96	5.46	114.83

5.1.2.2. RL optimization approach results

The initialization process of RL optimization (SARSA) is also like the greedy approach. At the start of the optimization, the practitioner selects the area required; later, the starting edge is selected as the starting location for crane mat placement. The RL agent generates the centroid locations for all the crane mat combinations within the required area. Each centroid location provides two states (horizontal and vertical crane mat placement) for the RL agent. The RL agent places the crane mat on a state selected based on exploration or exploitation at each episode. At each state, the RL agent receives a shaping reward to update the Q-value of the state. As the Q-value is updated, the optimization of crane mats also refines. The outcome is shown in Figure 5.14.

Compared to Figure 5.13, the crane mat layout optimization using RL saves crane mats and covers more area with fewer crane mats. The outcome from the RL optimization is tabulated in Table 5.1. Case 4 is the same for both optimization approaches. However, in the remaining three cases, the results from RL optimization are more cost-effective, elegant, and favourable. The RL optimization took more computation time than the greedy approach but saved more crane mats and covered more area. Practitioners also perform crane mat optimization like RL optimization. A practitioner prepares a preliminary crane mat layout plan/drawing and continuously revises it to obtain the optimal solution. The methodology followed by the RL agent mimics the behaviour of a practitioner preparing a crane mat layout plan/drawing manually.

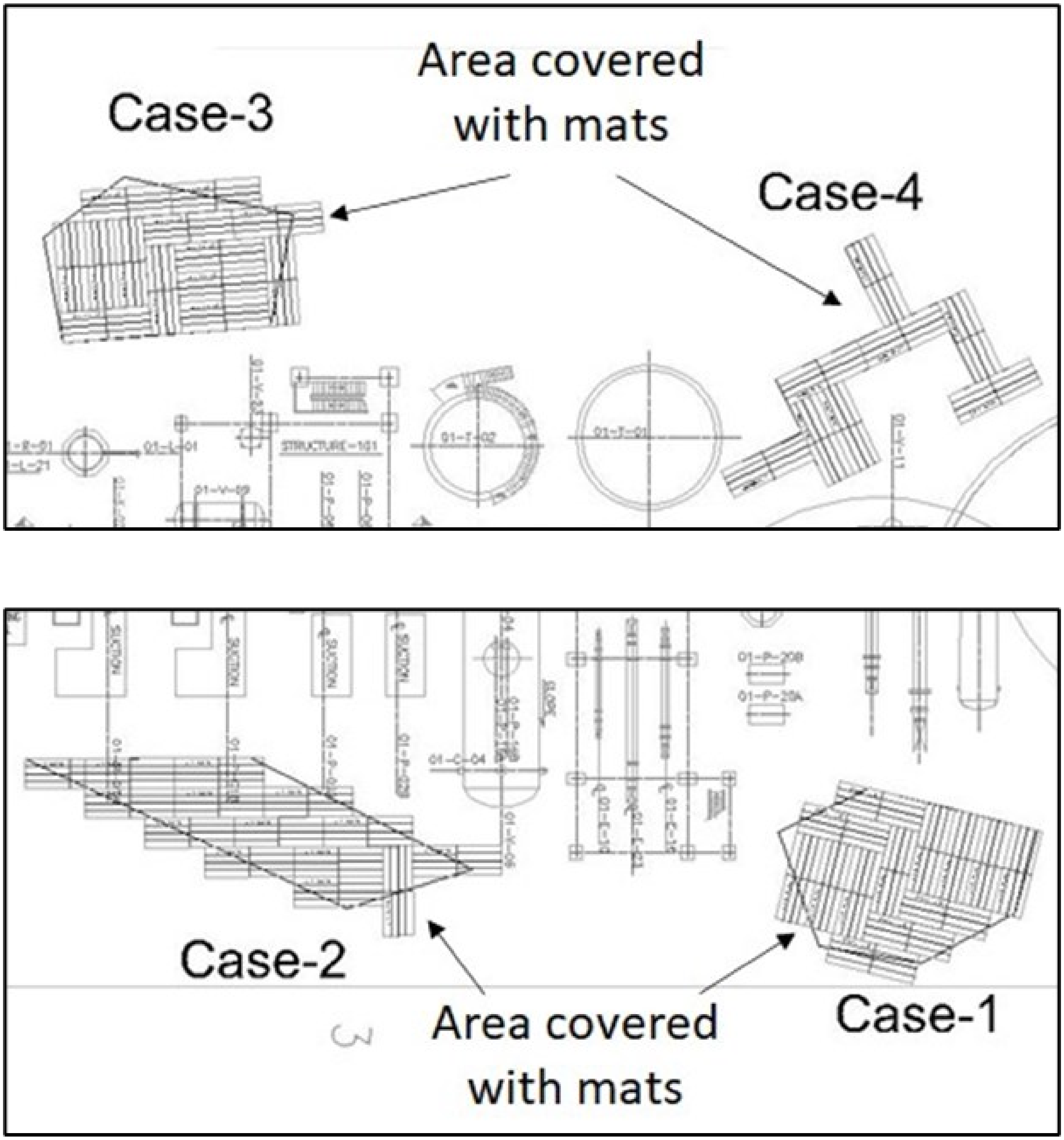

Figure 5.14: Crane mat layout using RL approach

Figure 5.15 shows the value of reward and area remaining against RL episodes for all four cases. Case 4 took close to 1,000 episodes to reach the final state with the maximum area covered and minimum crane mats used. Case 1 and Case 2 each used close to 2,000 episodes to reach the optimal solution. For Case 2, the number of episodes was close to 10,000, with the maximum computation time consumed. The primary reason was the irregular shape of the area required (Case

2), which shows that as the area becomes more irregular in shape, the episodes and the computation time consumed also increase exponentially.

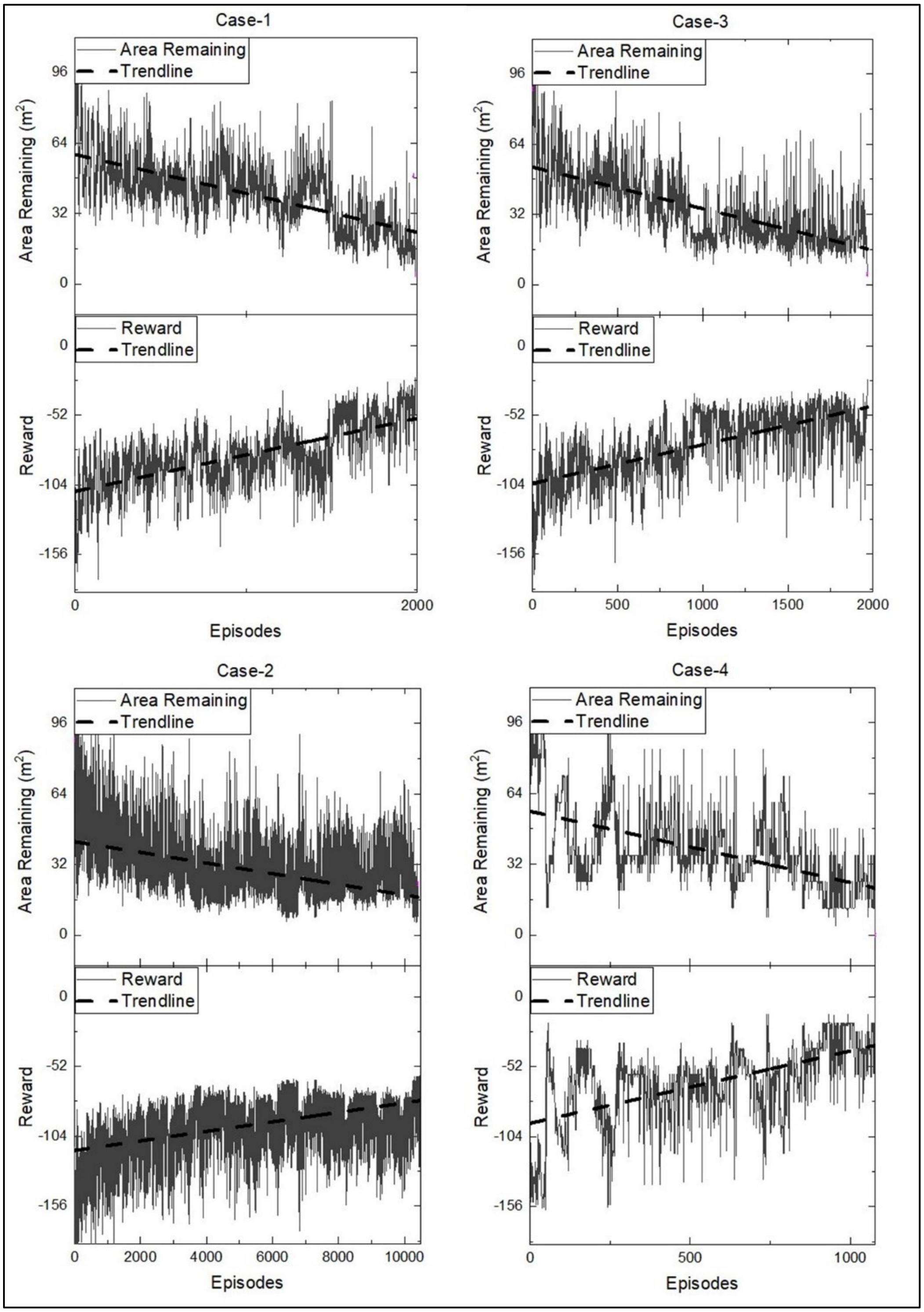

Figure 5.15: Area remaining and reward against each episode for all four cases

5.2. Chapter summary

The chapter-5 comprises the optimization process for crane mat layout plans. Two major optimization approaches (greedy and RL agent) are used for the optimization. Not only that but the comparison between both approaches is also presented in this chapter. The comparison shows that greedy can save practitioners time in preparing crane mat layout plans. The RL agent can save crane mats but takes more processing time. Four cases were used to compare the results. The crane mat layout planning approaches will assist in minimizing the crane mat wastage on a construction site, which is directly linked with wood wastage and CO_2 emissions.

CHAPTER 6: ALLOWABLE SOIL BEARING CAPACITY FOR MOBILE CRANES

This chapter presents an approach to calculating soil bearing capacity. As stated in Chapters 2 and 3, the traditional approach employed by crane rental companies for determining the allowable soil bearing capacity is to simply use the information provided by the client. However, this approach fails to take into account the impact of crane tracks/outriggers/crane mats on the allowable soil bearing capacity (Onyelowe 2017, Du et al. 2017, Gaonkar et al. 2021, Patwardhan and Metya 2021, Tahmid et al. 2021). In this chapter, a computer application developed in Visual Basic to calculate allowable soil bearing capacity as per the mobile crane and the construction site requirements is presented. The developed application can assist practitioners in estimating the allowable soil bearing capacity for crane work. Based on the values obtained from this application, practitioners can evaluate the ground preparation requirements accordingly, as shown in Figure 2.8. In addition to providing the capacity profiles, which are paramount from a safety perspective, the developed application allows practitioners to reduce the time and cost required for site preparation. The results of various case examples (using the developed application) as presented below suggest that the allowable soil bearing capacity varies depending on the crane track/outrigger/crane mat width, and that it is not constant for every type of crane work. The developed methodology as described in this chapter provides a better understanding of the soil bearing capacity underneath the mobile cranes. The developed application obtains the information required for the computation from the geotechnical report of the construction. However, if geotechnical data is not available, the developed application provides a rough estimate of each required variable for the practitioner's reference.

6.1. Methodology for allowable soil bearing capacity

The ultimate soil bearing capacity q_u, also known as geotechnical bearing resistance at the ultimate limit state is shown in Figure 6.1 (Canadian Geotechnical Society Foundations Committee 2006). The resistance of soil balances the pressure exerted by the crane combined loading. The soil cohesion and weight of soil exert pressure to stabilize the crane to avoid track/outrigger/crane mat sinking. Many researchers developed equations to estimate the ultimate soil bearing capacity. The current research conducted in this thesis compares four practical approaches to provide a result in the form of computer application output.

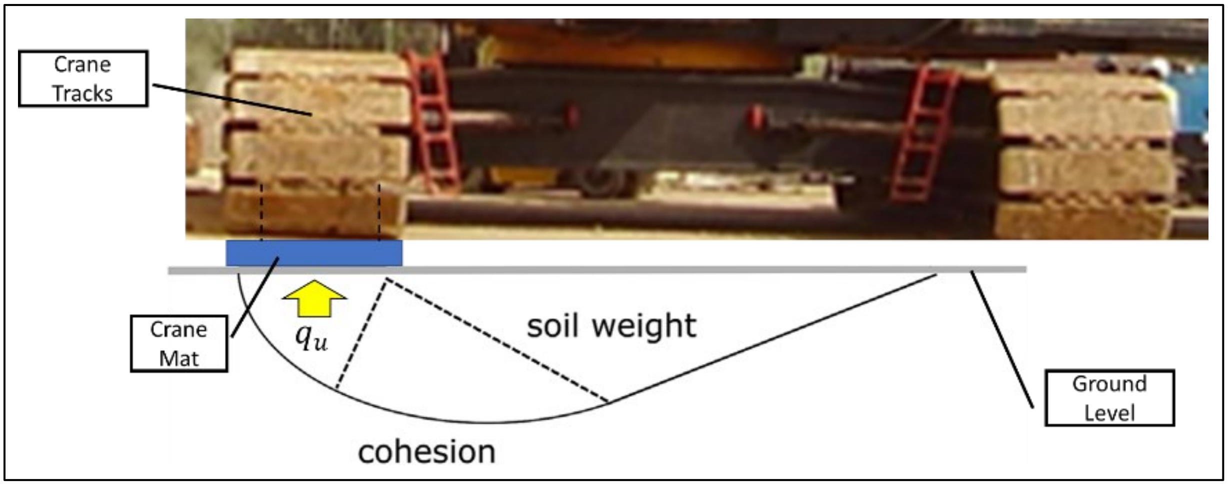

Figure 6.1: Ultimate ground bearing pressure to counter crane loading (Ground bearing pressure)

6.1.1. Methodology for allowable soil bearing capacity

The methodology developed relies on four basic approaches for soil bearing capacity calculations. These approaches are derived from Terzaghi (1943), Meyerhof (1963), Hansen (1970), and Vesic (1975) soil bearing capacity estimation work. For foundation design, the construction industry widely uses these four approaches. These four approaches are as below:

6.1.1.1. Terzaghi (1943)

Terzaghi (1943) formulated an equation to estimate the ultimate soil bearing capacity based on general shear failures of shallow strip footings (Ralph B. Peck et al. 1974, Coduto 2001). He developed the primary form of the equation, as shown in Equation (45).

$$q_u = cN_c + q_s N_q + \frac{1}{2}\gamma B N_\gamma \tag{45}$$

where c is soil cohesion, N_c, N_q, N_γ are dimensionless bearing capacity factors, q_s is vertical stress at the elevation of the base of crane track/outrigger/crane mat, γ is soil unit weight, and B is the least plan dimension of crane track/outrigger/crane mat. Equation (45) by Terzaghi (1943) is for the strip footing beneath the ground level, but for crane work, the crane track/outrigger/crane mat is always above the ground level and the value of q_s decreases to 0. This change shows that only cohesion and soil weight affect the soil bearing capacity, as shown in Figure 6.1.

To calculate the allowable soil bearing capacity q_{all}, the factor of safety FS is integrated into Equation (45) to form Equation (46). The value of the safety factor is usually based on onsite construction requirements and usually varies between 2 to 5.

$$q_{all} = \frac{q_u}{FS} \tag{46}$$

The developed application calculates the dimensionless bearing capacity factors using the following equations based on internal friction angle $\emptyset$.

$$N_q = \frac{a^2}{2cos^2(\pi/_4 + \emptyset/_2)} \tag{47}$$

where $a = e^{\left(0.75\pi - \emptyset/_2\right)tan\emptyset}$.

$$N_c = \left(N_q - 1\right)cot\emptyset \tag{48}$$

$$N_\gamma = \frac{tan\emptyset}{2}\left(\frac{K_{p\gamma}}{cos^2\emptyset} - 1\right) \tag{49}$$

where $K_{p\gamma}$ = passive pressure coefficient. It is also important to mention that $N_c = 5.7$ when $\emptyset = 0$. In Terzaghi's approach Terzaghi (1943), the value of $K_{p\gamma}$ is determined by means of a graphical method. Later Coduto (2001) presented a way to calculate the value of $K_{p\gamma}$ numerically using the following equation.

$$N_\gamma \approx \frac{2\left(N_q + 1\right)tan\emptyset}{1 + 0.4\sin\left(4\emptyset\right)} \tag{50}$$

6.1.1.2. Meyerhof (1963)

Meyerhof (1956, 1963) refined Equation (45) by adding dimensionless modification factors to make it closer to reality. Equation (51) below describes the modifications proposed by Meyerhof (1956, 1963).

$$q_u = cN_cS_c + q_sN_qS_q + \frac{1}{2}\gamma N_\gamma BS_\gamma \tag{51}$$

where S_c, S_c, S_c are dimensionless modification factors for crane track/outrigger/crane mat shape, inclination, depth, tilt, and ground slope. The modified dimensionless factors reported by

Meyerhof are as follow (Meyerhof 1956, 1963, Canadian Geotechnical Society Foundations Committee 2006):

$$N_q = e^{\pi tan\emptyset} tan^2 \left({}^{\pi}/_{4} + {}^{\emptyset}/_{2} \right) \tag{52}$$

$$N_c = \left(N_q - 1\right) cot\emptyset \tag{53}$$

$$N_\gamma = \left(N_q - 1\right) tan(1.4\emptyset) \tag{54}$$

$$S_c = 1 + 0.2\, tan^2 \left({}^{\pi}/_{4} + {}^{\emptyset}/_{2} \right) \frac{B}{L} \tag{55}$$

$$S_q = S_\gamma = 1, for\ \emptyset = 0 \tag{56}$$

$$S_q = S_\gamma = 1 - 0.1 tan^2 \left({}^{\pi}/_{4} + {}^{\emptyset}/_{2} \right) \frac{B}{L} \quad for\ \emptyset > 0 \tag{57}$$

where B is the width of the crane track/outrigger/crane mat and L is the length of the crane track/outrigger/crane mat.

6.1.1.3. Hansen (1970)

Hansen (1970) also presented modifications and adjustments to the ultimate soil bearing capacity Equation (51). Hansen (1970) presented some modifications to the values of N_γ, S_c, S_q & S_γ as below:

$$N_\gamma = 1.5\left(N_q - 1\right) tan\emptyset \tag{58}$$

$$S_c = 1 + \frac{N_q B}{N_c L} \tag{59}$$

$$S_q = 1 + \frac{B}{L} sin\emptyset \tag{60}$$

$$S_\gamma = 1 - 0.4 \frac{B}{L} \tag{61}$$

6.1.1.4. Vesic (1975)

Vesic (1975) further modified the ultimate soil bearing capacity Equation (50) and updated the values of N_γ and S_q as below:

$$N_\gamma = 2\left(N_q - 1\right) tan\emptyset \tag{62}$$

$$S_q = 1 + \frac{B}{L} tan\emptyset \quad (63)$$

6.1.2. Development of *ASBC*

An application named *ASBC* (Allowable soil bearing capacity calculator for mobile cranes) is developed in this section. Figure 6.2 shows the appearance of *ASBC*. The practitioner must provide the values of $L, B, \emptyset, c, \gamma,$ and FS, so that the application can calculate accordingly. The application *ASBC* provides dimensionless factors values under each approach and provides the allowable soil bearing capacity value using each approach as mentioned in Section 6.1.1. The final values are in the unit of metric tons/m^2. Figure 6.3 shows the flowchart of the processes (algorithm) involved in calculating allowable soil bearing capacity.

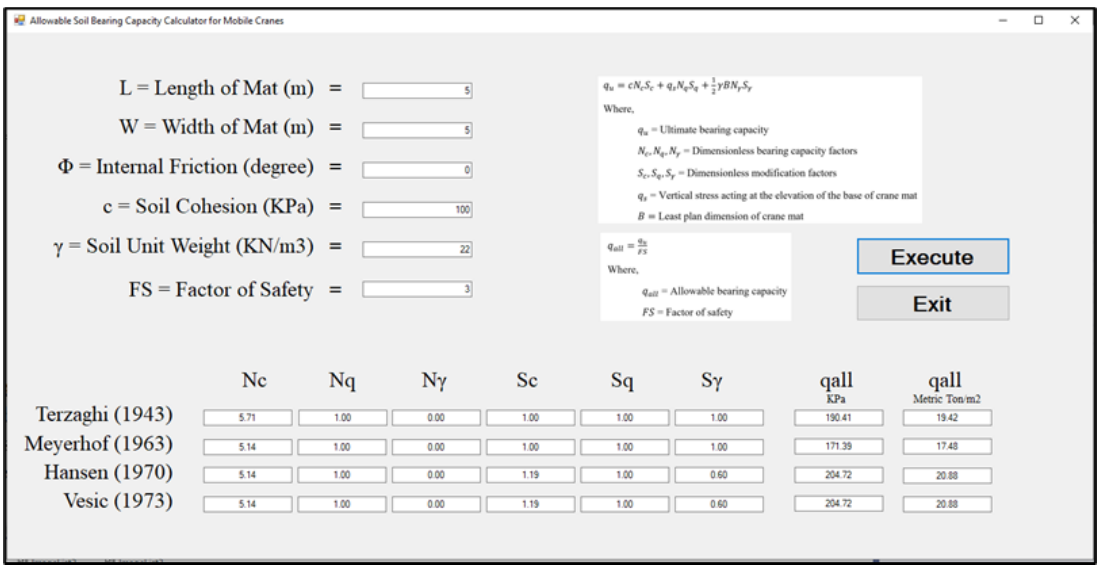

Figure 6.2: Computer application (ASBC) for calculating allowable ground bearing pressure for crane work

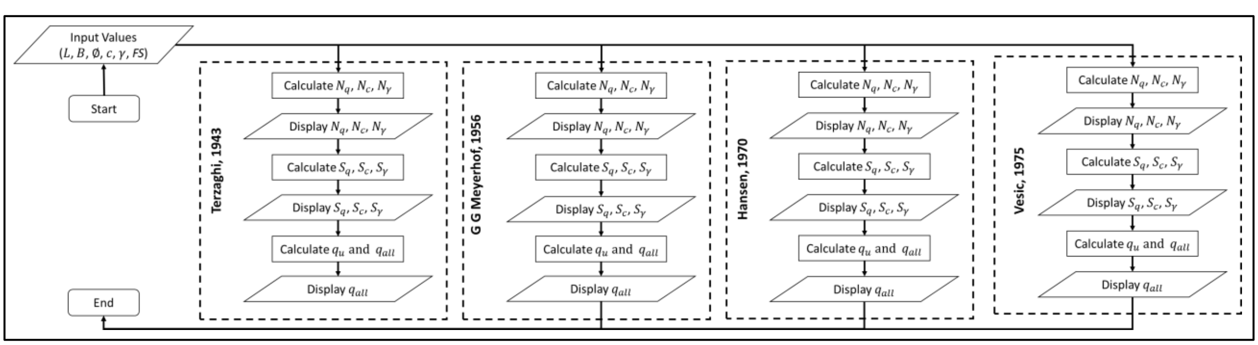

Figure 6.3: Flowchart for allowable soil bearing capacity calculations (ASBC)

6.2. Case examples and discussion

6.2.1. Soil parameters for allowable soil bearing capacity

The prerequisites for the application are the values of $L, B, \emptyset, c, \gamma$ and FS. The dimensions of the crane track/outrigger/crane mat of the crane used for the crane lift provide the values of L and B. The value of FS is perceived between 2~5 and depends mainly on the construction site constraints. The main concern is the values of $\emptyset, c$ and γ, which geotechnical reports of the construction site can provide. Usually, the geotechnical reports provide the values of shear strength of soil S_u and unit soil weight, γ, and in some cases the value of $\emptyset$. In case the value of shear strength is provided, Coulomb's equation, shown below, can be used to calculate the value of soil cohesion (Yokoi 1968):

$$c = S_u + p\ tan\emptyset \tag{64}$$

where S_u is shear strength value, and p is the effective pressure normal to the surface of failure. According to Canadian Foundation Engineering Manual (Canadian Geotechnical Society Foundations Committee 2006), for short-term foundation stability, the value of $\emptyset = 0$, so the value of S_u becomes c. For crane work, as the crane stability is a short-term constraint, the value of $\emptyset = 0$ for all the equations for ultimate soil bearing capacity (Canadian Geotechnical Society Foundations Committee 2006).

The value of $\emptyset$ is usually 0, as most crane work involves only short-term loading. For crane work being carried out over a long duration (long-term foundation stability), however, the value of $\emptyset$ needs to be obtained and incorporated into the calculation in determining the ultimate soil bearing capacity values. The geotechnical reports provide these values.

If the shear strength value is not available, Table 6.1 provides possible intervals for this parameter as a function of the soil type (Canadian Geotechnical Society Foundations Committee 2006). Equation (64) can be used to calculate the value of soil cohesion. Another aspect that needs attention is the value of unit soil weight γ, obtained using Table 6.2 (Ralph B. Peck et al. 1974). The values of various soil types in Table 6.2 are tabulated into the saturated and dry states. For the soil bearing capacity calculations, the saturated value is used in the application for short-term stability. The practitioners can incorporate dry unit weight for long-term usage for allowable soil bearing capacity calculations.

Table 6.1: Values of undrained shear strength of various soil types

	Soil Type	Undrained shear strength S_u value (kPa)
1	Very soft	<12
2	Soft	12 to 25
3	Medium Stiff	25 to 50
4	Stiff	50 to 100
5	Very Stiff	100 to 200
6	Hard	200 to 300
7	Very Hard	>300

Sources: Data adapted from Canadian Geotechnical Society Foundations Committee. (1985). Canadian foundation engineering manual. Canadian Geotechnical Society

Table 6.2: Values of unit weights of various soil types

	Description	Unit Weight (kN/m^3)	
		γ (dry)	γ (saturated)
1	Uniform sand, loose	14.1	18.5
2	Uniform sand, dense	17.1	20.4
3	Mixed-grained sand, loose	15.6	19.5
4	Mixed-grained sand, dense	18.2	21.2
5	Windblown silt (loess)	13.4	18.2
6	Glacial silt, very mixed-grained	20.4	22.8
7	Soft glacial clay	11.9	17.3
8	Stiff glacial clay	16.7	20.3
9	Soft, slightly organic clay	9.1	15.4
10	Soft, very organic clay	6.8	14.0
11	Soft montmorillonitic clay (calcium bentonite)	4.2	12.6

Sources: Data adapted from Peck, R. B., Hanson, W. E., & Thornburn, T. H. (1974). *Foundation Engineering* (2nd ed.). Wiley.

The last piece of the puzzle is the value of soil friction angle $\emptyset$. Ortiz et al. (1986) developed a table with the values of soil friction for various types of soils, as shown in Table 6.3. The practitioners can use the values from Table 6.3 to calculate the allowable soil bearing capacity.

6.2.2. Case example (soil friction angle = 0°)

For uniform sand ($\approx$ dense), the value of γ is 20 kN/m^3 (Table 6.2). Since the value of S_u is the same as of c, so for very stiff soil, the value of c is taken as 150 kPa. The values are incorporated in the application to obtain the allowable soil bearing capacity. Before that, the dimensions of the crane track/outrigger/crane mat are essential. For this case example, the length L is 10 m, but the width B is considered variable from 1, 2, ······, 10 m. This variation of width helps to generate a sensitivity analysis to observe the variation of allowable soil bearing capacity along B/L as shown in Figure 6.4a. The FS is 3 for this case example (between 2~5).

Table 6.3: Typical friction angle values (°) for various soil types

	Description	Friction angle ∅ (°)
1	Gravel	32~34
2	Gravel, sandy with few fines	32~35
3	Gravel, sandy with silty or clayey fines	32~35
4	Gravel and sand mixture, with fines	22~28
5	Sand, uniform, fine grained	30~32
6	Sand, uniform, coarse grained	30~34
7	Sand, well graded	32~33
8	Silt, low plasticity	25~28
9	Silt, medium to high plasticity	22~25
10	Clay, low plasticity	20~24
11	Clay, medium plasticity	10~20
12	Clay, high plasticity	6~17
13	Organic Silt or Clay	15~20

Sources: Data adapted from Ortiz, J.M.R., Mazo, C.O., Gesta, J.S., and de Arquitectos de Madrid, C.O. 1986. Curso aplicado de cimentaciones, 3rd edition. Colegio Oficial de Arquitectos de Madrid.

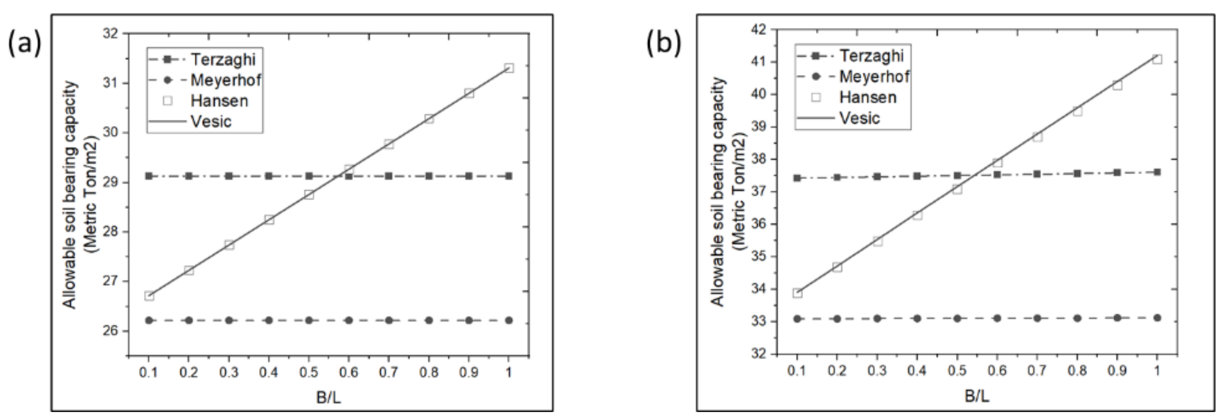

Figure 6.4: (a): Variation of allowable soil bearing capacity q_{all} along B/L (∅=0, γ = 20 kN/m^3, c=150 kPa, $L = 10m, B = 1, 2, 3 \ldots, 10m$), (b): Variation of allowable soil bearing capacity q_{all} along B/L (∅=6, γ = 20 kN/m^3, c = 150 kPa, $L = 10m, B = 1, 2, 3 \ldots, 10m$) Flowchart for allowable soil bearing capacity calculations (ASBC)

The graphical representation shows that the allowable soil bearing capacity values generated using Hansen (1970), and Vesic (1975) increases as the B/L reaches 1. With the increase in value of B, the allowable soil bearing capacity also increases. On the other hand, the values generated using Terzaghi (1943) and Meyerhof (1963) remains constant. The constant value of allowable bearing capacity with Terzaghi (1943) and Meyerhof (1963) is due to the values of S_q and S_γ. When $\emptyset = 0°$, the conservative approach takes the minimum value of allowable soil bearing capacity for ground preparation.

6.2.3. Case example (soil friction angle = 6°)

If the crane work at a given location is long-term, the value $\emptyset$ is incorporated in the application for the allowable soil bearing capacity calculations. For the soil composed of clay, high plasticity, the value of $\emptyset = 6°$ is considered for this case example for the allowable soil bearing capacity calculations. All other values are the same as the case example with $\emptyset = 0°$.

The graphical representation, Figure 6.4b, shows that all the four approaches generate ascending values along B/L. The slope of allowable soil bearing capacity along B/L of Hansen (1970) and Vesic (1975) is more significant as compared to Terzaghi (1943) and Meyerhof (1963). The results also show that when the value of B increases, the allowable soil bearing capacity also increases, regardless of the approach used for the calculations.

6.3. Chapter summary

The aim of this chapter was to assist practitioners in estimating the allowable soil bearing capacity for safe mobile crane operation. The estimation of allowable soil bearing capacity is a prerequisite for the crane mat selection, in conjunction with the GBP exerted by the mobile crane. The value of allowable soil bearing capacity is estimated using four different theorems widely used in the construction industry. Using *ASBC* will help minimize the crane mat wastage on a construction site by removing the assumption that allowable soil bearing capacity remains the same regardless of the crane ground footings.

CHAPTER 7: CONCLUSION

This chapter summarizes to fill the gaps identified in the scholarship and industry practice with respect to the calculation of ground bearing pressure (GBP) under mobile cranes, crane mat strength analysis, crane mat optimization, and the calculation of the allowable soil bearing capacity for mobile crane work. In addition, the limitations of the research are discussed in this chapter, and recommendations for future research work in this area are proposed.

7.1. Ground bearing pressure under mobile cranes

7.1.1. Crawler cranes

The results described in Section 3.1.3 reveal that the traditional method for calculating GBP under crawler tracks is limited and can lead to potentially deceiving results. The higher the crane capacity, the more significant the discrepancy between the traditional 4-point calculations and the proposed 8-point method using a combined loading approach. With the increased use of heavy cranes, ignoring the GBP at the edges and only taking an average can lead to poor ground operation for crane construction sites. This poor ground stability can lead to ground failure resulting in crane tipping. Practitioners around the world have significant concerns about ground stability and crane tipping. Historically, most construction crane failures are linked to ground failure leading to crane tipping. Crane failure due to crane tipping is consistently a grave concern for the safety of workers working around cranes. Shapiro and Shapiro (2010) explained the phenomenon of crane tipping in detail. It is thought that when R surpasses E_f (see Figure 3.3), the crane approaches tipping quickly. This tipping reduces the actual total bearing area (ATBA) to the effective total bearing area (ETBA) (see Figure 3.4), and for this reason, the pressure at the payload side of the crane increases, and the ground under the track close to the payload settles a little deeper. This settling raises the track on the opposite side (see Figure 2.7), thus further reducing the ETBA, which pushes the crane further towards tipping. It is imperative to conduct future research pertaining to the calculations of GBP values in the context of soil bearing capacity and soil elasticity (Shapiro and Shapiro 2010). Moreover, it is also vital to re-examine all the GBP software to determine the reliability of the calculated GBP values, which take the average of two edges.

The best approach to mitigate the risk by utilizing crane mats for load distribution is to avoid ground failure under a crawler crane. When selecting the crane mat, it is crucial to consider the actual GBP values under the crawler tracks instead of taking an average along the track width. Finite element analysis (FEA) simulation also verified that 4-point GBP values could be deceiving. Especially for higher-capacity cranes, the edges of the crawler track exert more pressure. Most importantly, the GBP is not consistent along the width of the track. This variation of GBP along the width of the track needs to be accounted for in the design and selection of the crane mats.

For scenarios in which $R > E_f$ (see Figure 3.3), GRG nonlinear optimization is used to obtain the coordinates of the ETBA. Future research can minimize the non-linear optimization constraints and utilize other optimization techniques to obtain these values. It would also be essential to develop a general algorithm to calculate the 8-point GBP values without switching from $R \leq E_f$ to $R > E_f$. The research presented herein only calculated these values separately, but they can be combined to generate a generic algorithm for 8-point GBP calculations in the future. Furthermore, a computer application can be developed based on this algorithm, which can be helpful for practitioners on construction sites to obtain the GBP values under a crawler crane for any type of critical lift utilizing crawler cranes. This application could be updated with the crane data to suit the site requirements. The developed application would make it easy for practitioners to generate GBP charts instead of using the raw equations to generate spreadsheets. The application should incorporate the non-linear optimization approach to calculate ATBA reduction to ETBA. Ultimately, this computer application will be the practical application of this new 8-point methodology of GBP calculations. For the practical application, the crane data (crane part COGs and their locations) for any crane must be accurate to generate the GBP profile under each crawler crane track.

The research conducted in the context of this thesis has determined that the GBP varies along the width of the track, which, by extension, requires that construction site management undertake a careful examination of the calculation of crane mats for a crane lift. The higher GBP values require an increase in the strength of the crane mat to overcome this, which can be accomplished by using higher strength mats or by applying an extra layer of mats. An alternative could be to compact the area to increase the soil bearing capacity. All these options will have an impact on the workload on site. Not only that, the construction site schedule and cost baseline will be affected due to work related to these remedies for higher GBP values. It is essential for construction site management to develop a contingency plan for these lifts that considers the GBP values obtained using the proposed method because they are higher when compared to traditional GBP calculations.

7.1.2. Hydraulic cranes

The significance of a critical lift always raises concerns among practitioners. It is vital to compare the GBP calculation with the allowable soil bearing capacity. As mentioned above, if the GBP is greater than the soil bearing capacity, crane mats made of wood (timber) or steel are used to distribute the load and decrease the GBP's magnitude, lowering it within the allowable soil bearing capacity limits. With the increased use of heavy cranes due to modularization, ignoring the GBP at the edges of the crane mat and only taking the average over the crane mat surface area can lead to poor ground preparation for crane operation. It is crucial to calculate an accurate GBP distribution under hydraulic crane mats to determine whether the soil can bear the load or not and select the appropriate crane mat for the crane task. Crane failure due to crane tipping is consistently a grave concern for the safety of workers working around cranes. Historically, the construction site crane failures mainly were linked to ground failure leading to crane tipping. Shapiro and Shapiro (2010) explained the phenomenon of crane tipping in detail, as stated in Section 7.1.1.

Moreover, the GBP results from the GBP output section of the application *CoLMA* (developed in this thesis) reveal that the traditional method for calculating GBP under hydraulic crane mats is limited and can lead to potentially deceiving results. The higher the crane's weight, the more significant the discrepancy between the traditional GBP calculations and the proposed 16-point GBP method. It requires that the construction site management undertake the GBP values using the 16-point combined loading method for the site preparation. Further to the crane mat requirement, it is advised for the safe crane operation to prepare the ground by compacting the soil to meet the required GBP. The application *CoLMA* can only utilize one type of crane mat at a time for GBP calculations. The results show that the value of GBP under outrigger mats varies. Variable crane mat size can optimize the crane mat usage based on the variable GBP values.

Another limitation with the conducted research was the availability of various hydraulic crane data. Only one type of hydraulic crane data was used for the examples. Future research can implement various hydraulic crane data to verify novel GBP methodology. Concerning future integration, the aim is to introduce more mobile hydraulic crane data to make this application versatile. Currently, the end-user needs to incorporate the crane data for the calculations. The plan is to update the application with the built-in crane data to make it more user-friendly. The proposed update requires crane data in detail for a maximum number of cranes to expand its utilization circle.

7.2. Crane mat structural analysis

Regarding mat structural analysis, the combination of soil and mat is much more complicated than the equations incorporated in the developed application *CoLMA* (Duerr 2010, Duerr and Duerr 2019). Due to soil/mat configuration complexity, it is vital to apply engineering judgment for the mat design selection criteria (Duerr 2010, Duerr and Duerr 2019). Moreover, this thesis provides a practical method developed in the form of a computer application *CoLMA* to select a crane mat based on five major design parameters. Practitioners can use this application for any mat type, provided that all relevant physical properties (e.g., f_b, f_v, f_c, d_p, etc.) and design factors (e.g., K_D , C_t , K_T, etc.) are available with the user (see Section 2.3).

To further validate the proposed methodology, it is advisable to use stress and deflection monitoring sensors on a hydraulic crane mat to observe the impact of static and dynamic loading. The application '*CoLMA*' can add more design factors and parameters to incorporate full failure modes of a crane mat under dynamic loading. It will be helpful for the practitioners to verify them further using finite element analysis (FEA), like Mahamid et al. (2017) and Mahamid and Torra-Bilal (2019) made a comparison of mat model with FEA and verified them from lab testing the cross-laminated timber mat.

Another aspect that requires incorporation in this application is the design criteria for the crane mat under two loads. Currently, the application can only handle one load at a time. A design criterion needs to be developed and added to the application if a single long mat supports two outriggers. As stated above, it is reasonable to integrate the crawler cranes and the hydraulic cranes under the banner of mobile cranes, using the same methodology to calculate GBP under the mobile cranes. This integration will assist the practitioners on the construction site in estimating the ground support for a particular lift. With the adaptation of modular construction, the utilization of mobile cranes surged and needs proper estimation of GBP for appropriate ground support for the execution of construction projects. Nevertheless, this new methodology can also be used for offshore cranes, formulating this approach as universal crane loading calculations (Chen and Sun 2021).

7.3. Crane mat optimization

7.3.1. Reinforcement learning (Q-Learning and SARSA)

Although the application of reinforcement learning (RL) within the construction industry is relatively new, RL has the potential to be applied for rapid and robust design optimization. Beyond construction, researchers are already exploring ways to use RL to minimize the time required for design. One example is the use of RL for the design of a rocket engine using the ANSYS platform. The traditional procedure involves trial-and-error to fine-tune the rocket engine design parameters. To minimize this development time for a primary fluid dynamic problem with diverse parameters as inputs and outputs, Mehr (2019) integrated RL with FEA. The input values were manipulated to obtain the desired output values following the typical procedure for RL.

Following the same approach, RL can be used to minimize the amount of time required for the extensive trial-and-error and fine-tuning of parameters involved in designing a ground support mat for crane work. The parameters used for this multi-objective optimization problem are the crane ground bearing pressure, soil composition, soil capacity, and design parameters (e.g., beam placement, beam type, plate thickness, etc.) and mat configuration. It is important to note that other parameters (transportation, fabrication constraints, lifting constraints, etc.) can be added later as required.

In addition to crane mat design, the future intention can be outlined to develop a novel generic norm for RL in machine/product design. Machine/product design is a complex problem with many contributing factors. Due to this complexity, machine/product design takes a relatively long time from concept to prototype. The application of FEA in machine/product design was a great help, but at the same time, the processing time for FEA increases exponentially ("*curse of dimensionality*") with the addition of more design parameters (Bach 2017). The back and forth from manual design to FEA consumes a large amount of the design engineer's time. This time could be reduced by developing an algorithm that can mimic the behaviour of a design engineer.

7.3.2. Agent-based crane mat optimization

Both of the developed approaches (greedy and RL) are shown to be capable of saving practitioners time and reducing human error in optimizing the crane mat layout on a construction site based on an automated approach. A task that would take minutes to complete using the traditional manual approach can be completed in seconds with the adoption of crane mat optimization algorithms for preparing the crane mat layout plans/drawings. The output in the form of a crane mat layout provides the practitioner with the exact resource requirements for timely planning and execution. In this research, it should be noted, only one crane mat size (one that is widely used within the construction industry) is used in the greedy and RL optimizations. Using multiple different crane mat sizes to achieve the required coverage can decrease the crane mat usage and wastage. This aspect will be incorporated in future research efforts.

Furthermore, in this research, the results from the greedy optimization are used as target numbers for the RL optimization. There is a possibility that the RL agent would achieve a better result working without any target numbers, but doing so raises a question as to where to stop the episodes, as the RL agent can continue for an infinite number of episodes. Future work will explore the breaking point for RL optimization based on a quality metric. The function of the quality metric to be developed will be to stop the episodes once a defined level of improvement has been attained.

Another way to optimize crane mats is using a brute-force algorithm, although this entails considerably more computation time compared to the greedy approach. For example, for Case 2 (referenced in Chapter 5), the number of possible combinations is 8^{15}, and the computation time required to process them using the brute-force algorithm is 2.83×10^{13} seconds, which is considerably more than the time taken by the RL agent to optimize the crane mat layout.

Researchers are exploring RL as a way to minimize the time required for generic machine design (product development). One example is the use of RL for the design of a rocket engine using the FEA (i.e., ANSYS) platform. The traditional method consists of manual trial-and-error to refine the parameters associated with the rocket engine design. To minimize the time for the development phase, the researcher used RL to integrate FEA. Following the norms of RL, the input values were manipulated to obtain the desired output values (Mehr 2019, Waxenegger-Wilfing et al. 2020). Based on the results of the present research, it is also expected that RL can be used to optimize various other complex problems within the construction domain, including optimization of the crane mat design itself. In particular, RL can be helpful for reducing the computation time required compared to the current practice, which involves extensive trial-and-error and fine-tuning of the parameters involved in the crane mat design. Such an application would approach the crane mat design as a multi-objective optimization problem encompassing parameters such as crane ground bearing pressure, soil composition, soil capacity, design parameters (beam placement, type of beam, plate thickness, etc.), and crane mat configuration.

7.4. Allowable soil bearing capacity for mobile cranes

In both case examples (Sections 6.2.2 and 6.2.3), soil bearing capacity calculations show that the change in the width of the crane track/outrigger/mat changes the allowable soil bearing capacity value. This outcome contradicts the traditional approach of obtaining a single allowable soil bearing capacity value from a client for crane work. A single value of allowable soil bearing capacity can be misleading, as the width of the crane track/outrigger mat varies. Using a conservative value from all four approaches is advisable to estimate ground preparation for crane work. It is expected that in the future, more approaches shall be incorporated in this application to estimate the allowable soil bearing capacity for crane work. For future validation, the use of FEA can be helpful. The FEA can further elaborate and portray the soil behaviour under the crane footing.

7.5. Research contributions

7.5.1. Academic contributions

The combined loading approach to the GBP calculations overcomes the limitations of the traditional approach to GBP calculations and provides a set of novel equations for this purpose. These equations will aid practitioners and researchers in visualizing the GBP profile under the crawler crane tracks (or hydraulic crane mats, as the case may be). Moreover, the mat strength analysis (in the form of graphical representation) can be used by practitioners and researchers to observe the suitability of a given crane mat for a particular job (see Figure 7.1).

Another major academic contribution is the use of RL for crane mat optimization. There are many algorithms available for optimization, such as greedy, brute-force, and dynamic programming.

However, as mentioned in Section 7.3, brute-force and dynamic programming in particular are time-consuming, and all three lack the exploratory aspect that RL offers (Waxenegger-Wilfing et al. 2020). The research work described herein introduces the use of RL for solving optimization problems in construction. As noted earlier, RL is already being used by researchers and practitioners in fields ranging from gaming to healthcare (Yu et al. 2021), Natural Language processing (NLP) (Paulus et al. 2017), and the automobile industry (in the development of self-driving cars) (Kiran et al. 2021).

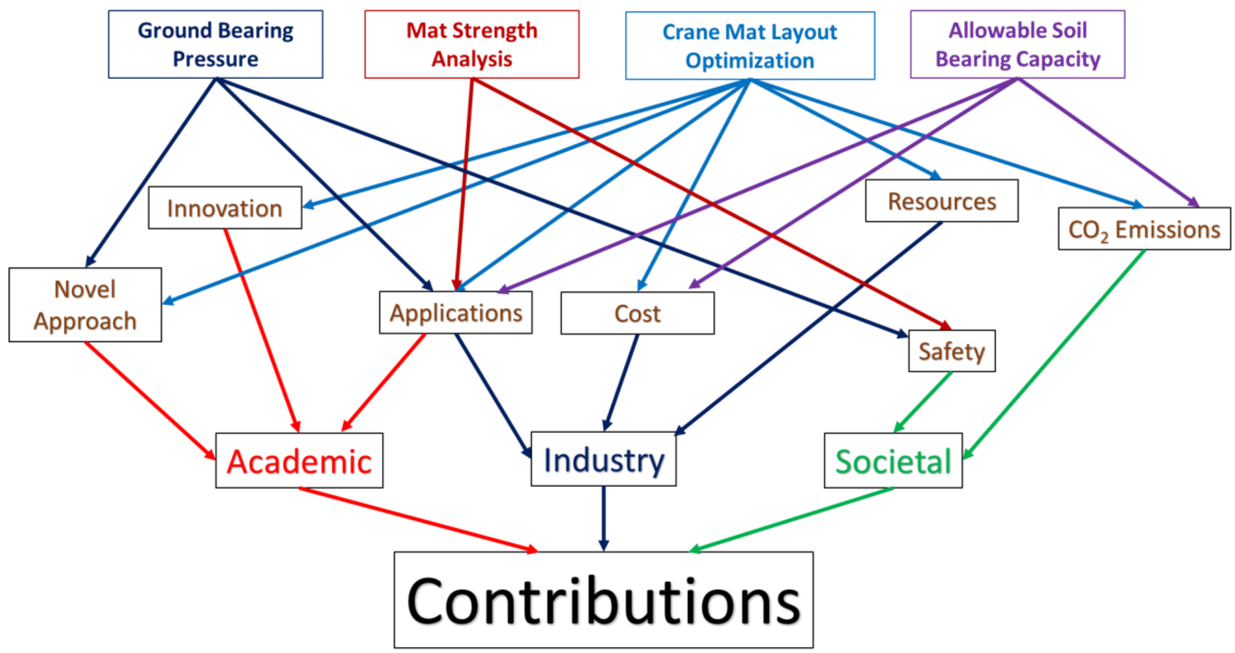

Figure 7.1: Mind map of contributions

These applications in other industries underscore the potential of RL as a solution to optimization problems encountered in the construction industry. Based on previous project data, an RL-based application may be useful for decision support and for promoting safety on construction sites. Moreover, the exploratory aspect of RL lends itself to design optimization based on analysis of worst- and best-case scenarios. Indeed, the use of RL for crane mat optimization may be a first step towards the broader practical application of RL within the construction industry. For instance, much of the decision-making conducted by project engineers in construction could be improved and expedited leveraging the exploratory aspect of RL. The optimization of resources, for instance, is always a major concern in construction management. Construction enterprises are continually seeking the best solution to increase productivity and minimize the resources required. Nevertheless, the construction industry is failing to keep pace with other industries in terms of productivity (Graham 2019), and RL is a promising solution for addressing this deficiency, given its successful application in other industries. The comparison between RL and the greedy approach presented herein also shows that the number of crane mats required for a given coverage area can be reduced further through the application of RL, thereby reducing waste and increasing productivity.

7.5.2. Contributions to industry practice

The developed application, *CoLMA*, can be used by industry to estimate the GBP under a hydraulic crane mat. Although *CoLMA* is still in a raw form at this juncture, it can be improved to make it a more user-friendly application. *CoLMA* can also assist practitioners in confirming the suitability of a given crane mat for a particular job. Moreover, the use of combined loading for GBP calculations can assist practitioners in generating and understanding the GBP profile under the crawler crane (or hydraulic crane) tracks. It should be noted that, in current practice, practitioners typically use a safety factor in determining the crane mat requirement in order to overcome the limitations of the traditional approach to GBP calculations, but this increases the capital and operational costs associated with the crane mats (see Figure 7.1 and Figure 7.2).

The crane mat optimization approaches mentioned in this thesis can assist practitioners and save them time. As mentioned in Chapter 1 and in Chapter 5, the crane mat optimization approaches proposed herein allow the practitioner to perform in seconds what may have required minutes or even hours following the traditional approach. Not only that, but the number of crane mats required can be reduced, thereby decreasing the capital and operational costs associated with crane mat manufacture, transport, and stacking.

Furthermore, the results generated by the proposed soil bearing capacity application, *ASBC*, show that, as the capacity of the crane increases with an increase in the ground footing, the allowable soil bearing capacity of the soil under the mobile crane increases accordingly, thus reducing the crane mat requirement. While the traditional approach is to use the same allowable soil bearing pressure value for every type of crane and crane mat on a construction site, regardless of crane ground footing. These results demonstrate that the crane mat requirement can be safely reduced in accordance with increasing dimensions of the ground footing, thereby reducing the capital and operational costs associated with the crane mats.

7.5.3. Societal contributions

Safety of workers is a matter of paramount concern on any construction site. As mentioned in Chapter 1, crane tipping has been a factor in many injuries and fatalities on construction sites (Abdul Hamid et al. 2019). The results of the combined loading approach indicate that the GBP values calculated using the traditional approach are limited and can lead to crane tipping. The GBP values determined using combined loading show some variation towards higher GBP under a crane track or crane mat. For example, considering a Manitowoc 18000 crawler crane with the same configuration used in Chapter 4 and a payload of 54 metric ton, the maximum GBP value with 60° slew angle using the traditional approach to GBP calculations is about 66.3 metric tons/m^2. Using the combined loading approach, however, the maximum GBP value is 67.9 metric tons/m^2, a difference of 1.6 metric tons/m^2. In other words, using the traditional GBP value as the basis for the crane mat design may increase the risk of crane tipping by underestimating the GBP (by a margin of 1.6 metric tons/m^2 in this case) (see Appendix A and Figure 7.2). As noted above, practitioners typically apply a safety factor when designing the crane mats to mitigate the risk of "unknown unknowns", but this practice results in overdesign of the crane mats and increases the resource usage and cost.

The main objective of this research with regard to crane mat optimization was to minimize the usage of crane mats on construction sites, and a decrease in crane mat usage will reduce the CO_2 emissions associated with crane mats. To illustrate this, we can consider a hypothetical construction project requiring crane in Yellowknife, Northwest Territories. For the purpose of calculating the corresponding CO_2 emissions, it is estimated that the number of timber mats (3.6449 m × 2.4384 m × 0.2032 m) used in this case can be reduced by 8 by applying the optimization approaches developed in this research. The maximum lifespan of a timber mat is approximately three years (Muhammad et al. 2021). The total volume of 8 timber mats is 14.448 m^3, and the density of Coastal Douglas-Fir is about 0.52997 metric tons/m^3 (SImetric.co.uk 2011). Based on this density, the weight of these mats is 7.657 metric ton. Equation (65), proposed by Bergman et al. (2014), can be used to calculate in metric ton the CO_2 emissions involved in the manufacture of the timber mats based on 0.7272 metric ton of wood weight.

$$CO_2\ (Manufacturing) = 0.7272 \times W_g \tag{65}$$

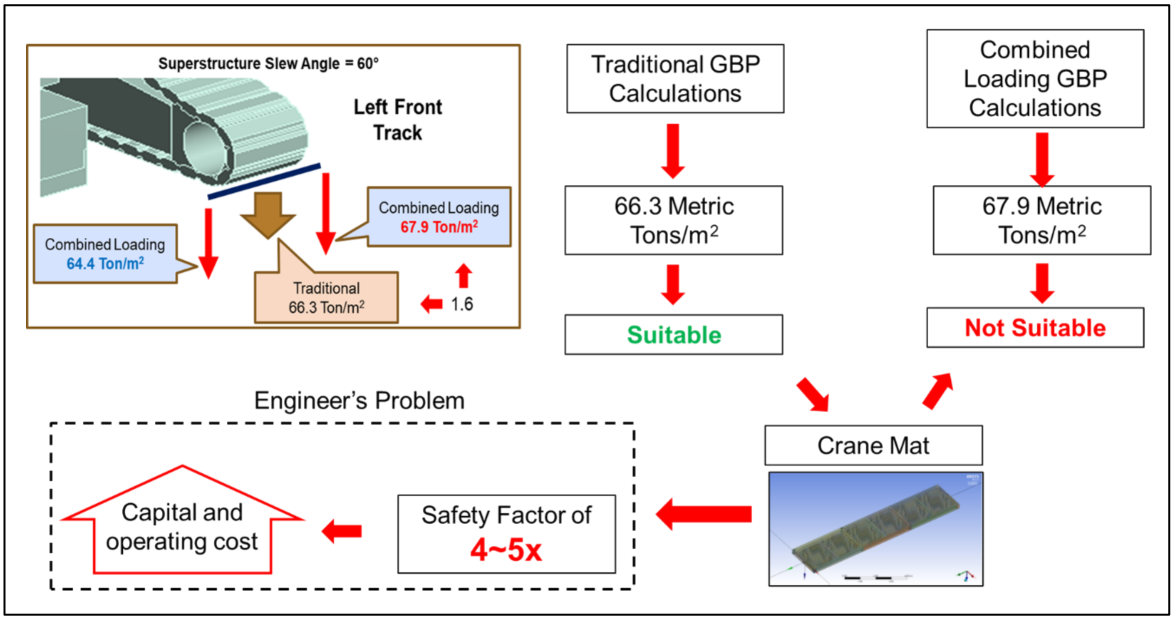

Figure 7.2: GBP variation and its impact on crane mat design

One of the significant sources of indirect CO_2 emissions in the crane mat lifecycle is transportation, both from the location where the timber is harvested to the manufacturing plant, and from the manufacturing plant to the crane yard. Equation (66), proposed by Whittaker et al. (2010), can be used to calculate the emissions associated with these transportation activities:

$$CO_2\ (transport) = 0.032 \times W_g \times (D_m + D_y) \tag{66}$$

where W_g = weight of the wood (metric tons), D_m = distance travelled from forest to manufacturing plant, and D_y = distance from manufacturing plant to the crane yard. Given that Coastal Douglas-Fir is readily available as a raw material in Canada, the average distance for the raw/finished product to travel is about 500 km $(D_m + D_y)$ (assumption), and the total CO_2 emissions is about 0.1225 metric tons.

Next we can calculate the indirect CO_2 emissions for one month of timber mat usage. As noted above, the maximum life span of a timber mat is three years, and if only timber mats are used on the construction site, they last for just eight months per year (Muhammad et al. 2021). Based on these constraints, the CO_2 emissions (metric tons) for one month can be calculated using Equation (67).

$$indirect\ CO_2 = \left(\frac{CO_2\ (Manufacturing) + CO_2\ (transport)}{8 \times 3}\right) \times\ n \tag{67}$$

where n = number of months for timber mat usage. According to this calculation, the indirect CO_2 emissions associated with the reduced crane mats (8) in the case project is about 0.237 metric tons. For direct CO_2 emissions, it is assumed that the crane yard is in Edmonton, Alberta, Canada, and the distance between Edmonton and Yellowknife is 1,452 km, meaning that the total travelling distance for the timber mats (round trip) is about 2,904 km. The direct CO_2 emissions is thus approximately 0.122 metric tons based on 1,452 km travelling distance and 7.657 metric tons (wood weight). Accordingly, the total monthly CO_2 emissions associated with the reduction in timber mats (8) for the case project is approximately 0.949 metric tons (indirect + direct CO_2 emissions) (see Table 7.1).

Table 7.1: CO_2 emissions calculations for 8 timber mats

	Description	8 Timber mats
1	Indirect CO_2 emissions	0.237 metric tons
2	Direct CO_2 emissions	0.712 metric tons
3	Total CO_2 emissions	0.949 metric tons

The calculations state that about 0.949 metric tons of CO_2 emissions can be saved if 8 timber mats are saved using the crane mat optimization approaches. It should be noted that, for the calculations for energy wastage, 1 metric ton of CO_2 emissions is assumed to be equal to 1,414.43 kWh or 112.53 gal of gasoline (EPA 2021). Accordingly, the 0.949 metric tons of CO_2 emissions (see Table 2) represents 1,342.30 kWh of energy saved, or 106.79 gal of gasoline. This shows that a reduction in crane mat usage is directly linked with a reduction in CO_2 emissions.

Furthermore, the developed application for determining the allowable soil bearing capacity can be applied to reduce the crane mat requirement as described above, and this reduction also serves to diminish the CO_2 emissions associated with crane mat use.

7.6. Executive summary

The theme of this research was to minimize crane mat wastage on a construction site and to improve the safety of construction workers working around heavy cranes by reassessing the ground support for mobile crane operation. The outcome of objective-1 can improve the stability of a mobile crane by removing the assumption of uniform GBP. This will help the practitioners to estimate the crane mat requirement without any significant safety factor, which can minimize crane mat wastage. The outcome of objective-2 can save the practitioner's time in preparing crane mat layout plans by using greedy, and RL approaches. This outcome, in the form of a computer application, can assist practitioners in estimating the crane mat requirement on a construction site without any assumption for unknown-unknown factors. The objective was to minimize the usage of crane mats on a construction site by optimizing the crane mat layout plans. The last objective will reduce the crane mat requirement for heavy cranes on a construction site by estimating the allowable soil bearing capacity by integrating mobile crane ground footings. The results show that allowable soil bearing capacity increases as the crane ground footing area increases.

7.7. Research Limitations

1) Ground bearing pressure under mobile cranes:
   a) Crane data of various mobile cranes are required.
   b) The non-linear optimization techniques were used to obtain the GBP values, which make the whole process complex.
2) Crane mat structural analysis:
   a) For the analysis, the crane mats were considered solid; in reality, they are flexible in nature.
   b) The soil is also considered rigid.
3) Crane mat layout optimization:
   a) One size of crane mat is used in the case examples.
   b) The greedy algorithm can be stuck at the local optimum.
   c) The RL approach takes each case as a separate environment without sharing any data.
   d) The layout planning is constrained to one layer of crane mats only.
4) Estimating allowable soil bearing capacity for crane work:
   a) The soil is considered linear in nature.
   b) One of the constraints was the non-availability of soil data.

7.8. Future Aspects

i. A computer application comprising all types of mobile cranes is required to be developed to estimate GBP under mobile cranes using a combined loading approach.

ii. Non-linear optimization needs to be investigated further to obtain the GBP values without trial and error and to make the GBP process user-friendly.
iii. The crane mat's structural stability needs to be integrated with the non-linear behaviour of soil under crane mats.
iv. For crane mat layout optimization, 2 or 3 layers of crane mat layout optimization are required to be investigated.
v. Various crane mat sizes can be integrated in the crane mat layout optimization process to make it further economical and environmentally friendly.
vi. The RL agent considers each case a separate environment without sharing data. Future work can investigate how the data can be shared from one case example to the next to minimize processing time.
vii. For allowable soil bearing capacity, the latest research should be incorporated to define the relationship between crane ground footing and allowable soil bearing capacity.
viii. For future validation, the use of FEA can be helpful. The FEA can further elaborate and portray the soil behaviour under the crane footing.

REFERENCES

Abdul Hamid, A.R., Azhari, R., Zakaria, R., Aminudin, E., Putra Jaya, R., Nagarajan, L., Yahya, K., Haron, Z., and Yunus, R. 2019. Causes of crane accidents at construction sites in Malaysia. *In* IOP Conference Series: Earth and Environmental Science, The 12th International Civil Engineering Post Graduate Conference (SEPKA), The 3rd International Symposium on Expertise of Engineering Design (ISEED). Johor, Malaysia. p. 11. doi:10.1088/1755-1315/220/1/012028.

Aikhuele, D. 2019. Evaluation of the root cause of failure in a crawler crane machine using hybrid MCDM model. Transactions of the Royal Institution of Naval Architects Part A: International Journal of Maritime Engineering, **161**(Part A3): 219–228. doi:10.3940/rina.ijme.2019.a3.523.

Al-Hussein, M., Alkass, S., and Moselhi, O. 2005. Optimization Algorithm for Selection and on Site Location of Mobile Cranes. Journal of Construction Engineering and Management, **131**(5). doi:10.1061/(ASCE)0733-9364(2005)131:5(579)).

Al-Hussein, M., Alkass, S., and Moselhi, O. 2011. D-CRANE: A database system for utilization of cranes. Canadian Journal of Civil Engineering, **27**: 1130–1138. doi:10.1139/cjce-27-6-1130.

Al-Hussein, M., Manrique, J.D., and Mah, D. 2009. North Ridge CO_2 analysis report: comparison between modular and on-site construction. University of Alberta: Edmontom, AB, Canada.

Ali, G.M. 2018. Competitive Analysis and Value Proposition of Frozen Silt Mats as an alternative to Crane Timber Mats. University of Alberta. https://doi.org/10.7939/R3BR8MZ12.

Ali, G.M., Al-Hussein, M., Bouferguene, A., and Kosa, J. 2019. Competitive finite element analysis (ANSYS) for the use of ice & frozen silt as a supporting structural material, an alternative to the traditional crawler crane mat material (S355, G40.21 & Coastal Douglas-fir). *In* CSCE Annual Conference Growing with youth – Croître avec les jeunes. CSCE, Laval, QC. p. 10.

American-Hoist. 1973. AH-9310 Lifting capacities. American Hoist 900 Series.

American-Hoist. 1979. AH-11320 Lift ratings. American Hoist 1100 Series.

American Wood Council. 2018. National Design Specification for wood construction. American Wood Council, Leesburg, VA. Available from https://awc.org/codes-standards/publications/nds-2018.

Apolinarska, A.A., Pacher, M., Li, H., Cote, N., Pastrana, R., Gramazio, F., and Kohler, M. 2021. Robotic assembly of timber joints using reinforcement learning. Automation in Construction, **125**: 103569. https://doi.org/10.1016/j.autcon.2021.103569.

Apostolos, F., Alexios, P., Georgios, P., Panagiotis, S., and George, C. 2013. Energy Efficiency of Manufacturing Processes: A Critical Review. Procedia CIRP, **7**: 628–633. https://doi.org/10.1016/j.procir.2013.06.044.

ASME. 2018. B30.5 Mobile and Locomotive Cranes. ASME.

Bach, F. 2017. Breaking the curse of dimensionality with convex neural networks. The Journal of Machine Learning Research, **18**(1): 629–681. JMLR. org. Available from https://www.jmlr.org/papers/volume18/14-546/14-546.pdf?ref=https://githubhelp.com.

Bang-Jensen, J., Gutin, G., and Yeo, A. 2004. When the greedy algorithm fails. Discrete Optimization, **1**(2): 121–127. https://doi.org/10.1016/j.disopt.2004.03.007.

Beavers, J., R. Moore, J., Rinehart, R., and R. Schriver, W. 2006. Crane-related fatalities in the construction industry. Journal of Construction Engineering and Management, **132**(9): 901–910. doi:10.1061/(ASCE)0733-9364(2006)132:9(901).

Becker, R. 2001. The great book of mobile and crawler cranes: Handbook of mobile and crawler crane technology, 2nd edition. René Hellmich, Griesheim, Germany.

Bellman, R. 1957. A Markovian Decision Process. Journal of Mathematics and Mechanics, **6**(4): 679–684.

Bergman, R., Puettmann, M., Taylor, A., and Skog, K.E. 2014. The Carbon Impacts of Wood Products. Forest Products Journal, **64**(7–8): 220–231. doi:10.13073/FPJ-D-14-00047.

Bird, R., and de Moor, O. 1993. From dynamic programming to greedy algorithms. *In* Formal Program Development: IFIP TC2/WG 2.1 State-of-the-Art Report. *Edited by* B. Möller, H. Partsch, and S. Schuman. Springer Berlin Heidelberg, Berlin, Heidelberg. pp. 43–61. doi:10.1007/3-540-57499-9_16.

Braden, B. 1986. The Surveyor's Area Formula. The College Mathematics Journal, **17**(4): 326–337. Mathematical Association of America. doi:10.2307/2686282.

Canadian Geotechnical Society Foundations Committee. 2006. Canadian foundation engineering manual. *In* 4th edition. Canadian Geotechnical Society.

Chen, H., and Sun, N. 2021. An Output Feedback Approach for Regulation of 5-DOF Offshore Cranes With Ship Yaw and Roll Perturbations. IEEE Transactions on Industrial Electronics,: 1. doi:10.1109/TIE.2021.3055159.

Cho, C.-S., Boafo, F., Byon, Y.-J., and Kim, H. 2017. Impact analysis of the new OSHA cranes and derricks regulations on crane operation safety. KSCE Journal of Civil Engineering, **21**(1): 54–66. doi:10.1007/s12205-016-0468-7.

Coduto, D.P. 2001. Foundation design: Principles and practices, 2nd ed. Prentice-Hall.

Cormen, T.H., Leiserson, C.E., Rivest, R.L., and Stein, C. 2009. Introduction to Algorithms, 3rd edition. MIT Press, Cambridge, MA.

Coulton, J.J. 1974. Lifting in early Greek architecture. The Journal of Hellenic Studies, **94**: 1–19. https://doi.org/10.2307/630416.

Deen, A.M.S.A., Ramesh, B.N., and Koshy, V. 2005. Collision Free Path Planning of Cooperative Crane Manipulators Using Genetic Algorithm. Journal of Computing in Civil Engineering, **19**(2): 182–193. doi:10.1061/(ASCE)0887-3801(2005)19:2(182).

Deisenroth, M.P., Neumann, G., and Peters, J. 2013. A survey on policy search for robotics. Foundations and trends in Robotics, **2**(1–2): 388–403.

Dhalmahapatra, K., Singh, K., Jain, Y., and Maiti, J. 2019. Exploring causes of crane accidents from incident reports using decision tree. *In* Information and Communication Technology for Intelligent Systems. Smart Innovation, Systems and Technologies. *Ed.* S.C. Satapathy and A. Joshi. Springer Singapore, Singapore. pp. 175–183. doi:10.1007/978-981-13-1742-2_18.

Di, W., Yuanshan, L., Xin, W., Xiukun, W., and Shunde, G. 2011. Algorithm of crane selection for heavy lifts. Journal of Computing in Civil Engineering, **25**(1): 57–65. doi:10.1061/(ASCE)CP.1943-5487.0000065.

Doran, J., and Michie, D. 1966. Experiments with the Graph Traverser Program. Proceedings of the Royal Society A: Mathematical, Physical and Engineering Sciences, **294**: 235–259. doi:10.1098/rspa.1966.0205.

Drud, A. 1985. CONOPT: A GRG code for large sparse dynamic nonlinear optimization problems. Mathematical Programming, **31**(2): 153–191. doi:10.1007/BF02591747.

Du, P., Liu, X., and Zhang, Y. 2017. Discussion of the Method to Determine the Ultimate Bearing Capacity of Soil Foundation. {IOP} Conference Series: Earth and Environmental Science, **100**: 12007. {IOP} Publishing. doi:10.1088/1755-1315/100/1/012007.

Duerr, D. 2010. Effective Bearing Length of Crane Mats. *In* Crane & Rigging Conference. 2DM Associates, Inc, Houston, TX. 8 pages.

Duerr, D., and Duerr, D. 2019. Mobile crane support handbook, 2nd edition. Industrial Training International.

EPA. 2021. Greenhouse Gases Equivalencies Calculator - Calculations and References. Available from https://www.epa.gov/energy/greenhouse-gases-equivalencies-calculator-calculations-and-references [accessed 4 September 2021].

Eslami, A., and Gholami, M. 2005. Bearing capacity analysis of shallow foundations from CPT data. *In* Proceedings of the 16th International Conference on Soil Mechanics and Geotechnical Engineering. IOS Press. pp. 1463–1466.

Fan, J., He, H., Hu, T., Li, G., Qin, L., and Zhou, Y. 2018. Rasterization Computing-Based Parallel Vector Polygon Overlay Analysis Algorithms Using OpenMP and MPI. IEEE Access, **6**: 21427–21441. doi:10.1109/ACCESS.2018.2825452.

Foster, E.L., Hormann, K., and Popa, R.T. 2019. Clipping simple polygons with degenerate intersections. Computers & Graphics: X, **2**: 100007. https://doi.org/10.1016/j.cagx.2019.100007.

Fylstra, D. 2019. Frontline’s history. Available from https://www.solver.com/frontline-systems-company-history#What-If Solver [accessed 30 October 2019].

Gamayunova, O., Radaev, A., Petrichenko, M., and Shushunova, N. 2019. Energy audit and energy efficiency of modular military towns. E3S Web of Conferences, **110**: 1088. doi:10.1051/e3sconf/201911001088.

Gaonkar, A., Arondekar, S., Mungarwadi, A., Gaude, P., Gaude, V., Haldankar, V., Sail, S., and Kudchadkar, A. 2021. Estimation of Ultimate Bearing Capacity of Soil for Shallow Foundation. *In* Recent Trends in Civil Engineering. *Edited by* B.B. Das, S. V Nanukuttan, A.K. Patnaik, and N.S. Panandikar. Springer Singapore, Singapore. pp. 305–316.

Garza-Reyes, J.A. 2015. Lean and green – a systematic review of the state of the art literature. Journal of Cleaner Production, **102**: 18–29. https://doi.org/10.1016/j.jclepro.2015.04.064.

Golden Environmental Mat Services, C. 2015. 2014 ACCESS MAT RESEARCH: PERSPECTIVES ABOUT THE INDUSTRY AND ASSET TRACKING CONCEPT. Calgary.

Government of Canada. 2018. Canada's greenhouse gas and air pollutant emissions projections. Gatineau, QC. Available from http://www.publications.gc.ca/site/eng/9.866115/publication.html.

Graham, S. 2019. Implementation of blockchain technology in the construction industry.

Greiner, G., and Hormann, K. 1998. Efficient Clipping of Arbitrary Polygons. ACM Trans. Graph., **17**(2): 71–83. Association for Computing Machinery, New York, NY, USA. doi:10.1145/274363.274364.

Grove. 2019. GMK Legacy Models Outrigger Pad Load Calculator. Available from https://www.manitowoccranes.com/en/Tools/lift-planning/Outrigger-Pad-Load-Calculators/All-Terrain [accessed 5 March 2020].

Gullapalli, V., and Barto, A.G. 1992. Shaping as a method for accelerating reinforcement learning. *In* Proceedings of the 1992 IEEE International Symposium on Intelligent Control. pp. 554–559. doi:10.1109/ISIC.1992.225046.

Gutin, G., Yeo, A., and Zverovich, A. 2002. Traveling Salesman Should not be Greedy: Domination Analysis of Greedy-Type Heuristics for the TSP. Discrete Applied Mathematics, **117**: 81–86. doi:10.1016/S0166-218X(01)00195-0.

Hally, D. 1986. Calculation of the moments of polygons. Applied Mathematics Notes. Available from https://apps.dtic.mil/sti/citations/ADA183444.

Han, S.H., Al-Hussein, M., Al-Jibouri, S., and Yu, H. 2012. Automated post-simulation visualization of modular building production assembly line. Automation in Construction, **21**: 229–236. https://doi.org/10.1016/j.autcon.2011.06.007.

Hansen, J.B. 1970. A revised and extended formula for bearing capacity. *In* Bulletin No. 28, Danish Geotechnical Institute, Copenhagen. Copenhagen. Available from https://trid.trb.org/view/125129.

Hasan, S., Al-Hussein, M., Hermann, U., and Safouhi, H. 2010. Interactive and dynamic integrated module for mobile cranes supporting system design. Journal of Construction Engineering and Management, **136**(2): 179–186. doi:10.1061/(ASCE)CO.1943-7862.0000121.

Hibbeler, R.C. 2011. Mechanics of Materials, 8th edition. Pearson Prentice Hall.

Hilgard, E.R., Marquis, D.G., and Kimble, G.A. 1961. Hilgard and Marquis' Conditioning and Learning. Appleton-Century-Crofts, Inc, East Norwalk, CT.

ISO. 2014. Mobile crane - determination of stability. ISO4305:2014. ISO, Geneva, Switzerland. Available from https://www.iso.org/standard/57220.html.

Jituri, S., Fleck, B., and Ahmad, R. 2018a. A methodology to satisfy key performance indicators for successful ERP implementation in small and medium enterprises. International Journal of Innovation, Management and Technology, **9**(2): 79–84. doi:10.18178/ijimt.2018.9.2.792.

Jituri, S., Fleck, B., and Ahmad, R. 2018b. Lean OR ERP – A Decision Support System to Satisfy Business Objectives. Procedia CIRP, **70**: 422–427. https://doi.org/10.1016/j.procir.2018.02.048.

Kiran, B.R., Sobh, I., Talpaert, V., Mannion, P., Al Sallab, A.A., Yogamani, S., and Pérez, P. 2021. Deep reinforcement learning for autonomous driving: A survey. IEEE Transactions on Intelligent Transportation Systems. IEEE.

Kormushev, P., Calinon, S., and Caldwell, D.G. 2013. Reinforcement Learning in Robotics: Applications and Real-World Challenges. Robotics, **2**(3): 122–148. doi:10.3390/robotics2030122.

Korte, B.H., Vygen, J., Korte, B., and Vygen, J. 2011. Combinatorial optimization. Springer.

Koskela, L., Bølviken, T., and Rooke, J. 2013. Which are the wastes of construction?

Lakshmanan, A., Elara Mohan, R., Ramalingam, B., Vu Le, A., Veerajagadeshwar, P., Tiwari, K., and Ilyas, M. 2020. Complete coverage path planning using reinforcement learning for Tetromino based cleaning and maintenance robot. Automation in Construction, **112**: 103078. https://doi.org/10.1016/j.autcon.2020.103078.

Kurinov, I., Orzechowski, G., Hämäläinen, P., and Mikkola, A. 2020. Automated Excavator Based on Reinforcement Learning and Multibody System Dynamics. IEEE Access, **8**: 213998–214006. doi:10.1109/ACCESS.2020.3040246.

Lei, Z., Taghaddos, H., Hermann, U., and Al-Hussein, M. 2013. A methodology for mobile crane lift path checking in heavy industrial projects. Automation in Construction, **31**: 41–53. https://doi.org/10.1016/j.autcon.2012.11.042.

Liftinglogistics.com. 2016. Ground bearing pressure & mat strength analysis. Available from Liftinglogistics.com.

Lillicrap, T.P., Hunt, J.J., Pritzel, A., Heess, N., Erez, T., Tassa, Y., Silver, D., and Wierstra, D. 2015. Continuous control with deep reinforcement learning. arXiv preprint arXiv:1509.02971.

Lim, C., Cho, S., Lee, Y.C., and Choi, J. 2005. Basic construction of intelligent expert system for riser design using database system and optimisation tools. International Journal of Cast Metals Research, **18**: 195–201. doi:10.1179/136404605225022937.

Lin, M., Duong, N., Deng, L., Hermann, U., Zubick, T., Lei, Z., and Adeeb, S. 2017. An Investigation of the Distribution of Mobile Crane loads for construction projects. *In* CSCE Leadership in Sustainable Infrastructure.

Liu, H., Sydora, C., Sadiq Altaf, M., Han, S., and Al-Hussein, M. 2019. Towards sustainable construction: BIM-enabled design and planning of roof sheathing installation for prefabricated buildings. Journal of Cleaner Production, 235, 1189–1201. doi:10.1016/j.jclepro.2019.07.055.

Madireddy, M., Medeiros, D.J., and Kumara, S. 2011. An agent based model for evacuation traffic management. *In* Proceedings of the 2011 Winter Simulation Conference (WSC). pp. 222–233. doi:10.1109/WSC.2011.6147753.

Mahamid, M., Brindley, T., Triandafilou, N., and Domagala, S. 2017. Behavior and Strength Characteristics of Cross-Laminated Timber Mats: Experimental and Numerical Study. *In* Structures Congress 2017. pp. 254–268. doi:10.1061/9780784480427.022.

Mahamid, M., and Torra-Bilal, I. 2019. Analysis and Design of Cross-Laminated Timber Mats. Practice Periodical on Structural Design and Construction, **24**(1): 4018031. doi:10.1061/(ASCE)SC.1943-5576.0000390.

Manitowoc. 2019. Ground Bearing Pressure Estimator.

Manitowoc. 2020. GMK7550. Available from https://www.manitowoc.com/grove/all-terrain-cranes/gmk7550.

Mazyavkina, N., Sviridov, S., Ivanov, S., and Burnaev, E. 2021. Reinforcement learning for combinatorial optimization: A survey. Computers & Operations Research, **134**: 105400. https://doi.org/10.1016/j.cor.2021.105400.

Mehr, E. 2019. Using Reinforcement Learning to Design a Better Rocket Engine. Available from https://blog.insightdatascience.com/using-reinforcement-learning-to-design-a-better-rocket-engine-4dfd1770497a [accessed 30 December 2021].

Meyerhof, G.G. 1956. Penetration tests and bearing capacity of cohesionless soil. Journal of the Soil Mechanics and Foundations Division, **82**(1): paper no. 866 doi:10.1061/JSFEAQ.0000001.

Meyerhof, G.G. 1963. Some Recent Research on the Bearing Capacity of Foundations. Canadian Geotechnical Journal, **1**(1): 16–26. doi:10.1139/t63-003.

Milazzo, M.F., Ancione, G., Spasojević-Brkić, V., and Valis, D. 2016. Investigation of crane operation safety by analysing main accident causes.

Muhammad, A.G., Joe, K., Ahmed, B., and Mohamed, A.-H. 2021. Competitive Assessment of Ice and Frozen Silt Mat for Crane Ground Support Using Finite-Element Analysis. Journal of Construction Engineering and Management, **147**(6): 4021038. doi:10.1061/(ASCE)CO.1943-7862.0002046.

CSA Group. 2019. CSA 086:19, Engineering design in wood. Canadian Standard Association. Available from https://www.csagroup.org/store/product/CSA O86%3A19/.

Nourinejad, M., and Roorda, M.J. 2016. Agent based model for dynamic ridesharing. Transportation Research Part C: Emerging Technologies, **64**: 117–132. https://doi.org/10.1016/j.trc.2015.07.016.

Onyelowe, K.C. 2017. Mathematical advances in soil bearing capacity. Electronic Journal of Geotechnical Engineering, **22**(12): 4735–4743.

Ortiz, J.M.R., Mazo, C.O., Gesta, J.S., and de Arquitectos de Madrid, C.O. 1986. Curso aplicado de cimentaciones, 3rd edition. Colegio Oficial de Arquitectos de Madrid. Available from https://books.google.ca/books?id=10rVSgAACAAJ.

van Otterlo, M., and Wiering, M. 2012. Reinforcement Learning and Markov Decision Processes. *In* Reinforcement Learning: State-of-the-Art. *Edited by* M. Wiering and M. van Otterlo. Springer Berlin Heidelberg, Berlin, Heidelberg. pp. 3–42. doi:10.1007/978-3-642-27645-3_1.

Mitropoulos, P., and Tatum, .C.B. 1999. Technology Adoption Decisions in Construction Organizations. Journal of Construction Engineering and Management, **125**(5): 330–338. doi:10.1061/(ASCE)0733-9364(1999)125:5(330).

Patwardhan, K., and Metya, S. 2021. A Comparative Study on Commonly Used Methods for Calculating Bearing Capacity in Shallow Foundation. Advances in Sustainable Construction Materials: Select Proceedings of ASCM 2020, **124**: 167. Springer Nature. doi:10.1007/978-981-33-4590-4_17.

Paulus, R., Xiong, C., and Socher, R. 2017. A deep reinforced model for abstractive summarization. arXiv preprint arXiv:1705.04304.

Sivakumar, P.L., Varghese, K., and Babu, N.R. 2003. Automated Path Planning of Cooperative Crane Lifts Using Heuristic Search. Journal of Computing in Civil Engineering, **17**(3): 197–207. doi:10.1061/(ASCE)0887-3801(2003)17:3(197).

Polydoros, A.S., and Nalpantidis, L. 2017. Survey of Model-Based Reinforcement Learning: Applications on Robotics. Journal of Intelligent & Robotic Systems, **86**(2): 153–173. doi:10.1007/s10846-017-0468-y.

Ralph B. Peck, Hanson, W.E., and Thornburn, T.H. 1974. Foundation engineering, 2nd edition.

Wiley, New York, NY.

Raviv, G., and Shapira, A. 2018. Systematic approach to crane-related near-miss analysis in the construction industry. International Journal of Construction Management, **18**(4): 310–320. Taylor & Francis. doi:10.1080/15623599.2017.1382067.

Reddy, H.R., and Varghese, K. 2002. Automated Path Planning for Mobile Crane Lifts. Computer-Aided Civil and Infrastructure Engineering, **17**(6): 439–448. doi:10.1111/0885-9507.00005.

Sartoretti, G., Wu, Y., Paivine, W., Kumar, T.K.S., Koenig, S., and Choset, H. 2019. Distributed Reinforcement Learning for Multi-robot Decentralized Collective Construction. *In* Distributed Autonomous Robotic Systems. *Edited by* N. Correll, M. Schwager, and M. Otte. Springer International Publishing, Cham. pp. 35–49.

Shapiro, J., and Shapiro, L. 2010. Cranes and Derricks. *In* 4th edition. McGraw-Hill Professional. doi:10.1036/9780071625586.

SImetric.co.uk. 2011. Wood - seasoned & dry. Available from https://www.simetric.co.uk/si_wood.htm [accessed 4 September 2021].

Simmons, B.I., Hoeppke, C., and Sutherland, W.J. 2019. Beware greedy algorithms. Journal of Animal Ecology, **88**(5): 804–807. https://doi.org/10.1111/1365-2656.12963.

Smeers, Y. 1977. Generalized reduced gradient method as an extension of feasible direction methods. Journal of Optimization Theory and Applications, **22**(2): 209–226. doi:10.1007/BF00933163.

Soman, R.K., and Molina-Solana, M. 2022. Automating look-ahead schedule generation for construction using linked-data based constraint checking and reinforcement learning. Automation in Construction, **134**: 104069. https://doi.org/10.1016/j.autcon.2021.104069.

Stueland, S. 1994. The Otis steam excavator. Technology and culture, **35**(3): 571. Wayne State University Press, Detroit, MI.

Sutton, R.S. 1988. Learning to Predict by the Method of Temporal Differences. Machine Learning, **3**: 9–44. doi:10.1007/BF00115009.

Sutton, R.S. 1996. Generalization in reinforcement learning: Successful examples using sparse coarse coding. Advances in neural information processing systems,: 1038–1044. Citeseer.

Sutton, R.S., and Barto, A.G. 2018. Reinforcement learning: An introduction, 2nd edition. MIT Press, Cambridge, MA.

Taghaddos, H., Hermann, U., and Abbasi, A. 2018. Automated Crane Planning and Optimization for modular construction. Automation in Construction, **95**: 219–232. https://doi.org/10.1016/j.autcon.2018.07.009.

Tahmid, A., Junaed, S., and Hossain, A.S.M.F. 2021. A Comparative Study of Measuring Soil Bearing Capacity for Shallow Foundations Using Analytic Approaches and Empirical Formulas with SPT at Various Locations of Dhaka City. Journal of Remote Sensing, Environmental Science & Geotechnical Engineering, **6**(2): 23–32.

Tam, C., K. L. Tong, T., and K. W. Chan, W. 2001. Genetic Algorithm for Optimizing Supply Locations around Tower Crane. Journal of Construction Engineering and Management, **127**(4): 315–321. doi:10.1061/(ASCE)0733-9364(2001)127:4(315).

Terzaghi, K. 1943. Theoretical Soil Mechanics. John Wiley. doi:10.1002/9780470172766.

The Canadian Press. 2014. Canada's greenhouse gas emissions. Available from https://www.cbc.ca/news/politics/canada-s-greenhouse-gas-emissions-1.2791282 [accessed 2 September 2021].

The International Organization for Standarization. 2014. ISO 4305 - Mobile Cranes - Determination of Stability, Third Edition. Geneva, Switzerland.

Truss Plate Institute of Canada. 2019. Truss design procedure and specifications for light metal plate connected wood trusses. Truss Plate Institute of Canada, Markham, ON, Canada. Available from https://tpic.ca/wp-content/uploads/2019/06/tpic_2019.pdf.

Union of Concerned Scientists. 2020. Each Country's Share of CO_2 Emissions. Available from https://www.ucsusa.org/resources/each-countrys-share-co2-emissions [accessed 2 September 2021].

Vesic, A.S. 1975. Bearing Capacity of Shallow Foundations. *In* Foundation Engineering Handbook, 1st edition. Van Nostrand Reinhold, New York, New York, N.Y. pp. 121–147.

Wang, Y.H., Li, T.H.S., and Lin, C.J. 2013. Backward Q-learning: The combination of Sarsa algorithm and Q-learning. Engineering Applications of Artificial Intelligence, **26**(9): 2184–

2193. Pergamon. doi:10.1016/J.ENGAPPAI.2013.06.016.

Watkins, C. 1989. Learning From Delayed Rewards. Doctoral dissertation, King's College, Cambridge, UK.

Watkins, C., and Dayan, P. 1992. Technical Note: Q-Learning. Machine Learning, **8**: 279–292. doi:10.1007/BF00992698.

Waxenegger-Wilfing, G., Dresia, K., Deeken, J.C., and Oschwald, M. 2020. A reinforcement learning approach for transient control of liquid rocket engines. arXiv preprint arXiv:2006.11108. Available from https://arxiv.org/pdf/2006.11108.pdf.

Whittaker, C.L., Mortimer, N.D., and Matthews, R.W. 2010. Understanding the carbon footprint of timber transport in the united kingdom. *In* North Energy Associates Limited and Forest Research for the Confederation of Forest Industries (UK) Ltd on behalf of the Timber Transport Forum.

Wiering, M.A., and Van Hasselt, H. 2008. Ensemble algorithms in reinforcement learning. IEEE Transactions on Systems, Man, and Cybernetics, Part B (Cybernetics), **38**(4): 930–936. IEEE. https://doi.org/10.1109/TSMCB.2008.920231.

Wolfe, P. 1963. Methods of nonlinear programming. *In* Recent Advances in Mathematical Programming. McGraw-Hill, New York, NY, USA.

Yokoi, H. 1968. Relationship between soil cohesion and shear strength. Soil Science and Plant Nutrition, **14**(3): 89–93. Taylor & Francis. doi:10.1080/00380768.1968.10432750.

Yu, C., Liu, J., Nemati, S., and Yin, G. 2021. Reinforcement learning in healthcare: A survey. ACM Computing Surveys (CSUR), **55**(1): 1–36. ACM New York, NY.

Zelentsov, L., Mailyan, L., and Pirko, D. 2021. Methodology of making organizational and technological decisions at the stage of operational management of construction operations based on the forecasting system. Journal of Physics: Conference Series, **2131**(2): 22114. {IOP} Publishing. doi:10.1088/1742-6596/2131/2/022114.

Zhao, K., Jin, B., Fan, H., and Yang, M. 2020. A Data Allocation Strategy for Geocomputation Based on Shape Complexity in a Cloud Environment using Parallel Overlay Analysis of Polygons as an Example. IEEE Access, **8**: 185981–185991.

doi:10.1109/ACCESS.2020.3030700.

Appendix A - FEA and 8-point manual difference from the 4-point GBP values

Crane		8-point vs. 4-point (metric ton/m^2)							FEA vs. 4-point (metric ton/m^2)						
		0	30	60	90	120	150	180	0	30	60	90	120	150	180
	P1	0.0	0.4	0.7	0.8	0.7	0.4	0.0	0.1	0.5	0.7	0.8	0.6	0.3	−0.1
	P2	0.0	−0.4	−0.8	−0.9	−0.8	−0.4	0.0	0.1	−0.4	−0.8	−0.9	−0.9	−0.5	−0.1
	P3	0.0	0.4	0.7	0.8	0.7	0.4	0.0	0.0	0.4	0.8	0.9	0.8	0.5	0.0
18000	P4	0.0	−0.4	−0.8	−0.9	−0.8	−0.4	0.0	0.0	−0.4	−0.7	−0.8	−0.7	−0.4	0.0
(Case 1)	P5	0.0	0.4	0.8	0.9	0.8	0.4	0.0	0.0	0.4	0.7	0.8	0.7	0.4	0.0
	P6	0.0	−0.4	−0.7	−0.8	−0.7	−0.4	0.0	0.0	−0.4	−0.8	−0.9	−0.8	−0.5	0.0
	P7	0.0	0.4	0.8	0.9	0.8	0.4	0.0	−0.1	0.4	0.8	0.9	0.9	0.5	0.1
	P8	0.0	−0.4	−0.7	−0.8	−0.7	−0.4	0.0	−0.1	−0.4	−0.7	−0.8	−0.6	−0.3	0.1
	P1	0.0	1.3	1.7	2.0	1.7	0.3	0.0	0.1	1.3	1.7	1.9	1.6	0.3	0.0
	P2	0.0	−0.8	−1.9	−2.2	−1.9	−1.9	0.0	0.1	−0.8	−1.9	−2.2	−2.0	−1.8	0.0
	P3	0.0	0.7	1.7	2.0	1.7	1.8	3.1	0.0	0.8	1.8	2.1	1.8	1.8	3.2
18000	P4	0.0	−1.4	−1.9	−2.2	−1.9	−0.4	3.1	0.0	−1.4	−1.8	−2.0	−1.8	−0.4	3.2
(Case 2)	P5	0.0	−0.6	1.9	2.2	1.9	0.0	0.0	0.0	−0.6	1.8	2.0	1.8	0.0	0.0
	P6	0.0	−2.7	−1.7	−2.0	−1.7	0.0	0.0	0.0	−2.7	−1.8	−2.1	−1.8	0.0	0.0
	P7	0.0	0.0	1.9	2.2	1.9	1.4	3.1	0.0	0.0	1.9	2.2	2.0	1.4	3.1
	P8	0.0	0.0	−1.7	−2.0	−1.7	−0.7	3.1	0.0	0.0	−1.7	−1.9	−1.6	−0.7	3.1
	P1	0.0	0.1	0.2	0.2	0.2	0.1	0.0	0.0	0.1	0.2	0.2	0.2	0.1	0.1
	P2	0.0	−0.1	−0.2	−0.2	−0.2	−0.1	0.0	0.0	−0.1	−0.1	−0.2	−0.1	−0.1	0.1
	P3	0.0	0.1	0.2	0.2	0.2	0.1	0.0	0.1	0.1	0.2	0.2	0.2	0.1	0.0
AH-11320	P4	0.0	0.0	−0.1	−0.1	−0.1	−0.1	0.0	0.1	−0.1	−0.1	−0.2	−0.1	−0.1	0.0
(Case 1)	P5	0.0	0.1	0.2	0.2	0.2	0.1	0.1	0.0	0.1	0.2	0.3	0.2	0.2	0.1
	P6	0.0	−0.1	−0.1	−0.2	−0.1	0.0	0.1	0.0	0.0	−0.1	−0.1	−0.1	0.0	0.1
	P7	0.0	0.2	0.2	0.3	0.2	0.2	0.0	0.1	0.2	0.2	0.3	0.2	0.1	0.0
	P8	0.0	0.0	−0.1	−0.1	−0.1	0.0	0.0	0.1	0.0	−0.1	−0.1	−0.1	0.0	0.0
	P1	0.0	1.2	1.2	1.4	1.3	0.4	0.0	−0.1	1.1	1.1	1.3	1.2	0.3	0.0
	P2	0.0	−0.4	−1.5	−1.7	−1.4	−1.3	0.0	−0.1	−0.5	−1.6	−1.7	−1.5	−1.3	0.0
	P3	0.0	0.4	1.3	1.4	1.2	1.2	0.0	0.0	0.3	1.2	1.3	1.1	1.1	−0.1
AH-11320	P4	0.0	−1.3	−1.4	−1.7	−1.5	−0.4	0.0	0.0	−1.3	−1.5	−1.8	−1.6	−0.5	−0.1
(Case 2)	P5	0.0	1.0	1.5	1.7	1.5	0.0	0.0	−0.1	0.9	1.4	1.6	1.4	0.0	0.0
	P6	0.0	−0.6	−1.2	−1.4	−0.8	0.0	0.0	−0.1	−0.7	−1.2	−1.4	−0.8	0.0	0.0
	P7	0.0	0.0	1.5	1.7	1.5	1.0	0.0	0.0	0.0	1.4	1.6	1.5	0.9	−0.1
	P8	0.0	0.0	−0.8	−1.4	−1.2	−0.6	0.0	0.0	0.0	−0.8	−1.5	−1.2	−0.6	−0.1

Appendix B – Algorithm for GBP under hydraulic crane mats

Algorithm 1: Calculations for GBP under hydraulic crane mats.

Inputs:

$\{W_l, W_s, W_c\} \leftarrow$ Weight of payload and crane parts

$\{d_l, d_s, d_c\} \leftarrow$ Horizontal distance of payload and crane parts' COG to the crane rotational axis

$\{\theta_s\ \theta_c\} \leftarrow$ Angle between the crane parts' COG and the X-Axis

$\{w_{m,} l_m\} \leftarrow$ Width, length of crane mat

$\{C_1, C_2\} \leftarrow$ Offset distance for the right and left rear outrigger from the crane rotational axis

$\{B_c, L_c\} \leftarrow$ Outrigger distance from the center, distance between outriggers lengthwise (center to center)

$\{U_{limit}, L_{limit}\} \leftarrow$ upper tolerance limit, lower tolerance limit

Initialization:

$\theta_l \leftarrow \{0°, \cdots, 360°\} \in \mathbb{R}$, Payload slew angle (lifting radius)

$P_i(x_i, y_i) \leftarrow$ calculate crane mat corners, $x_i, y_i \in \mathbb{R}$, $i \in [1,16]$

$A_o \leftarrow$ calculate area of crane mats calculations using $P_i(x_i, y_i)$

$\{I_{xx}, I_{yy}, I_{yy}\} \leftarrow$ calculate using Equations (9), (10) and (11), $I_{xx}, I_{yy}, I_{yy} \in \mathbb{R}$

$P'_i(x'_i, y'_i) \leftarrow$ calculate using centroid of $A_o$as the origin for cartesian coordinates

$\{I_{x'x'}, I_{y'y'}, I_{x'y'}\} \leftarrow$ calculate using Equations (9), (10) and (11) using $P'_i(x'_i, y'_i)$,

$\beta \leftarrow$ calculate using Equation (12)

$P_i(x_i, y_i) \leftarrow P''_i(x''_i, y''_i) \leftarrow$ calculate updated $P'_i(x'_i, y'_i)$ using β as the cartesian coordinates rotation

$\{I_{xx}, I_{yy}, I_{yy}\} \leftarrow \{I_{x''x''}, I_{y''y''}, I_{x''y''}\} \leftarrow$ calculate using Equations (9), (10) and (11) using $P''_i(x''_i, y''_i)$

For $\theta_l \leftarrow$ 0°to 360° **DO**
- $\sigma_i \leftarrow$ GBP at crane mat corners, calculate using Equation (8), $\sigma_i \in \mathbb{R}$, $i \in [1,16]$
- **IF** $\sigma_i < 0$ **THEN**
  - **WHILE** [$\sigma_N \leq L_{limit}$ **OR** $\sigma_N \geq U_{limit}$] **DO**
    - $\{N_1(N_{1x}, N_{1y}), N_2(N_{2x}, N_{2y})\} \leftarrow$ calculate neutral axis coordinates, $\{N_{1x}, N_{1y}, N_{2x}, N_{2y}\} \in \mathbb{R}$
    - $\{\text{factor}_a, \text{factor}_b\} \leftarrow$ calculate polygon clipping factors, $\{\text{factor}_a, \text{factor}_b\} \in \mathbb{R}$
    - $A'_0 \leftarrow$ calculate area of crane mats after polygon clipping
    - $P'_i(x'_i, y'_i) \leftarrow$ calculate using updated centroid of A'_0
    - $\{I_{x'x'}, I_{y'y'}, I_{x'y'}\} \leftarrow$ calculate using Equations (9), (10) and (11) using $P'_i(x'_i, y'_i)$,
    - $\beta \leftarrow$ calculate using Equation (12)
    - $P''_i(x''_i, y''_i) \leftarrow$ calculate updated $P'_i(x'_i, y'_i)$ using β
    - $\{I_{x''x''}, I_{y''y''}, I_{x''y''}\} \leftarrow$ calculate using Equations (9), (10) and (11) using $P''_i(x''_i, y''_i)$
    - $\sigma_i \leftarrow \sigma'_i \leftarrow$ calculate Equation (8) using A'_0, $P''_i(x''_i, y''_i)$ and $\{I_{x''x''}, I_{y''y''}, I_{x''y''}\}$
    - $\sigma_N \leftarrow$ Equation (8) at neutral axis, $\sigma_N \in \mathbb{R}$, $N \in \{1,2\}$
    - $P_i(x_i, y_i) \leftarrow P''_i(x''_i, y''_i)$
  - **END LOOP**
- **END IF**

END LOOP

Return: $\sigma_{i\theta_l} \leftarrow \sigma_i$ along θ_l, $\sigma_{i\theta} \in \mathbb{R}$, $i \in [1,16]$, $\theta_l \in [0,360]$

Appendix C – For the payload of 35,000 kg, 16-point and FEA GBP values difference from traditional GBP values (metric tons/m^2)

	Crane Superstructure Slew Angle (°)							
	16-point GBP values vs. traditional GBP values				FEA GBP calculations vs. traditional GBP values			
	0	30	60	90	0	30	60	90
P1	0.72	0.90	0.82	0.52	0.56	0.72	0.64	0.35
P2	−0.95	−0.57	−0.05	0.48	−1.07	−0.73	−0.22	0.31
P3	−0.99	−1.18	−1.06	−0.66	−1.12	−1.32	−1.20	−0.80
P4	0.67	0.29	−0.18	−0.62	0.52	0.13	−0.34	−0.76
P5	0.99	1.14	0.99	0.58	0.99	1.14	0.99	0.58
P6	−0.67	−0.33	0.12	0.55	−0.67	−0.33	0.11	0.54
P7	−0.72	−0.94	−0.89	−0.59	−0.71	−0.93	−0.89	−0.59
P8	0.95	0.53	−0.01	−0.55	0.95	0.54	−0.01	−0.55
P9	0.76	0.97	0.93	0.64	0.77	0.99	0.95	0.66
P10	−0.91	−0.50	0.05	0.60	−0.89	−0.48	0.07	0.62
P11	−0.95	−1.11	−0.96	−0.54	−0.93	−1.08	−0.93	−0.50
P12	0.71	0.36	−0.08	−0.50	0.73	0.39	−0.05	−0.47
P13	0.93	1.13	1.00	0.59	0.94	1.14	1.02	0.60
P14	−0.74	−0.35	0.12	0.55	−0.72	−0.33	0.14	0.56
P15	−0.78	−0.96	−0.89	−0.59	−0.76	−0.93	−0.86	−0.56
P16	0.88	0.52	−0.01	−0.55	0.90	0.54	0.02	−0.52

Appendix D – Algorithm for Hydraulic crane mat strength calculations

Algorithm 2: Hydraulic crane mat strength calculations.

Inputs:

$\{Allowable\ Soil\ Bearing\ Capacity\} \leftarrow$ Allowable soil bearing capacity
$\{w_m, l_m, O_s\} \leftarrow$ width, length of crane mat and width/length of outrigger
$\{n, d_p\} \leftarrow$ Number of cranes mats stacked one over other, thickness of the crane mat
$\{K_D, C_t, K_T, K_H, K_{Sb}, K_{Sc}, K_Z, \emptyset_{bv}, \emptyset_c\} \leftarrow$ Wood external design factors
$\{f_b, f_v, L_{def}, f_{cp}\} \leftarrow$ Mat strength design parameters (Section 2.2)

Initialization:

$\sigma_{max} \leftarrow$ retrieve maximum GBP under hydraulic crane outrigger mats **(Algorithm-1)**
$\{L_m, L_{min}, L_{eff}\} \leftarrow \{0, \cdots, 40\} \in \mathbb{R}$, variable, minimum, and effective length of crane mat
$\{L_{min}, L_{eff}\} \leftarrow \{40, 0\}$
$\{UC_{gbp}, UC_{bend}, UC_{shear}, UC_{def}, UC_{comp}\} \leftarrow [0,1], \in \mathbb{R}$

For $L_m \leftarrow$ 0 to 40 **DO**
  $l_m \leftarrow L_m$ replace for Equation-15, 16, 17, 18 & 19
  $\{UC_{gbp}, UC_{bend}, UC_{shear}, UC_{def}, UC_{comp}\} \leftarrow$ Calculate using Equation-15, 16, 17, 18 & 19
  IF $L_{min} = 0$ **AND** $[UC_{gbp}$ **OR** UC_{bend} **OR** UC_{shear} **OR** UC_{def} **OR** $UC_{comp}]=1$ **THEN**
    $L_{min} \leftarrow L_m$
  END IF
  IF $L_{max} = 40$ **AND** $[UC_{gbp}$ **OR** UC_{bend} **OR** UC_{shear} **OR** UC_{def} **OR** $UC_{comp}]=1$ **THEN**
    $L_{max} \leftarrow L_m$
  END IF
  Return: $\{UC_{gbp}, UC_{bend}, UC_{shear}, UC_{def}, UC_{comp}\}$ along L_m, graphical representation
END LOOP
For $l_m \leftarrow O_s, L_{min}, L_{eff}, l_m$ **DO**
  $\{UC_{gbp}, UC_{bend}, UC_{shear}, UC_{def}, UC_{comp}\} \leftarrow$ Calculate using Equation-15, 16, 17, 18 & 19
  IF UC_{comp} at $O_s = 1$ **THEN**
    Return: {"*Crane mat not Suitable, Compression*"}
  ELSE
    IF $L_{min} > l_m$ **OR** $L_{min} = 0$ **THEN**
      Return: {"*Crane mat not Suitable, GBP*"}
    ELSE
      IF $L_{eff} < L_{min}$ **THEN**
        IF $[UC_{bend}\ at\ L_{eff}] = 1$ **THEN**
          Return: {"*Crane mat not Suitable, Bending*"}
        ELSE IF $[UC_{shear}\ at\ L_{eff}] = 1$ **THEN**
          Return: {"*Crane mat not Suitable, Shear*"}
        ELSE IF $[UC_{def}\ at\ L_{eff}] = 1$ **THEN**
          Return: {"*Crane mat not Suitable, deflection*"}
        END IF
      ELSE
        Return: {"*Crane mat Suitable*"}
      END IF
    END IF
  END IF
  Return: $\{UC_{gbp}, UC_{bend}, UC_{shear}, UC_{def}, UC_{comp}\}$
END LOOP

Appendix E – Algorithm for crane mat optimization using Greedy Approach

Algorithm 3: Crane Mat optimization using Greedy approach.

Inputs:

$\{M_i(x_{ij}, y_{ij})\} \leftarrow$ Mat coordinates (8 options), $x_i, y_i \in \mathbb{R}$, $i \in [1,8], j \in [1,8]$
$\{Mat_l\} \leftarrow$ Mat drawings (8 options) for mat placement, $l=i \in [1,8]$
$\{P_n(x_n, y_n)\} \leftarrow$ Polygon coordinates (area required) with *n* vertices, $x_n, y_n \in \mathbb{R}$, $n \in [3, \mathbb{R}]$
$\{R_k(x_k, y_k)\} \leftarrow$ Starting polygon vertex for Mat laying, $x_k, y_k \in \mathbb{R}$, $k \in [1,2]$

Initialization:

$\{O_m(x_m, y_m), f_m\} \leftarrow$ Location for mat placement, $x_m, y_m \in \mathbb{R}$, $f_m \in$ ["$Accept$", "$Reject$"], $m=0$
$AM \leftarrow$ calculate area of mat using $M_1(x_{1j}, y_{1j})$
$\{O_m(x_m, y_m), f_m\} \leftarrow$ Update with $R_1(x_1, y_1)$, as first mat placement location, $m=1$, with $f_m =$ "$Accept$"
$\{Area_o, DC_o\} \leftarrow \{0, \infty\} \leftarrow$ Area covered & distance of mat centroid from $R_k(x_k, y_k)$
For $r \leftarrow$ 1 to 8 **DO**
  $A_o \leftarrow$ Generate polygon region
  $M'_i(x'_{ij}, y'_{ij}) \leftarrow$ calculate using $O_1(x_1, y_1)$, as mat placed at the available location, $i = r$
  $A_i \leftarrow$ Generate mat region using $M'_i(x'_{ij}, y'_{ij})$, $i = r$
  $A'_o \leftarrow A_o \cap A_i$
  $d_i \leftarrow$ Calculate distance between centroid of $M'_i(x'_{ij}, y'_{ij})$ and $R_k(x_k, y_k)$, $i = r$
  IF $d_i < DC_o$ **AND** $area\{A'_o\} > Area_o$ **THEN**
    $\{AC_o, AR_o, final_r\} \leftarrow \{A'_o, A_o \setminus A'_o, r\}$
    $\{DC_o, Area_o\} \leftarrow \{d_i, area\{A'_o\}\}$
    $\{O_m(x_m, y_m), f_m\} \leftarrow$ Update by adding $M'_i(x'_{ij}, y'_{ij})$, $m=m+j$, $f_m =$ "$Accept$" for added locations
  END LOOP
END LOOP
$MAT_k \leftarrow$ Place mat Mat_l using $M'_i(x'_{ij}, y'_{ij})$, where $l=final_r$, at $O_1(x_1, y_1)$, $k=1$
WHILE $area\{AR_o\} \leq (AM/2)$ **DO**
  $\{Area_o, DC_o, k\} \leftarrow \{0, \infty, k = k+1\} \leftarrow$ Area covered, mat centroid from $R_k(x_k, y_k)$
  For $s \leftarrow$ 1 to m **DO**
    IF $f_s =$ "$Accept$" **THEN**
      For $t \leftarrow$ 1 to 8 **DO**
        $M'_i(x'_{ij}, y'_{ij}) \leftarrow$ calculate using $O_s(x_s, y_s)$, $i = t$, mat placed at the available location
        $A_i \leftarrow$ Generate mat region using $M'_t(x'_{tj}, y'_{tj})$, $i = t$
        IF $area\{AC_o \cap A_i\} \approx 0$ **THEN**
          $\{AC'_o, AR'_o\} \leftarrow \{AC_o \cup A_i, AR_o \setminus A_i\}$
          $d_i \leftarrow$ Calculate distance between centroid of $M'_i(x'_{ij}, y'_{ij})$ and $R_k(x_k, y_k)$, $i = t$
          IF $d_t < DC_o$ **AND** $area\{AC'_o\} > Area_o$ **THEN**
            $\{AC''_o, DC_o, Area_o, AR''_o, M''_t(x''_{tj}, y''_{tj})\} \leftarrow \{AC'_o, d_t, area\{A'_o\}, AR'_o, M'_t(x'_{tj}, y'_{tj})\}$
            $\{O_f(x_f, y_f), final_r\} \leftarrow \{O_s(x_s, y_s), t\}$
          END IF
        ELSE
          $f_s =$ "$Reject$"
        END IF
      END LOOP
    END IF
  END LOOP
  $\{AC_o, AR_o\} \leftarrow \{AC'_o, AR'_o\}$
  $\{O_m(x_m, y_m), f_m\} \leftarrow$ Update by adding $M''_t(x''_{tj}, y''_{tj})$, $m=m+j$, $f_m =$ "$Accept$" for added locations
  $MAT_k \leftarrow$ Place mat Mat_l using $M''_t(x''_{tj}, y''_{tj})$, where $l=final_r$, at $O_f(x_f, y_f)$
END LOOP

Return: $area\{AR_o\}, k, \{k \times AM\}, \{(k \times AM) - area(AC_o)\}$

Appendix F – Algorithm for crane mat optimization using Reinforcement Learning

Algorithm 4: Crane Mat optimization using Reinforcement Learning approach.

Inputs:

$\{M_i(x_{ij}, y_{ij})\} \leftarrow$ Mat coordinates (2 options), $x_i, y_i \in \mathbb{R}$, $i \in [1,2], j \in [1,8]$
$\{Mat_l\} \leftarrow$ Mat drawings (2 options) for mat placement, $l{=}i \in [1,2]$
$\{G\} \leftarrow$ Number of mats used by Greedy approach (Algorithm-1), $G \in \mathbb{R}$
$\{P_n(x_n, y_n)\} \leftarrow$ Polygon coordinates (area required) with n vertices, $x_n, y_n \in \mathbb{R}$, $n \in [3, \mathbb{R}]$
$\{R_k(x_k, y_k)\} \leftarrow$ Starting polygon vertex for mat laying, $x_k, y_k \in \mathbb{R}$, $k \in [1,2]$
$\{\alpha, \gamma\} \leftarrow$ Learning rate, Discount factor, $\alpha, \gamma \in \mathbb{R}$

Initialization:

$\{O_m(x_m, y_m)\} \leftarrow$ all locations for mat placement, $x_m, y_m \in \mathbb{R}$, $m \in [1, \mathbb{R}]$, based on $R_k(x_k, y_k)$
$\{f_m\} \leftarrow$ Availability, against each Location, $f_m \in$ ["$Accept$", "$Reject$"]
$\{E_{im}\} \leftarrow$ Exploration, against each Location, $E_{im} \in [0,1]$, $i \in [1,2]$, $Explored = 1, Unexplored = 0$
$\{Q_{im}\} \leftarrow$ Q value against each mat location, $Q_{im} \in [0, \mathbb{R}]$, $i \in [1,2], m \in [1, \mathbb{R}]$
$\{AM\} \leftarrow$ calculate area of mat using $M_1(x_{1j}, y_{1j})$
WHILE $area\{AR_o\} \leq (AM/2)$ **DO**
  $\{f_{in}\} \leftarrow \{$"$Accept$"$\}$, for each combination, $i \in [1,2]$ and $n{=}m$
  $del(MAT_n) \leftarrow$ Delete any mats from previous episode, $n = G$
  $del(AC_o, AR_o) \leftarrow$ Delete any previous mat covered region & polygon region from previous episode
  $AC_o \leftarrow$ Generate mat area region with zero area
  $AR_o \leftarrow$ Generate polygon region
  For $n \leftarrow$ 1 to G **DO**
    $\varepsilon = (\sum_{i=1}^{m} E_m)/m$
    IF $\varepsilon \geq 0.1$ **THEN**
      $\{R_{mat}, R_{loc}\} \leftarrow \{rand \in [1,2], rand \in [1, m]\}$
    ELSE
      $\{R_{mat}, R_{loc}\} \leftarrow \{i, m\}$ for $maxi(Q_{im})$, with f_m = "$Accept$"
      $\varepsilon \leftarrow \{0.1\}$
    END IF
    $E_{im} \leftarrow 1, m = R_{loc}, i = R_{mat}$
    $M'(x'_j, y'_j) \leftarrow M'_i(x'_{ij}, y'_{ij})$, calculate using $O_m(x_m, y_m)$, $m = R_{loc}, i = R_{mat}$
    $A_i \leftarrow$ Generate mat region using $M'(x'_j, y'_j)$, $i = R_{mat}$
    $f_m \leftarrow \{$"$Reject$"$\}$, for all $O_m(x_m, y_m)$ covered by A_i, $i = R_{mat}$
    $AR_o \leftarrow AR_o \setminus A_i$, $i = R_{mat}$
    $AC_o \leftarrow AC_o \cap A_i$, $i = R_{mat}$
    $d_i \leftarrow$ Calculate distance between centroid of $M'(x'_j, y'_j)$ and $R_k(x_k, y_k)$, $i = R_{mat}$
    $Reward \leftarrow$ Calculate reward based on the mat placement A_i, d_i, AC_o and AR_o, $i = R_{mat}$
    $Q_{avail} \leftarrow Q_{im}$ at $m = R_{loc}, i = R_{mat}$
    $\{Q_{max}, Q_{mean}\} \leftarrow \{maxi(Q_{im}), mean(Q_{im})\}$, with corresponding f_m = "$Accept$"
    $Q_{sarsa} \leftarrow \varepsilon Q_{mean} + (1-\varepsilon) Q_{max}$
    $Q_{im} \leftarrow Q_{avail}(1-\alpha) + \alpha\{Reward + \gamma Q_{sarsa}\}, m = R_{loc}, i = R_{mat}$
    $MAT_n \leftarrow$ Place mat Mat_l using $M'(x'_j, y'_j)$, at $O_m(x_m, y_m)$, $l{=}R_{mat}, m = R_{loc}$
  END LOOP
END LOOP

Return: $area\,\{AR_o\}, k, \{k \times AM\}, \{(k \times AM) - area(AC_o)\}$

Appendix G – Q-Learning for global optimization

As stated before in Section 2.4.2., the structure of RL is composed of four parts: policy, a reward signal, a value function, and a model. A policy is a way an RL agent behaves at a given time. The value function defines the amount of reward and punishment the RL agent gets, and the model (optional) mimics the behaviour of the environment (Sutton & Barto, 2018). Q-learning is one of the RL algorithms with a model-free approach that can optimize the stochastic states and rewards (Lillicrap et al. 2015, Sutton and Barto 2018). The equation of Q-learning is as shown in Equation (17). The same application of RL is used in this section to train an agent to reach the global optimized location by trial-and-error. As the agent proceeds with the iterations (episodes), the value of Q is updated continuously. Accordingly, the RL agent updated the Q-table for states involved in each episode. The Q-learning will motivate the value function for decreasing the time required to reach the global optimization solution. A learning factor of 0.1 and a discount factor of 0.9 are employed in this simulation.

G.1. Methodology

This Appendix G divides the methodology into three main parts, the hypothetical structural support design, the greedy algorithm and its limitation, and the development of the Q-learning algorithm.

G.2. Hypothetical structural support methodology

A hypothetical design compares RL (Q-Learning) with the greedy algorithm in design optimization. A hypothetical steel plate of 0.25 m thick with dimensions of 112 m × 112 m is supported by four supports (as shown in Figure G.1). A couple of weights, forces, and moments act randomly and simultaneously on the plate, as shown in Figure G.1 and Figure G.2.

The four supports are permanent at the corners of the plate. Another adjustable support is meant to be placed anywhere under the plate (as shown in Figure G.3. There are 10^4 possible locations for the adjustable support. The objective is to find the location using an FEA platform so that the deflection in the steel plate is the minimum. ANSYS (19.2) is used in the current research as the FEA platform for the simulation.

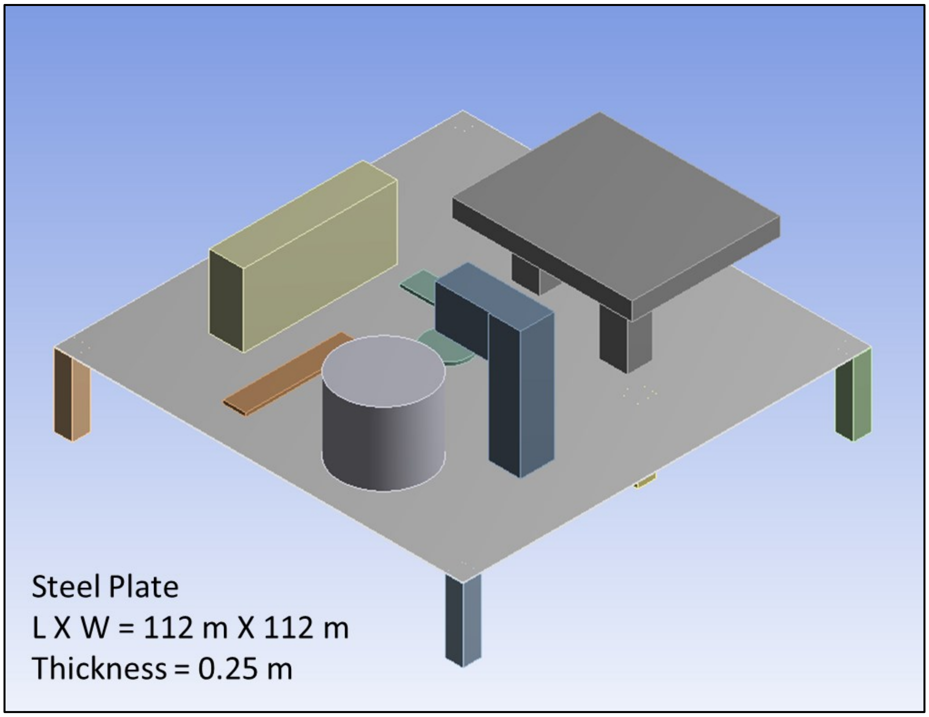

Figure G.1: Basic configuration of steel plate with random objects

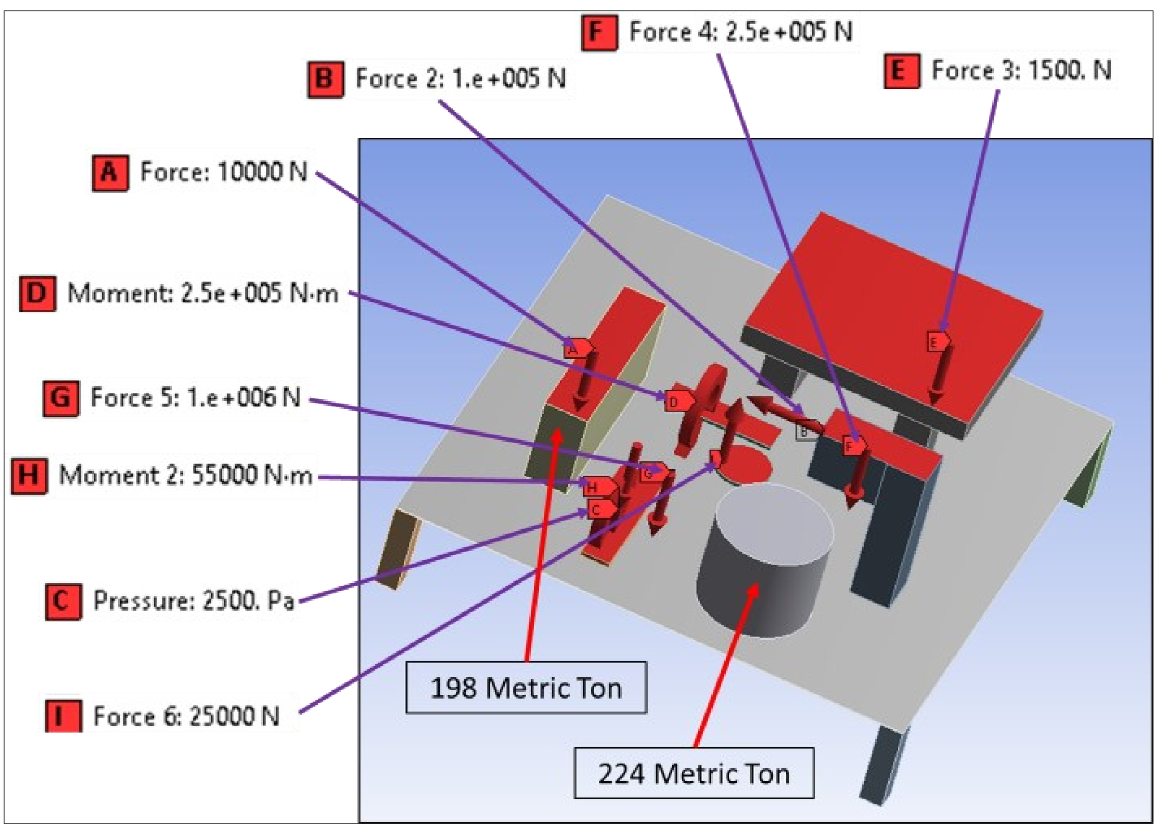

Figure G.2: Steel plate with randomly acting forces and moments

Figure G.4 shows the overall process. The RL agent is not aware of the model; it can only select the action in the form of the location of the adjustable support, and based on the action, it receives the reward and new state to move on. ANSYS takes approximately 30–40 seconds (Intel(R) Core(TM) i7-6700 CPU @ 3.40 GHz using 16.0 GB RAM, running Windows 10) on average to simulate each location of the adjustable support, and delivers the deflection of the plate as the outcome of each state. The deflection in the plate determines whether the action was favourable or not, which in return, using the value function, provides a scalar value of reward or punishment to the agent.

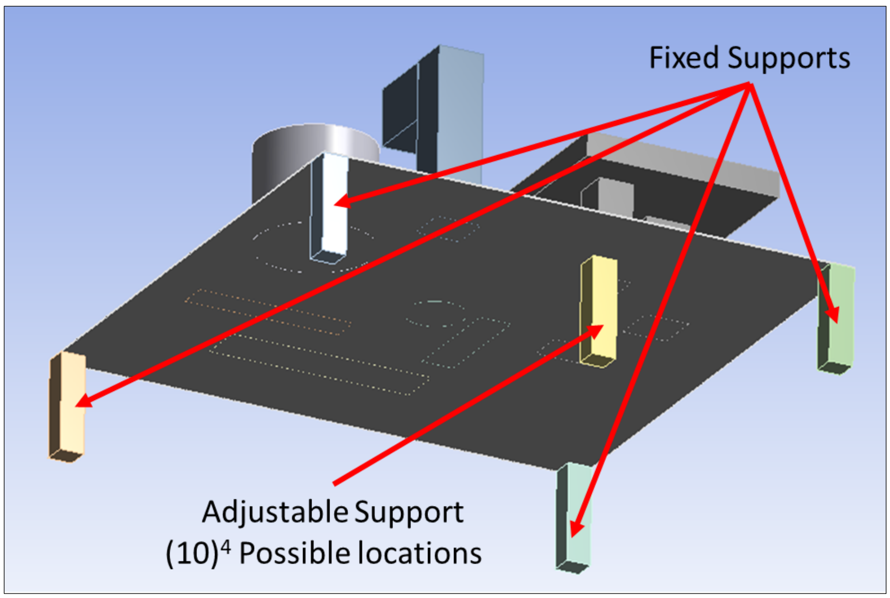

Figure G.3: Steel plate with adjustable support

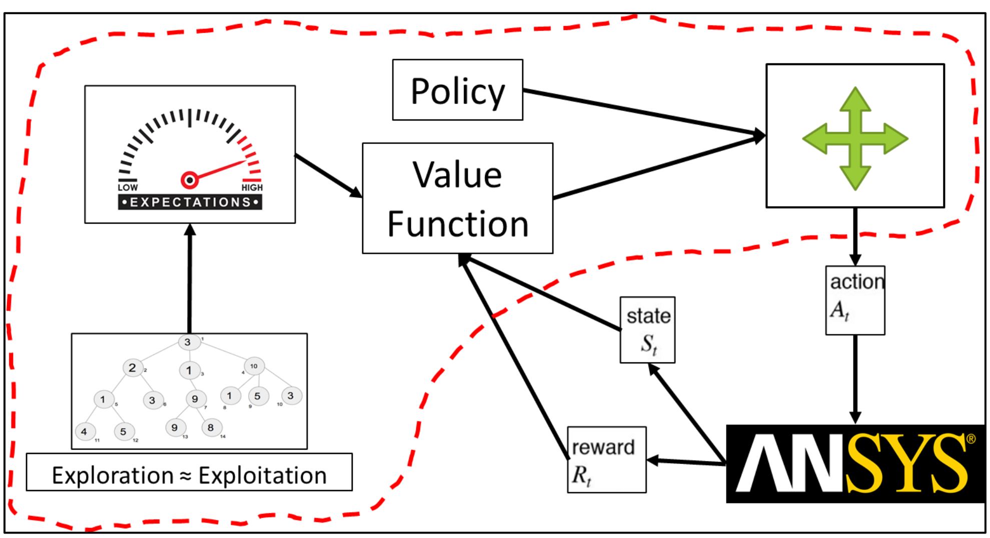

Figure G.4: Basics model of RL

The first approach was to explore all the possible locations and the respective deflection. The topography of the deflection with respect to each state is shown in Figure G.5. The latitudinal (along x-axis) movement is stated as x-move (100 steps), and the longitudinal (y-axis) movement is stated as y-move (100 steps). There are 10,000 combinations of x-move and y-move, as the position of the fifth support under the plate, to minimize the deflection. The optimal location is also indicated in Figure G.5. The total time taken by FEA to explore all the states was 101.94 hours (Intel(R) Core(TM) i7-6700 CPU @ 3.40 GHz using 16.0 GB RAM, running Windows 10), which is equal to 4.25 days in total.

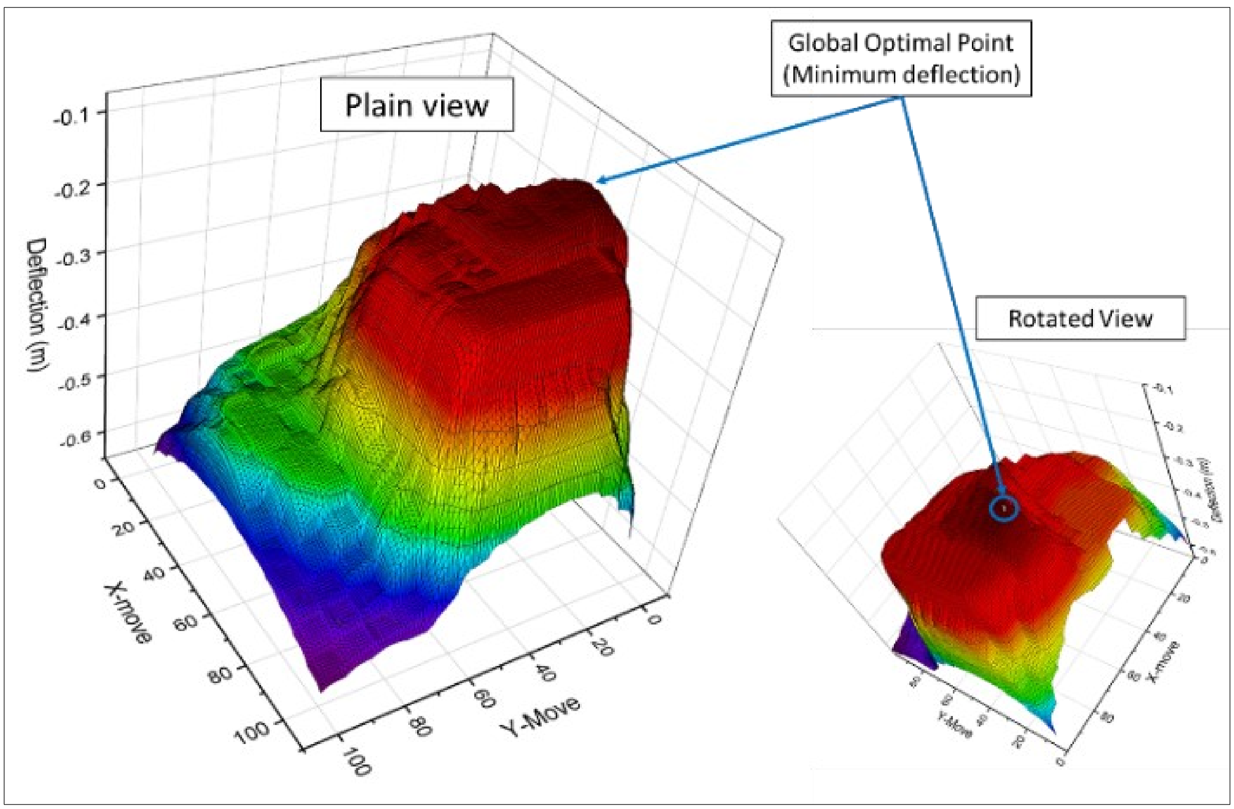

Figure G.5: All the possible states with deflection

G.3. Greedy algorithm approach and its limitations

For both RL and greedy algorithms, it is assumed that the final deflection is known but not the final location of the support. The easiest way to reach the optimal location starting from any edge is to use the greedy algorithm; however, the problem is that the greedy algorithm can confine to a local optimal location, and the local optimum location can become a sink for the greedy agent. This is the same as in the case of this problem. There are many local optimal locations. One of them is shown in Figure G.6. The greedy algorithm agent can only transcend this local optimization point by probing the heuristic tree further below (future actions). It is not easy to foretell the number of layers of the heuristic tree to be explored. It can be a trial-and-error method to search the greedy algorithm's level to find the minimum to maximum point to proceed further to the global optimization point. For this problem, the greedy agent goes several steps down in the heuristic tree for some local optimization locations to find the path towards the minimum deflection value (global optimum).

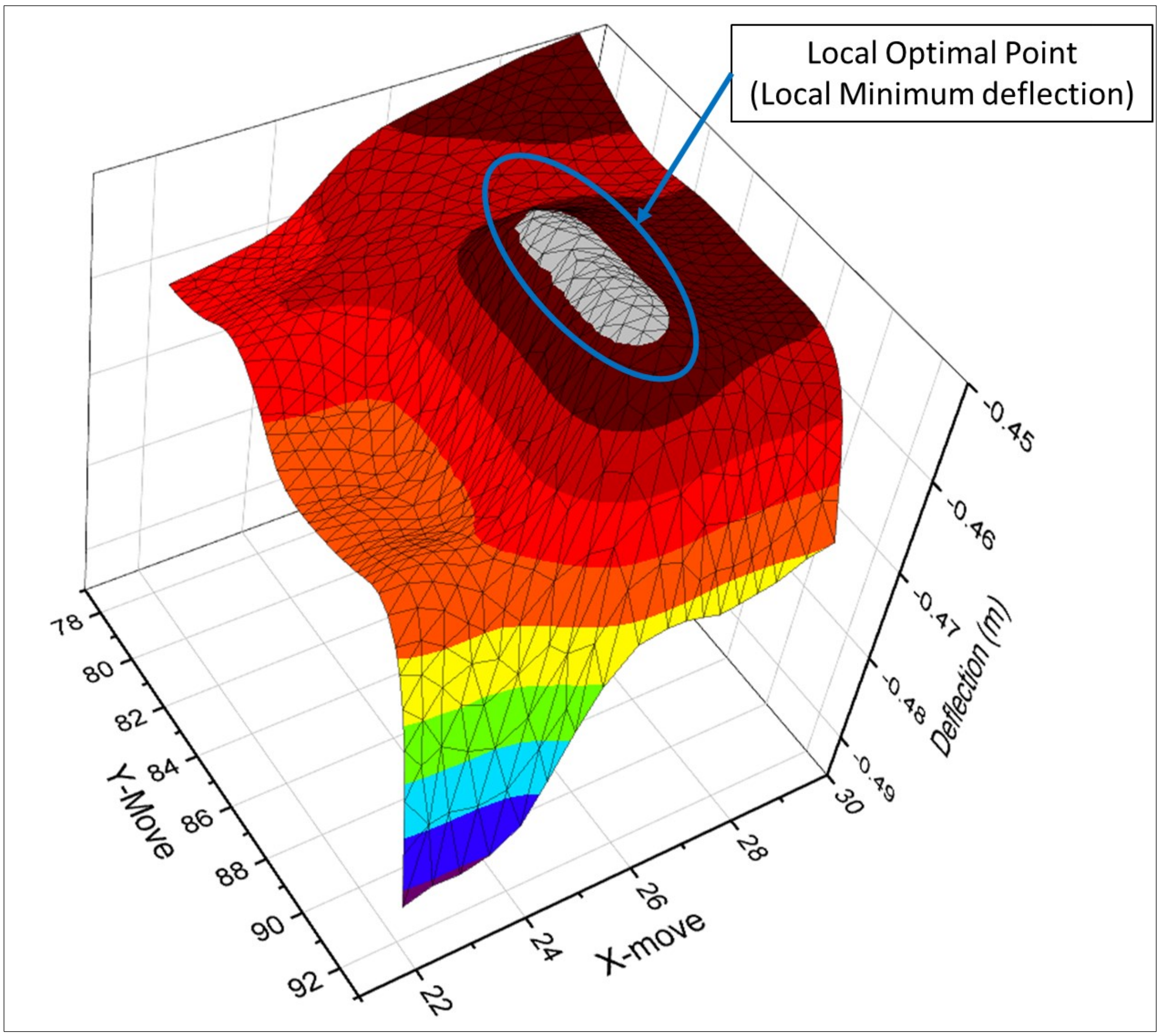

Figure G.6: Local optimization location

G.4. Development of Q-learning algorithm

Due to the limitations of the greedy algorithm, RL is explored in this example. Q-learning is used as the RL agent to search the minimum deflection. RL is a trade-off between exploration and exploitation. If the RL Agent does not explore the maximum states, the agent will promote exploration. As the percentage of explored states increases, the RL agent switches from exploration to exploitation to refine policy and reward value function. The exploration for the RL agent is defined in Equation (68).

$$P_t = \begin{cases} 1 - \dfrac{\sum_{j=1}^{m} s_{xj}}{\sum_{i=1}^{n} s_i} & if\ \dfrac{\sum_{j=1}^{m} s_{xj}}{\sum_{i=1}^{n} s_i} > 0.1 \\ 0.1 & if\ \dfrac{\sum_{j=1}^{m} s_{xj}}{\sum_{i=1}^{n} s_i} \leq 0.1 \end{cases} \tag{68}$$

where P_t is the probability of exploration at the current state, s_t, $\sum_{j=1}^{m} s_{xj}$ is the sum of the states explored after reaching s_t throughout all the episodes completed, and $\sum_{i=1}^{n} s_i$ is the total states ($i, j = 1,2,3, \ldots ,10{,}000$). As the states explored increase, the probability of exploration decreases, and the agent tends to move toward exploitation instead of exploration.

One of the significant features of RL is the value function for reward. There are two ways to define the reward function, one is the sparse reward function, and the other one is the shaping reward function. After reaching the final state, the sparse function provides a significant scalar reward value. On the other hand, the shaping reward function provides a fraction of the final reward on each state and increases the intensity of the reward as the agent moves closer to the final state (Gullapalli & Barto, 1992). The shaping reward function is used in the present study to expedite the agent's learning. The shaping reward function is formulated in Equation (69).

$$R_t = \begin{cases} -\left(\dfrac{D_t - D_f}{D_{max} - D_f}\right)^{sf} & if\ (D_t - D_f) > 0 \\ 1000 & if\ (D_t - D_f) = 0 \end{cases} \tag{69}$$

where D_t is the deflection of the plate at a state s_t, D_{max} the maximum deflection, D_f is the global optimized deflection, and sf is the shaping factor. The shaping factor can be of any real number. Results with various shaping factors are explored in this research. As the RL agent get closer to the minimum deflection D_f, the reward it gets increases. To speed up the learning and convergence (policy and value function), the sparse reward is also used when the agent reaches the global optimal location, when $(D_t - D_f) = 0$. This sparse reward will trickle down the effect in the form of an updated Q value. The Q-learning approach is formulated like the greedy approach. The agent starts randomly from any edge (400 options) and proceeds towards the final state (global optimal location).

G.5. Outcome and discussion

For the greedy algorithm, in some cases, the greedy agent needed to overcome the local optimum location by exploring 20 steps further (in the future). If the minimum deflection is known, it becomes easy for the greedy agent to explore the future steps until it comes out of the sink and proceeds towards the global optimum location. Over 1,000 episodes, 318 times, the greedy agent looked 20 steps ahead to overcome the local optimum sink, as shown in Figure G.7.

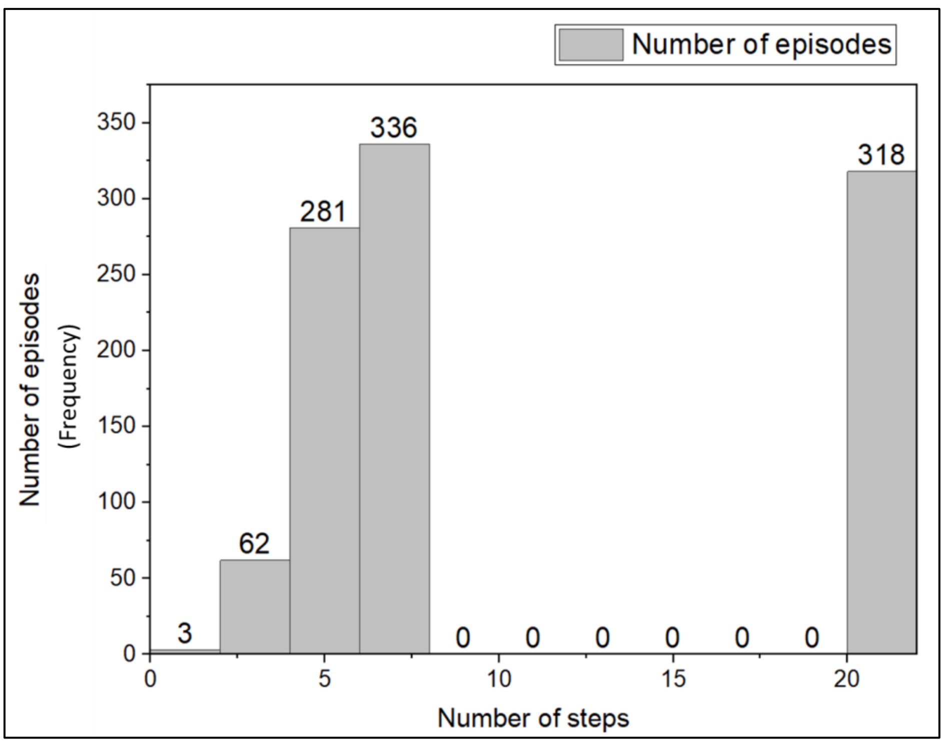

Figure G.7: Frequency of number of steps over 1,000 episodes

Q-learning is free of such drawbacks; however, the main problem with Q-learning is that it requires a state of exploration at the start and refines the Q-learning table to proceed with exploitation. The Q value for the states involved in the episode is updated towards reward and policy refinement with each episode. Due to its exploratory behaviour at the start, the RL agent requires more time to reach the global optimal location. The greedy agent takes approximately 6.1 hours (average over 1,000 episodes) to reach the global optimal location, whereas the RL agent needed approximately 30 hours (Intel(R) Core(TM) i7-6700 CPU @ 3.40 GHz using 16.0 GB RAM, running Windows 10) to reach the final state in the first episode. That was due to exploration instead of exploitation. As the RL agent moves from exploration to exploitation, the RL agent outperforms the greedy algorithm. Figure G.8 shows how quickly the RL agent overcomes the greedy algorithm in searching and reaching the final state. The RL agent learns the path, refines it, and improves each episode.

The outcome corresponds to various shaping factors for comparison purposes in Figure G.8. The results show that the RL agent with a shaping factor of 0.5 was slow in finding the final state. The agent became efficient with a shaping factor of 1.5, 2, 2.5, or 3. A shaping factor above 1 effectively ramps up the RL agent's learning process in this case.

Another vital aspect to observe was the number of actions taken by the RL agent to reach the final state (as shown in Figure G.9). The RL agent with a shaping factor of 1.5, 2, and 2.5 initiated fewer actions per episode to reach the final state.

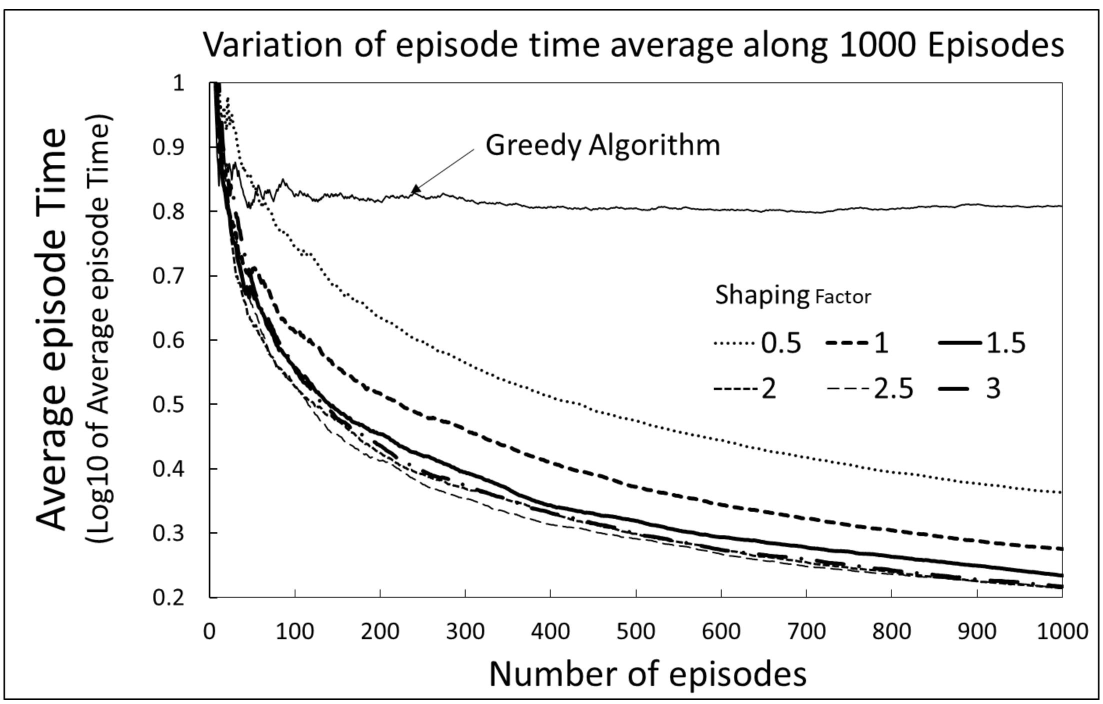

Figure G.8: Average episode time with various shaping factors

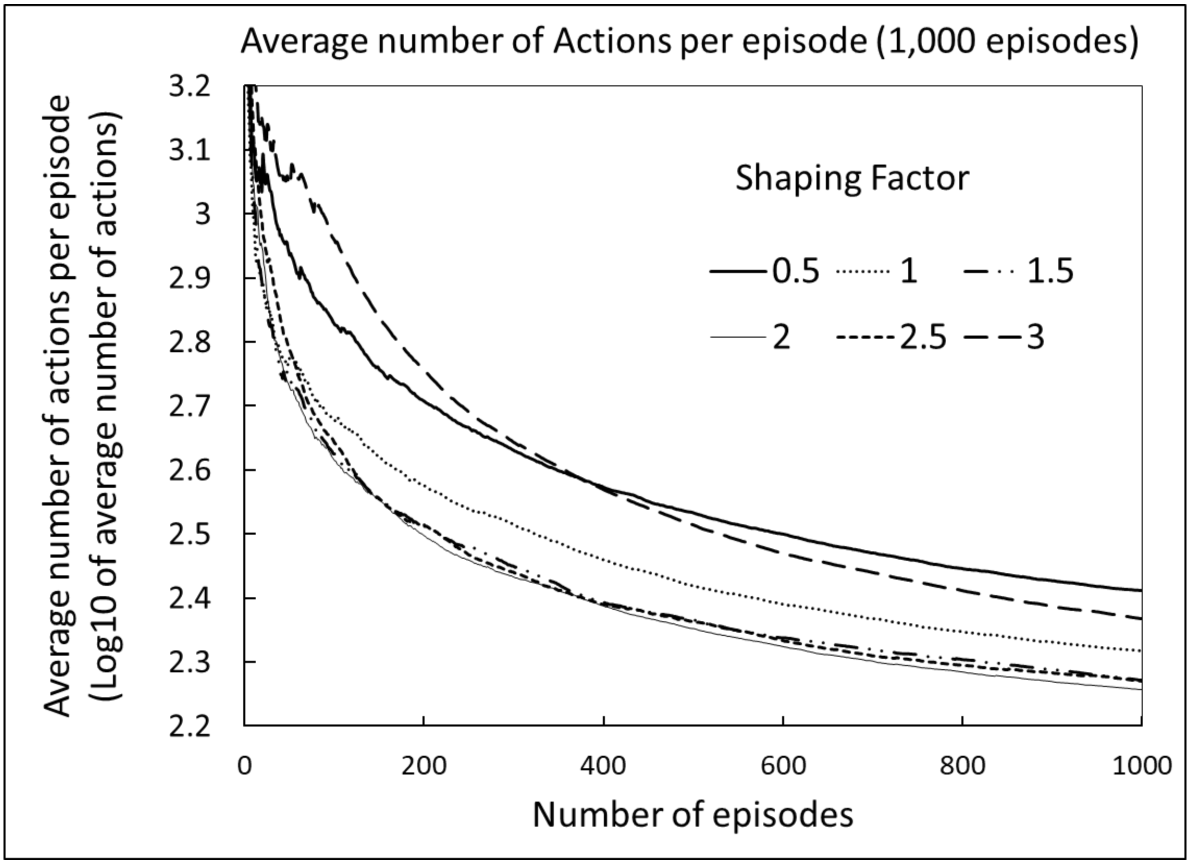

Figure G.9: Average number of actions per episode

Based on the data obtained for the case example used, the question arises as to which shaping factor was most effective for the RL agent to learn quickly, diminish the time required by shortening the path towards the final state and maximize the reward over the episode. The product of average time and average actions per episode can define the selection criteria. Figure G.10 shows that the value is minimum for a shaping factor of 2. This means that a shaping factor of 2 maximizes the learning process for the current case study.

Moreover, an additional sensitivity analysis could include the variation of states explored over 100 episodes, providing the ranking for these shaping factors. Figure G.11 shows that the RL agent with a shaping factor of 2 completed 100 episodes with just 89% states explored.

The RL agent needs to learn how to decrease the average amount of time for each episode, which is the outcome of the policy of the RL agent to maximize the cumulative reward along with each episode. The RL agent refines the policy and value function after each episode. The best example in this case, where the policy maximizes the reward by minimizing the path towards the final state along with the number of episodes.

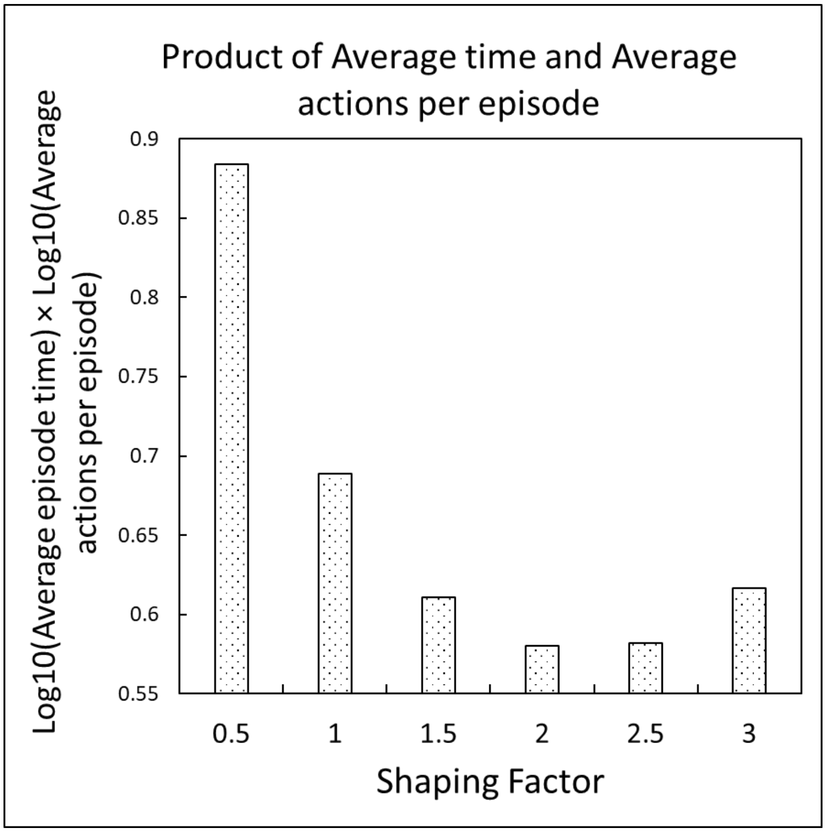

Figure G.10: Product of average time and average actions per episode

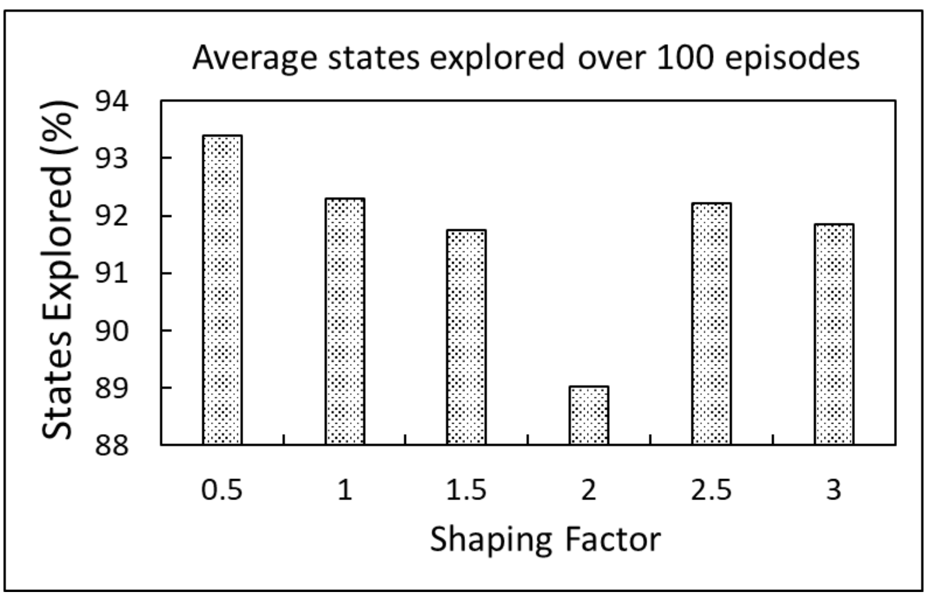

Figure G.11: Average states explored over 100 episodes

Figure G.12 shows the trendlines for episode time and reward over 100 episodes for the RL agent (with a shaping factor of 2). The trendlines converge towards the optimum for episode time and each episode's cumulative reward (value function).

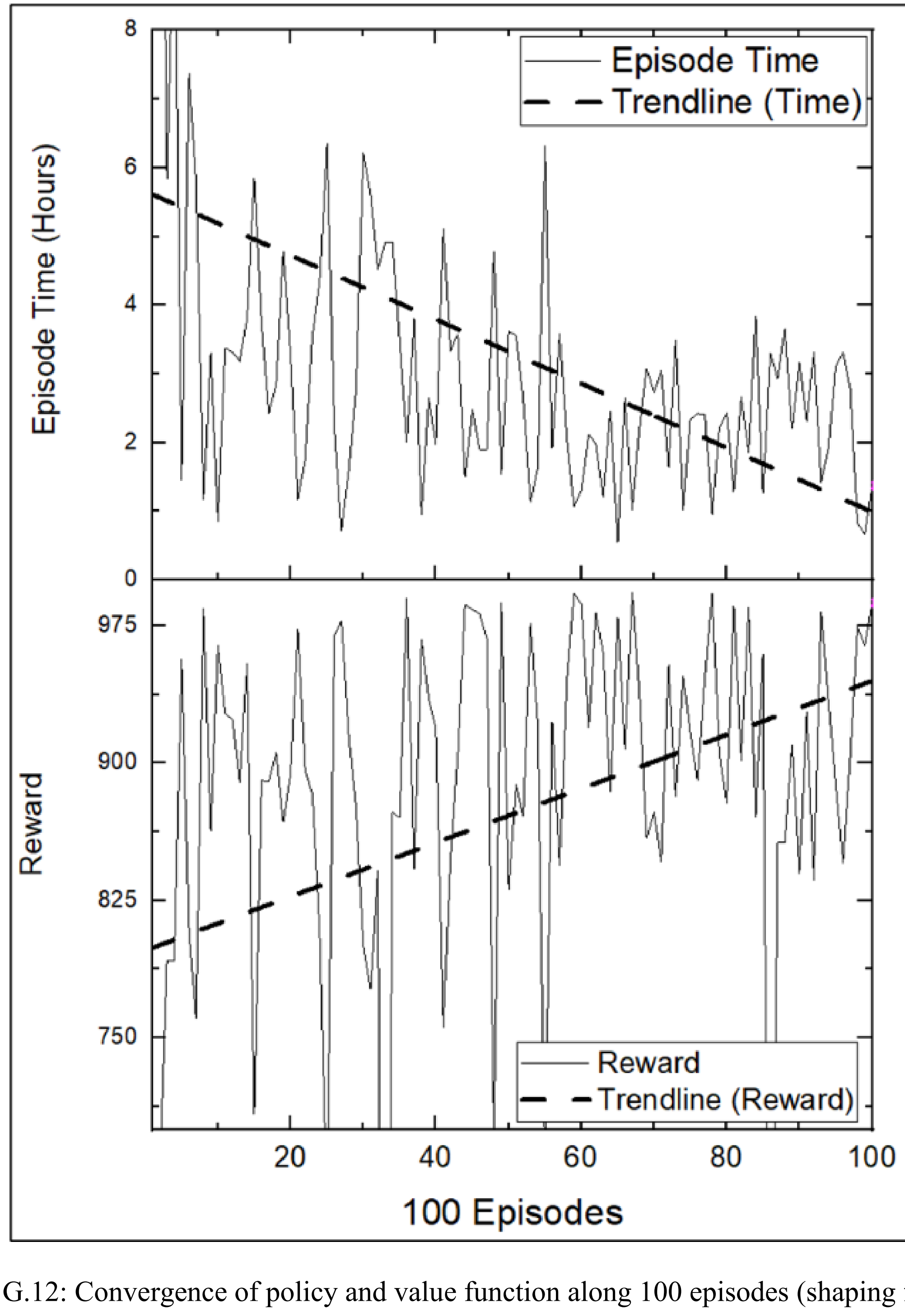

Figure G.12: Convergence of policy and value function along 100 episodes (shaping factor 2)

The RL agent cannot surpass the greedy algorithm approach for locating the global optimal point on the first try (first episode). Nevertheless, the greedy agent cannot overcome the local optimal location until it knows to search the steps further away from the local optimal location. The greedy agent becomes stable after overcoming the local optimal location. However, there is no dilemma of local optimal location for the RL agent. It is important to mention that, in the example above, there were 400 starting points for greedy algorithm and RL agent. The greedy algorithm, starting from the stochastic starting point for each iteration (after overcoming the local optimal location), takes a uniform cumulative average time to find the global optimal location. However, for the RL agent, the cumulative average time decreases along with the progression of episodes. After exploring the states, the RL agent refines itself with each episode and reaches the optimal location quicker than the greedy algorithm.